Fast methods for magnetic resonance angiography (MRA)

Bahareh Vafadar
Department of Electrical and Computer Engineering

A thesis presented for the degree of
Doctor of Philosophy
University of Canterbury,
Christchurch, New Zealand.
May 5th, 2014

To my husband, Navid
For his support and love throughout all my days in New Zealand

Acknowledgments

I would like to express my deepest gratitude to my supervisor, Professor Philip J. Bones for his support and excellence guidance throughout the research. He inspired me greatly to work in this project and led me to the right way. It was a great pleasure working with him. I also would like to thank to Dr Bing Wu for his generous help.

I would also thank my husband and best friend, Navid, for standing beside me and his faithful support. He has been my inspiration and motivation for continuing to improve my knowledge and move my life forward. I also thank my wonderful son, who has been the greatest blessing of my life and always making me smile.

Many thanks to my parents, who have always been an endless source of unconditional love. Thanks to them for allowing me to realize my own potential.

Abstract

Magnetic resonance imaging (MRI) is a highly flexible and non-invasive medical imaging modality based on the concept of nuclear magnetic resonance (NMR). Compared to other imaging techniques, major limitation of MRI is the relatively long acquisition time. The slowness of acquisition makes MRI difficult to apply to time-sensitive clinical applications. Acquisition of MRA images with a spatial resolution close to conventional digital subtraction angiography is feasible, but at the expense of reduction in temporal resolution. Parallel MRI employs multiple receiver coils to speed up the MRI acquisition by reducing the number of data points collected. Although, the reconstructed images from undersampled data sets often suffer from different different types of degradation andartifacts.
In contrast-enhanced magnetic resonance imaging, information is effectively measured in 3D k-space one line at a time therefore the 3D data acquisition extends over several minutes even using parallel receiver coils. This limits the assessment of high flow lesions and some vascular tumors in patients. To improve spatio-temporal resolution in contrast enhanced magnetic resonance angiography (CE-MRA), the use of incorporating prior knowledge in the image recovery process is considered in this thesis.

There are five contributions in this thesis. The first contribution is the modification of generalized unaliasing using support and sensitivity encoding (GUISE). GUISE was introduced by this group to explore incorporating prior knowledge of the image to be reconstructed in parallel MRI. In order to provide improved time-resolved MRA image sequences of the blood vessels, the GUISE method requires an accurate segmentation of the relatively noisy 3D data set into vessel and background. The method that was originally used for definition of the effective region of support was primitive and produced a segmented image with much false detection because of the effect of overlying structures and the relatively noisy background in images. We proposed to use the statistical principle as employed for the modified maximum intensity projection (MIP) to achieve better 3D segmentation and optimal visualization of blood vessels. In comparison with the previous region of support (ROS), the new one enables higher accelerations MRA reconstructions due to the decreased volume of the ROS and leads to less computationally expensive reconstruction.
In the second contribution we demonstrated the impact of imposing the Karhunen-Loeve

transform (KLT) basis for the temporal changes, based on prior expectation of the changes in contrast concentration with time. In contrast with other transformation, KLT of the temporal variation showed a better contrast to noise ratio (CNR) can be achieved.

By incorporating a data ordering step with compressed sensing (CS), an improvement in image quality for reconstructing parallel MR images was exhibited in prior estimate based compressed sensing (PECS). However, this method required a prior estimate of the image to be available. A singular value decomposition (SVD) modification of PECS algorithm (SPECS) to explore ways of utilising the data ordering step without requiring a prior estimate was extended as the third contribution. By employing singular value decomposition as the sparsifying transform in the CS algorithm, the recovered image was used to derive the data ordering in PECS. The preliminary results outperformed the PECS results.

The fourth contribution is a novel approach for training a dictionary for sparse recovery in CE-MRA. The experimental results demonstrate improved reconstructions on clinical undersampled dynamic images.

A new method recently has been developed to exploit the structure of the signal in sparse representation. Group sparse compressed sensing (GSCS) allows the efficient reconstruction of signals whose support is contained in the union of a small number of groups (sets) from a collection of pre-defined disjoint groups. Exploiting CS applications in dynamic MR imaging, a group sparse method was introduced for our contrast-enhanced data set. Instead of incorporating data ordering resulted from prior information, pre-defined sparsity patterns were used in the PECS recovery algorithm, resulting to a suppression of noise in the reconstruction.

Contents

Chapter 1

Introduction

This introductory chapter consists of an overview of the research and its objectives; and a guide to the structure of this thesis.
Magnetic resonance imaging (MRI) is a highly flexible and non-invasive medical imaging modality based on the concept of nuclear magnetic resonance (NMR). Compared to other imaging techniques, MRI has several unique aspects, which make it ideal in many clinical applications. MRI offers high resolution with high signal to noise ratio (SNR) and excellent soft tissue contrast without exposure of humans to ionizing radiation. MRI sensitivity to a wide range of contrast mechanisms, offers an easy assessment of both morphology and physiology, also gives access to parameters like flow, diffusion, perfusion, blood oxygenation, and many others.

A major limitation of MRI is the relatively long acquisition time due to the discomforts patients experience during a slow data acquisition. The slowness of acquisition makes MRI difficult to apply to time-sensitive clinical applications. This disadvantage limits the MRI capability to temporally resolve dynamic processes such as cardiac motion, brain hemodynamics or the passage of a contrast agent bolus in angiography. In dynamic imaging, the speed at which each individual frame from an MRI sequence can be acquired is limited by physical and physiological constraints. For example In applications such as cardiac MRI, the high speed of the moving object (heart) results in a compromise between the achievable spatial and temporal resolution of the reconstructed sequence. Data undersampling has been proposed as a good means of improving the temporal resolution in exchange for spatial resolution. The increase in the data acquisition speed is achieved by sampling the imaged object more sparsely in the k-space (frequency domain). The reduced amount of acquired data for each time frame results in an ill-posed reconstruction problem leading to significant artifacts and aliasing in the reconstruction.

Parallel MRI is a technique that exploits the intrinsic spatial encoding of multiple receiver coils (array coils) with distinct spatial sensitivities to speed up the MRI data acquisition. In parallel MRI (pMRI) reconstruction algorithms, the missing information is synthesized using sensitivity encoding information from the receiver coils. Moreover many other reconstruction techniques such as compressed sensing or imposing spatial-temporal constraints have been employed to compensate for the missing data acquisitions to remove the image artifacts. In dynamic contrast enhanced (DCE) imaging, a series of T1-weighted acquisitions (T1 is a relaxation constant which is explained in the next chapter) are utilized to quantify the pharmacokinetics of an injectable contrast bolus. Dynamic CE-MRI allows assessment of tissue properties such as the formation of plaque or vascular permeability. Clinical applications of DCE, like detection, localization, and staging of cancer or rational assessment of the chemotherapy efficacy, will benefit from improvements in spatiotemporal resolution. In this thesis we mainly focus on the pMRI reconstruction methods which incorporate additional prior knowledge to improve the image quality in Dynamic CE-MRI. A brief outline describing the focus of each chapter is provided below.

1.1 Thesis Outline

Chapter 2 is a compact insight to the MRI principle including the necessary introduction for the spatial encoding techniques in MRI. Also the effect of undersampling during the acquisition and parallel MRI are then briefly described. Since the parallel MRI modifies the acquisition process, it is necessary to know the principles of MRI to fully describe how parallel MRI works.

In chapter 3, a parallel MRI reconstruction formulation which has been presented as GUISE (Generalized UnalIasing using Support and sensitivity Encoding) which has been developed at University of Canterbury is reviewed. Once the basics of GUISE have been covered, we formulate the problem of imposing prior knowledge into the parallel MRI reconstruction. A new way to define the regions of support is introduced then and the performance of GUISE is investigated using different regions of support.

Chapter 4 lays out three different pMRI reconstruction methods and then describe algorithms we have developed for deriving a small set of temporal basis functions. A Karhunen-Loeve transformation (KLT) is proposed and applied to 3D contrast-enhanced magnetic resonance angiography (CE-MRA). We then present results which demonstrate by imposing a temporal basis based on prior knowledge of the contrast flow dynamics, the time resolution of CE-MRA sequences can be improved. We show a significant reduction in artifacts caused by the under-sampling of k-space is achieved by KLT basis derived from

prior expectation.

Chapter 5 primarily focus is on the compressed sensing theory and recovery algorithms. Then will see how the CS fundamentals have been extended in MRI recovery direction. A novel approach is then presented which is an alternative approach to capture the underlying information needed for optimal reordering in prior estimate based compressed sensing in parallel MRI (PECS). Finally, the performance of new method, SPECS is investigated using experimental data sets.

We focus on two CS techniques in CE-MRA and develop different frameworks to make accurate reconstructions from a small subset of k-space samples in chapter 6. Firstly, we focus on the two main sparsifying paths and one of the most well-known algorithms K-SVD dictionary learning. Next, we present a novel approach for training a spatio-temporal dictionary for CE-MRA using K-SVD for constructing effective dictionaries for the image series. The experimental results demonstrate improved reconstructions, on clinical undersampled dynamic images.
To cover the second proposed approach, a brief overview of topics related to group sparse modeling is given, aiming to exploit the structure of the MR images in sparse representation. We propose a reconstruction method that exploits the sparse representation structure and sparsity within dynamic MR images. Our method is an extension of the PECS that allows a prior knowledge of the underlying image to be incorporated in the CS recovery. The sparse representation of prior estimate is incorporated in the reconstruction process by assigning the pixels of sparsity domain to groups. Finally, the method implementation in time-resolved CE-MRA are presented. The performance and characteristics are investigated using volunteer study.

Chapter 7 is a summary of the work presented in this thesis and also provides suggestions for the future work.

Chapter 2

Magnetic resonance imaging

This chapter briefly provides the background of magnetic resonance imaging (MRI) including the nuclear magnetic resonance physics (NMR), image formation and parallel Magnetic Resonance Imaging (pMRI). More precisely, the method that may be used to acquire MRI images from the Nuclear Magnetic Resonance (NMR) signal and physical phenomena behind it are detailed in section (2.1). Section (2.2) describes the theoretical background of MR imaging. Parallel MR Imaging is introduced in Section (2.11), followed by a brief review of pMRI reconstruction methods. For more thorough and complete references see [123, 131].

2.1 Nuclear Magnetic resonance

Magnetic Resonance Imaging (MRI) is a flexible and non invasive medical imaging modality. In contrast to the other medical imaging methods which expose patients to ionizing radiation, MRI uses strong non-ionizing electromagnetic fields in the radio frequency range. In the last years, MRI became a common method for medical examination that produces 3D images of high-resolution with a high signal-to-noise ratio especially useful for soft tissues. MRI relies on the nuclear magnetic resonance (NMR), a quantum-physical phenomenon by which magnetically polarized nuclei emit an electromagnetic signal. Producing an NMR signal from a patient's body requires exposure only to non-ionizing radio frequency electromagnetic radiation.

The NMR phenomenon was described for the first time independently by Felix Bloch and Edward Purcell in 1946. Six years later, they were awarded the Nobel prize for Physics for their discovery. NMR relies on the fact that each proton of a tissue sample has a

quantum property called *spin*, which refers to its nuclear angular moment at the quantum mechanical level. By applying an external magnetic field, every element with nuclear spin may be excited and shifted to a higher energy level by absorbing a photon at a specific frequency. After some time, the excited elements return back to the energy equilibrium state, meanwhile releasing the absorbed energy as photons. The emitted electromagnetic signal gives information about physical and chemical properties of the excited elements. First MR images were obtained by Paul Lauterbur in 1973. Richard Ernst introduced an improved method of image acquisition in 1975, which has been used until today.

In the following, the attention is restricted to hydrogen nuclei (^1H) with only one unpaired proton. Such nuclei behaves as small magnetic dipoles with a random orientation. This assumption is reasonable, since in clinical MR imaging we primarily focus on the hydrogen atoms in water molecules in the patient's body. This is because living tissues consist mostly of water and fat which contain many hydrogen atoms and, therefore, approximately 63% of atoms in human body are hydrogen atoms. Other molecoules present in the body are able to produce an NMR signal, but (^1H) is by far the most abundant. Since (^1H) atoms exhibit the quantum spin angular momentum property, they are commonly called spins in MRI parlance.

Each spin has a microscopic magnetic moment $\vec{\mathbf{m}}$. If no external magnetic field is applied, the orientations are random: $\vec{\mathbf{M}} = \sum \vec{\mathbf{m}} = \vec{\mathbf{0}}$. However, if an external magnetic field $\vec{\mathbf{B_0}}$ is applied, protons will align along its orientation and a resulting magnetization $\vec{\mathbf{M}} \neq \vec{\mathbf{0}}$ will appear like shown in Fig.(2.1). In clinical imaging, the NMR signal is produced by applying three different electromagnetic fields to the spins in a patient's body. The first field is a strong, static field used to align the magnetic moments of the spins. This field is of constant magnitude and direction throughout the field of view (FOV). By convention, its direction is defined as the $\hat{z}$ axis, and it is called the $\vec{\mathbf{B_0}} = B_0\hat{z}$ field. In typical clinical imaging systems, $\vec{\mathbf{B_0}}$ is 1.5 to 3 Teslas.

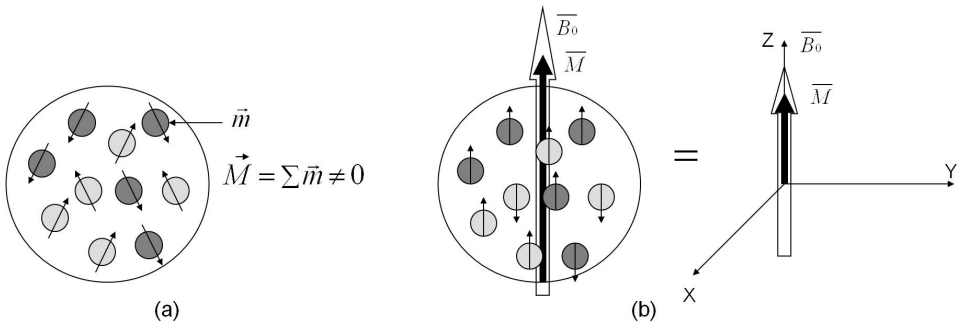

Figure 2.1: (a): magnetic moment at the initial equilibrium state; (b): magnetic moment in the presence of a stationary magnetic field of magnitude B_0

Actually, spins are not perfectly aligned along $\vec{\mathbf{B_0}}$, but have a circular movement around it at the Larmor resonance frequency $f_0 = \frac{h\gamma}{2\pi}B_0$, where γ is the gyromagnetic ratio related to the properties of the atom, h is Planck's constant and B_0 is the magnitude of the magnetic field $\vec{\mathbf{B_0}}$. For instance, the hydrogen atom, which is abundantly present in the human body and especially in the brain, has a gyromagnetic ratio $\gamma/2\pi = 42.58$ Mhz/Tesla. In general, $\vec{\mathbf{M}}$ can be split into two components as follows:

$$\vec{\mathbf{M}} = \vec{\mathbf{M}}_{xy} + \vec{\mathbf{M}}_z \tag{2.1}$$

where $\vec{\mathbf{M}}_{xy}$ and $\vec{\mathbf{M}}_z$ are the transversal and longitudinal components, respectively. The transversal component $\vec{\mathbf{M}}_{xy}$is in the $(x-y)$ plane, while the longitudinal component is colinear to the $\hat{z}$ axis. At the new equilibrium state, $\vec{\mathbf{M}}$ is aligned along $\hat{z}$ without transversal component (see Fig.(2.1)). Therefore, we have $\vec{\mathbf{M}}_{xy} = \vec{\mathbf{0}}$ and $\vec{\mathbf{M}}_z$ grows with both the concentration of protons in the tissue and the intensity of $\vec{\mathbf{B}}_0$.
Indirect measurement of $\vec{\mathbf{M}}$ is possible through switching its orientation in the $(x-y)$ plane, using an additional magnetic field $\vec{\mathbf{B}}_1$ at the Larmor frequency (see Fig.(2.2a)). This radio frequency (RF) magnetic field should have an angular frequency $f_1 = f_0$ in order to make the spins resonate and change their energy level.

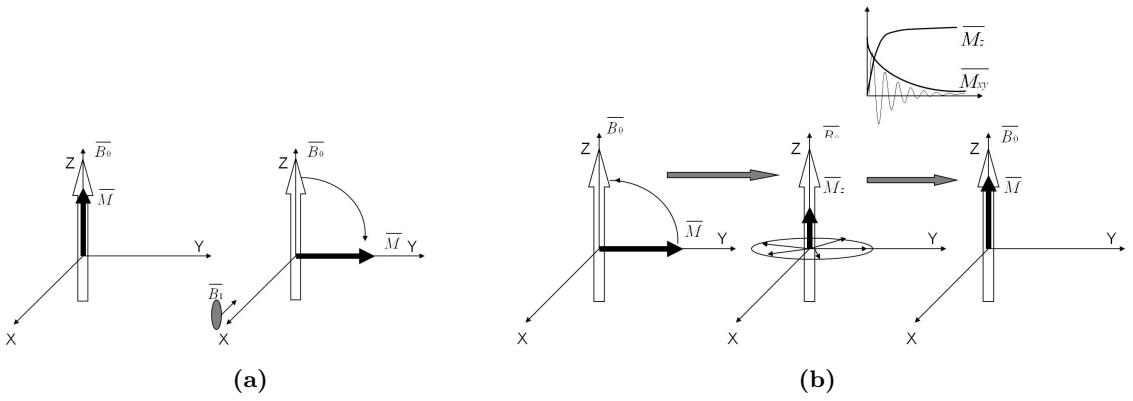

Figure 2.2: Precession movement of the magnetic moment(a): While the $\vec{\mathbf{B}}_0$ field is applied, $\vec{\mathbf{B}}_1$ (RF field pulse) is applied along the x axis with a frequency equal to the Larmor frequency (resonance), the net magnetization tips to the xy plane (on the y axis here). Tipping is proportional to strength of RF pulse; (b): After applying $\vec{\mathbf{B}}_1$ for a short duration, the spins relax back to their equilibrium state along z axis and will lead to a precession movement of the magnetic moment.

Classically, the angle that the magnetization vector makes to the main axis is known as the flip angle. The size of the flip angle is determined by the amplitude of the RF magnetic field applied and is an important parameter in MR pulse design. In Fig.(2.2a)the magnetization

vector is flipped to the transverse plane, so flip angle is 90°.

From an energetic viewpoint after excitations, spins are not stable. When returning to their equilibrium state, the spins will lead to a precession movement of the magnetic moment $\vec{\mathbf{M}}$ as shown in Fig.(2.2b). The energy difference between the states is used to measure the NMR signal and is called *free induction decay* (FID). This FID signal is acquired using a receiver coil put in the $(x-y)$ plane. The longitudinal projection $\vec{\mathbf{M}}_z$ returns back to its initial state in an exponential way parameterized by a time constant T_1 called the spin-lattice relaxation time. In practice, the constant T_1, which generally takes its values between 100 ms and 1000 ms, corresponds to the time when $\vec{\mathbf{M}}_z$ returns to 63% of its original value. Simultaneously, but independently the transversal projection $\vec{\mathbf{M}}_{xy}$ gradually decrease, and T_2 is the time constant (also known as the transverse or spin-spin relaxation time) that describes the rate at which net magnetisation in the transversal plane decays. The T_2 relaxation time is typically around 40-100 ms and corresponds to the time when $\vec{\mathbf{M}}_{xy}$ is at 37% of its value just after the spin excitation. Different body tissues are characterized by a given couple of time constants T_1 and T_2, which allow one to distinguish between the different tissues within the same MRI T_1 or T_2 weighted image. In fact, in brain imaging for instance, these time constants allow us to distinguish between the white matter, gray matter and cerebral spinal fluid (CSF).
More precisely, the voxel intensity in an image is related to the number of protons in the voxel weighted by the T_1 and T_2 relaxation times. These time constants across tissues generate what is called a contrast. T_1 and T_2-weighted MRI images are defined depending on the importance of the T_1 or T_2 constants in the images. By inserting appropriate delays into the pulse sequence between $\vec{\mathbf{B}}_1$ pulses and signal measurement, the strength of the signal is made to vary among the various tissues present in the FOV.

2.2 Magnetic Resonance Imaging

In this section, the technique for spatial encoding of the NMR signal is described which allows us to generate MR images. This was proposed for the first time by Lauterbur in 1973 who showed that it is possible to reconstruct images from the NMR signal using a superposition of linear magnetic field gradients. The MR Imaging procedure consists of three stages: 1)slice selection, 2)phase encoding and 3)frequency encoding.

Gradient fields

Spatial localization is achieved by applying spatially varying magnetic fields on top of the static magnetic field $\vec{\mathbf{B}}_0$. An RF field applied at the Larmor frequency simultaneously

excites all the molecules and gives an output that is the sum of the spins, which does not provide any spatial information. In MRI, to localize the spin excitations, three gradient coils are used to generate additional gradient fields $\vec{\mathbf{G}}$. These gradient coils have linearly varying field strengths in x, y and z direction respectively. The total intensity of the magnetic field at coordinate (x, y, z) is as follows:

$$|\mathbf{B}(x,y,z)| = |\mathbf{B}_0(x,y,z)| + |\mathbf{G}(x,y,z)| = |\mathbf{B}_0(x,y,z)| + xG_x + yG_y + zG_z, \tag{2.2}$$

where G_x, G_y and G_z are the gradient strengths. Gradient magnetic fields $\vec{\mathbf{G}}$ are fields oriented along the z axis and superimposed on the main magnetic field. As a result, overall field strength is made to vary linearly along a certain direction and be position dependent. This consequently makes the resonance frequency also spatially dependent position.

Bloch equation

According to the Bloch equation, the behavior of the magnetization vector $\vec{\mathbf{M}}$ in time is represented by:

$$\frac{\partial \mathbf{M}}{\partial t} = \gamma(\mathbf{M} \times \mathbf{B}), \tag{2.3}$$

where $\vec{\mathbf{B}}$ denotes the total magnetic field consisting of the main magnetic field $\vec{\mathbf{B}}_0$, the excitation pulse $\vec{\mathbf{B}}_1$ and the gradient fields $\vec{\mathbf{G}}; \vec{\mathbf{B}} = \vec{\mathbf{B}}_0 + \vec{\mathbf{B}}_1 + \vec{\mathbf{G}}$. A simpler coordinate system is the rotating frame, in which the $(x - y)$ plane rotates around the z-axis at a frequency $\Omega = -\gamma B_0$. Since the vector $\vec{\mathbf{M}}$ is observed in the rotating frame, the precession because of the $\vec{\mathbf{B}}_0$ is not seen. The magnetization vector $\vec{\mathbf{M}}$ consists of two components, longitudinal M_z and transversal M_T, each of which is dependent on a relaxation parameter, thus:

$$\frac{\partial M_z}{\partial t} = -\frac{M_z(t) - |\mathbf{M}_0|}{T_1}, \qquad \frac{\partial M_T}{\partial t} = -\frac{M_T(t)}{T_2}. \tag{2.4}$$

where M_0 is the magnetization vector in the equilibrium state. The above equation is a general form of the equation of motion of the spin system that describes the precession of the net magnetization vector about the z axis. The behavior of the magnetization vector

M can be described as:

$$\begin{bmatrix} \frac{\partial M_x}{\partial t} \\ \frac{\partial M_y}{\partial t} \\ \frac{\partial M_z}{\partial t} \end{bmatrix} = \begin{bmatrix} -1/T_2 & \Omega & -\gamma B_y^r \\ \Omega & -1/T_2 & -\gamma B_x^r \\ \gamma B_y^r & B_x^r & -1/T_1 \end{bmatrix} \begin{bmatrix} M_x \\ M_y \\ M_z \end{bmatrix} + \begin{bmatrix} 0 \\ 0 \\ |\mathbf{M}_0| / T_1 \end{bmatrix} \tag{2.5}$$

where the components of $\vec{\mathbf{B}}$ have been written with r superscripts to denote that it is a rotating frame.

2.3 Slice selection

Although 3D imaging techniques have been developed more recently (3D- EPI [2] or EVI [150]), the MRI technique generally proceeds by a 2D acquisition (slice by slice). Doing so, the first step in spatial encoding is selective excitation. Consider acquiring a slice located at some z position in the Cartesian coordinate system (x, y, z). In order to excite the spins belonging to a slice in (x-y) plane, a magnetic field gradient $\vec{\mathbf{G}}_z$ orthogonal to the plane (x-y) is applied. For the excited spins, the related Larmor frequency is dependent on $\vec{\mathbf{B}}_0$ as well as the gradient field along the z direction at the acquisition time.

$$f(x, y, z) = \frac{\gamma}{2\pi}(|\mathbf{B}_0(x, y, z)| + zG_z) \tag{2.6}$$

Hence, the Larmor frequency of these spins can be distinguished from spins belonging to the rest of the imaged object.

The intensity of gradient fields is on the order of several μT and they are switched on and off during the acquisition in order to encode the spatial position of the NMR signal. Fig.(2.3) shows a simple example of the spatial encoding by a linear gradient field. The next step aims at spatially encoding the NRM signal measured from a given slice by applying frequency and phase encodings.

2.4 Frequency encoding

In frequency encoding step, the spatial position along the x-axis is encoded using the precessing frequency of the spins. The x direction is also called the read-out direction since the frequency encoding gradient is turned on during the signal read-out (acquisition of the NMR signal). Subject to this frequency encoding gradient $\vec{\mathbf{G}}_x$ is applied in the

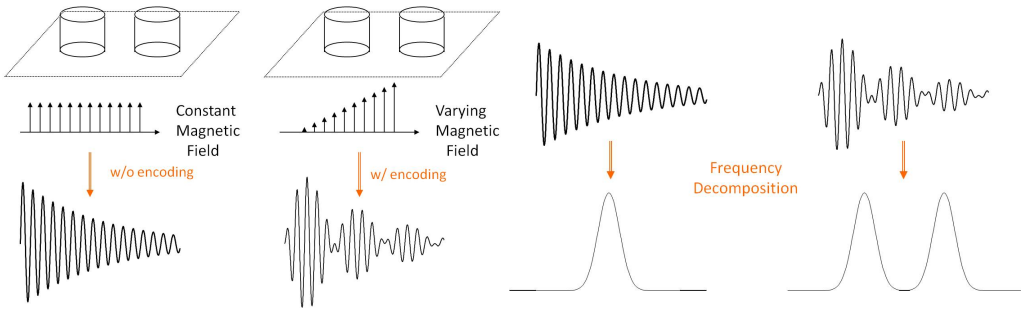

Figure 2.3: Selective excitation by applying a linear gradient field. (a) A simple example of Spatial Encoding; when the patient is under an uniform magnetic field B_0, all the spins along the z axis (field direction) will be simultaneously excited at the same Larmor frequency. A linearly varying field only excite molecules a certain frequency band by applying a RF pulse sequence. (b) Spatial Decoding of the MR Signal can be achieved by frequency decompositon of the obtained signal.

x direction, the spins will precess at a Larmor frequency. So the precessing frequency becomes dependent on x and the longer the applied gradient field $\vec{\mathbf{G}}_x$, the higher the spatial frequency in the measured 1D signal:

$$f(x,t) = \frac{\gamma}{2\pi}\left|\mathbf{B}_0\right| + x\frac{\gamma}{2\pi}G_x(t) \tag{2.7}$$

If a receive coil is placed near the object, the oscillating magnetization vector induces a voltage in the coil. This voltage is the MR signal that is used for imaging. The measured frequency encoded signal from the excited Field of View (FOV) is as follow:

$$\begin{aligned} F(t) &\propto \int\int_{slice} \rho(x,y)e^{-i2\pi f_x t}dxdy \\ &= \int\int_{slice} \rho(x,y)e^{-i\gamma G_x x t}dxdy \end{aligned} \tag{2.8}$$

Here, ρ denotes the spin density in the imaged volume. The received signal is a sum of harmonic functions with different frequencies and amplitudes. The amplitudes correspond with the magnetization of the tissue and the frequency of the wave is related to the position on the x-axis. Fourier transformation is used to analyze the signal and retrieve the magnitudes and frequencies of all harmonics present in the measured signal.

2.5 Phase encoding

The spatial position of the received NMR signal along the third spatial direction, i.e. the y-axis is required to be encoded. Phase encoding is performed by imposing a gradient field $n\vec{\mathbf{G}}_y$ in the direction of the y-axis for a time interval T_y before the readout where the integer n changes for each acquisition. This affects the precessing frequency only for the short time when the gradient is turned on. During this time, the spins precess at different Larmor frequencies. After the gradient has been switched off, the precession frequency returns to a constant value over the plane, while the imprinted phase remains proportional to y. Their phase shift is:

$$\varphi(y) = \frac{\gamma}{2\pi} y n G_y T_y, \tag{2.9}$$

This process is called phase encoding. Therefore within a given slice, spins located at a spatial position (x,y) precess at a unique frequency.

$$F(n, T_y) = \int \int_{slice} \rho(x, y) e^{-i2\pi\varphi(y)} dx dy \tag{2.10}$$

However, in contrast with frequency encoding while the gradient $n\vec{\mathbf{G}}_x$ was applied once, the phase encoding step needs to be repeated by changing either the gradients module $n\vec{\mathbf{G}}_y$ or duration T_y to cover all the imaged space.

2.6 Fourier imaging

This section describes the the principles of Fourier MR imaging in 2D and 3D Cartesian coordinate. Given that the thin region to be imaged has been selectively excited, then the objective is to form a contrast map of different tissues within the excited region. The acquired Fourier coefficients of the overall magnetization, known as k-space, are employed to reconstruct the real image by an inverse Fourier transform according to Eq.2.11. The idea of using the k-space to describe gradient encoding was introduced by Ljunggren and Twieg independently in 1983, and this convention had a major impact in the understanding of the time-domain signal and even creation of MR acquisition sequences [187], [187].

MR imaging relies on three major pulse sequences: spin echo, inversion recovery, and gradient recalled echo. The following definitions of parameters are used in the sequence:
TE: Echo Time: the time between the RF excitation and the signal acquisition time or

equivalently the time duration which the transversal magnetization returns to its initial value. Consider two different tissues belonging to the same imaged FOV, each of them has its own T_2 relaxation times. If TE is long comparing to the relaxation times in tissues, their initial transversal magnetizations will be recovered, and it will be impossible to distinguish the tissues although they have different transversal relaxation times. However, if TE is short, the magnetization of the tissue with the faster T_2 will return faster than the other one to its initial situation. The measured signal from the tissue with slower T_2 will therefore be bigger, which defines the T_2 contrast.
TR: Time of Repetition: the time between successive excitation pulses for a given slice. If time of repetition is less than the time required for M_z to fully relax, the available magnetization will be reduced. Therefore the longitidunal relaxation, and so the T_1 contrast of a given MRI sequence is influenced by TR. In fact, the measured signal from the tissue with fast T_1 will be stronger, which defines the T_1 contrast.

As an example, the description of an often used GRadien-Echo (GRE) excitation sequence is shown in Fig.(2.4). The simultaneous application of a negative gradient in the k_x and k_y direction leads to the diagonal traversal of k-space shown in Fig.(2.4b). At this point, signal acquisition can take place. During signal acquisition, a positive gradient G_x is applied, which causes the magnetization to rephase, or in terms of k-space moves the signal toward the center of k-space in the read out direction. A complete rephasing of the spins results in magnetization echo and the continued application of the read gradient results in a further dephasing of the spins. The echo occurs at the point where the gradient moments are completely compensated. For a readout gradient with the same amplitude as the dephasing gradient which is applied for twice the time, the echo is in the middle of the readout line.

In the described experiment in Fig.(2.4) only one line in k-space is acquired. In order to obtain a full coverage of the 2D k-space, the experiment has to be performed multiple times with different step in the phase encoding. Then a 2D inverse Fourier transform of the completed k-space data set gives an image of the underlying magnetization. For example, for a matrix size of 128×128, 128 data points have to be acquired in the read direction and 128 phase encoding steps has to be performed. Remember that the time between two subsequent excitation pulses with TR (repetition time), the total time for the experiment is equal to 128 TR. In 3D imaging (3D spatial encoding), the whole imaging volume is excited and two phase encoding gradients and one read gradient are applied. For an imaging matrix of $128 \times 128 \times 128$, 128×128 phase encoding steps have to be performed, that drastically increases the acquisition time.

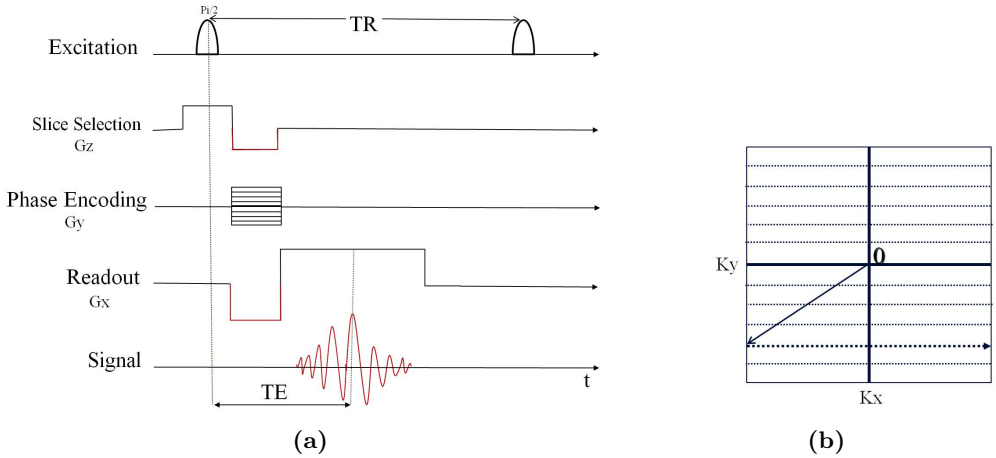

Figure 2.4: A typical diagram for MRI frequency encoding, Gradient-echo imaging. (a) A pulse sequence diagram showing the relative timing of the RF and gradient pulses applied as part of the three step process to localize and encode the MR signal for image formation. The frequency-encoded MR signal echo is measured during a sampling period centered at the echo time, TE. Additional gradient pulses (outlined in red) are required immediately after the slice selection gradient and before the frequency encoding gradient. These additional pulses ensure that any de-phasing of the transverse magnetization caused by the imaging gradients is canceled out once the echo time, TE, is reached. This results in the echo reaching its maximum possible signal at this point. (b) Traversal of k-space for the gradient echo sequence shown in a). The k-space is filled line by line.

2.7 Signal equation

The total transversal magnetization M_T is represented as a complex number using $M_T = M_x + iM_y$, where i is the complex unit. The complex signal F(t) is acquired by integrating the Bloch equation in Eq.(2.5). Assuming $m(x, y)$ as the magnetization on coordinates (x, y) after the excitation, the received signal $F(t)$ corresponds to the integral of the magnetization over the whole excited slice is:

$$F(t, n) = \int \int_{x,y} m(x, y) e^{-i(xk_x + yk_y)} dxdy \tag{2.11}$$

Assuming $k_x = \gamma G_x(t - T_E)$ and $k_y = -\gamma n G_y T_y$, the values of k_x and k_y are functions of the time $(t - T_E)$ and the number of phase-encoding steps n. The measured signal $F(t, n)$ can, therefore, be written as a function $F(k_x, k_y)$. The domain of F is the (k_x, k_y) plane which is referred to as the k-space. Practically, k-space values of $F(k_x, k_y)$ are acquired at discrete grid by sampling the signal $F(k_x, k_y)$ at appropriate time intervals t_f and for appropriate phase encoding gradients nG_y with $n = -Y/2, ..., Y/2$. The image in discrete domain f is obtained as a discrete inverse Fourier transform: Therefore regarding

the precession frequency of the excited spins after a frequency and phase encoding steps, discrete time domain image can be expressed generally as:

$$f(x,y) = \frac{1}{XY} \sum_{k_x=-X/2}^{X/2} \sum_{k_y=-Y/2}^{Y/2} F(k_x,k_y)\ exp^{i(k_x x + k_y y)}, \tag{2.12}$$

where the number of the sampling steps are denoted by X and Y, respectively.

2.8 Data acquisition considerations

2.8.1 Resolution and FOV

The field of view (FOV) refers to the area that is covered by imaging. In Fourier imaging, there are two sampling criteria that determine a proper image recovery: the k-space data sampling frequency and k-space size, which respectively determine the field of view (FOV) and image spatial resolution. In uniform Cartesian sampling, the k-space sampling frequency needs to satisfy the Nyquist sampling requirement [166]. For the case of a constant read gradient G_x, sampling is performed along the frequency encoding direction by taking data at uniform intervals Δt in time with the k-space step as follow:

$$\Delta_{k_x} = \gamma G_x \Delta t \tag{2.13}$$

Note that the discrete uniform sampling of k-space results in periodic repetition in the image space. If the encoded FOV is smaller than the object to be imaged, aliasing occurs. In order to avoid aliasing artifacts, which refers to the overlapping of the repetitions, the sampling rate needs to satisfy the sampling theorem for signal recovery (Nyquist sampling limit). Thus the sampling frequency of a spatially (or temporally) varying signal must be at least double the highest frequency you wish to record. The smallest step in k-space Δ_{k_x} and Δ_{k_y} determine the largest wavelength, or so called the size of the FIeld-of-view (FOV_x, FOV_y).

$$FOV \propto \frac{1}{\Delta k} \tag{2.14}$$

Therefore the image resolution is inversely proportional to the maximum extent of the covered k-space sampled as illustrated in Fig.(2.5) [1].

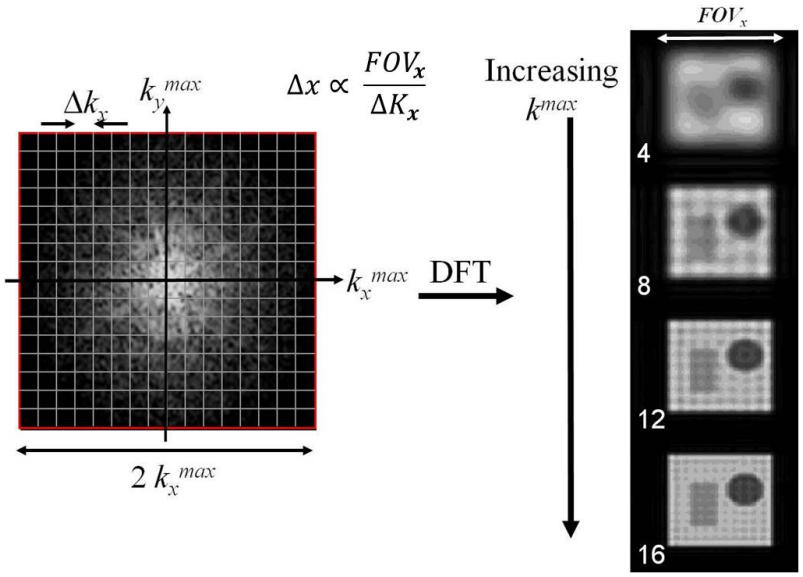

Figure 2.5: Field of view and resolution in Cartesian sampling. The number of samples to be measured in each direction determines the area of k-space coverage and so affect the spatial resolution of the image. Also the spacing between the k-space samples in each direction determines the respective size of FOV. The FOV in the image domain is inversely proportional to the k-space sampling interval. Denser sampling of k-space corresponds to larger FOV. If the encoded FOV is smaller than the object to be imaged, aliasing occurs.

Although high spatial resolution images are usually desirable in the image domain, there is a trade-off between spatial resolution and the data acquisition time. The data acquisition for a 3D volume (either by acquiring consecutive 2D slices or direct 3D Fourier imaging) might be performed within 15 to 20 minutes which this long scanning time easily leads to several potential problems, like ghosting artifacts. Ghosting artifacts are in the most cases caused by motion of the imaged object (e.g., arterial pulsations or respiratory motion). The fundamental approach to reduce the motion artifacts is to shorten the scan time, either employing a faster imaging sequence or reducing the amount of data acquisition.

2.8.2 K-space trajectories

Since the image reconstruction is achieved by a simple two-dimensional Fast Fourier Transform (2-D FFT) in Cartesian k-space sampling, it is the most frequently used sampling pattern. However, the k-space acquisition in MRI is not limited to the rectilinear

[1]Figure reproduced from Image formation course lecture slides (by Karla Miller), available at http://users.fmrib.ox.ac.uk/ karla/grad-program/image-formation.html

Cartesian sampling. In fact, due to the flexibility of advanced gradient systems, different trajectories to traverse the k-space can be achieved. A few examples of the most popular Cartesian trajectories are shown in Fig.(2.6).

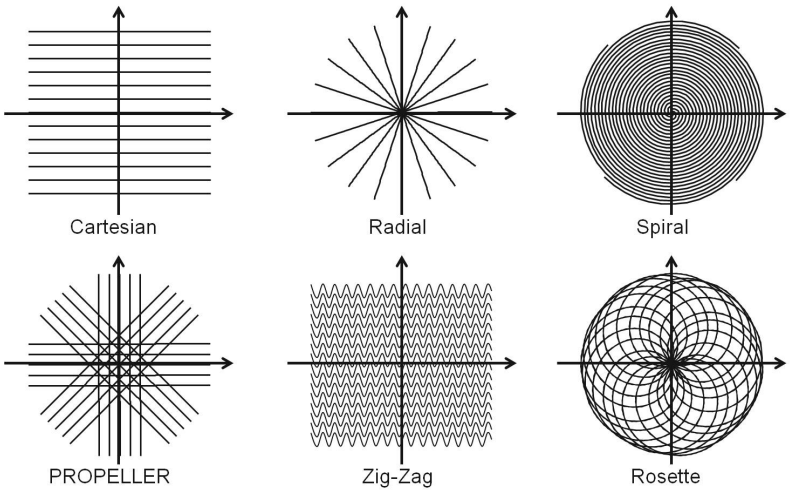

(a)

Figure 2.6: Six possible k-space trajectories

The radial trajectory, also known as projection reconstruction (PR), is the most popular non-Cartesian trajectory since the center of k-space is often resampled during the acquisition, making such a dataset relatively robust against motion artifacts [95]. In the spiral sampling, k-space coverage is achieved with a few interleaved spiral readouts, with longer read duration. Spiral MRI has several advantages over Cartesian MRI such as faster acquisitions, reduced demand in gradient and robustness against bulk physiologic motion [67], [11]. The advantage of PROPELLER trajectory as a hybrid between Cartesian and radial sampling, is its overlapping central parts of k-space which can be used for motion correction [141]. In trajectories with variable sampling density, like radial or variable-density spiral, artifacts caused by undersampling are not as pronounced as in Cartesian sampling.In respect to the Nyquist sampling theorem, for nonuniform sampling, the Nyquist limit is applied to the largest distance between two samples in k-space or in another generalization to the average sampling rate [136]. Clearly the disadvantage of non-Cartesian trajectories is that the image reconstruction becomes more complicated. In these cases, the gridding algorithm is the common and robust approach to resample the k-space data set before applying inverse FFT.

2.8.3 SNR and imaging speed limitations

An important limitation in MRI, the trade off between the signal-to-noise ratio (SNR) and the imaging speed, will be briefly described here. The relationship between the MR signal and the amount of image noise present is defined as the signal-to-noise ratio (SNR). Mathematically, the SNR can be expressed as the measured signal intensity in a region of interest (ROI) divided by the standard deviation of the signal intensity in a region outside the anatomy or object being imaged (i.e. a region from which no tissue signal is obtained). A high SNR is desirable in MRI and depends on the parameters such as slice thickness and receiver bandwidth, FOV and magnetic field strength. One way to improve the SNR is using an array of small surface coils placed close to the body. Compared to whole body coils, coil arrays have the ability to capture a strong signal from a local region and a contribution of both signal and noise from the rest of the sample. Therefore, a higher signal-to-noise-ratio over a large FOV is received [157]. Some conditions such as the magnetic field strength, the size and number of detector coils and the preamplifier used to acquire the MR signal, can also affect noise sources. However in modern MR scanners, coil noise is usually smaller than the noise from the imaged sample. Besides the above mentioned noise parameters, the acquisition parameters can have impact on the SNR as well. The receiver (or acquisition) bandwidth is the range of frequencies that the receiver accepts to sample the MR signal. The bandwidth depends on the frequency encoding gradient strength and the data sampling frequency and is defined by BW = Sampling Rate / Number of Samples. The received noise power has a direct relationship to the square root of the receiver bandwidth $SNR = 1/\sqrt{BW}$ at which the signal has been sampled. small bandwidth improves SNR, but can cause spatial distortions, also increases the chemical shift, whereas a larger bandwidth reduces SNR, but allows faster imaging. One common method to increase the SNR is repeating the experiment several times and signal averaging. The signal intensity increases by the number of averages, whereas the noise increases by the square root of the averages, leading to improvement of the SNR at the expense of a longer acquisition time. The SNR can also be improved by sampling larger voxel size (increasing the field of view and slice thickness which corresponds to a loss of spatial resolution).
As explained above it is generally not possible to improve SNR, image resolution and acquisition time simultaneously, rather these quantities must be traded off.

2.9 Dynamic Contrast-Enhanced MRI

In the dynamic contrast enhanced (DCE-MRI) technique, multiphase MRI scans are acquired following the intravenous injection of a contrast agent bolus. DCE-MRI has

been widely used in clinical practice, from demonstrating the nature of a lymphoma to the differential diagnosis of salivary gland tumors. One of the most common assessments of DCE-MRI is using the characteristics of the time-intensity curve (TIC) regarding the regions of interest (ROIs), which are delineated by the observers. Simple quantification of the pattern of the TIC, like the time to peak enhancement or the wash-out ratio are also commonly used in the subjective assessment.

We already explained that the return to equilibrium is described by the relaxation time, T_1. When T_1-weighted sequences are used, therefore, the magnitude of the magnetization signal increases with decreasing T_1 times. Further, the contrast between two tissues also enhances with increasing difference in T_1 times between the two tissues. Sometimes sufficient contrast is of particular importance in differentiating pathological tissues whose inherent difference in T_1 relaxation time is not long.

MR contrast agents act by selectively shortening T_1 (or T_2) relaxation times of tissue water through spin interaction between electron spins of the metal containing contrast agent and water protons in tissue. For example, using a gradient echo sequence, an RF pulse is applied at regular intervals and due to shorter T_1, faster recovery of the longitudinal magnetization results in larger transverse magnetization. As the result, the receiver coil detects stronger magnetization signal from the spins in those areas, which in turn increase intensity in the reconstructed images. The concentration of the contrast agent in the tissue, and also the contrast agent of choice as well as magnetic field strength affect the degree of T_1 shortening.
One of the (DCE-MRI) based imaging application where considerable time and effort has been expended on the diagnosis, is its use in cancer research. Tumor cells grow and spread more rapidly than healthy tissue cells, and thus need increased blood flow. To meet the nutritional needs, tumor cells produce proteins which encourage tumor angiogenesis (growth of new blood vessels) and vascular permeability. This mechanism results in faster delivery of an injected contrast agent to tumor tissue, and so higher concentration of contrast agent is seen in tumor tissue compared to healthy tissue[89].

2.10 Fast imaging sequences

The total imaging time needed to form an image in the conventional Fourier data acquisition, is roughly given by the number of required RF excitations times the repetition time TR. This means that for a 3D image the total acquisition time is

$$T_{acq} = N_y \, N_z \, TR \tag{2.15}$$

where N_y and N_z are the number of phase encoding steps in y and z directions, respectively. Decreasing the repetition time TR therefore improves the imaging speed. For the gradient echo sequence already explained, one way to shorten the minimum TR and keep the same FOV and resolution, is applying stronger gradients. On the other hand, high gradient amplitudes and rapid switching can cause peripheral nerve stimulation and limit feasibility of the system [43]. One approach to reduce data acquisition time is to acquire multiple k-space lines within a single repetition time interval. Echo planar imaging (EPI) is one of the fast MR imaging techniques designed to measure all k-space lines in one repetition time [118]. However, in practice EPI implementation has notable disadvantages, such as the demands on the MR hardware to achieve the gradient field switching required and the occurrence of specific EPI artifacts [72].

In fast spin echo (FSE) sequences, the interval of time after the first echo is used to receive the echo train, to fill the other k-space lines in the same slice. Since the required number of repetition time is reduced, the k-space can be filled faster and slice acquisition time is reduced [74]. Due to the intrinsic constrained of the fast acquisition sequences, data under-sampling has been proposed as a good means of speeding up imaging. For instance, the phase encoding lines are skipped in the k-space, at the cost of reduced resolution or the FOV. However, the smaller FOV leads to decreased SNR and if the FOV size is smaller than the imaged object, foldover artifacts arise.

In recent years many techniques have been developed to address drawbacks of under-sampling. Incorporating prior knowledge of the image can be used to compensate the missing Fourier coefficients. In half (or partial) Fourier imaging just over one half of k-space is acquired and k-space symmetry is used to infer the remainder of the non-acquired dataset. Since the imaged object is always real in practice, Hermitian symmetry is present in the k-space dataset. Thus in principle only half of the symmetrical k-space needs to be measured, and the other half can be estimated as the complex conjugates of the measured samples. Parallel imaging is another powerful method to accelerate scans that exploits spatially varying radio frequency coil sensitivities.

2.11 Parallel Magnetic Resonance Imaging

Even though the acquisition time for a single slice has been decreased from minutes to hundreds of milliseconds, the acquisition time for a 3D scan or to achieve high spatial resolution is still substantial. To improve spatio-temporal resolution of images while reducing scan time, parallel MRI acquisition with multiple RF receiver coils has emerged since the early 90s as a powerful method. As explained before, the number of phase encoding steps determines the acquisition time since each phase encoding step is applied

after a single excitation.

In pMRI, each coil has different sensitivity to the magnetization signal within the FOV (also called coil sensitivity profile), and a reduced number of phase encoding (PE) steps can be performed to accelerate scan time. The decrease of the data amount per coil is compensated by the use of multiple receiver coils with distinct spatial sensitivities. To reconstruct unaliased images from acquired undersampled k-space data, several widely-used reconstruction techniques have been proposed. Receiver coils spatial sensitivities bring additional information about the spatial position of the signal to compensate undersampling. The advantages reported for using Parallel MRI include:
The patient comfort during an MRI exam is improved by shortening the global acquisition time and also by less acoustic noise since not all the k-space is acquired [47]; Geometrical distortion artifacts are reduced since the phase-encoding bandwidth has been increased [47, 101]; A shorter TE is associated with less magnetic susceptibility artifacts.
However, using pMRI generally leads to lower acquisition SNR than with conventional MRI due to four main artifact sources: 1)Aliasing artifacts related to the undersampling effect; 2) Acquisition noise; 3)Inaccurate sensitivity estimations (error in the estimated coil sensitivity profile propagates into the reconstructed images); 4)Suboptimal coil-array geometry (the so called g-factor) to provide sufficient independent complementary information from all the array. These artifacts can lead to the failure of pMRI reconstruction and result in large noise amplification.

2.11.1 History of pMRI

Faster acquisition not only increases the number of patients that are examined per day but also reduces the severity of motion artifacts caused by an unintentional patient movement during the session. Parallel MRI decreases the acquisition time of a single slice and, thus, allows to increase the frame rate in dynamic imaging of moving objects. As the result, it helps to avoid temporal aliasing artifacts and to examine the object thoroughly.
First attempts were made planned to reduce the number of phase encoding lines by using multiple receiver coils in late 1980s. Hutchinson and Raff [78] in 1988 and then subsequently in 1991 Kwiat and Einav [93] proposed the first extreme idea of having a single receiver coil for each pixel. Theoretically, coils with strongly localized sensitivities were employed in their algorithm so that each coil covered only a single pixel. Therefore, during the first excitation the whole image was acquired with no need to use spatial encoding. However practically, such arrays of receiver coils can not be reconstructed with current technology. In 1989, Kelton tried to speed up the acquisition by undersampling the k-space by a factor of 1/2 in the phase-encoding direction and recovered the missing information using

two receiver coils [88]. His principle of k-space undersampling inspired modern methods that are widely used nowadays like SMASH [171] or SENSE [145]. Kelton's method was modified by Ra and Rim in 1991, introducing more receiver coils [149]. They used the knowledge of the distinctive coil sensitivity profiles to remove the aliasing artifacts caused by the under-sampled k-space data sets. The next attempt by Carlson was to employ two receiver coils [34]: one coil with a homogenous coil sensitivity and one with a linear varying sensitivity over the FOV. The partial k-space data set was acquired simultaneously in each coil, and in the post processing stage the missing k-space lines were estimated by a combination of the acquired k-space lines based on the sensitivity profiles knowledge. However their approach was infeasible due to its requirement for a linear sensitivity profile.

The first clinical study using pMRI was introduced by Sodickson in 1997, named as the simultaneous acquisition of spatial harmonics (SMASH) technique [171]. SMASH works directly in the k-space by reconstructing the skipped PE lines as a weighted combination of the adjacent k-space lines. Although the initial implementation of SMASH was subject to further extensions and optimizations, the first clinical images from accelerated scanning were obtained by him. Subsequently the Sensitivity encoding method (termed as SENSE) was published in 1999 by Pruessmann [145]. SENSE worked in the spatial domain and explicitly relies on the knowledge of coil sensitivity weighting to remove the aliasing artifacts. SENSE has greatly advanced the clinical application of pMRI due to its simple implementation and high image reconstruction fidelity. Following SMASH and SENSE, current pMRI methods can be classified into two kinds: k-space and image plane methods, depending the domain in which final image reconstruction is carried out.

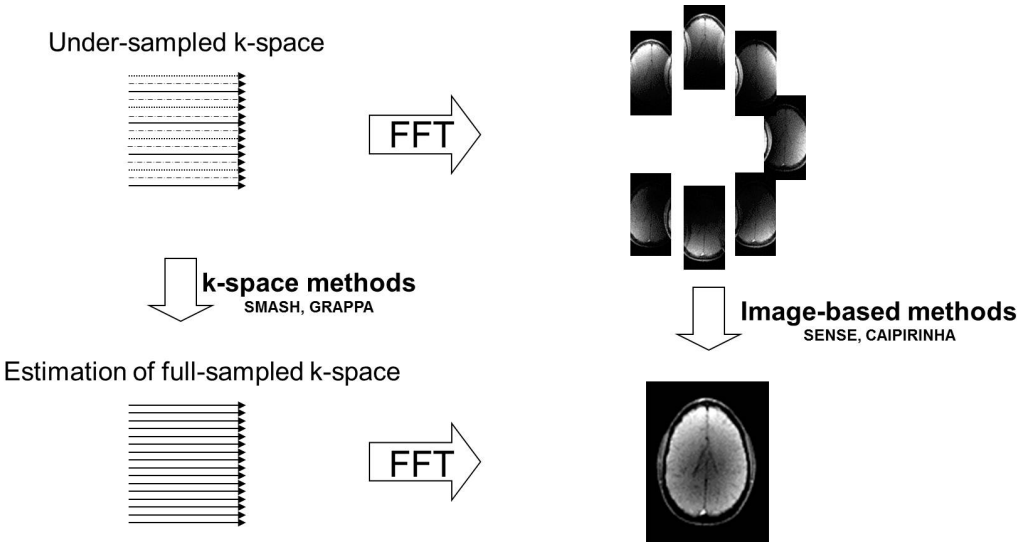

Figure 2.7: A scheme describing different pMRI reconstruction approaches

2.11.2 Coil sensitivities

In conventional MRI, a single receiver coil (also known as a body coil) with an approximately homogeneous spatial sensitivity is employed to form an image with an uniform background. However, it is desirable for the receiver coil to have a high sensitivity profile which leads in a high SNR level. The characteristics of the coil sensitivities are dependent upon their geometries which are categorized as either whole-volume coils or surface coils. volume coils are used for surrounding either the whole body or a specific region. Surface coils are designed to be placed on or around the surface of a patient and bring receiver system closer to patients. They have a relatively good SNR for superficial tissues such as the head or a limb whereas the magnetic field homogeneity is worse than the volume coils.

In parallel MRI, an array of M receiver coils with distinct spatial sensitivities are arranged to cover the desired FOV to be imaged. Using coil array brings an additional information about the spatial position of the received signal. For multiple-channel receiver, all coils receive signal in parallel and, thus, the acquisition time remains the same in comparison with a single coil. The simultaneously required k-space data sets in multiple receiver coils contains redundancy which will be then exploited using the knowledge of the coil sensitivity profile. They provide high SNR over a large FOV. Fig.(2.8) illustrates three different receiver coils: volume coil, surface coil and an 8-channel array of coils [2]. In pMRI, the

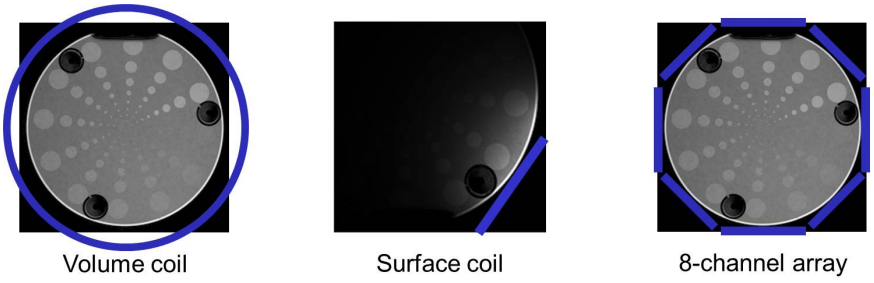

Figure 2.8: Illustration of three receiver coils. On the left, a volume coil is shown, signal and noise come from entire volume. These receivers give good coverage with moderate SNR. On the middle, localized signal and noise are received by a surface coil. They are sensitive to signals close to the coil, which means that the signal in an organ of interest is detected more efficiently. But they also amplify noise signals more efficiently too. They feature reduced coverage and good SNR. Multi-channel coils array of independent surface coils are depicted on the right. They provide high SNR over a large FOV.

utilized coil arrays are the phased coil arrays which refer to the fact that the received signal is polarized with respect to differently orientated receiver coils to retain the phase

[2]Figure reproduced from Image formation course lecture slides (by Karla Miller), available at http://users.fmrib.ox.ac.uk/ karla/grad-program/image-formation.html

information [158]. Phased coil arrays are essentially a number of overlapping coils each with their own receiver detection circuitry. Also the arrays are decoupled coil arrays which means the signal reception in different receiver coils are mutually independent (lead to higher SNR level).

Increasing the acceleration factor extends the distance between the phase-encoding lines. As the maximum gradient intensity remains the same, this means a reduced FOV and aliasing in the image domain. Fig.(2.9) shows the result of skipping some lines in the phase encoding direction (acceleration factor of $R = 2$ and $R = 3$). For instance in Fig.(2.9b), only half of total number of phase encoding steps are acquired at doubled sample spacing, while maintaining the same k-space coverage and consequently the spatial resolution.

(a) **(b)** **(c)**

Figure 2.9: The image (a) has a full FOV. The phase-encoding sampling density is reduced by a factor (b) 2 and (c) 3. This causes aliasing that is visible as a fold-over or a wrap-around effect in images (b) and (c).

Fig.(2.10) shows three sensitivity-weighted images obtained using an 8-channel head coil array. In Fig.(2.9a), complete image reconstructed from all of receiver coils was shown. In the parallel MRI, exact knowledge of coil sensitivities is essential to be able to form

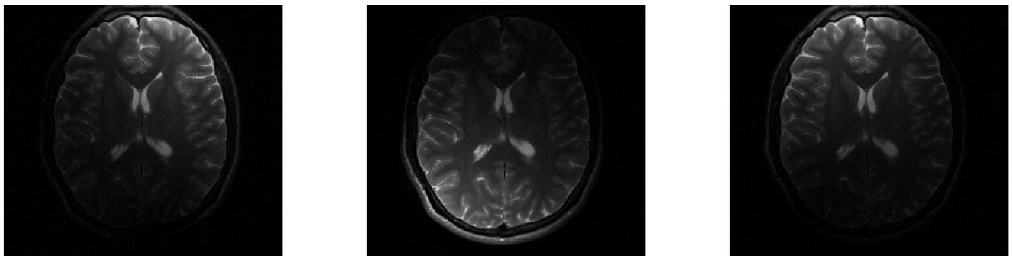

(a) **(b)** **(c)**

Figure 2.10: Three images of a head acquired by 8 coils with different spatial sensitivities are shown. Spatially localized sensitivity is clearly visible in the images.

an image without sensitivity modulation. Each coil element in the arrays is characterized by its distinctive spatial coil sensitivity profile over the FOV. The image received in each

receiver coil can be seen as the underlying magnetization, weighted by the receiver coil sensitivity. A basic mathematical method to obtain coil sensitivities is as follows:

$$\hat{C}_m(x,y) = f_m(x,y)/f(x,y), \tag{2.16}$$

where $\hat{C}_m(x,y)$ denotes the estimate of the the sensitivity maps, $f_m(x,y)$ is an array-coil image (like in Fig.2.10) and $f(x,y)$ is a body-coil image with a homogeneous coil sensitivity [170]. Full FOV images without aliasing are used for the sensitivity estimation. Ideally, an object covering the whole FOV without signal-free areas should be used. Practically, zero mean Gaussian noise is present in both real and imaginary parts of the signal as well which complicates the sensitivity estimation process.
Instead of using the body-coil image with homogeneous sensitivity, $C = 1$, the sensitivities can be approximated using the array-coil images only. One straightforward method is pixel-wise summing all of the images but that is susceptible to phase-cancellation artifacts [121]. To avoid this, the image can be reconstructed by taking the sum-of-squares combination of the individual receiver coil images:

$$f^{SoS}(x,y) = \sqrt{\sum_{m=1}^{M} |f_m(x,y)|^2} \tag{2.17}$$

In the sum-of-squares combination, the knowledge of coil sensitivity is not needed and phase-cancellation artifacts are reduced, though the computed magnitude is biased and SNR is degraded [121, 27, 158]. In Fig.(2.11) sensitivity profiles of three coils that used to acquired images in Fig.(2.10) are illustrated. A critical condition to ensure the feasibility

(a) **(b)** **(c)**

Figure 2.11: Magnitude of coil sensitivity profiles for 3 coils in an 8-channel head coil whose corresponding sensitivity-weighted images were depicted in Fig.(2.10).

of the parallel MRI reconstruction is the number of coils M which must be higher than the acceleration factor, otherwise the problem becomes singular.

2.12 Parallel MRI reconstruction methods

Practically in pMRI, the FE direction is always fully sampled, so reconstructing a 2D image can be decomposed into reconstructing a series of 1D lines along the FE direction. With the same perspective, 3D image reconstruction can be decomposed into reconstructing a series of 2D planes perpendicular to the FE direction. In contrast to conventional 2D imaging where only one phase encoding direction is available for scan time reduction, 3D volumetric imaging with a second phase encoding direction offers the potential to choose the direction in which undersampling is performed, or even to split the acceleration between the two phase-encoding directions.

The following sections are devoted to the pMRI reconstruction methods and will explain some of the most common methods and strategies.

2.12.1 k-space domain pMRI methods

Simultaneous acquisition of spatial harmonics (SMASH)

In k-space pMRI methods, images are reconstructed by calculating the necessary coefficients to interpolate missing k-space data in the accelerated scans (see Fig.(2.7)). In SMASH, the missing phase encoding lines are estimated in post processing using a proper linear combination of the adjacent k-space data [171]. A linear combination of the sensitivity profiles is utilized to form the desired composite sensitivity profile C_n^{copm} of the order n:

$$C_n^{copm}(x,y) = \sum_{m=1}^{M} w_m^{(n)} C_m(x,y) \cong e^{i(n\Delta_{k_y} y)} \tag{2.18}$$

where Δ_{k_y} is the size of the phase encoding step in the k-space and y is the PE direction. Here, w_m are appropriate linear weights, while n is an integer, specifying the order of the generated spatial harmonic. The only unknowns in this linear equation are the linear weights $w_m^{(n)}$, which can be estimated by fitting (in the least square sense) the coil sensitivity profiles C_m to the spatial harmonic $e^{i(n\Delta_{k_y} y)}$ of order n.
The signal acquired in the coil m, $F_m(k_y)$ in phase encoding direction, is the Fourier transformation of the spin density $\rho(y)$ weighted with the corresponding coil sensitivity profile $C_m(y)$, so:

$$F_m(k_y) = \int \rho(y) C_m(y) e^{ik_y y} dy \tag{2.19}$$

From Eq.(2.18) and Eq.(2.19), using the weighting coefficients, shifted k-space lines $F(k_y + n\Delta_{k_y})$ can be generated:

$$\begin{aligned}\sum_{m=1}^{M} w_m^{(n)} F_m(k_y) &= \int dy\ \rho(y) \sum_{m=1}^{M} w_m^{(n)} C_m(y) e^{ik_y y} \\ &\cong \int dy\ \rho(y) e^{in\Delta_{k_y} y} e^{ik_y y} \\ &= F^{comp}(k_y + n\Delta_{k_y})\end{aligned} \tag{2.20}$$

This basic SMASH equation explains how the linear combination of the lines with coordinate k_y with weights $w_m^{(n)}$ generates shifts of $n\Delta_{k_y}$ in the k-space, almost the same manner as magnetic field gradients in conventional phase-encoding. Therefore, in post processing these synthesized harmonic modulation will be used to reconstruct skipped k-space lines from the undersampled coil images.

In order to form a composite data set at acceleration factor of R, R sets of fitting coefficients $a^0, a^1 ... a^{R-1}$ are required to produce harmonic spatial modulation up to the Rth order. Consequently, all the data for an image of a given resolution and field of view may be acquired in $\frac{1}{R}$ of the normal acquisition time. Fig.(2.12) illustrates the k-space geometry of SMASH acquisition strategy. Here, in order to reconstruct 5 lines of k-space for each application of a phase-encoding gradient, 4 spatial harmonics need to be generated. This procedure represents an acceleration factor of five in acquisition time, as compared with a conventional acquisition.

In general, though, the disadvantages of SMASH are that it requires a separate coil sensitivity map estimation and also suitable coil configurations to generate the desired spatial harmonics in phase encoding direction. Obtaining pre-scan images increases the total scan time. Practically these difficulties makes SMASH prone to reconstruction errors. In contrast with SMASH, the autocalibrated methods were proposed which proceed by acquiring a few additional k-space lines to derive coil sensitivity maps without a reference scan. The auto-calibration technique was introduced in AUTO-SMASH and Variable Density AUTO-SMASH (VD-AUTO-SMASH) [80, 73] to allow reconstruction with arbitrary coil configurations [122]. In AUTO-SMASH [80], $R-1$ auto-calibration signals, F_m^{ACS} are acquired as well as a fraction $\frac{1}{R}$ (R is the accelerated factor) of all k-space lines and are used to calibrate the method without the explicit need for sensitivity maps extraction. To perform calibration, an unaliased, though low resolution, image is needed, so the auto-calibrating lines are usually acquired from the k-space center. SMASH and the auto-calibration SMASH reconstruction methods have been successfully used in the past for pMRI reconstruction [71, 172, 169]. Despite their lower reconstruction quality, SMASH

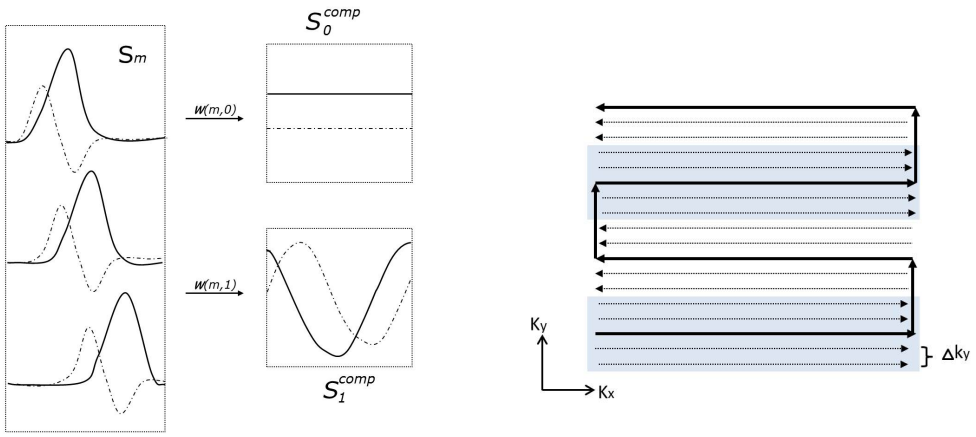

(a) Estimation **(b)** Reconstruction

Figure 2.12: Schematic estimation and reconstruction processes in a sample SMASH acquisition (a) Coil sensitivity profiles are combined to produce a composite profile and harmonic modulation. Full and dashed lines represent the real and the imaginary part of the signal and sensitivity, respectively. (b) Frequency encoding gradient and phase encoding gradient steps are indicated by thick horizontal and vertical lines, respectively. k-space lines derived from harmonics of the fundamental spatial frequency Δ_{k_y} are shown as dashed lines. Five harmonics have been used, for a total of five lines per frequency encoding readout (grouped by shading).

and its extensions are less computationally demanding compared to image-based methods.

Generalized Autocalibrating Partially Parallel Acquisition (GRAPPA)

The GRAPPA method was represented as a more generalized implementation of the VD-AUTO-SMASH approach in 2002 by Griswold et al [70]. For each coil, instead of forming the composite, the extra acquisition lines of the center k-space (named as component coil ACS signals) are fitted to linear combinations of blocks of acquired data. Then the fitting coefficients are used to estimate the missing k-space data, by interpolation of acquired data. Using sum of squares to reconstruct the final image from single coil images Eq.(2.17), each coil contributes maximally in regions where its sensitivity is high and minimally in regions where its sensitivity is low. Fig.(2.13) gives a schematic description of VD-AUTO-SMASH and GRAPPA reconstruction procedures.

GRAPPA as a blockwise method extends the algorithm introduced in [121, 28] where more than one acquired k-pace lines are linearly combined to reconstruct each skipping line. Indeed, data fitting has been extended to include a few neighboring lines which improves data fidelity. The following equation is accomplished to reconstruct the missing k-space lines of the j_{th} coil:

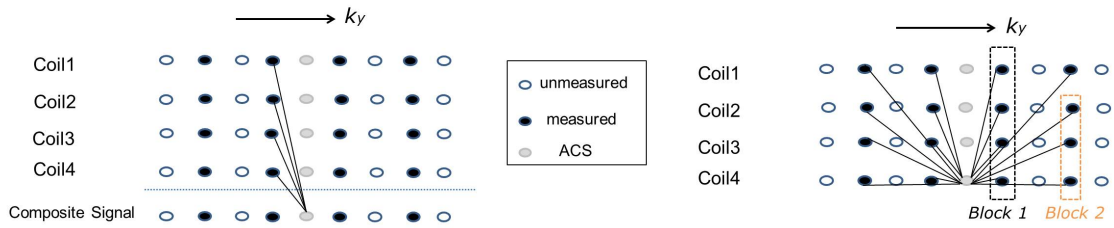

(a) VD-AUTO-SMASH **(b)** GRAPPA

Figure 2.13: Schematic description of VD-AUTO-SMASH and GRAPPA at acceleration factor of 2. Each dot represents a line in k-space in a single coil of the receiver array. (a)In AUTOSMASH and VD-AUTO-SMASH, a single line from all coils is fit to a single ACS line in a composite k-space. (b)In GRAPPA, multiple measured lines from all coils are used to fit one line in one coil (here coil 4). This procedure needs to be repeated for every coil, resulting an image for each coil, which may be finally combined using a sum of squares reconstruction. As illustrated by the block 1 and block 2, there often exist multiple ways of producing a target data point (here block 1 was used).

$$F_j(k_y - n\Delta_{k_y}) = \sum_{m=1}^{M} \sum_{b \in B} w(j,b,m,n)\ F_m(k_y - bL\Delta_{k_y}), \tag{2.21}$$

where $w(j,b,m,n)$ specifies the weights. The variable b is the reconstruction block which is formed from L k-space lines. The measured k-space line $F_m(k_y - bL\Delta_{k_y})$ from the block b is used for the reconstruction of the skipped line $F_j(k_y - n\Delta_{k_y})$. The set B is a set of all reconstruction blocks used for the reconstruction. The number of the blocks in the set B is a determining parameter of the reconstruction. Using several different sets of blocks for the reconstruction, called sliding-block approach, was suggested by GRAPPA's authors [70]. The number of blocks might reduced to one, which makes GRAPPA equivalent to the original SENSE (see the next section).

Indeed, in the blockwise reconstruction more acquired lines are included, consequently data reconstruction fidelity improves without limiting it to specific coil configurations. However, the computational complexity and numerical instability increases due to the low SNR of the out-of-center k-space lines. It was shown that the GRAPPA method produces reconstructed images with a higher SNR and a lower level of artifacts than the original SMASH and VD-AUTO-SMASH [70].

Temporal GRAPPA and k-t GRAPPA are two applications of GRAPPA estimation process in dynamic imaging [76, 22]. In TGRAPPA a different subset of k-space lines is acquired in each frame. In order to generate a fully sampled k-space center for the calibration, TGRAPPA uses the acquired lines from the center of k-space in the following frames. A similar sampling pattern as TGRAPPA is used in k-t GRAPPA except that calibration

lines are acquired in the center of k-space in each time frame (see Fig.(2.14)). As shown, k-t GRAPPA utilizes neighboring k-space lines in the same time frame and also the lines from the adjacent time frames that have the same phase encoding coordinates as the reconstructed line. This method improves reconstruction quality when compared with standard GRAPPA by using the time correlation of the signal [22].

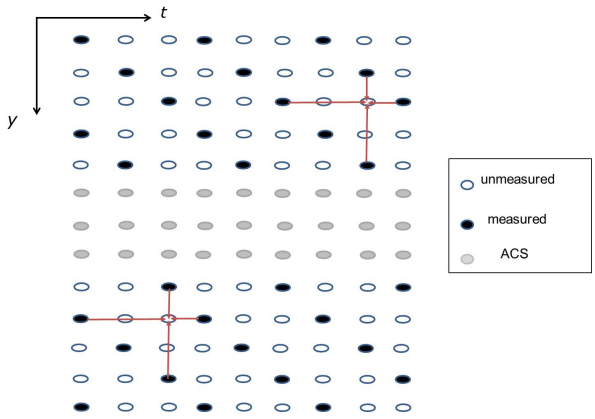

Figure 2.14: The dynamic acquisition scheme of k-t GRAPPA. Here, gray dots are the ACS lines in the central band of k-space. In order to interpolate a missing data in the k-t GRAPPA reconstruction, the adjacent lines in both phase-encoding axis and times axis are used as shown by red arrows.

2.12.2 Image domain pMRI methods

SENSE

In SENSitivity Encoding (SENSE), originally introduced by Pruessmann, the image reconstruction takes place in the image space and is comprised of reconstruction of reduced FOV images followed by a spatial unfolding procedure [145]. This technique requires an accurate estimation of coil sensitivity profiles using a reference scan. Of course, for the non-Cartesian sampling schemes, like spiral and radial acquisitions, SENSE reconstruction is more complicated and requires an iterative algorithm.
A linear encoding matrix $\mathbf{E}$ which describes the transformation from the ideal image f to the k-space values $F_m(k_x, k_y)$ is used in SENSE:

$$F_m(k_x, k_y) = \sum_{k_x, k_y} f(x, y)\ E_{m,k_x,k_y}(x, y), \tag{2.22}$$

where the elements of $\mathbf{E}$ are defined as:

$$E_{m,k_x,k_y} = e^{-i\pi(k_x x + k_y y)}\, C_m(x,y). \tag{2.23}$$

A reconstruction matrix $\mathbf{S}$ is defined to reconstruct the desired image:

$$\hat{f}(x,y) = \sum_{m,k_x,k_y} S_{m,k_x,k_y}(x,y) F_m(k_x,k_y), \tag{2.24}$$

From the above equations, $\mathbf{SE} = \mathbf{I}$, where $\mathbf{I}$ denotes an identity matrix. Since this linear system is underdetermined, there are degrees of freedom in the solution ($\mathbf{S}$) to minimize the noise propagation in the reconstruction. In the scope of SENSE, the diagonal entries in the matrix $\mathbf{F\Psi F}^H$ denote the noise variance in each reconstructed pixel, where $\mathbf{F}^H$ represents the Hermitian transpose (conjugate transpose) of the matrix $\mathbf{F}$. The SENSE solution, $\mathbf{S}$, can be concluded by minimizing this variance:

$$\mathbf{S} = (\mathbf{E}^H \mathbf{\Psi}^{-1} \mathbf{E})^{-1} \mathbf{E}^H \mathbf{\Psi}^{-1} \tag{2.25}$$

where $\mathbf{\Psi}$ is the sample noise correlation matrix, describing the level and the correlation of noise in signal samples. Let us assume that the same sampling strategy as SMASH is employed in Cartesian SENSE and the k-space is acquired using standard Cartesian sampling. To achieve an acceleration factor of R, the sample spacing in k-space has been increased by a factor of R, so the FOV along the phase encoding direction in the image plane has been reduced by a factor of R. Then, each aliased pixel's value is a linear combination of R pixel values, however the aliased pixels are weighted by the local spatial coil sensitivity map of each individual coil. In the example illustrated in Fig.(2.15) from $R = 2$, the pair of pixels f_a and f_b, and their superimposition in two different receiver coils, $f_{Alias,1}$ and $f_{Alias,2}$ can be presented in a linear system as:

$$\begin{bmatrix} f_{Alias,1} \\ f_{Alias,2} \end{bmatrix} = \begin{bmatrix} C_{1,a} & C_{1,b} \\ C_{2,a} & C_{2,b} \end{bmatrix} \begin{bmatrix} f_a \\ f_b \end{bmatrix} \tag{2.26}$$

where $C_{1,a}$, $C_{2,a}$, $C_{1,b}$ and $C_{2,b}$ denote the coil sensitivity weighings at the aliased pixels positions in the receiver coils. In a more general case, the encoding process Eq.(2.23) in

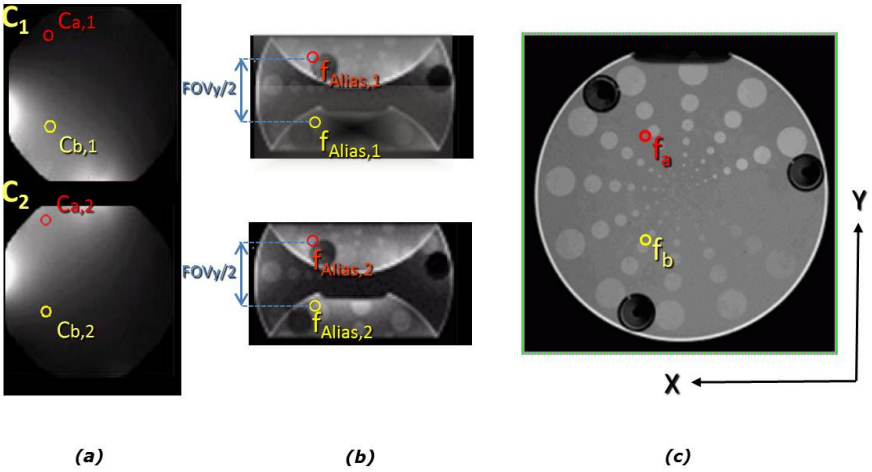

Figure 2.15: Illustration of the basic SENSE relation in pMRI acquisition. An acceleration factor of 2 results in an images with reduced FOV in the PE direction. (a) Spatially varying coil sensitivity weighting in the two receiver coils are represented. (b) Sampling at half of the Nyquist rate along the k_y direction results in the images with halved FOV in both receiver coils. Aliased pixels at two certain positions in the reduced FOV coil images are shown.(d) Using proper knowledge of the sensitivities at the corresponding positions, the unfolding process can be accomplished (reproduced from [145]).

the Cartesian sampling is simplified and rewritten in a matrix notation as:

$$\begin{bmatrix} f_{Alias,1}(x,y) \\ f_{Alias,2}(x,y) \\ . \\ . \\ . \\ f_{Alias,M}(x,y) \end{bmatrix} = \begin{bmatrix} C_1(x,y) & . & . & . & C_1(x,y+(R-1)Y/R) \\ C_2(x,y) & . & . & . & C_{2,R}(x,y+(R-1)Y/R) \\ . & . & . & . & . \\ . & . & . & . & . \\ . & . & . & . & . \\ C_M(x,y) & . & . & . & C_M(x,y+(R-1)Y/R) \end{bmatrix} \begin{bmatrix} f(x,y) \\ f(x,y+Y/R) \\ . \\ . \\ . \\ f(x,y+(R-1)Y/R) \end{bmatrix} \tag{2.27}$$

Or $\mathbf{f}_{Alias} = \mathbf{Cf}$, where $\mathbf{f}_{Alias}(x,y)$ represents the aliased pixel, $\mathbf{f}$ is the group of pixels that are aliased together and $\mathbf{C}$ denotes the corresponding sensitivity matrix. The formulation in Eq.(2.27) can be used for all $x = 1, ..., X$ and $y = 1, ..., Y/R$. R is the acceleration factor and XY is the FOV size in pixels

The reconstruction Eq.(2.25) becomes:

$$\mathbf{C}^{+}(x,y) = (\mathbf{C}^{H}\mathbf{\Psi}^{-1}\mathbf{C})^{-1}\mathbf{C}^{H}\mathbf{\Psi}^{-1}(x,y) \tag{2.28}$$

Consequently, the image $\hat{\mathbf{f}}$ is reconstructed from the input aliased image $\mathbf{f}_{Alias,m}$:

$$\begin{bmatrix} \hat{f}(x,y) \\ \hat{f}(x,y+Y/R) \\ . \\ . \\ . \\ \hat{f}(x,y+(R-1)Y/R) \end{bmatrix} = \mathbf{C}^{+}(x,y) \begin{bmatrix} f_{Alias,1}(x,y) \\ f_{Alias,2}(x,y) \\ . \\ . \\ . \\ f_{Alias,M}(x,y) \end{bmatrix} \tag{2.29}$$

This SENSE process has to be repeated for every pixel in the aliased image to finally compute the full FOV image. Unlike the k-space pMRI methods (except the original SMASH), in SENSE knowledge of the coil sensitivity map is explicitly involved in the image reconstruction. Therefore precise knowledge of coil sensitivity profiles is required in the reconstruction. Pruessmann proposed to obtain an estimation of the coil sensitivity map from a low resolution calibration scan [147].

In 3D Fourier imaging, the SENSE can be adapted to compensate for the aliasing in two PE directions [198]. In 2D SENSE, uniform undersampling is performed along both PE directions. (R1 - 1) and (R2 - 1) k-space lines are skipped in a regular manner in each PE direction to achieve an overall acceleration factor of R, where R = $R1 \times R2$. The 2D SENSE method offers more favorable results than standard SENSE since the coil-geometry related noise is reduced in the reconstruction [198].
To make the Eq.(2.25) calculations simpler, $\mathbf{\Psi}$ is assumed to be diagonal, in iterative SENSE. The advantage of this iterative method is that it does not restrict the sampling of the k-space and an arbitrary sampling pattern is allowed.

Controlled aliasing in parallel imaging (CAIPIRINHA).

In order to accelerate multislice imaging, significant improvements are provided using controlled aliasing in parallel imaging results in higher acceleration, (CAIPIRINHA) [24]. This method is based on a coinstantaneous acquisition of multiple slices and has been successfully applied to simultaneous multi-slice imaging (MS-CAIPIRINHA) and 3D imaging (2D-CAIPIRINHA). When two or more slices are acquired at the same time, it is not possible to separate the aliased pixel from each slice using the standard signal encoding. This is because, the coil sensitivity variation is too small for slices that are close to each other and hence, the problem becomes ill-conditioned. CAIPINRINA is an elegant approach which modifies the appearance of aliasing artifacts during data acquisition by providing individual slices with different phase cycles. In fact, aliasing pattern is controlled by altering the phase encoding sampling strategy, specifically by applying gradient offsets

during data acquisition. Since aliasing resulted from alternating multiband radio frequency (RF) pulses is not identical with the undersampling aliasing, the encoding performance is not the same. In CAIPINRINA, Breuer proposed using a modified slice superimposition in which one slice is shifted with respect to the other.

To perform CAIPINRINA, a volumetric sequence excites two spatially separated slices and the k-space is sampled using an undersampling pattern similar to the standard SENSE. As the result, two image slices are superimposed which can be separated using the knowledge of sensitivity encoding. Note that the coil sensitivity variation of the superimposed pixels is increased unlike the conventional approach since the additional coil sensitivity difference across different slices is exploited. Various studies reported that CAIPIRINHA significantly improved image quality and artifacts in comparison to the standard GRAPPA and SENSE.

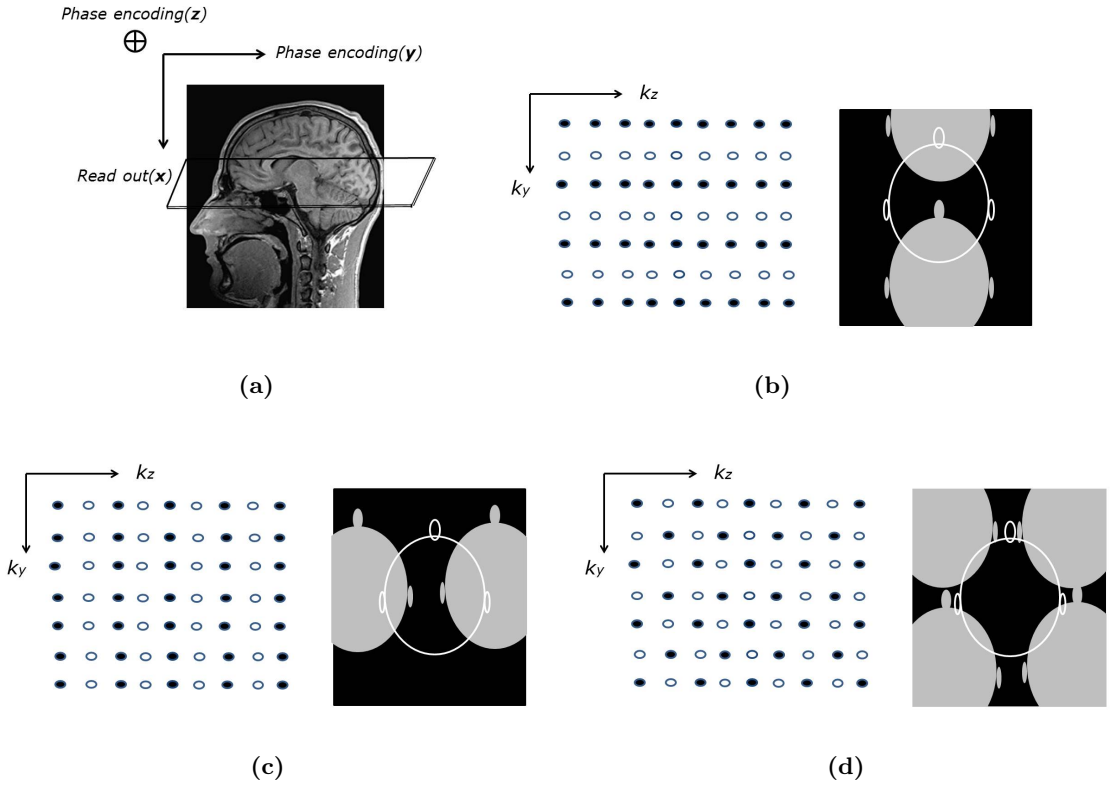

Figure 2.16: Various possible sampling schemes for an acceleration factor of 2 (R=2) in 3D imaging are demonstrated. Two slices are simultaneously excited using a volumetric sequence. Remember that two phase encoding direction are used in the 3D acquisition and the read out direction is into the page. A masked section of the head in the transversal plane demonstrates the aliased image correspondes to the undersampled phase encoding schemes displayed beside it. (a) sagittal view of the 3D imaging experiment is displayed. (b) and (c) the aliasing pattern resulted from a conventional 2D-SENSE experiment, (d) from a 2D-CAIPIRINHA experiment are shown.

The concept of CAIPIRINHA can also be transferred to 3D imaging, where data un-

dersampling can be performed along two phase encoding directions [23]. In contrast to CAIPIRINHA, 2D CAIPIRINHA does not need special RF pulses. Instead, the phase encoding sampling strategy is modified in order to control aliasing in 2D parallel imaging. Overlapping partitions are shifted from their normal positions in the undersampled 2D phase encoding scheme are with respect to each other according to the 2D sampling pattern (see Fig.(2.16)). The figure displays a simple example of a parallel acquisition scheme with acceleration factor of 2 (R=2). A masked section of the head in the transversal view illustrates the corresponding 2D aliasing patterns. In conventional 3D parallel imaging, three different undersampling patterns in the phase encoding directions, k_y and k_z, are possible. The result depends on the reduction direction, so aliasing artifacts appear only in the undersampled dimension. Acceleration factor in y directions, $R_y = 2$, results in Fig.(2.16b), where each slice is aliased two times in the y-direction. On the other hand, Fig.(2.16c) shows that after an acceleration factor in z directions, $R_z = 2$, two slices are superimposed directly on top of each other. Where both slices are aliased directly on top of each other, the scenario corresponds to the simultaneous two-slice SENSE experiment. Another undersampling pattern identical to 2D-CAIPIRINHA, is shown in Fig.(2.16d). In the aliasing pattern, the same slices are superimposed directly on top of each other, but now they are shifted in the phase encoding direction with respect to each other.

As seen here, 2D-CAIPIRINHA pattern takes advantages of the empty spaces in the FOV, resulting less overlap and better SNR. It is shown that CAIPIRINHA gives more optimal results than the normal sampling pattern for thin 3D imaging slices. The key point is that different multiband pulses (sampling scheme) could be optimal depending on the coil array and size of the imaging volume. Breuer suggested to examine the sampling patterns by considering their corresponding point spread functions (PSF). Those sampling pattern feature largest minimum distance between the non-zero elements in their PSF are considered to result in the best.

2.13 Medical applications

PMRI covers a wide variety of medical applications concerning the enhancement of the spatial and the temporal resolution of the images. An area that is particularly interesting for the application of pMRI is cardiac MRI. Monitoring of heart motion is crucial for the detection of a proper behavior or dysfunction of heart. Acquisition time in cardiac imaging can be efficiently shortened by SENSE [199], SMASH [82] or PILS [81]. High temporal resolution is also desired for a functional imaging of the brain. SENSE in combination with fast single shot techniques allows he acquisition of the whole brain fMRI scan in 1

second [68]. The spiral imaging SENSE reconstruction [146] was also successfully applied for BOLD fMRI imaging [201]. This technique resulted in enhanced resolution and reduced artifact level. However, the SENSE reconstruction of undersampled spiral images was computationally expensive.

In DCE-MRI, the acquisition time is limited by contrast agent's half-life (10-20 s) which this also limits the spatial and temporal resolution. SENSE technique can be employed to speed up the acquisition time [200, 116]. As a consequence, motion artifacts are reduced and examination procedure is more comfortable for patients since the angiography is often done in a breathold session. Moreover, fast switching of gradients during the k-space encoding produces high acoustic noises. This is more significant especially in the single-shot techniques which the frequency of gradients switching is high. The pMRI methods such as SENSE or GRAPA can be used to reduce the number of phase encoding steps and, thus, reduce the gradients switching rate. This reduces the acoustic noise and makes the examination more comfortable for the patient [47].

Chapter 3

Generalized UnalIasing using Support and Sensitivity Encoding (GUISE)

3.1 Motivations

In this chapter, a parallel MRI reconstruction formulation developed at University of Canterbury and presented as GUISE (Generalized UnalIasing using Support and sensitivity Encoding) is reviewed. The relationship between the GUISE formulation and other existing pMRI methods is explored. In the application of 3D MR imaging, its novel sampling strategy is discussed in conditioning the encoding matrix inversion. Attention is then paid in identifying the object region of support (ROS) which as an intrinsic constraint is incorporated in the reconstruction process. As a part of the support definition a modified Maximum Intensity Projection (MIP) for segmentation is developed and used. The performance of this projection strategy is compared with the other similar formulation. While GUISE itself has been previously published, the author has contributed new work; the ROS estimation presented in Section (3.6) to (3.10) [190].

3.2 pMRI general formulation

In the previous chapter a brief description of the most commonly used parallel MRI methods was given. For a more detailed description of GUISE, the general problem formulation in pMRI will be discussed here.

In the previous chapter, the MRI signal equation was described for 2D imaging. In pMRI, k-space measurement in the m_{th} coil, F_m can be represented in discrete multi-dimensional

Fourier transform as:

$$F_m[\mathbf{k}] = \sum_{n_1=0}^{N_1-1} \sum_{n_D=1}^{N_D-1} (c_m[\mathbf{n}] \circ f[\mathbf{n}]) e^{-i2\pi \mathbf{k}^T (\mathbf{n} \circ^{-1} \mathbf{N})}, \tag{3.1}$$

where $\circ^{-1}$ denotes the element-wise division and D is the imaging dimension: 2 or 3. $c_m[\mathbf{n}]$ and $f[\mathbf{n}]$ are the discrete sequences of coil sensitivity profile and object magnetization, respectively. This general discrete Fourier transform can be conveniently represented in the matrix form as:

$$\mathbf{F}_m = \mathbf{W} diag(\mathbf{c}_m)\mathbf{f}, \tag{3.2}$$

where $\mathbf{W}$ is the multi-dimensional Fourier matrix which accomplishes the DFT in 2D or 3D. The multi-dimensional quantities $\mathbf{c}_m[\mathbf{n}]$, $F_m[\mathbf{n}]$ and $f[\mathbf{n}]$ are presented in the stacked column vectors; $\mathbf{F}_m$, $\mathbf{c}_m$, and $\mathbf{f}$. Matrix elements on the main diagonal of $diag(\mathbf{c}_m)\mathbf{f}$ are the sensitivity weighted image elements in the m_{th} coil and zero elsewhere. In order to speed up image acqusition, some of the phase encoding lines are skipped which is equivalent to deleting the corresponding entries in $\mathbf{F}_m$. A binary sampling mask, $\mathbf{h}$ is imposed to the formulation so that in $\mathbf{h}$, 1 and 0 respectively correspond to measured and skipped sample positions. So the system can be expressed as:

$$diag(\mathbf{h})\mathbf{F}_m = diag(\mathbf{h})\mathbf{W} diag(\mathbf{c}_m)\mathbf{f}, \tag{3.3}$$

In the more general form of the above equation, the collective partial data set from all the receiver coils, $\mathbf{F}^c$ is presented as follow:

$$\mathbf{F}^c = \mathbf{E}\mathbf{f}, \quad \mathbf{E} = \begin{bmatrix} diag(\mathbf{h})\mathbf{W} diag(\mathbf{c}_1) \\ diag(\mathbf{h})\mathbf{W} diag(\mathbf{c}_2) \\ \cdots \\ diag(\mathbf{h})\mathbf{W} diag(\mathbf{c}_M) \end{bmatrix}, \quad \mathbf{F}^c = \begin{bmatrix} diag(\mathbf{h})\mathbf{F}_1 \\ diag(\mathbf{h})\mathbf{F}_2 \\ \cdots \\ diag(\mathbf{h})\mathbf{F}_M \end{bmatrix}, \tag{3.4}$$

where $\mathbf{E}$ is the general pMRI encoding matrix, which describes the mapping of the underlying object magnetization to the Fourier transform of the weighted image by the coil sensitivity.

In the image plane reconstruction methods, both the input and output of the process are in the image plane. Thereby, the output of the general encoding matrix is needed to be

transformed to spatial domain by an inverse Fourier transform:

$$\mathbf{f}_m = \mathbf{W}^{-1} diag(\mathbf{h}) \mathbf{F}_m = \mathbf{W}^{-1} diag(\mathbf{h}) \mathbf{W} diag(\mathbf{c}_m) \mathbf{f} \tag{3.5}$$

where $\mathbf{f}_m$ is the aliased image reconstructed from under-sampled data from the m_{th} receiver coil. In the same manner with the general pMRI encoding matrix, the imaged based encoding matrix is:

$$\mathbf{f} = \mathbf{E}\mathbf{f}, \quad \mathbf{E} = \begin{bmatrix} \mathbf{W}^{-1} diag(\mathbf{h}) \mathbf{W} diag(\mathbf{c}_1) \\ \mathbf{W}^{-1} diag(\mathbf{h}) \mathbf{W} diag(\mathbf{c}_2) \\ \cdots \\ \mathbf{W}^{-1} diag(\mathbf{h}) \mathbf{W} diag(\mathbf{c}_M) \end{bmatrix}, \quad \mathbf{f} = \begin{bmatrix} \mathbf{f}_1 \\ \mathbf{f}_2 \\ \cdots \\ \mathbf{f}_M \end{bmatrix}, \tag{3.6}$$

where the image plane encoding matrix, $\mathbf{E}$ maps the underlying object magnetization to coil sensitivity weighted aliased images in different receiver coils.

3.3 GUISE-formulation

A new pMRI method was presented and termed as Generalized UnalIasing using Support and sensitivity Encoding (GUISE) to emphasize the fact that both knowledge of coil sensitivity weighting and object support constraint are incorporated in inverting the encoding matrix [205]. The GUISE formulation can be seen as a variation of the general image plane encoding matrix, given in Eq.(3.6), with the incorporation of knowledge of object ROS. The key advantage of GUISE is the freedom of employing an adaptive sampling pattern for each image scan to improve the reconstruction results.

In practice, objects are often only supported (have non zero elements) on a particular region in the spatial domain. The FOV is determined by the k-space sampling density along each different direction which practically is in the shape of a rectangular parallelepiped. Since the FOV shape is unlikely to coincide with the natural form of the imaged object, the resulting object image generally only has a limited extent within the FOV and there are gaps between the object support and the frame of FOV. As a result, sampling at the Nyquisit rate in the frequency domain leads to gaps between the object replications in the spatial domain or sampling redundancy [119, 42]. Having such gaps in the spatial domain, means that the k-space samples are linearly dependent and a sample set at the Nyquisit rate contains redundancy. Also it was shown that the fundamental minimal

sampling density is dependent on the object support constraint [94]. Considering the region of support (ROS) constraint as a binary mask S, the knowledge of the support can be straightforwardly incorporated in the Fourier encoding in MRI:

$$\mathbf{F} = \mathbf{W}(\mathbf{s} \circ \mathbf{f}), \qquad s(\mathbf{n}) = \begin{cases} 1 & f(\mathbf{n}) \neq 0 \\ 0 & f(\mathbf{n}) = 0 \end{cases} \tag{3.7}$$

where $\mathbf{F}$ denotes the k-space measurement, $\mathbf{W}$ is the multi-dimensional Fourier matrix as introduced in the previous section, $\mathbf{f}$ is object magnetization and $\mathbf{s}$ is a column vector obtained by stacking the ROS mask S. By removing the zero elements outside the object support and the corresponding columns in the encoding matrix from the Eq. (3.7), the Fourier encoding in MRI can be rewritten as:

$$\mathbf{F} = \mathbf{W}[\rho]\mathbf{f}[\rho], \tag{3.8}$$

where ρ is the subset which corresponds to the pixels within the object support region. In linear algebra theory, knowledge of object support constraint allows full object, $\mathbf{f}[\rho]$, to be recovered from an incomplete measurement set with an acceleration factor up to $\alpha = 1/\phi$, where ϕ denotes the ratio of the ROS area to the total FOV area [65, 16]. Similarly, incorporating the region of support in the image plane MRI encoding matrix, GUISE can be formulated as:

$$\mathbf{F} = \mathbf{E}[\rho]\mathbf{f}[\rho], \tag{3.9}$$

where E denotes the encoding matrix in GUISE. Keep in mind that in pMRI, employing M receiver coils allows the maximum possible acceleration factor to be improved up to M. In GUISE on the other hand, incorporation of the ROS allows an acceleration factor up to $\alpha = M/\phi$ and ϕ equals the fraction of the total FOV occupied by the ROS.

3.4 GUISE sampling pattern design

It was shown previously that image recovery from under-sampled data sets involves inversion of the known encoding matrix ($\mathbf{E}$) in Section (3.2) (Eq.(3.6)). Due to the size of the general encoding matrix, its direct inversion is computationally expensive. To overcome this intractable challenge and obtain reconstruction efficiency, decomposition of the overall encoding matrix was suggested by using a periodic under-sampling pattern. In this manner

inversion of the overall encoding matrix was equivalently achieved by inverting a series of much smaller sub-matrices. It was shown that periodic sampling causes the sequence to have a sparse PSF with non-zero elements [18]. This property can be employed to develop a computationally efficient image reconstruction algorithm.

In 3D MR imaging, k-space under-sampling was considered the same as applying a 2D binary mask to the plane defined by the two PE directions. The sampling mask H of size N, is defined to consist of a 2D repeated block of size $C_1 \times C_2$, so that the sampling pattern is periodic. As noted before, periodicity causes sparsity in the point spread function (PSF) of the sequence, so that the non-zero elements regularly are separated by zero elements [18]. In other words, the PSF of the sampling mask only has non-zero elements separated by $L_1 = N_1/C_1$ and $L_2 = N_2/C_2$ in each direction. Regarding to the rule of convolution, applying the sampling mask h into the k-space is like convolving the PSF of the mask, h, with the image f.

In Fig.(3.1) it is shown that periodic sampling results in a regular, form of aliasing. Hence, a periodic k-space sampling pattern decomposes the image plane system into what is defined as a sub-sequence. A sub-sequence is formed only from the aliased image elements that are separated by integer multiples of L_1 and L_2 in two directions. The main feature of the image elements within each such aliased sub-sequence is that they are independent from the image elements in all other sub-sequences. So the overall reconstruction system can be decomposed into $L = L_1 L_2$ independent sub-sequences.

We know that the image reconstruction quality is affected by the encoding matrix, which is determined by three fundamental attributes: 1)sensitivity weighting function of each receiver, 2) the k-space sampling pattern, and 3) the region of object support. In clinical applications, the coil sensitivity functions and the ROS of the image are both dependent on the coil system and the choice of FOV respectively. Thus to optimize the image reconstruction, the sampling strategy can be adaptively determined based on the coil sensitivity knowledge and the ROS of the image. As discussed in the previous chapter all pMRI methods such as SMASH, SENSE, and CAIPIRINHA employed uniform sampling patterns. Although for single receiver coil MRI, some adaptive undersampling strategies have been designed, incorporating the knowledge of object ROS [153, 65, 66, 16]. However due to complicated nature of the encoding matrix in pMRI, the necessary computational complexity is expected to be much greater than the single receiver MRI. In SMASH [168] and SENSE [145] uniform under-sampling patterns were employed. SMASH's sampling pattern allows a uniform coverage of k-space, so that the unacquired k-space data is estimated from the nearest possible data. The uniform sampling pattern in SENSE leads to enlarged k-space sample spacing and hence Fourier imaging with reduced FOV. In

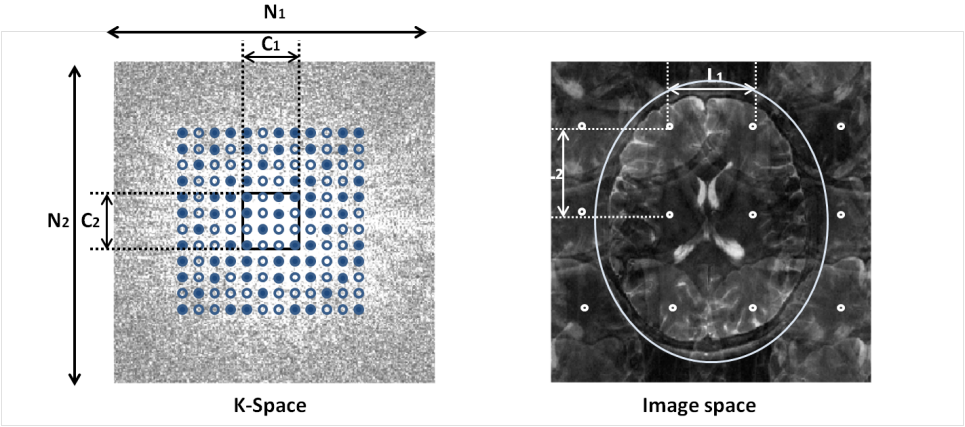

Figure 3.1: Image reconstruction using a periodic k-space sampling pattern leads to the decomposed image plane system. The k-space ($N_1 \times N_2$) is under-sampled using a ($C_1 \times C_2$) repeating pattern (dark and bright dots represent acquired and skipped samples, respectively). Then aliasing in the reconstructed image takes place in sub-sequences of image elements (regular set of white dots). The total number of independent sub-sequences is $L = L_1 \times L_2$. As depicted, image elements in each sub-sequence are separated by $L1$ and $L2$ in each direction. In each sub-sequence, only those elements which are in the ROS are required to be recovered. ROS region is outlined with the white line within the image. To reconstruct the final 2D image, all the recovered sub-sequences need to be assembled (figure reproduced from [208]).

GRAPPA [70] a densely sampled central k-space region and uniformly sampled k-space peripheral region are incorporated to achieve auto-calibration and exploit the high energy concentration level in the center of k-space. In GUISE, employing a periodic pattern minimizes the number of aliased image elements and is a heuristic attempt to advance the sensitivity encoding efficiency.

The sampling pattern design task consists of two steps in GUISE: selecting appropriate sampling block sizes, and then choosing samples locations within the block to be measured. Since the sampling block size in k-space determines the spatial location of the sub-sequences in the image plane, it determines which pixels are expected to be aliased together. The shape and the overall size of the repeating blocks need to be considered to make an appropriate decision.

Remember that blocks dimensions, C_1 and C_2, needs to be factors of N_1 and N_2 respectively, and moreover only those $C_1 \times C_2$ block sizes make applicable blocks that are an integer multiple of acceleration factor α. The repeating blocks' shape determines that along which dimension more spatial aliasing occur. Therefore, it is wiser to choose the larger dimension corresponds to the image direction which has a larger out of support region. Clearly this constraint leads to aliasing the free air region onto the object which is more advantageous

than aliasing the object region onto itself. Also the effect of block shapes depends on the coil sensitivity weighting and the object support. It is more suitable to choose the larger block dimension corresponds with the direction in which there is a greater variation in coil sensitivity. Comparing different repeated block dimensions, we concluded that to achieve the optimal reconstruction noise level, block dimension must be as large as possible [208]. However, not only using large block sizes is a challenging reconstruction task, but it also increases difficulties at designing sampling patterns for large blocks. Thereby, the possible block sampling patterns are constrained to the patterns with greatest minimal distance among the non-zero elements in their point spread functions.

In CE-MRA application, the size of the repeating block also determines achievable temporal frame rate in image reconstruction method. As the smallest possible temporal window shift limits the achievable temporal frame rate, the choice of larger block size results in the upper limit of temporal resolution. For clarification, with a block size of 4×4, shifting the temporal window by a single k-space subset potentially allows a temporal frame rate improvement factor of 16, whereas for a repeating block size of 16×16 temporal frame rate can be improved by a factor of 256.

Thus to achieve better-conditioned sensitivity matrix inversions, GUISE minimizes the degree of voxel aliasing while maximizing the sensitivity variation of aliased voxels. The PSF of the sampling pattern, and hence the aliasing pattern are determined by the designed sampling pattern in the repeated blocks. To design and achieve an optimal sampling pattern, computationally efficient algorithms were investigated. However, ideally finding the optimal sampling pattern is an intractable combinatorial problem. Reeves and Zhao analyzed the best combination of observations before acquiring the data in signal reconstruction problems [154].

In [153], Reeves et al. considered two sample selection methods based on the IT metric (IT metric is used for judging the noise immunity of different sampling patterns [208]) for the problem formulation set up as Eq.(3.8). In the proposed methods, branch and bound, and sequential backward selection (SBS), the IT metric was used in minimizing the least square errors to avoid exhaustive search through all the possible sampling patterns. In sequential forward selection (SFS) the sample that gives least increment to the IT metric is selected until the desired number of samples are obtained [65].

In pMRI, each sample selection in k-space corresponds to several measurements from all different sensitivity encoding in each receiver coil. Therefor the necessary computational complexity is much increased and therefore a new metric is required to accelerate sampling pattern design process. In GUISE, instead of directly computing the computationally

heavy IT metric, ST metric was proposed which depends on the relative separations among the k-space samples rather than their actual locations [208].

Investigation showed that both SFS and SBS perform consistently well while SBS cannot be implemented in real time [154]. However instead, SFS as an alternative approach that produces suboptimal results, is considered to be more efficient in pMRI implementation with prior consideration [65]. For instance, SFS allows data acquisition to be performed as soon as the first sample is selected, or in SFS for acceleration factors greater than 2, less sequential steps are required to be performed. Farther more, the sequentially acquired samples of data set in SFS embed temporal information which is favorable in dynamic imaging.

3.5 Prior knowledge in GUISE

In some versions of SENSE other prior knowledge or constraints were incorporated to achieve higher acceleration factors [75, 83, 29, 100]. In GUISE, as a generalized version of SENSE, an adaptive sampling pattern was employed that incorporated knowledge of multiple receiver coils and object ROS. Comparing sequential backward selection (SBS) and sequential forward selection (SFS) [154], SFS was chosen to achieve the necessary computational efficiency in sampling pattern design.

The key difference between GUISE and other image plane methods is the sampling patterns used in image reconstruction. The noise immunity of different sampling patterns employed in SENSE, CAIPIRINHA, and GUISE were simulated and compared [208]. Also sampling patterns obtained from an adaptive sampling pattern design were compared with the exhaustive search for the pattern that gives the smallest noise metric (IT metric). For a 2D binary phantom 128×128 pixels, exhaustive searches were performed for all the associated sampling patterns in relatively small block sizes (due to the demanding computational requirement) in two conditions: when knowledge of ROS is not known and when ROS is available. The simulation results demonstrated that incorporating perfect knowledge of ROS of the phantom in the image recovery leads to generally improved performance compared to when the entire FOV is recovered (ROS is not known). However, it was observed that increasing the repeated block size broadens the performance range of the different sampling patterns in both cases with and without the knowledge of ROS.
The best sampling pattern derived by the exhaustive search compared with the SFS results and showed a good trade-off between efficiency and optimality. IT metrics was used to rank all the possible sampling patterns for the block sizes that an exhaustive search was computationally feasible, and it was found that the sampling patterns designed by SFS

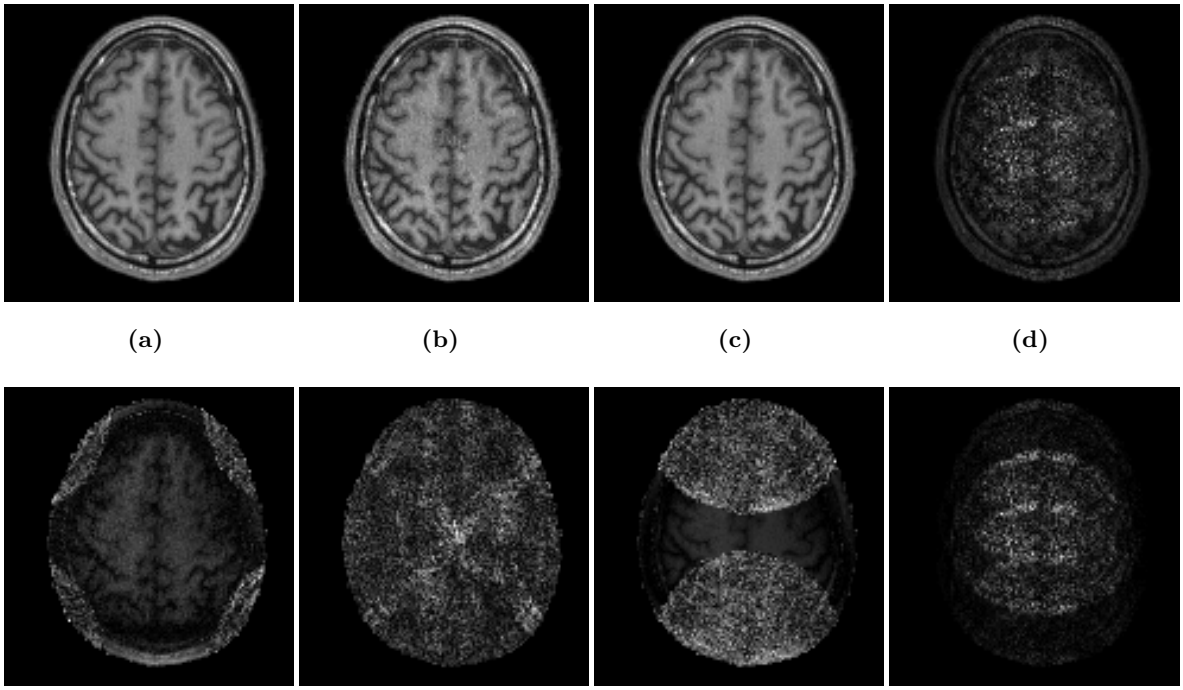

Figure 3.2: Image reconstructions using in-vivo data sets. (a-b) Reconstructed images using 2D GUISE (block size 8×8) at AF=2 and AF=6, respectively. (c-d) Reconstructed images using SENSE at AF=2 and AF=6, respectively. (e-f) GUISE corresponding noise profiles (difference between the reconstructions and a sagittal slice reconstructed from the full data acquisition) with the following reconstruction noise value, NRMS= 0.0233 and NRMS= 0.0959, respectively. (g-h) SENSE corresponding noise profiles (difference between the reconstructions and the reference image) with NRMS= 0.034 and NRMS= 0.667, respectively (figure reproduced from [208]).

were always among the best 15%.

Overall, it was concluded from the results that 2D SENSE pattern led to the highest noise amplification level whereas, a moderate block size combined with SFS approach gave favorable results when the ROS constraint is incorporated [208]. In in-vivo experiments, 3D images reconstructed using proposed GUISE sampling pattern with a repeated block size of 8×8 were compared with SENSE and CAIPIRINHA at a high acceleration factor of $\alpha = 8$. In GUISE object ROS was estimated using only the k-space center. From practical point of view, incorporating the low resolution approximation as a prior knowledge in reconstruction is possible since a low resolution image approximation is often accessible from the calibration scan process, and it is also required for estimating the coil sensitivity profiles.

As expected, the results shown in Fig.(3.2) supports the argument advanced earlier that GUISE reconstruction generates images with a lower overall noise level and a more uniform noise profile. A normalized root mean squared distance (NRMS) was defined and used to measure and compare the noise level:

$$NRMS = \sqrt{\frac{\sum_{i=1}^{P} \left(\left| f_i^{reference} \right| - \left| f_i^{reconstructed} \right| \right)^2}{\sum_{i=1}^{P} \left| f_i^{reference} \right|^2}}, \tag{3.10}$$

where P is the number of voxels recovered in the brain volume. In Fig.(3.2), a low resolution image approximation constructed using only the center of k-space (32×32) is used as an initial estimate for the ROS. Although 2D SENSE minimizes the sampling design effort, it results in the highest noise level. The other reconstruction approach, 2D CAIPIRINHA, elevates the exploitation of coil sensitivity weighting while could not efficiently utilize the knowledge of ROS.

3.5.1 Implementation and support definition of GUISE in CE MRA

Conventional Cartesian MRA reconstruction approaches use sliding window (SW) methods to improve the temporal resolution by k-space view sharing. Keyhole [192] and time-resolved imaging of contrast kinetics (TRICKS)[186] as the two most common 4D imaging techniques, exploit the fact that central data subset of the k-space conveys contrast information and need to be acquired repetitively. In Keyhole each such subset is updated over time and then combined with the data acquired from the peripheral regions of k-space to form Composite k-space data sets. To increases the temporal resolution in TRICKS, the K-space is divided into subsection regions which each region is updated with different frequencies. The sampling rate at the lower spatial frequencies is increased whereas at the higher spatial frequencies the sampling rate is reduced. Then, to form composite k-space data sets along the temporal axis, the new acquisitions from the central region of k-space is combined with the closest matching k-space from the peripheral regions. Although TRICK improved temporal fidelity over the Keyhole, more sophisticated versions of the TRICK achieved better spatial-temporal domain reconstruction fidelity [196].

Both high temporal frame rate and narrow footprint are desirable in MRA. The high temporal frame rate requires the ability to update a small portion of the k-space data set to reconstruct the next image, whereas it is not achievable in existing SW methods. On the other hand, the narrow footprint requires high image reconstruction acceleration factors, which can be gained by sacrificing the high spatial frequencies, and may lead to

ringing artifacts. To generate a high frame-rate image sequence, a new Cartesian sampling SW method was presented based on GUISE. In this Cartesian grids method, FE lines were sequentially acquired and then combined to perform SW reconstruction with high temporal frame rate. Recall that in GUISE to achieve the high computational efficiency, the partial k-space data set utilized for image recovery corresponded to a periodic sampling pattern. In sliding window reconstruction data from a short temporal window is used to form an image frame, then the next interval, overlapping with the previous interval, is utilized to reconstruct another image frame and so on. It is illustrated in Fig.(3.3) that the time frames are temporally correlated, since only a portion of the k-space data is updated for reconstructing the next time frame. SW reconstruction and the conventional time resolved imaging offer the same temporal footprint with the same acceleration factor, but SW reconstruction has higher temporal frame rate (determined by the length of window shift) without sacrificing other image reconstruction quality. Hence using SW is the most common method in cases where rapidly varying dynamic needs to be captured. As it is shown in

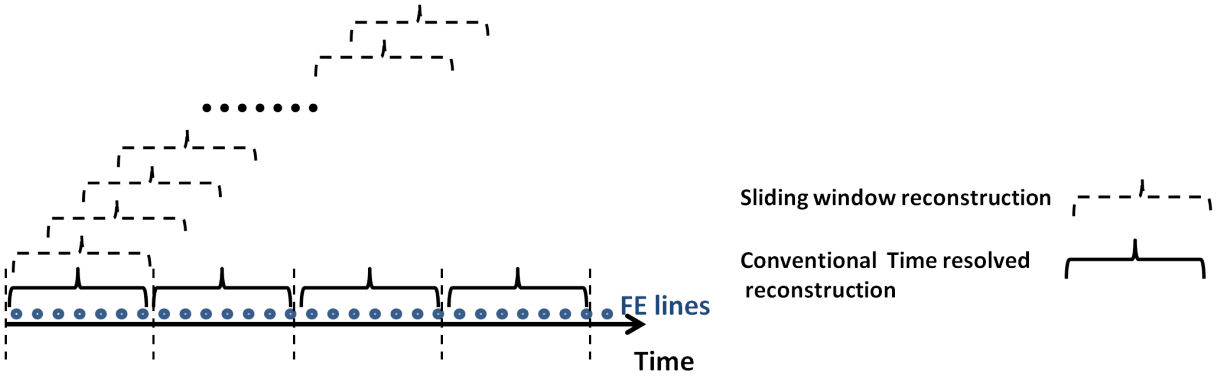

Figure 3.3: Comparing sliding window (SW) reconstruction and conventional time resolved reconstruction. The filled dots represent a subsets of k-space (a single or a group of FE lines) on Cartesian or non-Cartesian k-space trajectories (radial or spiral). The sequentially acquired k-space dataset is used to reconstruct images. Within the time interval (as indicated by the time windows) the image can be reconstructed using the consecutively acquired k-space dataset. As illustrated, in conventional time resolved imaging, data sets used for producing different time frames are different and temporally independent. Whereas the time intervals used in neighboring SW reconstructions are shared and overlapped in time. In the diagram the time window has been shifted with 2 data subsets while an individual reconstruction requires 6 data subsets,so the temporal frame rate has been improved by a factor of 3 in SW. Note that the temporal footprint, which is determined by the amount of data acquisition used for image reconstruction, is the same as conventional time resolved in SW reconstruction

Fig.(3.4) samples (FE lines) within repeated blocks are acquired sequentially in a predefined order. After performing a full k-space acquisition, data acquirement was repeated with the same sampling pattern, to have multiple acquisitions of the k-space for the time interval of

interest. Thereby the sequentially acquired data set reveals the temporal variation of the agent concentration over the time of interest. Using SW reconstruction, different temporal window length can be chosen to perform GUISE and achieve image sequences with different temporal resolution. CE-MRA imaging in GUISE was accomplished by performing direct inversion of the encoding matrix $\mathbf{E}[\rho]$, as discussed in Section (3.3).

There is a fundamental trade-off between the acceleration factor (temporal footprint)

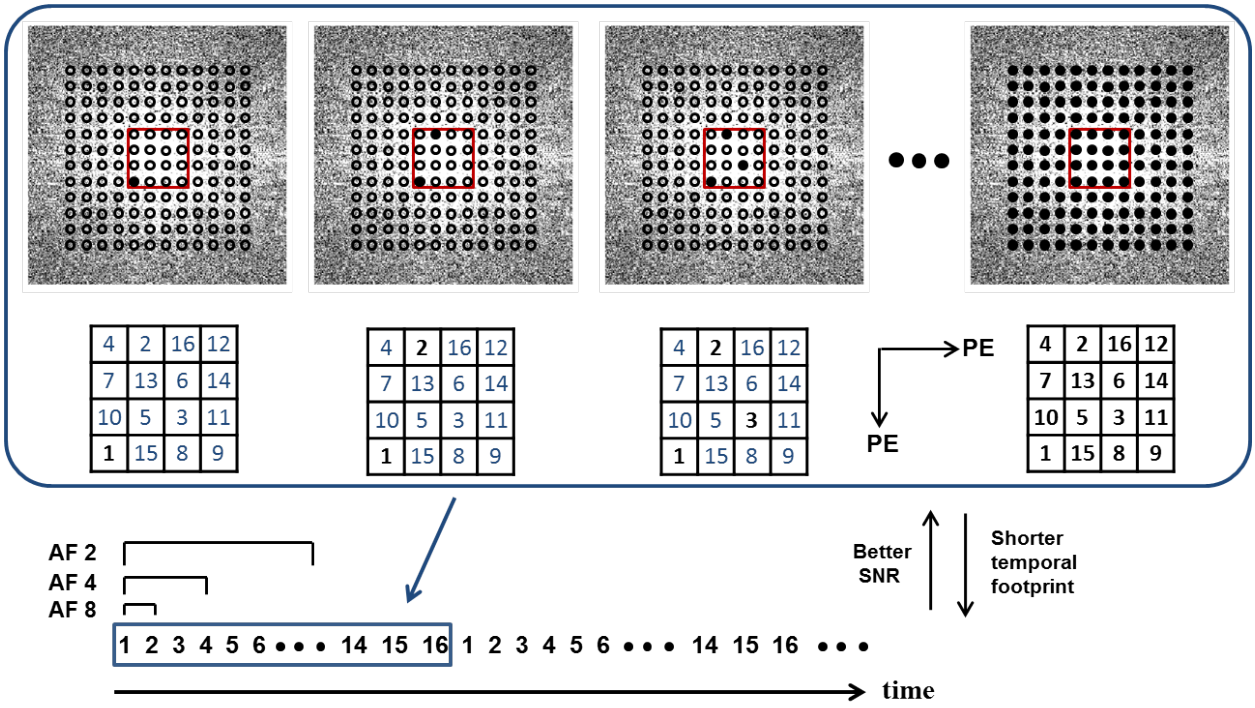

Figure 3.4: Illustration of the data acquisition scheme in the proposed SW method based on GUISE. A repeating block size of 4×4 gives 16 k-space subsets that are to be acquired sequentially in a pre-defined order. dark and bright dots represent acquired and skipped FE lines, respectively. The same acquisition order can be repeated to acquire multiple k-space dataset. In the post-processing, SW reconstruction is performed using the consecutively acquired k-space subsets with the freedom of choosing the temporal window length. In this example, using 2, 4 and 8 k-space subsets (out of 16) correspond to improvement factors of the temporal footprint of 8, 4 and 2 (the same as acceleration factor), respectively. As expected, a higher acceleration factor causes a deteriorated SNR in reconstructed images.

and the level of reconstruction artifacts (such as spatial blurring) in the existing image recovery techniques. In practice, the acceleration factor is figured out prospectively, prior to the actual scan. conventionally, this does not lead to an optimal trade-off between the temporal footprint and the reconstruction artifacts due to different fluid flow dynamics in patients. In GUISE, the acceleration factor can be determined regarding to the estimation of the contrast flow dynamics i.e., retrospectively. Thereby, the trade-off can be achieved

in a more optimal way. On the other hand, using the retrospective reconstruction, an image series with a low temporal resolution can be first reconstructed and used as prior knowledge for image reconstructing at higher temporal resolution.

In CE-MRA, the k-space data set consists of signals acquired from the blood vessels containing contrast agent and from the stationary background. Since it was sufficient to only reconstruct the vessels containing contrast agents, the anatomical background can be suppressed by the background subtraction. A k-space data set was acquired without the presence of the contrast and used to be subtracted from the k-space data set acquired with the contrast present as illustrated by an example in Fig.(3.5). Digital subtraction angiography (DSA) has been used in many practical applications to eliminate background and improve the image contrast [91, 63]. As the regions occupied by vasculature is a small portion of the FOV, the background subtraction results in significant reduction in the ROS. A smaller region of support improves the reconstruction SNR and hence offers the potential to increase the acceleration factor.

In CE-MRA, the ROS of the blood vessels can only be estimated in the presence of contrast agent during the post-processing phase. In GUISE to obtain a binary mask of the vasculature, after the anatomical background elimination, all the k-space repetitions over the imaging time interval was combined. Applying inverse Fourier transform, an image containing arterial and venous blood vessels was generated and then vessels were segmented from the free air region surrounding them. Traditional intensity-based thresholding underestimates the actual vascular region Due to the complicated vascular structures. In order to clearly depict the ROS in vascular visualization from 3D data, a visualization method called maximum intensity projection (MIP) was applied.

3.5.2 Maximum Intensity Projection (MIP)

In 3D MRI interpretation the method that reformats and displays 3D images data set plays an important role. Data originating from magnetic resonance angiography (MRA) exhibits some properties which make the application of some volume visualization techniques like ray casting or iso-surface extraction difficult. The maximum intensity projection (MIP) algorithm is a simple solution to this problem and has proven to be the most popular rendering algorithm for MRA. Note that the term *rendering* is here used to represent in a general sense a method to generate a 2-D image from a 3-D data set. To generate an MIP image, the voxels within the 3-D data set with maximum intensity that occur along parallel rays traced from the viewpoint are projected onto the visualization plane, as shown in Fig.(3.6). This method of projection is the most frequently employed because it

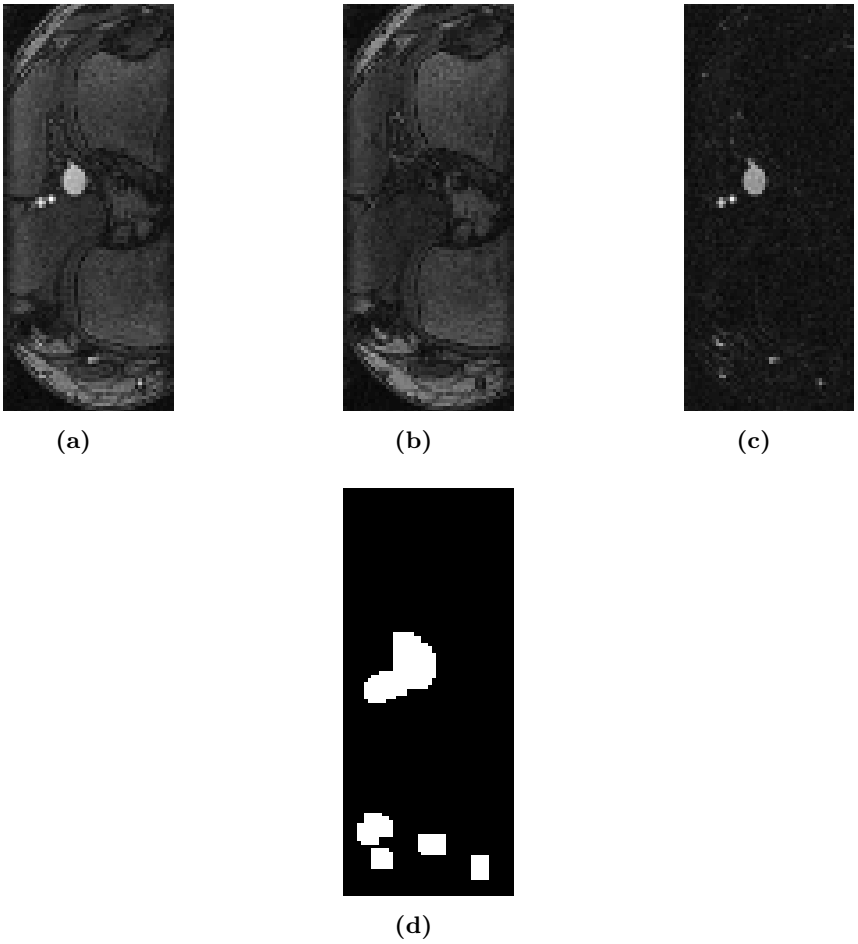

(a) **(b)** **(c)**

(d)

Figure 3.5: Illustration of the background subtraction. The acquired k-space data includes signals from both the contrast and the anatomy. a) The axial plane of the image consists of two FE directions is shown. As it is shown, it contains contrast and the anatomy and hence has a large ROS. Then background subtraction is performed using a data set which contains no contrast signal (the k-space was acquired prior to the contrast arrival). b) Image displays the background. c) The image depicts the result after reconstruction, which is contained only contrast in vascular region. d) As shown here, the subtracted data set has a much smaller ROS defined only by the vascular regions.

conveys the densitometric information of the original images without the need to tune any parameters and its implementation is relatively simple. The main limitations of MIP are that it cannot adequately depict the spatial relationships of overlapping vessels and large bright structures can occlude other structures along rays from two or more directions. The MIP algorithm is very simple and provides high signal-to-noise ratio (SNR) for large, bright vessels [178], [35]. However, by keeping the maximum background signal along each ray the algorithm causes the average background intensity in the MIP image to be larger than the background intensity in the original image data and thus small vessels, with low initial

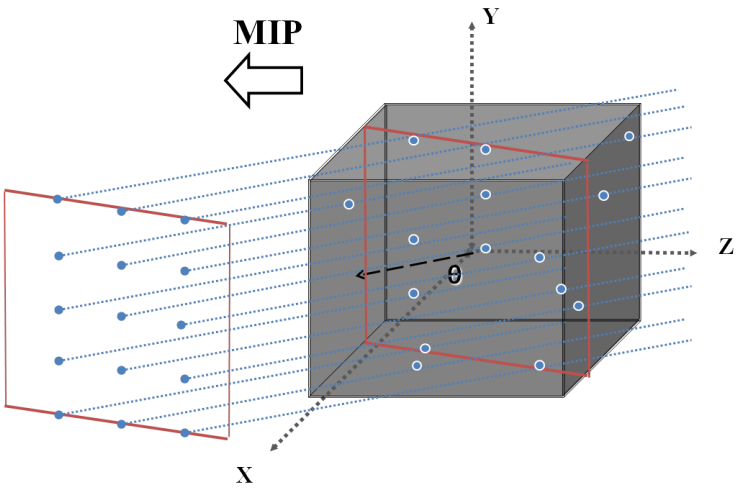

Figure 3.6: Maximum Intensity Projection (MIP) of a 3D volume. The highest intensity value in the Projection direction is selected. Projection of the entire 3D volume results in a 2D plane MIP as shown in the left. In principle, projection ray can be made along any angle(in the diagram θ)

SNR, have reduced conspicuity [26], [179]. Additionally, since only the maximum value is recorded, the MIP images provide no information regarding vessel overlap or the depth of the vessels. Fig.(3.7) shows an MIP for a 3D data set obtained by contrast enhanced MRA of the knee region of a normal healthy volunteer.

As well as requiring a rendering method for visualising 3D data sets for radiological assessment, we also require a method to segment the 3D set into those regions which have a high probability of containing significant blood vessels and the rest(the background). It was explained earlier that GUISE for accelerated parallel MRA relies on the use of a region of support (ROS), i.e. a region outside of which significant changes due to the presence of contrast are unlikely to occur. Knowledge of the ROS allows the elimination of the regions outside the object from the reconstruction, as they are known not to contribute to the signals received in the scanner coils. Comparison between reconstruction methods shows that the relative performance of this approach tends to improve with a smaller ROS, provided the ROS still encompasses the vessels of interest. The results have shown that this method is superior to the others in terms of giving lower overall noise levels. In addition, it could be very useful in cases where imaging speed is critical and a small ROS applies. The significance of establishing an ROS has been confirmed by others [208]. In the following we present an alternative rendering method to the MIP and demonstrate its use on 3D MRA data sets. We also use the new method to derive an ROS for the purpose of achieving better time resolved MRA image sequences.

Figure 3.7: Coronal MIP image formed from a set of contrast-enhanced MRA data obtained from the knee region of a healthy normal volunteer

3.6 A modified MIP for segmentation

To achieve better visualisation of blood vessels, as well as to enable better 3D segmentation results to be achieved, a method needs to be developed that increases the contrast-to-noise ratio. We propose a modification to MIP which aims to use the maximum value in optical rays which intersect at least one vessel, while selecting the mean value in other cases. In order to achieve this a model is required for the statistical distribution of intensities along rays. We conjecture that virtually all rays comprise a relatively high proportion of non-vessel voxels with intensities belonging to a population with a relatively low intensity (the background). Some rays include as well a relatively small proportion of bright voxels lying inside vessels. The intensity histograms of the latter type of rays therefore contain *outliers* with respect to the background population.

Fig.(3.8) illustrates the types of histograms which occur within a typical MRA data set. The background in each case forms a relatively large population of low intensities. When vessels are present they belong to a separate, more intense population. Therefore if a robust measure of the background population can be made, it should be possible to detect the presence of the outliers. A robust measure of data location, *median*, is used instead of

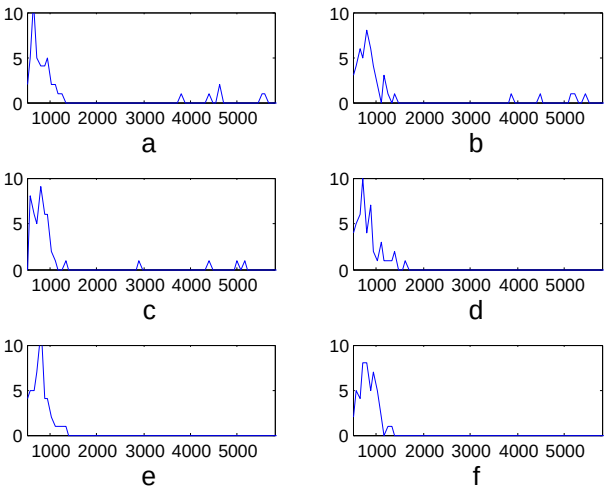

Figure 3.8: Intensity histograms of voxel intensities along 6 adjacent parallel rays in the 3D data set shown in Fig. 3.7. In the first three histograms (a to c), rays intersect the large vessel central in Fig. 3.7 and thus relatively bright voxels are encountered. The remaining three histograms (d to f) are for rays which lie just outside the vessel and appear to comprise background voxels only.

the mean and as a robust measure of data dispersion the *median absolute deviation about the median* (MAD) is used [120]. In order to normalize the latter so that it gives a value directly comparable to the standard deviation for a Gaussian distribution, a normalized quantity MADN is defined by

$$\text{MADN}(x) \;=\; \text{MAD}(x) \;/\; \text{MAD}(N(0,1)),$$

where $N(\mu, \sigma^2)$is a normally distributed random variable with mean μ and variance σ^2 [120]. As the intensities of voxels lying within vessels are expected to be significantly higher than the background distribution, a threshold for detection can be specified as:

$$T_{ray} = median + K \times MADN, \tag{3.11}$$

where the median and MADN quantities are estimated for the particular ray concerned and K is a positive scalar. To form a *modifed* MIP image, then, the threshold is calculated for every ray for a particular viewing direction (usually chosen to be in the direction of one of the cartesian axes). For each pixel in the 2D projection, if any voxel intensities in the corresponding ray exceed the threshold, the maximum voxel intensity for the ray is entered as the projected value, otherwise the median (background) level is entered, as

illustrated in Fig.(3.9).

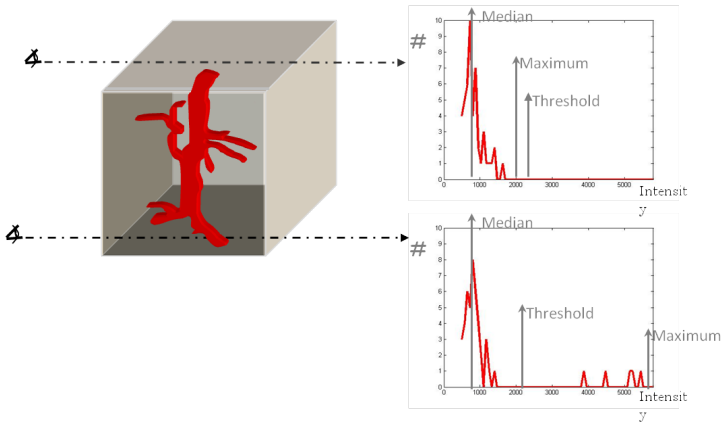

Figure 3.9: This diagram shows *modifed* MIP procodure for different rays. The top ray comprises a relatively high proportion of non-vessel voxels with intensities belonging to a population with a relatively low intensity (the background). With respect to the calculated threshold, the median of the background will be projected. In contrast the bottom ray includes as well a relatively small proportion of bright voxels lying inside the small vessels and the maximum intensity exceeds the threshold.

Fig.(3.10) shows modified MIP images for the same set of data and viewing direction as Fig.(3.7), for three different values of K. While the images in Fig.(3.10) are necessarily very similar to that in Fig.(3.7) in terms of the bright pixels associated with blood vessels, they show much less variation in the background. The contrast-to-noise ratio for the modified MIP images is therefore better than for the corresponding MIP. It has to be acknowledged, of course, that the improvement is as a result of lowering the background noise level without any improvement in the estimates of the object pixels. The result is relatively insensitive to the K value chosen.

3.6.1 Algorithmic complexity

Computation complexity (the notation O(expression)) represents the entire set of functions that grow slower than or at the same pace as the expression. For example, $O(n^2)$ represents the entire set of functions that grow slower than or at the same pace as n^2. Although Big-o notation is a way of describing the change in how long an algorithm will take to run based on the number of input values it must process, it is independent of how fast the computer can make calculations.

In general, the global computation complexity of the conventional maximum intensity projection is equal to the number of voxels within the volume (i.e., $O(n^3)$ steps for a $n \times n \times n$ data grid) since all voxels must be processed in order to find the maximum

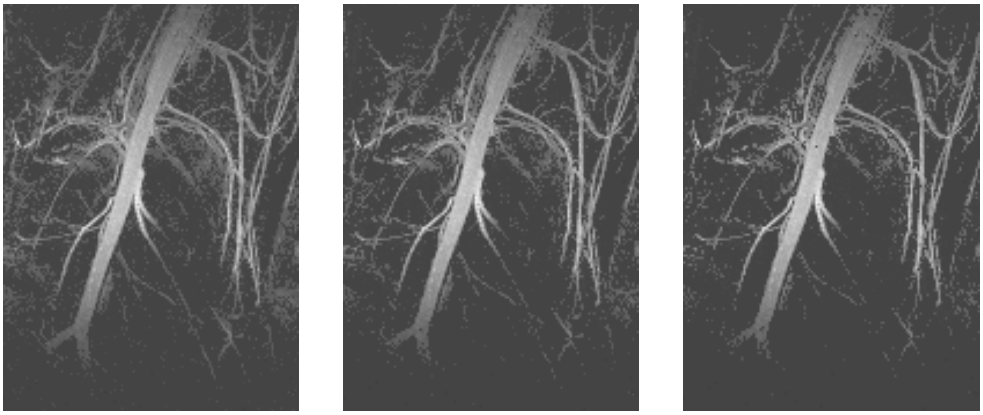

(a) (b) (c)

Figure 3.10: Coronal modified MIP images formed from the same set of contrast-enhanced MRA data obtained as shown in Fig. 3.7: (left) $K = 4.5$, (center) $K = 5.5$, and (right) $K = 6.5$.

intensitiy along the view directions. The only significant difference is that in the proposed MIP method there is an additional MADN calculation and *if expression (do) else (do)* required to be performed in the innermost loop of the algorithm. The general rule for a loop is that the running time is the sum, over each iteration of the loop, of the time spent executing the loop body for that iteration. Meanwhile, the running time of a fixed sequence of program steps, where each step may be an arbitrary program fragment with loops and branches is the running time of the steps with the longest running time [5]. Given the computation time for *if loop* and for MADN is $O(1)$, the maximum running time for inward loop can be concluded the same as before ($O(n)$ for finding the maximum value of the intensities in each ray). Thus, the proposed algorithm has the same complexity as conventional algorithm (equal to $O(n^3)$) although the CPU computation time for our algorithm is higher.

It can be considered that the non Cartesian coordinate system might also be used to produce multiple MIP images. While Cartesian trajectories are by far the most popular and computationally inexpensive method, other trajectories can be used. Efficient projection from non Cartesian coordination requires using interpolation schemes and the complexity of interpolation along a ray is equal to $O(ln(n))$.

3.7 3-D segmentation

In 3D contrast-enhanced MR angiography, the stationary anatomical background can be suppressed via a subtraction to reduce the effective ROS to a large extent, Fig.(3.5). In order to provide improved time-resolved MRA image sequences of the blood vessels, our

reconstruction algorithm, GUISE requires an accurate segmentation of the relatively noisy 3D data set into vessel and background. The method we have used to date for definition of that ROS is primitive, however. In brief, three orthogonal MIP images (axial, coronal and sagittal) were segmented by simple global thresholding and application of morphological dilation. Then three binary images so formed were backprojected within the 3D volume and combined by a logical AND operation to derive a crude ROS. For any 3D image, the support mask of the axial plane MIP is replicated along the superior-inferior (SI) direction to give a 3D support volume. To estimate the support mask, then the intersection of these three volume is taken. This approach has a similar concept to the back projection reconstruction method used in computed tomography, in which 3D volume is reconstructed using many Back-Projections. Due to the insufficient number of projections, regions outside the vessels might also be included in the estimated support region or vise versa. In order to connect disjoint regions or remove irrelevant regions resulted from global thresholding and finite projections, morphological operators were applied.
Morphological filters are, perhaps, the most well-known non-linear filters for image enhancement. They include erosion, dilation, opening and closing. Dilation increases the size of an object and is equivalent to an erosion of the background. The opening operation, erosion followed by dilation, removes small regions and smooths a 3D binary object. Since structuring elements determine the extent of the mathematical morphology operations, the action of a morphological filter depends on them. Morphological operators have been shown to be useful in removing noise from structures at the final stage of segmentation [64]. Use of morphological filters causes a lot of redundancy of information in the image. Regardless of this drawback, this redundancy potentially leads to a higher level of safety to ensure each voxel belongs to the vascular region is included in the support mask. In general, the described method produces a segmentation with many false detections because of the effect of overlying structures and the relatively noisy background in MIP images.

To achieve a more accurate 3D segmentation, we proposed therefore to use the same principle as employed for the modified MIP in Section(3.6). In the proposed method, for each voxel in the 3D data the histograms of the 3 orthogonal rays in the directions of the Cartesian axes which intersect with that voxel are evaluated. A threshold is calculated for each of the three rays in the same way as described in Section(3.6). Thus for the voxel three thresholds T_x, T_y and T_z are found. If the voxel intensity exceeds at least two of the thresholds (i.e., a majority) the voxel is classed as *vessel*, otherwise it is classed as *background*. Comparison of results shows that the best value to use for K in computing T_x, T_y and T_z is in the range 5 to 7.

3.8 In-vivo experiments

Studies on the knee region of three human volunteers were carried out to investigate the performance of the proposed methods. Both experiments were carried out using a 1.5T GE scanner equipped with an 8-channel receiver, in which the individual receiver channels are symmetrically placed around a cylinder. A T1-weighted 3D spoiled gradient recalled (SPGR) sequence was used, and the two PE directions were set to left-right (LR) and anterior-posterior (AP). Ethical approval was obtained from the Ethics Committee to make a single injection of gadolinium contrast into each subject. For the GUISE acquisition, the scan parameters used were: $TR = 5.4$ ms, $TE = 1.6$ ms, Flip angle $= 45$. A matrix size of $196 \times 128 \times 48$ was used to obtain a spatial resolution of $0.9 \times 0.9 \times 1$ mm. 20 ml of Gd-BOPTA (Multihance) was injected as a bolus. A repeating block size of 16×16 was used and the acquisition order was determined using sequential forward selection. A complete acquisition of the 3D k-space volume took 30 s, and 5 repetitions were made.
In both cases, data acquisition was commenced before the injection; the data acquired before the arrival of contrast was used for estimating the coil sensitivity profile and subtracted from the following repetitions to eliminate the stationary background.

3.9 Evaluation of the segmentation method

To facilitate a quantitative comparison for the modified MIP visualisation method, we used the contrast-to-noise ratio (CNR) which was calculated as follows:

$$\text{CNR} \;=\; \frac{(\mu_V \;-\; \mu_B)\,(N_V + N_B)^{\frac{1}{2}}}{(N_V\,\sigma_V^2 \;+\; N_B\,\sigma_B^2)^{\frac{1}{2}}}\,,$$

where μ_V and σ_V^2 are the mean and variance respectively of pixels lying within a vessel, μ_B and σ_B^2 are the mean and variance respectively of pixels lying within the background, N_V is the number of vessel pixels considered and N_B is the number of background pixels considered [26]. In order to check that comparable results were achieved from a range of data sets, we applied the modified MIP method to three data sets using $K = 7$. The data sets were each of the knee region and made with similar injections of contrast agent, but obtained from different subjects. In each case those pixels for which voxels in the corresponding ray exceeded the threshold were counted as vessel, while the remainder were counted as background. The resulting CNR values for the three data sets were: 5.2971,

6.7756 and 4.5528. Fig.(3.11) and Fig.(3.12) show images formed for the second and third of these data sets, both by the standard MIP method (left) and by the modified MIP method (right).

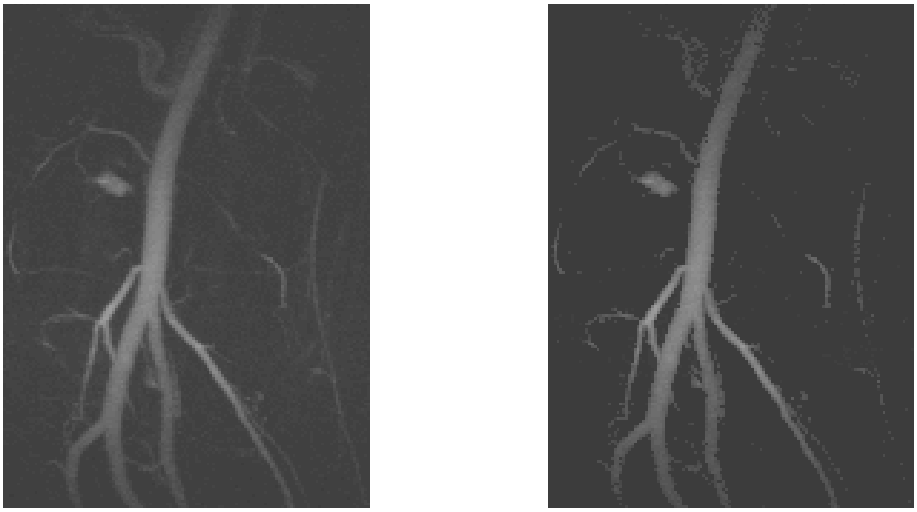

(a) **(b)**

Figure 3.11: Projection images for a second 3D data set of the knee region of a healthy volunteer obtained by contrast-enhanced MRA: (a) coronal MIP; and (b) coronal modified MIP (K = 7)

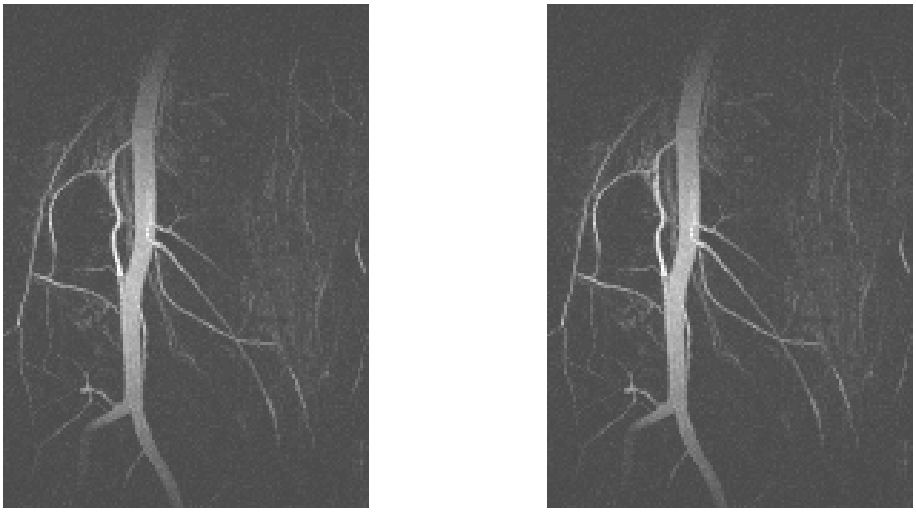

(a) **(b)**

Figure 3.12: Projection images for a third 3D data set of the knee region of a healthy volunteer obtained by contrast-enhanced MRA: (a) coronal MIP; and (b) coronal modified MIP (K = 7).

CNR values were also calculated with respect to specific features in the images. For example, for the coronal projection images shown in Fig.(3.7) and Fig.(3.10), patches were manually selected within the large central blood vessel and one of the small vessels. A

larger region was chosen within the part of the images clearly separated from the vessels. The patches chosen had sizes 66 pixels (large vessel), 19 pixels (small vessel) and 2296 pixels (background). The results are shown in Table 3.1.

	Standard MIP	Modified MIP
large vessel	43.45	84.22
small vessel	37.88	71.43

Table 3.1: CNR values based on patches chosen from the coronal projection images shown in Fig. 3.7 and Fig. 3.10.

To evaluate the success of using the new method for 3D segmentation, we present results for a single coronal slice in Fig. 3.13 and a single axial slice in Fig. 3.14 In each figure the left image shows the raw data for the 3D reconstruction (the same data set as used for Fig. 3.7 and Fig. 3.10, but a single slice only). The center image shows the crude segmentation generated for that slice by our original MIP-based segmentation [205]. The morphological dilation operations used in forming the ROS have clearly made the ROS a poor fit to the vessels present in the slice. The right image shows the result of performing our modified segmentation with those voxels segmented as back-ground shown black. It is clear that the algorithm successfully forms a tight support region around all sizeable vessels. In Fig.(3.15) sliding window GUISE reconstructions of 3 coronal plane MIP frames

(a) **(b)** **(c)**

Figure 3.13: 3D segmentation using the modified MIP method. A single coronal slice from the same 3D data set depicted in Fig. 3.7 is shown: (*left*) raw slice data; (*center*) slice segmented by the crude thresholding method; and (*right*) slice segmented into vessel and non-vessel by the modified MIP method.

(the 14th, 25th and 35th frames out of 121 frames) are shown for one of the volunteers

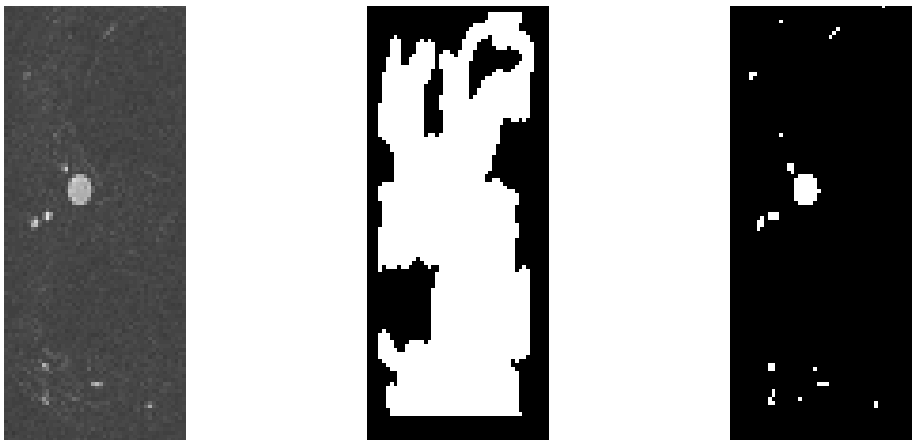

(a) (b) (c)

Figure 3.14: 3D segmentation using the modified MIP method. A single axial slice from the same 3D data set depicted in Fig.(3.7) is shown: (*left*) raw slice data; (*center*) slice segmented by the crude thresholding method; and (*right*) slice segmented into vessel and non-vessel by the modified MIP method.

studied. The frame width was 7.5 s (acceleration factor of 4) and the frame step was 0.93 s. Fig.(3.15d) shows the time intensity curves (TIC) that depict the image intensity variations over the data acquisition time period of selected arterial and venous regions (as indicated in the figure by different colors). As it is seen in TIC plot, GUISE acquisition features a high level of temporal noise and also these variations appear to have some periodic oscillation. Since different time frames are made from different portions of the k-space and also each frame has been sampled with different pattern, the noise in the reconstruction results have been sourced from two major sources. On one hand, k-space has a non-uniform energy distribution, the subsets used for different reconstructions have different levels of energy which leads to non-uniform reconstruction amplitudes. On the other hand, different sampling patterns used in different temporal windows lead to different levels of reconstruction artifacts. Note that the period of the two sources of variations is equivalent to the time interval for a complete k-space acquisition, 30 s.

3.10 Discussion

In this chapter, a new Cartesian based sliding window reconstruction method based on GUISE was discussed. In GUISE, temporal frame rate is constrained by the sampling pattern periodicity. On the other hand, without incorporating the prior knowledge into image reconstruction, GUISE performs similarly to the conventional SENSE recovery approach that reconstructs an image estimate by exploiting the distinctive coil sensitivity

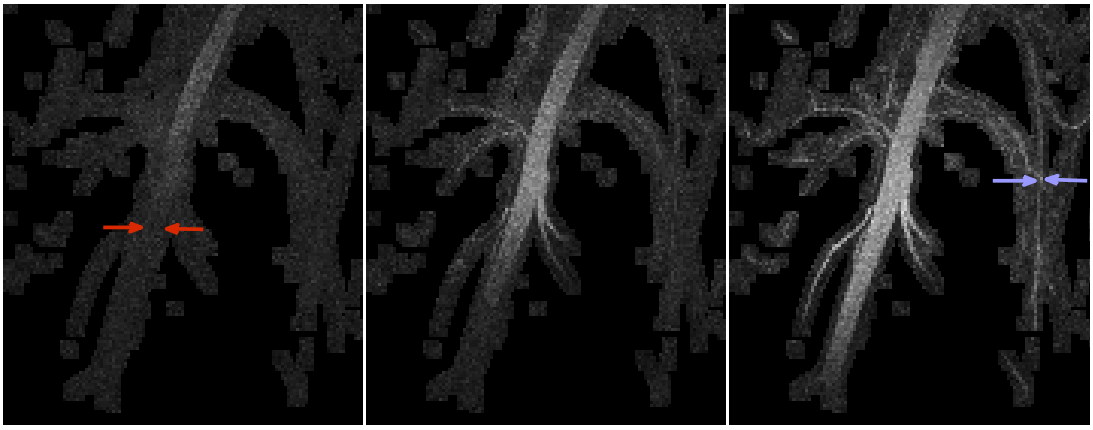

(a) (b) (c)

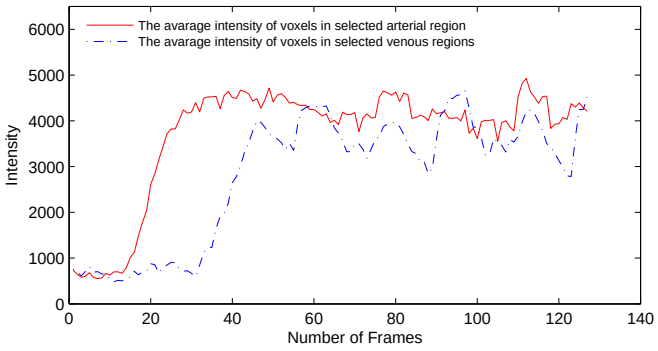

(d)

Figure 3.15: Sliding window reconstructions (coronal plane MIP) in a volunteer study at temporal footprint of 7.5 s and temporal frame rate of 0.93 s. (a), (b) and (c): Three frames selected from the sequence of 121 frames reconstructed by the PECS method, 14th, 25th and 35th frame respectively. (d) Intensity versus time plots for a group of voxels in the central artery (the average of 24 voxels, pointed by red arrow) and a small venous regions (the average of 6 voxels, pointed by blue arrow) is taken, respectively.

encoding. Since defining a tighter ROS allows a higher acceleration factor to be achieved and the SNR improvement, a new, modified segmentation approach was proposed. However, due to a potential risk for omitting vascular regions with low contrast level, the safer method was implemented. The presented segmentation methods, were based on maximum intensity projection (MIP). We proposed a modified MIP using a statistical model of the information stored along parallel rays within the data set to derive a 2D projection image.

Despite the simplicity and widespread acceptance of MIP technique for displaying three-dimensional (3D) magnetic resonance angiographic data, several disadvantages are associated with MIP. These include an elevated noise level in the background and low contrast

between small vessels and background tissue. We have developed a method to complement the conventional MIP and alleviate these problems. Significantly better CNR values are obtained with the modified MIP method according to our preliminary studies. The incorporation of a single parameter allows the new method to be tailored to specific viewing tasks. The main motivation in developing the modified MIP method was in seeking a way of segmenting 3D MRA data sets. Simple global thresholding of MIP images allowed only fairly gross approximations to the vascular region to be formed. By assessing each voxel on the basis of the three orthogonal rays passing through it and forming thresholds based on robust statistics, it is possible to better discriminate between voxels likely to lie within vessels and those likely to lie outside. A 3D segmentation method was introduced to form an ROS based on a modified maximum intensity projection (MIP) of images which resulted in a reasonably tight support region around all sizeable vessels [190]. In this segmentation method, the use of the majority operator reduces the possibility that an overlaying structure can influence the segmentation decision. The ROS formed by the new method (cf. right hand images in Fig.(3.13) and Fig.(3.14)) is *tight*. Best use of the ROS for MRA reconstruction algorithms requires a somewhat looser support, so we plan to use some form of 3D dilation operation following the segmentation. The work presented here is preliminary.

Overall, the TIC curves obtained from GUISE showed reconstruction artifacts, since the sliding windows are subjected to periodically varying sampling patterns. A low acceleration factor might reduce periodic artifacts at little expense regarding practical utility. In the next chapter a new method is presented that has been developed for GUISE noise reduction.

Chapter 4

Noise reduction in CE-MRA with Karhunen-Loeve and Wavelet transformation

4.1 Motivations

Coronary artery disease remains the leading cause of morbidity and mortality in industrialized nations and is rapidly becoming the primary cause of death. An accurate, noninvasive technique that allows for the assessment of stenoses would therefore be of great clinical value. Limited volume coverage, poor signal from deep body structures and long imaging times during which patient movement may degrade image quality, all limit the cardiovascular application of MRI. On the other hand, eliminating the risks of radiation, iodinated contrast and arterial catheterization are strong reasons to favour 3D contrast-enhanced magnetic resonance angiography (CE-MRA) [143], which has become a widely clinically accepted technique for assessing renovascular and peripheral vascular disease [24]. In 3D MRA, the requirements for a fast acquisition, reasonable spatial resolution and a high signal to noise ratio often compete with one another. Independent reconstruction of each of the frames of the MR image sequence results in very noisy images and ignores the strong correlation between frames.

In this chapter, we describe an algorithm we have developed for deriving a small set of temporal basis functions. A Karhunen-Loeve transformation (KLT) which provides a temporal basis from gamma variate prototypes is proposed and applied to 3D contrast-enhanced magnetic resonance angiography (CE-MRA). Wavelet transform was also applied to the image sequences to reduce noise. We present results which demonstrate the use of methods on different sets of CE-MRA data and evaluate them. The results show that wavelet transformation fails to preserve the details of image sequence changes in time

and consequently removes fine structures in images. Here we demonstrate the impact of imposing the KLT basis for the temporal changes, based on prior expectation of the changes in contrast concentration with time. By imposing a temporal basis based on prior knowledge of the contrast flow dynamics, the time resolution of CE-MRA sequences can be improved. We show a significant reduction in artifacts caused by the under-sampling of k-space is achieved by KLT basis derived from prior expectation.

4.2 Introduction

In contrast-enhanced magnetic resonance angiography (CE-MRA), vascular enhancement is achieved by injection of a contrast agent, but the requirements for a fast acquisition, reasonable spatial resolution and a high signal-to-noise ratio often compete with one another. In MRI, information is effectively measured in 3D k-space (spatial frequency space) one line at-a-time. A complete acquisition comprises many such lines but in order to improve temporal resolution reconstructions are made from partial sets of k-space data. However, the significant time needed to acquire data in MRI remains a severe limitation. While acquisition techniques such as fast spin echo (FSE) or various non-Cartesian sampling strategies can be used to acquire image data relatively rapidly, the acquisition time for a full set of data is still normally longer than one minute and some acquisition sequences take many minutes to complete.

The contrast material used in CE-MRA is a compound containing gadolinium (Gd), which alters the T1 property of the blood with which it mixes and differentiates it from the surrounding tissue. The contrast material is injected as a bolus, often by means of a powered syringe, usually into a peripheral vein [24]. Some seconds later it arrives in the arteries within the region being imaged, the field-of-view (FOV). In CE-MRA it is important to get sufficient time resolution to be able to observe the arrival and flow of the contrast material through the vessels within the FOV. A great deal of attention has therefore been directed at developing methods of acquiring and processing MR data to achieve a higher time resolution. Not all MRA methods require contrast material: the time-of-flight (TOF) method can be used in cases where injection of Gd is contraindicated or when repeated studies are required. However, it is generally considered to be inferior to CE-MRA in terms of diagnostic quality [210]. Only CE-MRA is considered here.

In parallel MR imaging (pMRI) a full image may be achieved when k-space is under sampled by exploiting the redundancy in the coil data sets to remove aliasing artifacts. However, a well known constraint of pMRI is that as the acceleration factor is increased, the amplitudes of reconstruction artifacts grow rapidly [145] and may compromise the diagnostic value

of the images. Towards overcoming this barrier, Generalized Unaliasing Incorporating Support constraint and sensitivity Encoding (GUISE), which incorporates multiple receiver coils and knowledge of object region of support (ROS) in adaptively designing a regular block-based sampling pattern, was introduced [206]. In GUISE the emphasize is on the fact that both knowledge of coil sensitivity weighting and object support constraint are incorporated in designing an adaptive periodic sampling pattern [208]. In practice, objects are often only supported (non-zero) on a particular portion of the FOV, the images spatial domain extent. As shown in [119], when such gaps exist, the k-space samples are linearly dependent, meaning that there is redundancy in sample set obtained at the Nyquist rate. In GUISE, the object region-of-support (ROS) within the FOV can be obtained from a low resolution scout scan as a byproduct of the coil sensitivity profile estimation. Knowledge of the ROS allows the elimination of the regions outside the object from the reconstruction, as they are known to generate zero signal. GUISE is thus particularly useful in cases where imaging speed is critical and a small ROS applies; this is the case in 3D CE-MRA, where only the relatively small vascular region containing contrast is required to be reconstructed.

It has been demonstrated that full image recovery is feasible from an incomplete k-space data set by incorporating the ROS knowledge [18, 16]. In order to achieve reconstruction computation efficiency, GUISE employs an optimal periodic under-sampling pattern so that the large encoding matrix is decomposed into a series of sub-matrices. In this manner, the 3D k-space volume consists of repeated blocks of samples. The data acquisition order determines which k-space subsets are to be consecutively acquired and used in image reconstructions; in turn it determines the sampling patterns that have a large impact on the outcome of the image reconstructions [208]. This technique leads to a reduction in the reconstruction noise level and allows an acceleration factor greater than the number of coils used. Both simulation and experimental results showed GUISE-type patterns with appropriate k-space block sizes are superior to the 2D SENSE and 2D CAIPIRINHA in terms of giving lower overall noise levels. In Applying GUISE to CE-MRA, k-space subsets that are acquired sequentially over time in a periodic fashion. Combining all these subsets gives a full k-space data set that corresponds to the entire data acquisition, from which the ROS for the blood vessels can be obtained. The data acquisition order in GUISE determines which samples will be consecutively acquired and hence determines the sampling patterns employed by individual sliding window reconstructions. A trade-off can be made between the image acceleration factor and reconstruction artifacts after the data has been acquired as demonstrated in previous work.

Many attempts have been developed so far to achieve high spatial and temporal resolution images in CE-MRA. In sliding window reconstructions, only a portion of the k-space data

is updated for each consecutive reconstruction [137]. In this manner the time between consecutive frames in a sequence can be made shorter than the time it takes to acquire sufficient k-space data to form a useful reconstruction. However, a temporal blurring due to contrast level variation during the data acquisition time period in a broad temporal footprint is anticipated. GUISE was explained in detail and brought into practice in the previous chapter.

A second method, which exploits the sparsity in a contrast-enhanced angiogram and allows image prior knowledge to be incorporated, is Prior Estimate based Compressed sensing (PECS) [207]. Compressed sensing allows a signal to be recovered from an incomplete measurement data set by exploiting its sparsity and its success is determined by the sparsity level of the underlying signal. The sparse nature of angiographic images make them appropriate for CS recovery methods. In PECS, a prior estimation of the signal is incorporated in the reconstruction to allow the underlying signal to be recovered in a form that has a higher sparsity level, and hence to achieve an improved signal reconstruction. The use of pixel intensity reordering as a means of improving image reconstruction by CS was first reported in 2008 [1, 205]. The process is to re-order the pixels such that their intensities monotonically decrease throughout the FOV. Any image manipulated in this way becomes relatively smooth and therefore more sparse than the original. In PECS [207] the sorting information is gained from a prior image estimate.

To design an acquisition order for PECS, a non-uniform sampling mask with a higher density in the centre of k-space at a given acceleration factor is created, then the acquisition order of the individual samples is formed by randomly picking the samples defined by the mask. In this manner the shift from one frame to the next can be as little as one single FE (frequency encoding) line, therefore a high temporal frame rate is feasible. Both approaches also allow retrospective selection of acceleration factors at the time of image reconstruction. More details of this method will be fully addressed in the next chapters.

Dynamic images of physiological processes often show a high degree of temporal correlation. Some signal changes are quasi-periodic, e.g., cardiac motion, or slowly varying, e.g., blood perfusion, which in either case leads to a series of images with substantially similar features between frames. The expected correlation between pixel intensities over time can be incorporated into the data analysis. A number of authors have previously attempted to introduce a temporal basis into medical image reconstruction. The majority of the work to date has been directed at cardiac imaging, where the approximately periodic nature of the motion and the availability of an independent synchronous signal, the electrocardiogram, can be exploited [3, 202, 108]. While the cardiac-related work helps to illustrate the potential for incorporating temporal constraints into the imaging process, it cannot be

directly applied to the CE-MRA case.

The effect of the order in which k-space samples are acquired in CE-MRA has also been studied [115, 210]. It was found that the best quality images were achieved when the centre of k-space was sampled at the time when the peak concentration of contrast material reached the region of interest. The difficulty is that it is often desirable to observe the complete vascular system in a region and during both the arterial and venous phases [210], therefore having repeated rapid re-sampling of the centre of k-space is expedient. Prince *et al* developed methods to automatically detect the arrival of the contrast material bolus at a particular point before commencing data acquisition [143]. While this helped to reduce the need for careful synchronisation of the contrast injection with the collection of data, it did not in itself assist with achieving a higher temporal resolution. Korosec *et al.* introduced 3D TRICKS (time-resolved imaging of contrast kinetics) in which a high sampling density was applied in the central area of k-space and temporal interpolation was applied within k-space [90]. There does not appear to be any report of research into applying a particular temporal basis for CE-MRA.

4.3 Karhunen-Loeve Transform

4.3.1 KL Transform Theory

The KarhunenLoeve transform is closely related to principal component analysis (PCA) and widely used in data analysis in many fields. PCA is probably the oldest and best known multivariate statistics method the goal of which is to lessen the data set dimensions consisting of a large number of interrelated variables, while keeping as much as possible of the variation in the original data set. This is accomplished by transforming to a new set of uncorrelated variables, the principal components (PCs), which are in descending order (the first few retain most of the variation present in all of the original variables).

The earliest descriptions of the Principal Component Analysis (PCA) technique were given by Pearson in 1901 and then independently developed by Hotelling in 1933, Karhunen in 1947 and by Loeve in 1948 [84]. Hotelling's motivation was that there may be a smaller fundamental set of independent variables, which specify the values of the original variables. He noticed that such variables have been named factors in the psychological literature, and introduces the alternative term components to avoid confusion with other uses of the word factor in mathematics. Hotelling chose his components so as to maximize their successive contributions to the total of the variances of the original variables, and calls the components that are derived in this way the principal components. The analysis that attains such

components is then called the "method of principal components". Hence, the Karhunen Love Transform is equivalent to principal component analysis (PCA). Application of KLT filtering in dynamic medical imaging was first proposed by [180]. It has also been used in cardiac nuclear scintigraphy to filter the series of cine images, representing a single cardiac cycle [14]. Recently, KLT filtering has been proposed to de-noise cardiac magnetic resonance (CMR) first-pass perfusion images [155], and to generate training images in the kt-BLAST reconstruction method [185]. Here we employ the KLT to generate a temporal basis for the CE-MRA image sequence.

Consider a time sequence of P images, each composed of N voxels at locations x_i, $i = 1, 2, \ldots, N$. The intensity at location x_i and time sample t_k is $\mathbf{f}(x_i, t_k)$ and the sequence for each voxel is formed into a column vector $\mathbf{f}_i$, $i = 1, 2, \ldots N$. The matrix $\mathbf{A}$ is then formed as

$$\mathbf{A} = [\mathbf{f}_1, \mathbf{f}_2 \ldots \mathbf{f}_N] \tag{4.1}$$

with dimensions $P \times N$. To apply PCA to this data set, form the $P \times P$ covariance matrix by

$$\mathbf{C} = (\mathbf{A} - \mathbf{m}_A \mathbf{1}_N^T)(\mathbf{A} - \mathbf{m}_A \mathbf{1}_N^T)^T \tag{4.2}$$

where $\mathbf{m}_A$ is the column vector formed by taking the mean of each row of $\mathbf{A}$ and $\mathbf{1}_N$ is the unity column vector of N elements. Note that the computation of covariance should include a scaling factor but that is unimportant in this context. The eigenvectors $\mathbf{v}_i$ and eigenvalues λ_i of $\mathbf{C}$ are defined:

$$\mathbf{C}\mathbf{v}_i = \lambda_i \mathbf{v}_i, \quad i = 1, 2 \ldots P. \tag{4.3}$$

Since $\mathbf{C}$ is positive definite and symmetric, it has P real eigenvalues and the eigenvectors are orthogonal [177]. These eigenvectors, or principal components, form a basis for the data set such that the eigenvector associated with the largest eigenvalue, $\mathbf{v}_1$ say, accounts for a larger portion,of the total variance across the voxels than any other eigenvector. For convenience then, order the eigenvectors according to their eigenvalues such that

$$\lambda_1 > \lambda_2 > \ldots > \lambda_P \tag{4.4}$$

and form a unitary matrix

$$\mathbf{\Phi} = [\mathbf{v}_1\mathbf{v}_2 \dots \mathbf{v}_P]. \tag{4.5}$$

$\mathbf{\Phi}$ can be interpreted as a set of basis functions for the data and the Karhunen-Loeve transform is defined as

$$\varphi_i = \mathbf{\Phi}^T\mathbf{f}_i \tag{4.6}$$

for single voxel vector or

$$\mathbf{\Psi} = \mathbf{\Phi}^T\mathbf{A} \tag{4.7}$$

for the entire data set. Because $\mathbf{\Phi}$ is unitary, $\mathbf{\Phi}\mathbf{\Phi}^T = \mathbf{\Phi}^T\mathbf{\Phi} = \mathbf{I}$. Thus the inverse transform is:

$$\mathbf{A} = \mathbf{\Phi}\mathbf{\Psi} \tag{4.8}$$

The KLT can be shown to form an optimal basis under certain conditions [79].

A reduced basis for the data can be formed by retaining only the first $K < P$ of the eigenvectors in $\mathbf{\Phi}$ to form

$$\mathbf{\Phi}_K = [\mathbf{v}_1\mathbf{v}_2 \dots \mathbf{v}_K]. \tag{4.9}$$

The process of formal transformation with $\mathbf{\Phi}_K^T$ followed by inverse transformation with $\mathbf{\Phi}_K$ therefore is equivalent to projecting the data onto a reduced basis set and thereby achieving a compression. Of more direct relevance to CE-MRA the process can be used to form a smooth temporal basis.

4.3.2 KLT temporal basis

One of the approaches we used in our work is based on prior knowledge of the contrast flow dynamics. A set of KLT temporal basis functions which are based on the contrast flow dynamics are applied to a sequence of image reconstructions. By imposing a basis for the temporal changes, based on prior expectation of the smoothness of the changes in

contrast concentration with time, it is demonstrated that a significant reduction in artifacts caused by the under-sampling of k-space can be achieved. The basis is formed from a set of gamma variate functions. In our method, the dataset represent each pixel time-intensity curve(ITC)for a p temporal series of 2D images, each with N pixels. So this approach can offer compressions of a sequence into fewer images and noise suppressing filters.

4.3.2.1 Modeling temporal variation

In CE-MRA a bolus of gadolinium-containing compound is injected into a peripheral vein. The injected material diffuses within the bloodstream as it is propelled to the right side of the heart, through the lungs, through the left side of the heart and then finally to the site of interest. The diffusion within the moving bloodstream is such that the concentration of contrast material, observed at some downstream point, rises from zero to a peak and then decays somewhat more slowly than it rose. If monitoring continues, it may be possible to see a later recirculation phase, but attention is normally directed to the first pass of the contrast material. A number of authors have analyzed the shape of the contrast-versus-time curve and concluded that it approximates to a gamma variate function [45, 109] (neglecting the recirculation, if present). Ample experimental evidence exists for the applicability of the gamma variate function to studies involving the use of a marker substance [13, 151]. In its most common form the gamma variate function can be expressed as:

$$y(t) = A(t - t_0)^{\alpha} \ \exp\left(-(t - t_0)/\beta\right), \quad t \geq t_0, \tag{4.10}$$

where t_0 is the point at which the function commences and α and β are real parameters. However Madsen [109] showed how it can be expressed in a more convenient form:

$$y(\tau) = y_{max} \ \tau^{\alpha} \ \exp\left(\alpha(1 - \tau)\right), \tag{4.11}$$

where $\tau = (t - t_0)/(t_{max} - t_0)$, t_{max} is the time at which the function peaks and y_{max} is the amplitude at that time. The shape of the gamma variate function in the form of Eq. 4.11 is controlled by the single parameter, α.

4.3.2.2 Forming a temporal basis

Within a sequence of CE-MRA images of a fixed FOV, the expectation is that different voxels will have distinctly different temporal variation throughout the sequence. Firstly,

those associated with areas free of significant bloodflow will have little temporal variation other than the inevitable noise and the artifacts likely to be caused if the sampling density in k-space is below the Nyquist limit. Those voxels associated with arteries will exhibit a relatively early and rapidly rising contrast pulse. Those associated with the venous drainage will exhibit a relatively later and more slowly rising pulse with lower peak amplitude than for the arterial voxels. The time of onset will depend on the relative distance from the FOV entry point for the bloodflow to the point of observation and the timing of the injection relative to the start of the data acquisition. While the gamma variate function provides a very useful model for the expected intensity variation in those parts of the image where blood vessels lie and therefore through which blood and contrast flows, the function has several parameters controlling the temporal variation, i.e., t_0, t_{max} and α, as presented above in Subsection 4.3.2.1. Our approach to constraining the temporal variation is to form a set of basis functions a linear combination of which can accurately represent the range of responses expected within the image.

4.3.2.3 Computing the temporal basis

As described above, a temporal basis was formed from a set of gamma variate functions sampled at times $t_k, k = 1, 2 \ldots P$ corresponding to the reconstructed frames in the sequence. A total of 100 functions were generated, so a matrix $\mathbf{G}$ of dimension was $100 \times P$ was formed. The first 10 of these functions are shown for one set of parameters in Fig.(4.1a). In each case the peak amplitude was fixed at unity while the three other parameters in Eq. 4.11 were randomly chosen with a uniform distribution from within particular ranges: for example, t_0 -2 to +5 seconds; t_{max} +2 to +7 seconds; and α 0.8 to 3.0. The ranges were chosen so that the 100 gamma variate functions represented a reasonable approximation to the spread of expected shapes of intensity-versus-time responses in the various parts of the FOV where blood vessels lay. The algorithm detailed above in Subsection 4.3.1, with $\mathbf{G}$ replacing $\mathbf{A}$, was then applied.

Experimentation indicated that a total of 4-6 temporal basis functions was sufficient to fit the set of sample functions in G within a small mean square error (MSE), so the results presented in the next sections are for 4-6 basis functions if not otherwise stated. Fig.(4.1b) shows the six basis functions generated by the process. While recomputing the basis functions for a different set of gamma variate exemplars with the same parameter ranges will generate a different basis, experience shows that the functions are very similar in nature each time. Likewise, making small changes to the ranges of the gamma-variate parameters was found to have relatively little effect on the basis functions formed by KLT, indicating that the process is reasonably robust [19].

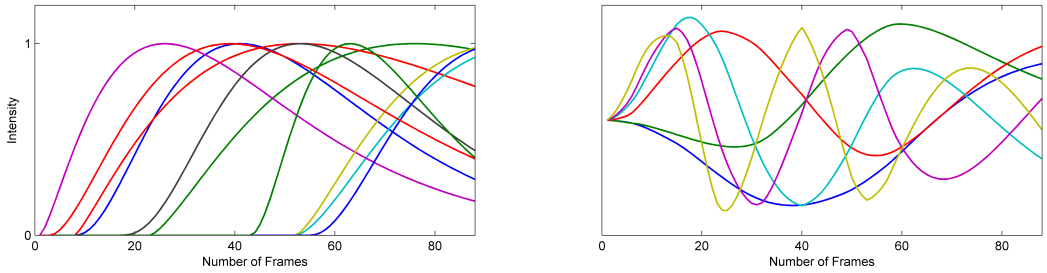

(a) **(b)**

Figure 4.1: Illustration of the formation of a temporal basis set: (a) the first 10 out of a set of 100 unit amplitude gamma variate functions with randomly assigned parameters, and (b) the first 6 basis functions generated from the training set.

The proposed algorithm can be summarized as follows:

1. A set of gamma variate functions, K in number, is formed with different randomly chosen characteristics in terms of Eq. 4.11 and the parameters t_0, t_{max}, and α; the set are stored in a matrix G, dimensioned $K \times N$, where N is the number of time samples over which the MRA sequence is to be modeled. In practice, N depends on the characteristics of the data acquisition sequences employed and the time resolution sought.

2. The KLT is applied to the set by computing the eigenvectors of the covariance matrix of G, $G\,G^T$.

3. The $\hat{K}$ eigenvectors associated with the largest eigenvalues of $G\,G^T$ are chosen as the temporal basis functions. Each eigenvector has N elements and represents a temporal basis function.

4. The sequence of intensity values for all pixels (voxels) in the MRA image sequence are projected onto the temporal basis. In this manner the N independent values associated with the time variation for each pixel is mapped onto $\hat{K}$ coefficients, where $\hat{K} < N$.

Since the number of temporal basis functions retained in the algorithm, $\hat{K}$, is chosen to be less than N, there is clearly compression occurring, which could be advantageous. However, the main benefit of applying the temporal basis is in the suppression of artifacts, since they are very unlikely to be correlated with the temporal basis functions. The simulations presented in the next section demonstrate how the algorithm achieves a significant improvement in image sequence quality.

4.3.3 KLT as a temporal image filter

Here an application of a temporal filter for dynamic MR image series based on the Karhunen Loeve transform (KLT) to remove random noise is described. First application of KLT filtering in dynamic medical imaging was represented by [180]. Moreover the KLT was employed as a filter in [156] to investigate the improvement of spatial resolution in rapid dynamic cardiac MRI perfusion sequences when a higher resolution reference frame either from the same sequence, or from a steady-state cine sequence, is available. Later in Ding's work the KLT filter application to remove random noise was described [49] and the trade offs between SNR gain and edge sharpness were presented there.

KLT can be applied retrospectively to an image sequence resulting in a set of eigenimages with the signal energy concentrated within a discrete first subsets of eigenimages while the remaining eigenimages consisting only noise. This transform is optimal in the least-squares sense and exploits data redundancy found in cine images. Such a filtering of image series may be carried out by zero-filling noise-only eigenimages in the KLT domain and inverting the transform. Therefore, truncation of higher order components provides excellent noise smoothing and meanwhile compression. For this noise suppression method, multiple MR images of the same tomographic slice obtained with different acquisition parameters. A temporal series of P 2D images, each with $N1 \times N2$ (N) pixels, can be represented by a matrix $\mathbf{A}$ $(P \times N)$ where each row corresponds to an image, including both signal and noise [180]. $\mathbf{C}$, the temporal covariance matrix of $\mathbf{A}$, is defined so that, $\mathbf{C} = \mathbf{A}\mathbf{A}^T$ with P eigenvalues,and corresponding eigenvector matrix $\mathbf{E} = \{e_{ij}\}$ (KLT matrix), with eigenvectors as rows. To compute the pixel's PC value and generate the corresponding PC images, eigenvalues and corresponding eigenvector matrix are required. The eigenimage matrix B is:

$$\mathbf{B} = \mathbf{E}\mathbf{A} \tag{4.12}$$

Where each row is one of the eigenimages, sorted in the same order as eigenvalues ($\lambda_1 \geq \lambda_2 \geq \ \ldots \geq \lambda_P$). From above, it follows that the original images can be obtained from their principal components by the inverse transform.

$$\mathbf{A} = \mathbf{E}^T\mathbf{B} \tag{4.13}$$

In a KLT filter, the filtered image $\widetilde{\mathbf{A}}$ matrix is reconstructed from the first K eigenimages. Let us assume that the input images are mutually correlated and that the last $P - K,\ 1 <$

$K < P$, PC components contain practically only noise, their contribution in the inverse transform can be eliminated by setting

$$\mathbf{B}_j = 0 \ , \ for \ K < j \leq P, \qquad \widetilde{a}_{ik} = \sum_{j=1}^{K} e_{ji}.\mathbf{B}_{jk}, \tag{4.14}$$

where $\widetilde{a}_{ik}$ is the (i,k) element of matrix $\widetilde{\mathbf{A}}$. Eigenimages associated with low variance (or small eigenvalues) have been removed and then to generate the filtered image series the inverse KLT is applied. The number of biggest retained PC images can act as the cut off point for noise reduction filter.

4.4 Wavelet Transform

In numerous applications, including image partial differential equations, denoising, image and video compression, signal recognition and robot positioning Wavelet transform has been applied. In this work, we shortly describe basics of the wavelet theory and apply it for noise reduction in magnetic resonance image

4.4.1 Wavelet Analysis Introduction

From a historical point of view, wavelet analysis is not an old method, though its mathematical underpinnings date back to the discoveries of Joseph Fourier in the nineteenth century. The attention of Mathematicians gradually turned from frequency-based analysis to scale-based analysis when it was investigated that an approach measuring average fluctuations at different scales might prove less sensitive to noise. Although Alfred Haar did not name his function a "wavelet", the first recorded mention of wavelets was in his thesis in 1909. Since then a lot of research into wavelets and the wavelet transform is performed. The wavelet analysis was introduced at the beginning of the 1980s for the first time, when Morlet evaluated seismic data and in the late 1980's Ingrid Daubechies, who is arguably the best known wavelet researcher, developed the theory of wavelet analysis [177]. The wavelet transform (WT) is a powerful signal processing tool for its multiresolutional possibilities, which enables an efficient analysis of the small details and the long-term properties of the signal simultaneously. Despite Fourier transform, it is possible to find out both frequency and temporal information with wavelet analysis, so that an event stays connected to the time occurrence. Wavelets are localized waves That have their energy concentrated in time or space and are suited to analysis of transient signals. It represents

a windowing technique with variable-sized regions. The long windows are used at low frequencies and short windows at high frequencies.

The wavelet analysis is done similar to the Short Time Fourier Transform (STFT) analysis. The signal to be analyzed is multiplied with a wavelet function just as it is multiplied with a window function in STFT, and then the transform is computed for each segment generated. However, unlike STFT, in Wavelet Transform, the width of the wavelet function changes with each spectral component. The Wavelet Transform, at high frequencies, gives good time resolution and poor frequency resolution, while at low frequencies, the Wavelet Transform gives good frequency resolution and poor time resolution. The wavelet coefficients is a measure of similarity in the frequency content between a signal and a chosen mother wavelet function. These coefficients are computed as convolution of the signal and the scaled wavelet function, which can be interpreted as a dilated band-pass filter. Consequently, low frequencies correspond to high scale and a dilated wavelet function. By wavelet analysis at high scales, we extract global information from a signal called approximations. Whereas at low scales, we extract fine information from a signal called details.

The most important properties of the wavelets transform are that they are functions which needs to satisfy defined mathematical requirements. For instance, wavelets should integrate to zero, waving above and below the x axis and insure quick and easy calculation of the direct and inverse wavelet transform [44].
Continuous wavelet transform (CWT) and discrete wavelet transform (DWT) are two types of wavelet transform, which the main idea remains the same. However, the method that transformation is being carried out differs. In CWT, an analyzing window is shifted along the time domain to pick up the information about the signal. In this process the information that has been picked up may overlap and result in redundancy. The discrete wavelet transform (DWT) requires less space utilizing the space-saving coding based on the fact that wavelet families are orthogonal or biorthogonal bases, and thus do not produce redundant analysis.

In practice, the DWT is computed by passing a signal successively through a high-pass and a low-pass filter. for each decomposition level, the high pass filter h_d forming the wavelet function produces the approximations A. The complementary low pass filter l_d representing the scaling function produces the details D.
The contribution of this part is in illustration of denoising utility of one dimensional discrete and continuous wavelet compression.

4.4.2 Methods

In the wavelet analysis a signal is decomposed into weighted coefficients of wavelet functions. The whole transform is based on two functions called the scaling function and the wavelet function,respectively ϕ and ψ. These to functions (the scaling function and the wavelet function) can be used to decompose or reconstruct a signal. Therefore in DWT, a wavelet base function needs to be selected first and then each possible scaling and translation of that wavelet is correlated with the function to be transformed. The correlation values thus obtained are the coefficients of the wavelet transform. The continuous wavelet transform (CWT) transforms a continuous signal into highly redundant signal of two continuous variables translation and scale. The resulting transformed signal is easy to interpret and valuable for time-frequency analysis. The continuous wavelet transform of continuous function, $f(x)$ relative to real-valued wavelet,$\psi(x)$ is described by:

$$W_\psi(s,\tau) = \int_{-\infty}^{\infty} f(x)\psi_{s,\tau}(x)dx \tag{4.15}$$

where,

$$\psi_{s,\tau}(x) = \frac{1}{\sqrt{s}}\psi(\frac{x-\tau}{s}) \tag{4.16}$$

s and τ are called scale and translation parameters, respectively. $W_\psi(s,\tau)$ denotes the wavelet transform coefficients and ψ is the fundamental mother wavelet. If $W_\psi(s,\tau)$ is given, $f(x)$ can be obtained using the inverse continuous wavelet transform (ICWT) that is described by:

$$f(x) = \frac{1}{C_\psi}\int_0^{\infty}\int_{-\infty}^{\infty} W_\psi(s,\tau)\frac{\psi_s,\tau(x)}{s^2}d\tau ds \tag{4.17}$$

where, $\Psi(u)$ is the Fourier transform of $\psi(x)$ and

$$C_\psi = \int_{-\infty}^{\infty}\frac{|\Psi(u)|^2}{|u|}du \tag{4.18}$$

The discrete wavelet transform can be estimated on the same form as Equation Eq.(6.19), which underlines the close relationship between CWT and DWT. The most significant difference is that the DWT uses scale and position values based on powers of two. The values of s and τ are $s = 2^j$, $\tau = k * 2^j$ and $(j,k) \in Z^2$ as shown here

$$\psi_{j,k}(x) = \frac{1}{s_0^j}\psi(\frac{x - k\tau_0 s_0^j}{s_0^j}) \tag{4.19}$$

The key issues in DWT and inverse DWT are signal decomposition and reconstruction, respectively. The basic idea behind decomposition and reconstruction is low-pass and high-pass filtering with the use of down sampling and up sampling respectively. The result of wavelet decomposition is hierarchically organized decompositions. One can choose the level of decomposition j based on a desired cutoff frequency. Figure (1.1a) shows an implementation of a three-level forward DWT based on a two-channel recursive filter bank, where $h_0(n)$ and $h_1(n)$ are low-pass and high-pass analysis filters, respectively, and the block $\downarrow 2$ represents the down sampling operator by a factor of 2. The input signal$x(n)$ is recursively decomposed into a total of four subband signals: a coarse signal and three detail signals.Figure(1.1b) shows an implementation of a three-level inverse DWT based on a two-channel recursive filter bank, where $h_{-0}(n)$ and $h_{-1}(n)$ are low-pass and high-pass synthesis filters, respectively, and the block $\downarrow 2$ represents the up sampling operator by a factor of 2.

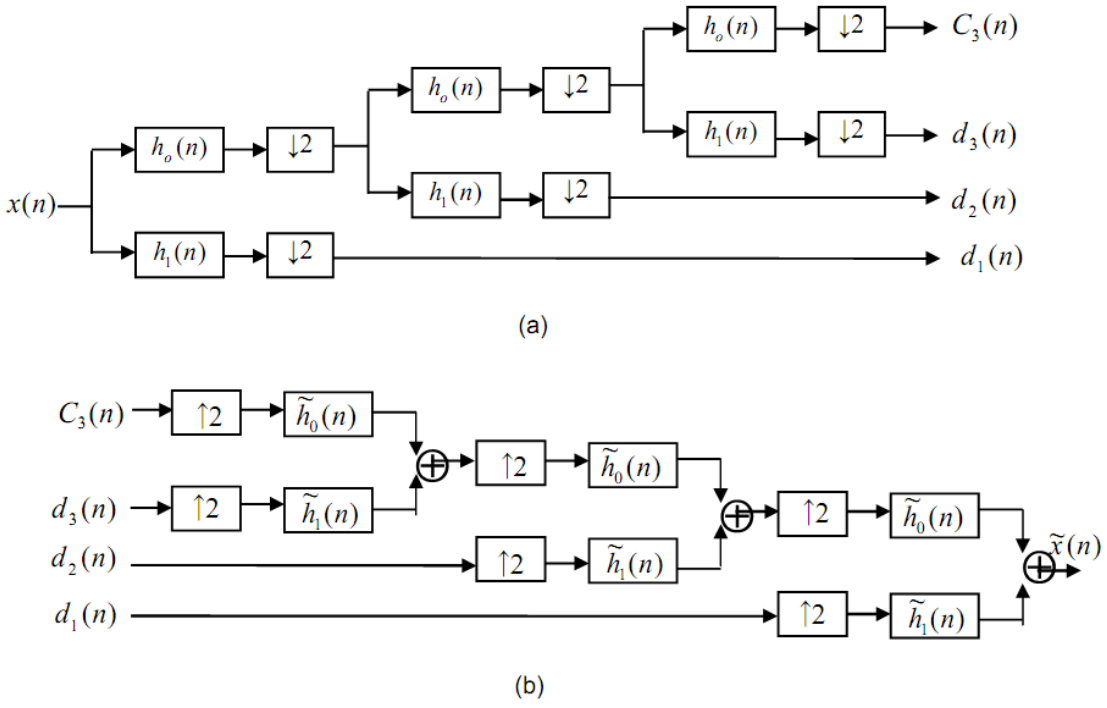

Figure 4.2: A three-level two-channel iterative filter bank (a) forward DWT (b) inverse DWT

so that the output of the inverse DWT is identical to the input of the forward DWT.

In data compression, the wavelet transform is used to exploit the redundancy in the signal. After the original signal is transformed into the wavelet domain, many coefficients are so small that no significant information is lost in the signal reconstructed by setting these coefficients to zero. In our implementation, each pixel's intensity over time was considered

as a 1D signal and Transformed into a wavelet coefficient domain. The transformed coefficients will represent image information on various scales. The wavelet coefficients obtained by applying hard thresholding to the them, transformed back to the image.The resulting image, when reconstructed, contains information only from wavelet coefficients above some threshold. In this work, a discrete Debauchee mother wavelet on 5 layer is used to compute the wavelet coefficients. A threshold selection strategy has been proposed for effective denoising. To highlight the characteristic of the fundamental area of image, three different regions of interest; arteries, veins and background, based on pixel intensities were thresholded. after wavelet transforming, Root Mean Square(RMS) of wavelet coefficients of these selected regions were used as the threshold for back transformation to the whole pixels.

4.5 Experiments

4.5.1 The "Reconstruction Challenge"

A sequence of spiral-sampled k-space data for a parallel MRI acquisition, called "Need for speed", in the annual conference of the International Society for Magnetic Resonance Imaging in Medicine (ISMRM2010) competition, was employed to investigate noise reduction in CE-MRI. In fact, the data was simulated by re-sampling an image sequence collected by X-ray digital subtraction angiography, but it closely resembled the sort of data expected for an MRI study. It provided a useful vehicle for testing our algorithm.

Data were simulated using a frontal projection X-ray sequence of a contrast bolus injection in the left vertebral artery of a patient with an arteriovenous malformation (AVM) in the brain. X-ray data were collected 3 frames per second, for a total of 10 seconds (31 collected frames) which span wash-in to wash-out. These were linearly interpolated in time between frames to create a total of 200 temporal images, each with 512×512 resolution. Coil sensitivity maps derived from an axial slice through a water phantom using an 8-channel head coil were superimposed on the image to create 8 coil images. Independent noise was added to each channel. After Fourier transformation, the k-space data were re-sampled over 200 trajectories, one per frame, each with 2000 points. For achieving the high temporal resolution required in CE-MRA, such as cardiovascular imaging, radial or spiral sampling trajectories may have advantages [130]. Spiral k-space trajectories have been modeled in the presented simulations.

In Fig.(4.3) is shown the first two consecutive spiral trajectories for sampling in k-space. The centre of k-space represents zero spatial frequency and sampling occurs out to radius

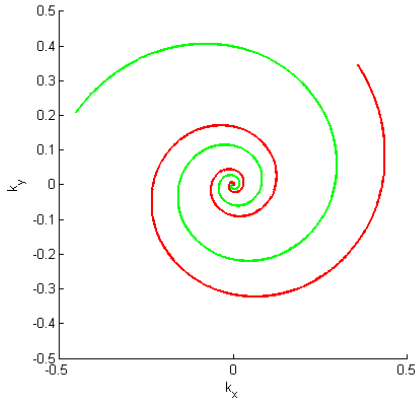

Figure 4.3: Illustration of the NFS data set. The sampling positions in k-space for the first two spiral trajectories.

0.5 on the scale shown, corresponding to an image FOV of 512×512. The series of spiral trajectories repeats every 13 spirals and the 13 are uniformly angularly spaced over 360deg. Note however that each spiral is rotated by approximately 111 deg from its predecessor in acquisition order. In Fig.(4.4) is shown two reconstructed images which were formed from

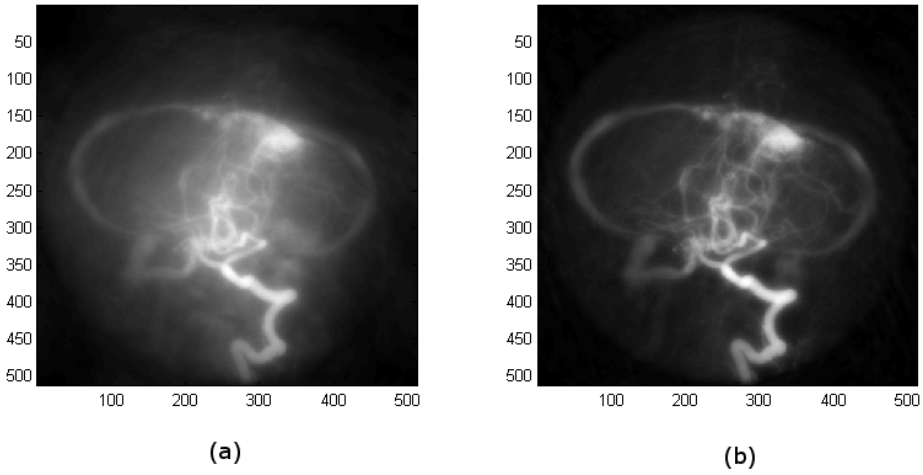

Figure 4.4: Single image formed from averaging over all coils and all time instants, (a) reconstructed 5 spirals at a time and (b) 13 spirals at a time

the k-space NFS data for all 8 coils over the acquisition sequence by taking RMS over the coils, summed over 40 frames in a) and 13 frames in b).

4.5.1.1 Reconstruction of images

Each spiral trajectory comprises 2000 samples, commencing at the centre of k-space. In principle an image can be reconstructed from any number of consecutive spirals: the fewer the number of spirals used, the better the time resolution, as seen in Fig.(4.4) We chose to use 5 consecutive spirals to reconstruct each frame, representing a frame rate of 4 frames / sec. 5 spirals represents a total of 10000 k-space samples, compared to approximately $\pi 256^2 = 205890$ samples in order to fully sample the Cartesian grid within a circular region. There is therefore a high degree of under-sampling in k-space. A number of methods have been used to re-grid under-sampled k-space data onto a Cartesian grid. However, the sparsity of the data in this case makes those methods relatively ineffective. Our approach instead has been to perform a simple nearest-neighbour allocation of samples onto grid points for each consecutive set of 5 spirals, using a complex average in cases where two or more samples have the same neighbouring grid point. The resulting array is then transformed via the inverse 2D FFT to form an image. The under-sampling generates significant artifacts on each reconstruction, but the use of the temporal basis (described below) reduces these to an acceptable level.

4.5.1.2 Combining data from coils

The simulated data was supplied in the form of multiple recordings, simulating the use of an 8-coil receiver unit, as described above, It was therefore possible to form 8 separate reconstructions, one for each 'coil'. It should however be possible to exploit the multiple recordings and knowledge of the individual coil sensitivities to improve the image reconstruction. In this case neither the SENSE or SMASH approaches seemed to offer much promise. SENSE requires a regular (patterned) form of under-sampling in order to apply a linear algebraic approach to lowering the effect of aliasing. SMASH only has the ability to recover regions of k-space immediately adjacent to the sampling points, which would have the effect of broadening the spiral trajectories, say to 3 or 5 pixels wide, instead of a single pixel wide. Observations of the corresponding sampling pattern point spread functions indicated that the effect on image quality would be relatively small. We adopted a simpler approach, therefore, as described below. For each pixel in a given frame, a vector of complex amplitudes, $\mathbf{d}$, dimensioned 8×1, is generated by means of inverse Fourier transformation from the array of spiral samples. A set of relative coil sensitivities, $\mathbf{c}$, also dimensioned 8×1 and also expressed as complex amplitudes, is available *a priori*. We seek

therefore to find the pixel magnitude $|f|$, according to the model

$$\mathbf{d} = f\ \mathbf{c}. \tag{4.20}$$

The MMSE solution to this is simply to minimise $|\mathbf{d} - f\ \mathbf{c}|^2$. In our implementation this has been encoded as

$$f\ =\ \left| \frac{\sum_{m=1}^{8} \left(\mathcal{R}(c_i)\mathcal{R}(d_i) + \mathcal{I}(c_i)\mathcal{I}(d_i)\right) + j \sum_{m=1}^{8} \left(\mathcal{R}(c_i)\mathcal{I}(d_i) - \mathcal{I}(c_i)\mathcal{R}(d_i)\right)}{\sum_{m=1}^{8} |c_i|^2} \right| \tag{4.21}$$

where $\mathcal{R}(x)$, $\mathcal{I}(x)$ denote the real, imaginary parts of x, respectively. This form allows the relatively efficient vector and matrix operations of MATLAB to be used for efficiency.

4.6 Results

4.6.1 Need for speed results

In the following the term 'frame width' is used to describe the time interval over which samples were acquired to generate a particular frame, while 'frame step' is used to describe the shift in time from one frame to the next. Both parameters are able to be chosen during the reconstruction. In Fig.(4.5) reconstructions of a single frame (the 10th out of a total of 40, with 5 spirals per frame and 4 frames per second) are shown for various methods. In all cases simple nearest-neighbour assignment of k-space data onto the Cartesian grid was used, with no attempt to enforce the Hermitian property in k-space in the missing samples. Near the centre of k-space where several spiral samples may fall within a particular k-space pixel, the complex average of the measurements was assigned. A direct inverse transformation from single-coil data without any compensation for the coil sensitivity and without any account taken of temporal variation is shown in Fig.(4.5a). Note the spiral-like artifacts; when the sequence of reconstruction is observed, the artifacts appear to swirl around the image. The effect of combining the data from all 8 coils, incorporating the sensitivity map information, is shown in Fig.(4.5b). The edge of the circular FOV appears because the coil sensitivity maps were only defined out to that boundary. There is some slight improvement in the level of sampling artifacts, but the appearance of the blood vessels is still noticeably affected by the presence of artifacts generated by the severe under-sampling in k-space. Corresponding reconstructions with a temporal basis applied are shown in Fig.(4.6a) and Fig.(4.6b). In both cases only the first 4 temporal basis functions were used. In Fig.(4.6a),

the reconstruction for single-coil data without any compensation for the coil sensitivity is shown, while in Fig.(4.6b), all coil data has been combined. In both cases the use of the temporal basis has had a dramatic effect in suppressing the background artifacts and, more significantly, improved the clarity of the vessels comprising the arterial tree greatly. The venous structure is not visible, since the frame is relatively early in the sequence.

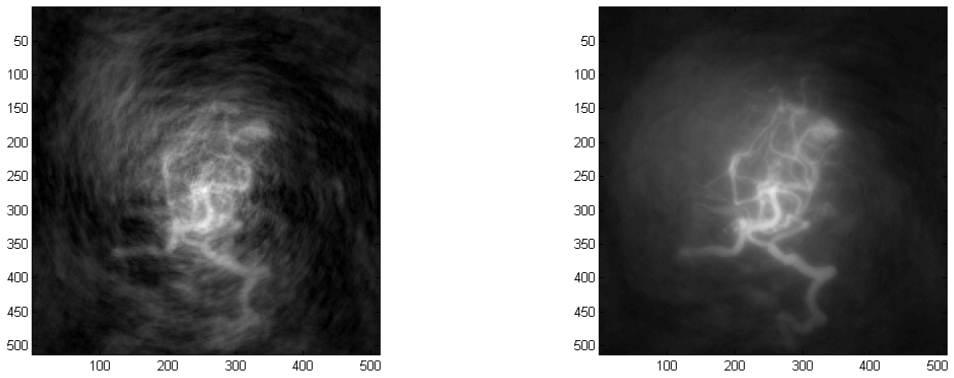

(a) **(b)**

Figure 4.5: Reconstructions of frame 10 out of 40 with 4 frames per second and each frame generated from 5 spirals:a)direct inverse transformation of k-space data for coil 1 and b) applying a temporal basis with 4 basis functions for coil 1 only.

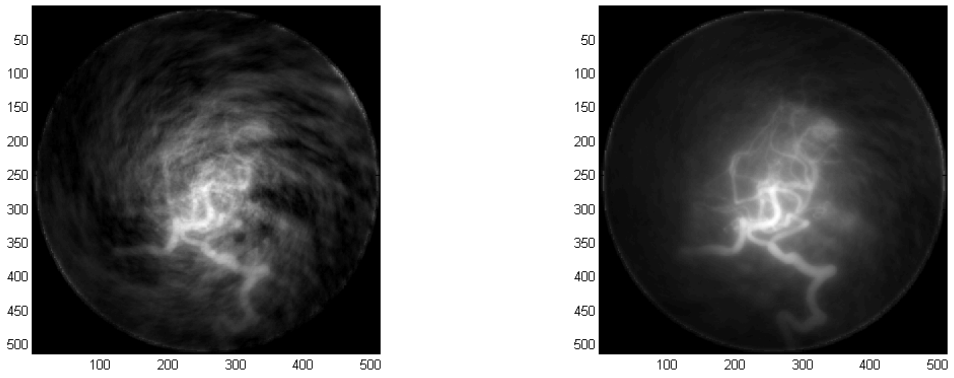

(a) **(b)**

Figure 4.6: Reconstructions of frame 10 out of 40 with 4 frames per second and each frame generated from 5 spirals: a) direct inverse transformation of k-space data for coil 1 and combining all coils with sensitivity adjustment; b) applying a temporal basis with 4 basis functions for all coils

Intensity versus time curves for selected regions within the FOV are shown in Fig.(4.7) Three small regions were segmented from the image: region A is within the prominent artery lower centre, region B is close to the centre, and region C is within the peripheral

venous region on the left of the FOV. The mean intensity of pixels within each region was calculated frame-by-frame to generate the curves. Fig.(4.7(a)) shows curves for regions A, B and C generated by direct inverse transformation and combining all coils (i.e. without any temporal constraints), while Fig.(4.7(b)) shows curves generated by applying the temporal basis (four basis functions only), combining all coils. The smoothing effect of applying the basis is clearly evident. For comparison, Fig.(4.7) shows the curves generated when an additional 2 basis functions are added; Fig.(4.7(b)) and 4.7(c) seem sufficiently similar to suggest that 4 basis functions is sufficient for the data we had. Later in the chapter Fig.(4.20) shows the variation in reconstructed intensity with time after applying extra basis functions (8 basis functions in total) for another set of data. Selecting the most favorable number of basis functions for each dataset could be investigated more in depth.

Fig.(4.8) shows 5 frames selected from the sequence of 40 frames. The temporal basis of 4 basis functions has been used and data from all coils combined. Note that the general quality is reasonable and there is a clear progression in time throughout the sequence.

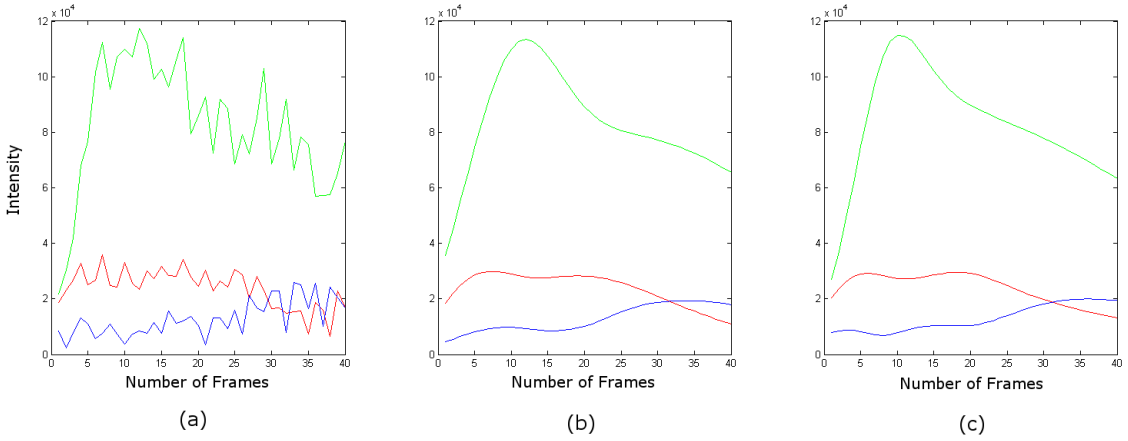

Figure 4.7: Study of the variation in reconstructed intensity with time within the vascular tree. Three small regions were segmented from the image: region A is within the prominent artery lower centre (green curves); region B is close to the centre (red curves); and region C is within the peripheral venous region upper left (blue curves). (b) Intensity versus time curves generated by direct inverse transformation and combining all coils (i.e. without any temporal constraints). (b) Intensity versus time curves generated by applying the temporal basis (four basis functions only), combining all coils. (c) is the same as (b), but using 6 basis functions.

In Fig.(4.9) the 4 main eigenimages corresponding to 4 largest eigenvalues on the data we had, which have been contributed to reconstruction, have been illustrated as described in section 4.3.3.

Fig.(4.10) demonstrates the Intensity Time Curve (ITC) in two regions of interest (arteries

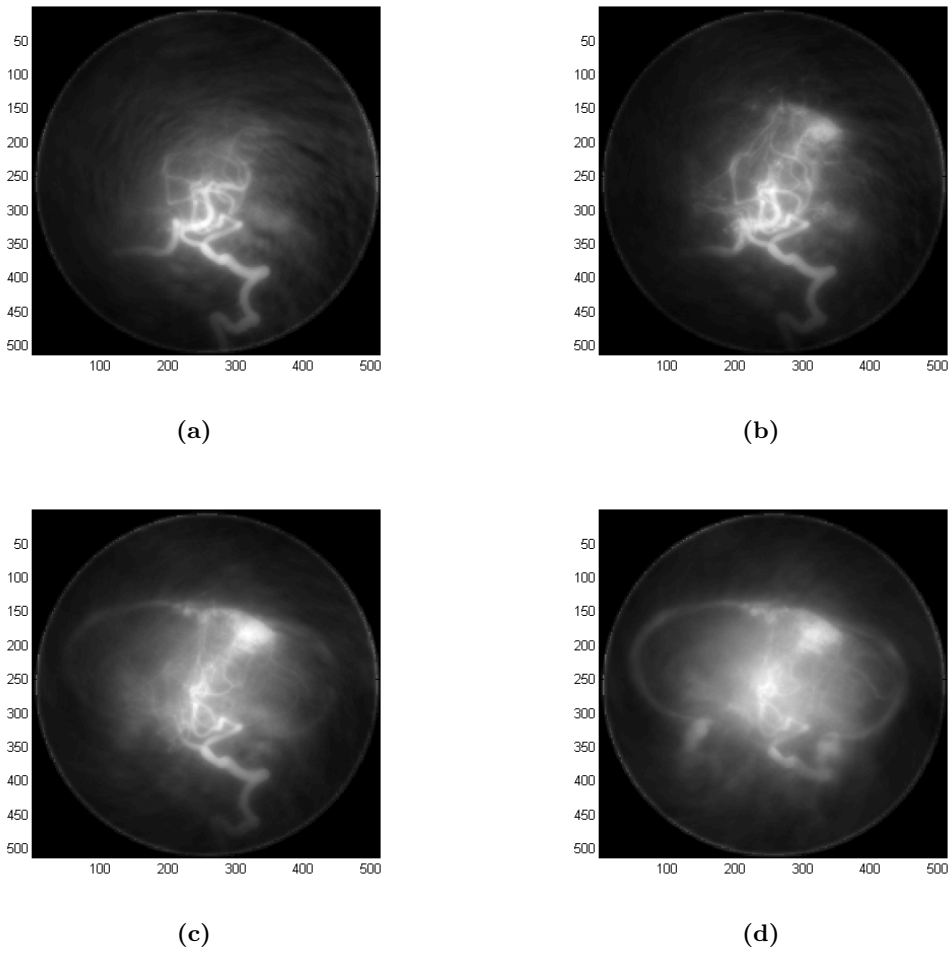

Figure 4.8: Reconstructions of four frames from a total sequence of 40 at 4 frames per second and each frame generated from 5 spirals: (a) frame 5; (b) frame 15; (c) frame 25;and (d) frame 35.

and veins) denoised by different approaches. As it is shown, applying the temporal basis of Gamma Variate Function results in a smoother varying intensity in the images than using KLT filter, while maintaining the physiological shape of contrast agent bolus propagation.

To evaluate Wavelet performance a DWT was applied to smooth the entire sequence of MR images. Each pixel's intensity in the image through time has been transformed into the Wavelet domain, then the Root Mean Square error of wavelet coefficients in the three regions of interest(background, arteries and veins) act as a threshold value to keep the coefficients or not. As Fig.(4.11) demonstrates two different masks used to define region of interest and compute RMS value.

Fig.(4.12) depicts one of the reconstructed image frames after retaining the coefficients thresholded by the RMS value of coefficients in a region of interest did not show proper

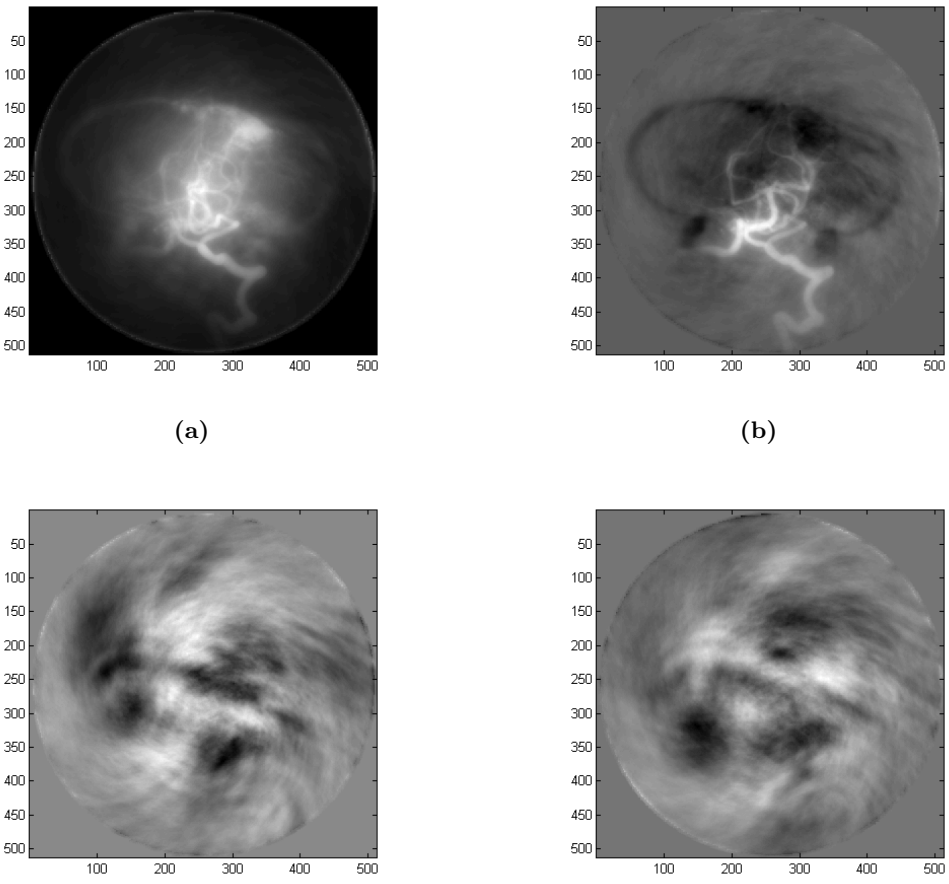

Figure 4.9: Demonstration of four first eigenimages of dataset which used to KLT smoothing method.

quality. This figure highlights the impact of background region size on the RMS of coefficient value and consequently on retaining each pixel's coefficients. Apparently this technique is not capable of ensuring the image quality.

Fig.(4.13) compares the noise level in consecutive frames resulting from different noise reduction methods. Noise is measured in image regions where the displayed signal is due entirely to the randomness of the acquisition process. To do noise measurements an air ring surrounding the patient was selected. These results clearly reveal that among the methods compared, images obtained from the imposing KLT temporal basis derived from gamma functions have less noises while preserving the important structural features. In addition visual analysis of image sequences supports that the images became less noisy, and the detection of small vessels was facilitated by applying the KLT basis. Feature-preserved denoising is of great interest in MR angiography and our primary results highlight the

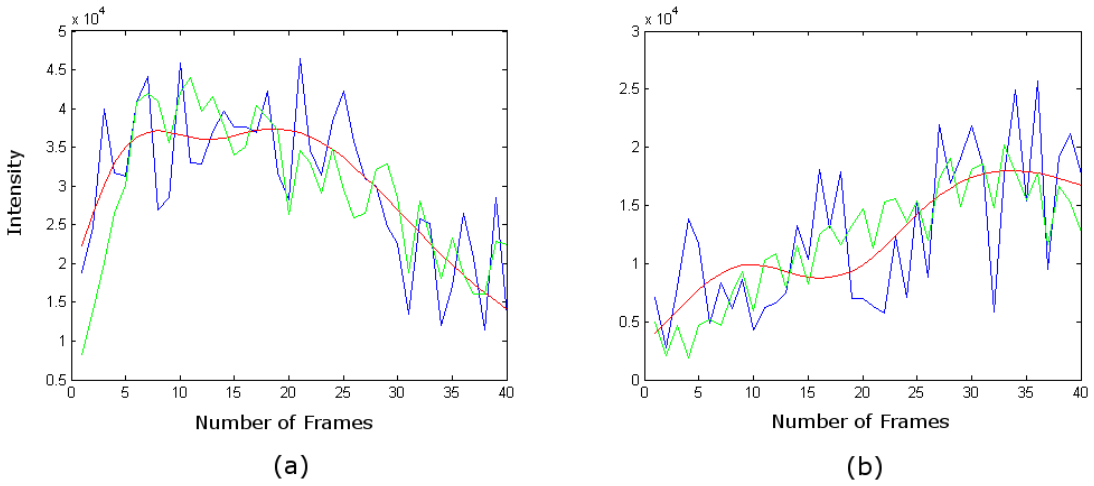

Figure 4.10: Illustration of Intensity Time Curve in different regions of interest. a) in Arteries and b) in Veins, Blue graph indicates changes in the initial series, Green generated after applying the temporal basis of Gamma Variate Function and Red after KLT smoothing. clearly, applying the temporal basis of Gamma Variate Function suggests a smoothly varying intensity. Note that the required contrast-agent propagation in vessel tree has not been well presented in the KLT filter.

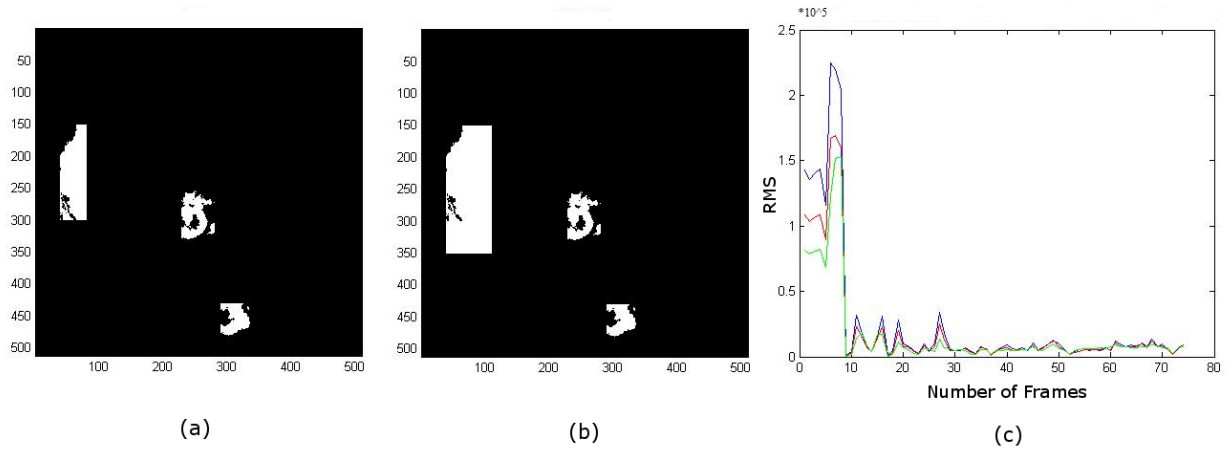

Figure 4.11: (a) and (b) show two different masks used to define regions of interest and compute RMS value. (c) Comparison between RMS value for each coefficient. Green graph depicts the RMS value of the coefficients when whole image's pixels are considered for the threshold selection. Red; the bigger mask (b) has been investigated for threshold estimation and Blue; for the smaller mask (a) covering smaller area of background.

superiority of applying KLT temporal basis on image sequences in terms of the tempo-spatial resolution. Observing the efficiency of imposing prior knowledge of the contrast flow dynamics, only the KLT basis was obtained from gamma variate prototypes and applied on GUISE and PECS reconstructed images.

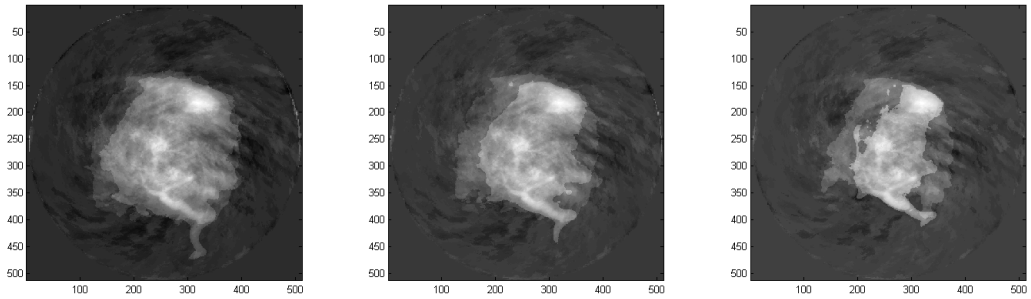

Figure 4.12: Reconstruction of the 25th frame out of 40 after wavelet transformation. (a) retained coefficients are thresholded by comparing each with the RMS value over whole image (b)and (c) retained coefficients are thresholded by comparing each with the RMS value obtained in the bigger selected regions and smaller respectively.

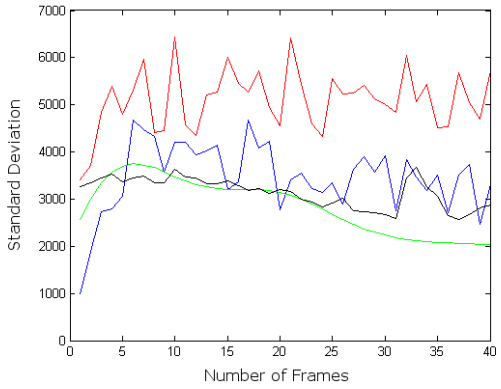

Figure 4.13: Plot shows a comparison between noise level in a ring region defined over the background in different frames Blue graph shows; standard deviation value of the background resulted from direct inverse reconstruction, Green; results of applying a temporal basis with 4 basis functions, Black; Wavelet compression and Red; after KLT smoothing filter.

4.6.2 In-vivo experiments results

Studies on the knee region of two human volunteers were carried out to investigate the performance of the proposed methods. Both experiments were carried out using a 1.5T GE scanner equipped with an 8-channel receiver, in which the individual receiver channels

are symmetrically placed around a cylinder. A T1-weighted 3D spoiled gradient recalled (SPGR) sequence was used, and the two PE directions were set to left-right (LR) and anterior-posterior (AP).

Ethical approval was obtained from the Upper South A Regional Ethics Committee (Ministry of Health, NZ) to make a single injection of gadolinium contrast into each subject.

For the GUISE acquisition, the scan parameters used were: $TR = 5.4$ ms, $TE = 1.6$ ms, Flip angle $= 45^o$. A matrix size of $196 \times 128 \times 48$ was used to obtain a spatial resolution of $0.9 \times 0.9 \times 1$ mm. 20 ml of Gd-BOPTA (Multihance) was injected as a bolus. A repeating block size of 16×16 was used and the acquisition order was determined using sequential forward selection. A complete acquisition of the 3D k-space volume took 30 s, and 5 repetitions were made.

For the PECS type acquisition: $TR = 4.8$ ms, $TE = 1.8$ ms, Flip angle$=45^o$. A matrix size of $196 \times 128 \times 48$ was used to obtain a spatial resolution of $1 \times 1 \times 1$ mm. 20 ml of Gd-BOPTA (Multihance) was injected as a bolus. A sampling mask was formed which comprised 2570 of the total k-space locations. 18 repetitions of the acquisition were performed with 7.5 s per repetition.

In both cases, data acquisition was commenced before the injection; the data acquired before the arrival of contrast was used for estimating the coil sensitivity profile and subtracted from the following repetitions to eliminate the stationary background.

In Fig.(4.14) sliding window GUISE reconstructions of 3 coronal plane MIP frames (the 15th, 20th and 30th frames out of 121 frames) are shown for one of the volunteers studied. The frame width was 7.5 s and the frame step was 0.93 s. Corresponding reconstructions with a temporal basis applied (first 6 basis functions) are shown in Fig.(4.15). The application of the temporal basis can be seen to reduce the noisiness of the images significantly and to improve the clarity of the small vessels.

In Fig.(4.16) sliding window PECS reconstructions of 3 coronal plane MIP frames (3th, 8th and 14th frame out of 85 frames) are shown for the second of the volunteers studied. The frame width was 7.5 s and the frame step was 1.07 s. Corresponding reconstructions with a temporal basis applied (first 6 basis functions) are shown in Fig.(4.17). In this case the use of the temporal basis has had a dramatic effect in suppressing the background artifacts and, more significantly, has improved the clarity of the vessels comprising the arterial tree. The venous structure is not visible, since the frames selected are relatively early in the sequence. Note that the general quality is reasonable and there is a clear progression in

(a) **(b)** **(c)**

Figure 4.14: (a), (b) and (c): Three frames selected from the sequence of 121 frames reconstructed by the GUISE method, 15th, 20th and 30th frame respectively.

(a) **(b)** **(c)**

Figure 4.15: (a)-(c) the same frames reconstructed by the GUISE method as in Fig.(4.14) after applying a temporal basis with 6 basis functions.

time throughout the sequence.

Intensity versus time curves for a selected region within the FOV are shown in Fig.(4.18) for GUISE reconstructions. A small region comprising 12 voxels was segmented within the prominent artery. The mean intensity of the voxels was calculated frame-by-frame to generate the curves, with and without the temporal basis application. Fig.(4.18(a)) shows plots for reconstructions using an acceleration factor of 4 (i.e., a frame width of 7.5 s). Fig.(4.18(b)) shows plots for reconstructions using an acceleration factor of 8 (i.e., a frame width of 3.75 s). The smoothing effect of applying the basis is clearly evident.

Fig.(4.19) illustrates intensity versus time curves for a selected region within the FOV for

(a) **(b)** **(c)**

Figure 4.16: (a), (b) and (c): Three frames selected from the sequence of 85 frames reconstructed by the PECS method, 3th, 8th and 14th frame respectively

(a) **(b)** **(c)**

Figure 4.17: (a)-(c) the same frames reconstructed by the PECS method as in Fig. 4 after applying a temporal basis with 6 basis functions.

reconstructions generated by the PECS method. The mean intensity of 12 neighbouring voxels within the prominent artery was calculated frame-by-frame, with and without the temporal basis application, to generate the curves. Fig.(4.19(a)) shows plots for reconstructions using an acceleration factor of 4 (i.e. a frame width of 7.5 s). Fig.(4.17(b)) shows plots for reconstructions using an acceleration factor of 16 (i.e. a frame width of 1.88 s). Again the smoothing effect of applying the basis is clearly evident.

For comparison Fig.(4.20) shows intensity versus time curves for the two methods when

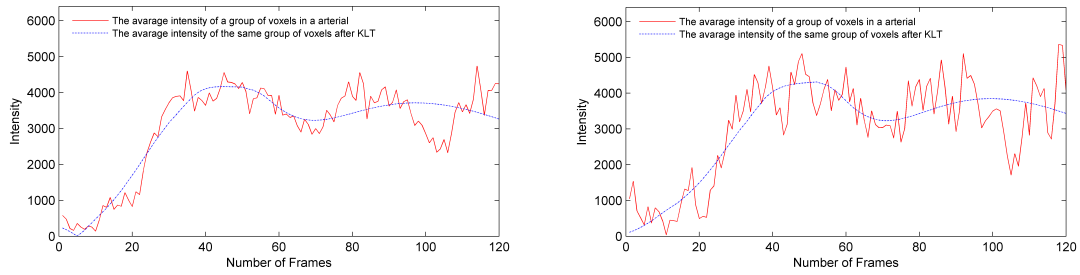

Figure 4.18: Intensity versus time plots for a group of voxels in the central artery (the average of 12 voxels) before and after incorporating the temporal basis (6 basis functions) with GUISE acquisition: a) sequence constructed with k-space sampled at an acceleration factor of 4; and b) sequence constructed with k-space sampled at an acceleration factor of 8.

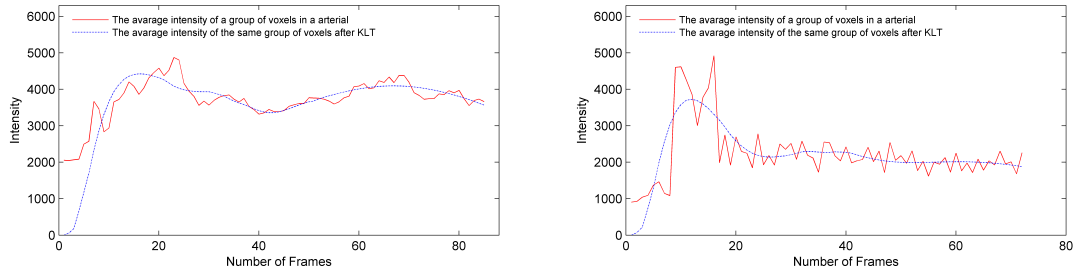

Figure 4.19: Intensity versus time plots for a group of voxels in the central artery (the average of 12 voxels) before and after incorporating the temporal basis (6 basis functions) with PECS acquisition: a) sequence constructed with k-space sampled at an acceleration factor of 4; and b) sequence constructed with k-space sampled at an acceleration factor of 16.

an additional 2 basis functions were incorporated (i.e., $K = 8$). In both plots, an acceleration factor of 4 was used. Thus Fig.(4.20(a)) should be compared to Fig.(4.18(a)) and Fig.(4.20(b)) should be compared to Fig.(4.19(a)). The plots seem sufficiently similar to suggest that 6 basis functions are sufficient for these datasets.

In Fig.(4.21) the standard deviation (SD) of a region in the FOV free from vessels (11×11 voxels in size) as a function of time has been illustrated on a relative scale. A substantially lower value of SD after KLT for both reconstruction methods is exhibited, indicating a better SNR has been achieved.

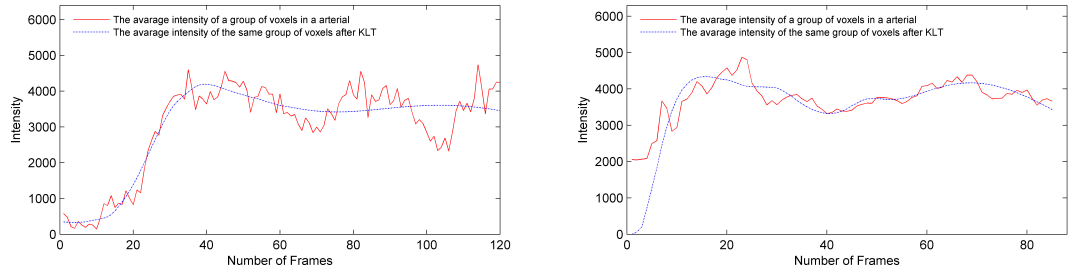

Figure 4.20: Time Intensity Curve of the same group of voxels in arterial regions before KLT and after incorporating 8 KLT basis function. a) GUISE acquisition with the same setting as Fig.(4.18(a)); b) PECS acquisition with the same setting as Fig.(4.19(a)).

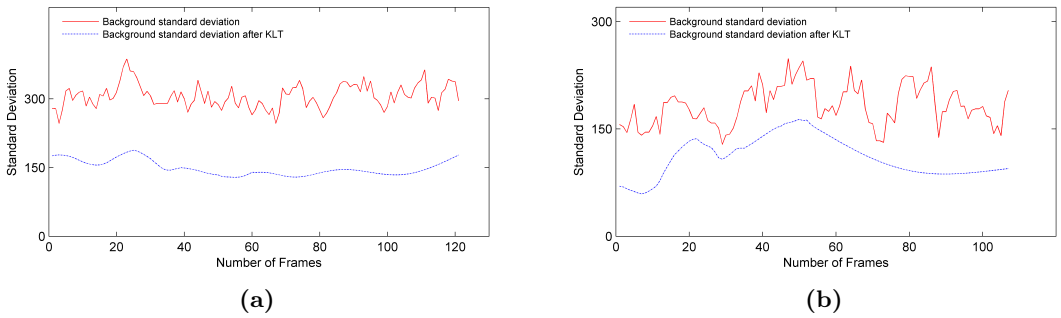

Figure 4.21: Comparing the standard deviation calculated within a selected region free of observable vessels (121 voxels) before and after applying the temporal basis for the two methods over time: a) GUISE acquisition; and b) PECS acquisition.

4.7 Discussion

Imposing a set of temporal basis functions derived by KLT from a model of the contrast flow dynamics in sequences of reconstructed images was investigated in this chapter. By imposing a basis for the temporal changes, based on prior expectation of the smoothness of the changes in contrast concentration with time, it was demonstrated that a significant reduction in artifacts caused by the under-sampling of k-space in CE-MRA can be achieved. Results were presented in the main for a set of 6 temporal basis functions formed by KLT. Adding a small number of additional basis functions was found to have little effect. Of course adding a considerable number of additional basis functions could lead to fitting of the noise in the signal. The number of 6 basis functions was chosen as the minimum required to achieve a reconstructed sequence consistent with expectations for the set of data. In general, the basis needs to be tailored to the specific imaging situation. For example, there is a considerable difference between arterial and venous contrast injection, so the

nature and number of basis functions need to be chosen accordingly. The application of the temporal basis presented in this chapter should be equally applicable to other sampling strategies and reconstruction methods. The key to virtually any imaging process is the SNR achieved in the collection of data and the reconstruction into an image. Generally in CE-MRA there is a definite trade-off between SNR and time resolution: improving the time resolution necessarily means relying on fewer measurements and a consequential loss of SNR. However, there is room to improve the SNR in a reconstructed sequence by exploiting more prior knowledge. We conjecture that the imposition of an appropriate temporal basis is a way of exploiting prior knowledge and thus has the potential to improve SNR without sacrificing significant temporal resolution.

The KLT has been frequently applied to the postprocessing of medical image sets before. Probably the first report was in 1994 [180], in which the authors studied the best use of multiple MR reconstructions of the same anatomy with different scan settings and temporal sequences. More recently, Ding *et al.* used KLT as a temporal filter to remove random noise from cardiac MR image sequences [49]. In the application of the KLT image filter, a temporal covariance matrix of the image series was used to generate eigenimages (their principal components). To generate the filtered image series, eigenimages associated with the largest eigenvalues were retained in generating the inverse KLT. The authors also point out that their approach means that the filtering must be carried out in postprocessing, since the filter is based on the complete data set [49]. We contend that the introduction of basis functions which represent the expected dynamics of changes of concentration of the contrast effectively introduces prior knowledge into the processing of the MRA image sequence. Furthermore, the basis set can be generated before acquisition, so the method we propose can in principle be used in realtime; in applying the temporal basis frame-by-frame, the quality of the reconstructions would then increase as the sequence proceeds.

Additional computation is involved in computing the temporal basis functions and projecting them onto the image sequences. Starting with a total of M vectors of gamma variate functions each of dimension P (where P is the image sequence length), KL transformation reduces the $M \times P$ matrix to a $K \times P$ matrix of basis vectors in such a way that the information is maximally preserved in minimum mean squared error sense, $K << P$. The analysis of the computational complexity of the algorithm can be partitioned into three steps. Step 1: computation of the cross-covariance matrix of the gamma variate function vectors which needs MP^2 multiplications and thus is of complexity $O(MP^2)$. Step 2: decomposition of the covariance matrix of the feature vectors to find its eigenvectors. The eigendecomposition of Step 2 can be accomplished by any of a number of matrix-diagonalization methods of varying complexity. For instance, singular value decomposition

(SVD) is widely used for this purpose due to its numerical stability. SVD decomposition finds all P eigenvectors such that its computational complexity is $O(P^3)$ [21]. However, we need only the first K eigenvectors to assemble transformation, assuming that the eigenvectors are sorted in order of descending eigenvector magnitude. As it has been already demonstrated, K can be much smaller than P (in our experiments, $K = 6$). There are iterative techniques like Hotelling's power method which find only the largest eigenvalues and their corresponding eigenvectors, which results in less computational time with $O(KP^2)$. Step 3: execution of the last step of the transformation process. Assuming that the entire image consists of N pixels over P temporal frames, an $N \times P$ matrix will be projected onto the reduced basis sets (the dimension of basis vector is $K \times P$) with the computational cost of $O(2KPN)$. Thus the overall run-time complexity for algorithm is $O(MP^2 + P^3 + 2KPN)$. Since K, P and M are all typically much smaller than N, especially for 3D image sequences, step 3 dominates the overall algorithm complexity which becomes $O(KPN)$.

A novel approach for constraining CE-MRA image sequences employing the Karhunen-Loeve transform has been demonstrated to substantially improve the reconstruction quality. The diffuse nature of the mixing of contrast agent and blood, coupled with the transient wash-in and wash-out during the recording of a CE-MRA sequence suggest that each frame in a sequence is highly correlated to the frames next to it in time. The method proposed uses the prior knowledge that the gamma variate curve is a useful model for the image intensity versus time observed in locations where contrast-containing blood flow is present. The results presented suggest that considerable improvement in the quality of reconstructed sequences of images in CE-MRA can be achieved by incorporating an appropriate temporal basis.

Chapter 5

Compressed Sensing

5.1 Motivations

In recent years compressed sensing (CS), also known as compressive sampling or sparse recovery, has attracted considerable attention in different areas of mathematics, digital signal processing, imaging devices and computer science. The motivation behind compressive sensing is to do 'sampling' and 'compression' at the same time. Today, after only 6 years, the theoretical and practical aspects of compressed sensing are explored in more than 1000 articles in astronomy, biology, medicine, radar, and seismology applications.

In this chapter, we are providing a review of the CS theory basics. We focus primarily on the theory and recovery algorithms and then will see how the CS fundamentals have been extended in MRI recovery direction. A novel approach is then presented which is an alternative approach to capture the underlying information needed for optimal reordering in PECS.

5.2 Compressed Sensing introduction

The traditional Shannon-Nyquist sampling theorem specifies that a band limited analog signal can be perfectly reconstructed from captured samples if the sampling rate is at least twice the signal bandwidth. In applications like remote surveillance, spectroscopy, medical imaging and genomic data analysis, data acquisition at a high sampling rate is difficult to implement or sometimes physically impossible. To address this challenge, Candes and Donoho in two groundbreaking papers [33] and [52] showed it is practical to recover a certain type of signal accurately from a small number of linear, random samples or

measurements. Their results predict that it is possible to sense sparse signals by acquiring far fewer measurements than the Shannon-Nyquist limit using highly nonlinear methods. They initially utilized the terminology 'compressed sensing' for random sensing matrices. Nowadays, in general the term 'compressed sensing' is more often used interchangeably with 'sparse recovery'.

CS relies on the fundamental fact that many types of images and signals can be represented by using only a few non-zero coefficients in a suitable basis or dictionary. These types of signals are called very sparse or highly compressible and lossy compression techniques like JPEG and MP3 exploit the property. A compression is obtained by storing only the largest basis coefficients. As an example, a typical image is very sparse or compressible over the DCT basis. It means very likely only a small fraction of DCT coefficients, say, 10 to 20 percent of DCT coefficients, are influential in image recovering, while the rest of DCT coefficients are insignificant in many compression algorithms. A compression is obtained by storing only the largest basis coefficients. When full information of the signal is available, a reasonable strategy for reconstructing the signal is to set the non-stored coefficients to zero. However, when the signal first has to be acquired by a difficult measurement (sensing) procedure, this method is a waste of resources (energy, observation time etc.), since after a large effort is made to obtain full information on the signal, most of the information is thrown away at the compression stage.

Of course measuring directly the large coefficients as suggested above without knowing *a priori* their locations is not possible. However it has been shown that the precise number of required measurements for an accurate recovery of compressed version of the original signal, is comparable to the compressed size of the signal [30]. Based on the fundamental theorem of linear algebra, 'as many equations as unknowns' (Cramer's rule), it is not possible to recover a unique signal from an insufficient set of linear measurements. Interestingly many natural signals such as real-world images are often sparse or compressible over some basis, such as smooth signals. This feature promises these signals recovery accurately or even exactly from incomplete linear measurements. Two principles make sensing a sparse object by taking as few measurements possible: sparsity, which pertains to the signals of interest, and incoherence, which pertains to the sensing modality. As stated above, sparsity theorems express that many natural signals are sparse or compressible in the sense that they have concise representations when expressed in the proper basis. Incoherence reveals the idea that signals having a sparse representation in any defined domain must be spread out in the domain in which they are acquired [105, 62]. In another words in compressed sensing and sparse signal recovery the necessary assumption is that the measurement matrix has uncorrelated columns. An incoherent measurement system

is shown to inherently satisfy the restricted isometry property (RIP) [30]. In general the representation basis is not incoherent with the measurement basis induced by Dirac operators, randomized measurements basis then were considered to become incoherent with any representation basis. Since the signal is vastly undersampled, the linear system describing the measurements is underdetermined and therefore has infinitely many solutions. The key idea in CS is that the sparsity helps in isolating the original vector by using efficient algorithms. The reconstruction algorithm searches for the sparsest vector that is consistent with the linear measurements.

5.3 Mathematical formulation for sparse recovery

We consider the problem of sensing an unknown signal $\mathbf{x} \in \Re^N$. In CS, relying on linear dimensionality reduction, we do not acquire $\mathbf{x}$ directly but rather acquire M linear measurements using an $M \times N$ CS matrix $\mathbf{y} = \mathbf{\Phi x}, \quad M < N$. $\mathbf{y}$ is referred as the measurement vector. The fact that $M < N$ renders the matrix $\mathbf{\Phi}$ rank-deficient, meaning that for any particular signal $\mathbf{x}_0 \in \Re^N$, the number of signals $\mathbf{x}$ which yield the same measurements $\mathbf{y}_0 = \mathbf{\Phi x}_0 = \mathbf{\Phi x}$ is infinite. Therefore, there is a motivation behind the optimal design of the matrix $\mathbf{\Phi}$ that allows distinct signals $\mathbf{x}$; $\mathbf{x}_0$ within a class of signals of interest to be uniquely identifiable from their measurements $\mathbf{y} = \mathbf{\Phi x}$, $\mathbf{y}_0 = \mathbf{\Phi x}_0$. Let $\mathbf{x}_k$ be the vector consisting of the k largest coefficients of $\mathbf{x} \in \Re^N$ in magnitude; $\mathbf{x}_k = \underset{\|\tilde{x}\|_0 \leq k}{\arg\min} \ \|\mathbf{x} - \tilde{\mathbf{x}}\|_2$, when $\|\mathbf{x}\|_0 = |\{i : \mathbf{x}_i \neq 0\}|$. With the above definition, $\mathbf{x} - \mathbf{x}_k$ is the tail of the signal, consisting of the smallest $N - k$ entries of $\mathbf{x}$. Then with this in mind, if $\mathbf{x}$ is *k-sparse*, $\mathbf{x} - \mathbf{x}_k = 0$.

Often, the signal of interest does not have a sparse or compressible representation. In another words, any given signal $\mathbf{x}$ can be represented in a given basis $\{\psi_i\}_{i=1}^N$, in terms of N coefficients $\{\mathbf{s}_i\}_{i=1}^N$ as $\mathbf{x} = \sum_{i=1}^N \psi_i \mathbf{s}_i$. Arranging the ψ_i as columns into the $N \times N$ matrix $\mathbf{\Psi}$ and the coefficients $\mathbf{s}_i$ into the $N \times 1$ coefficient vector $\mathbf{s}$, leads to $\mathbf{x} = \mathbf{\Psi s}$. In a general setting, $\mathbf{\Psi}$ is referred as the sparsifying dictionary. The signal $\mathbf{x}$ is *k-sparse* in the basis or frame $\mathbf{\Psi}$ if in vector $\mathbf{s} \in \Re^N$ only $k < N$ nonzero entries exist. The main feature of a *k-sparse* signal is that can be efficiently compressed by preserving only the values and locations of its nonzero coefficients, using $O(Klog_2N)$ bits.

In CS, our aim is to recover $\mathbf{x}$ from $\mathbf{y}$ by exploiting its sparsity. But remember we only have access to the CS measurement $\mathbf{y}$, instead of having the signal $\mathbf{x}$ directly. Based on the efficient reconstruction objective, CS process consists of two complementary tasks; designing an appropriate $M \times N$ sensing matrix $\mathbf{\Phi}$ and designing an efficient reconstruction algorithm. If a matrix $\mathbf{\Phi}$ satisfies the restricted isometry property (RIP) introduced in

[33] by Candes and Tao, then this is sufficient for a variety of algorithms to be able to successfully recover a sparse signal from noisy measurements. It was also considered how many measurements are necessary to achieve the RIP. As observed in [33],in order to perform an efficient recovery of any *k-sparse* vector from the measurement vector, we need to have at least $M = O(K \log(N/k))$measurements [33, 12]. A general matrix $\mathbf{\Phi}$ which satisfies a property like RIP [53] has a combinatorial computational complexity, since in each case one must essentially consider $\binom{N}{k}$ submatrices. So it is preferable to use properties of $\mathbf{\Phi}$ that are easily computable to provide more recovery guarantee. The coherence of a matrix is one such property [53, 182]. It can be shown that random matrices satisfy the RIP with high probability if the entries are chosen according to a Gaussian, Bernoulli, or more generally any sub-gaussian distribution [183]. Furthermore, it is theoretically seen when the distribution used has zero mean and finite variance, then the coherence converges as well. Having defined the relevant properties of matrix $\mathbf{\Phi}$ in the context of CS, the matrix reconstruction needs to be performed.

There exists a wide variety of approaches to recover a sparse signal $\mathbf{x}$ from a small number of linear measurements. Two distinct major approaches for sparse recovery have been presented with different benefits and shortcomings. We begin by considering the first approach for the problem of sparse recovery. The CS recovery process consists of a search for the sparsest signal $\mathbf{x}$ that yields the measurements $\mathbf{y}$. l_0 defines *norm* of a vector $\|\mathbf{x}\|_0$ as the number of nonzero entries in $\mathbf{x}$ (this is not precisely a norm, it is a standard abuse of terminology [12, 30]), thus the simplest way to pose a recovery algorithm is using the optimization;

$$\hat{\mathbf{x}} = \arg\min_{x \in \Re^N} \|\mathbf{x}\|_0 \quad Subject \quad To \quad \mathbf{y} = \mathbf{\Phi}\mathbf{x}. \tag{5.1}$$

Solving the above equation relies on an exhaustive search and is successful for all $\mathbf{x}$ with the same sparsity domain when the matrix $\mathbf{\Phi}$ has the sparse solution uniqueness property. This approach uses greedy methods (matching pursuit). While there is no guarantee that matching pursuit computes sparse representations, it is easily implemented, converges quickly, and has good approximation properties [69]. Due to combinatorial computational complexity for solving the algorithm, a computationally feasible algorithm is preferred. An alternative to the l_0 norm used in Equation(5.1) is to use the l_1 norm, defined as $\|x\|_1 = \sum_{n=1}^{N} |x(n)|$ The resulting adaptation of Equation(5.1), known as basis pursuit (BP) [38], is formally defined as;

$$\hat{\mathbf{x}} = \arg\min_{x \in \Re^N} \|\mathbf{x}\|_1 \quad Subject \quad To \quad \mathbf{y} = \mathbf{\Phi}\mathbf{x}. \tag{5.2}$$

Then the recovery error from (l_1) is proportional to the measurement error and the tail of the signal. This means that for compressible signals, those whose coefficients obey a power law decay, the approximation error is very small, and for exactly sparse signals it completely vanishes. l_1-minimization methods provides strong guarantees of exact recovery and stability, but relies on Linear Programming and carries the burden of polynomial time and increased implementation complexity [128].

There are also other algorithmic approaches for compressed sensing based on greedy algorithms including Orthogonal Matching Pursuit [117], Iterative Thresholding [17], Compressive Sampling Matching Pursuit [128], and many others. In contrast with their stability, the complexity of these algorithms grows super-linearly in the problem dimension. Equation(5.2) can be converted into an unconstrained optimization as:

$$\hat{\mathbf{x}} = \underset{x \in \Re^N}{\arg\min} \quad (\|\mathbf{y} - \mathbf{\Phi}\mathbf{x}\|_2 + \lambda\|\mathbf{x}\|_1 + \beta\Xi(\mathbf{x})) \tag{5.3}$$

where λ denotes a weighting coefficient that controls the trade-off between measurement consistency and the sparsity of the reconstructed signal. $\Xi(\mathbf{x})$ represents the additional image constraints with the corresponding weighting coefficient β. The constraints can either be an object-specific prior knowledge such as the object ROS, a phase constraint or an image prior estimate that can be incorporated in the reconstruction process. Alternatively it could be other forms of more generic constraint such as the total variation (TV). Theoretically and empirically it has been confirmed that the use of total variation (TV) regularization in CS problems makes the recovered signals or image quality sharper by preserving the edges or boundaries more accurately. In image processing the use of TV minimization concept, which is closely connected to l_1-minimization and compressive sensing, was introduced first by Rudin, Osher, and Fatemi [163]. The TV constraint has been used in denoising applications, image restoration and widely applied to suppress additive noise while preserving image edges [163]. TV regularization would succeed when the gradient of the underlying signal or image is sparse. In another words, for a given discrete signal $\mathbf{x}$ of length N, TV measures the total absolute variations in the signal, and can be written as:

$$TV(\mathbf{x}) = \sum_{n=2}^{N} |(\mathbf{x}_n - \mathbf{x}_{n-1})| \tag{5.4}$$

In this form, TV operator is equivalent to a finite-difference measure of the signal, and hence the use of it in Eq.(5.3) can be viewed as an additional sparsifying transform in the finite-differences domain [105].

5.4 Sparsifying transforms

According to restricted isometry property (RIP) condition [30], for a given amount of data, the sparser a signal is, the better the reconstruction that can be expected. Therefore sparse approximation is at the heart of many efficient compression and compressed sensing algorithms. However, fixed common orthogonal sparsifying transforms are not flexible enough to capture the complex characteristics of different signals of interest in particular applications. The signal sparsification problem can be attacked in two ways, either non-adaptively or adaptively. An extensive body of work investigated different non-adaptive and adaptive sparsifying transforms that exploit the image characteristics for accurate reconstruction [51, 138, 134, 148, 9]. When certain characteristics of the signal are known, a dictionary might be selected from the vast class of already well explored representation systems such as the wavelets or Fourier basis. Although the achieved sparsity might not be optimal, various mathematical properties of these transforms are well-known and fast associated transformations are available.

For example the wavelet transform fails to compress regular edges efficiently. In [32] this problem was addressed by use of the curvelets transform. Recently, adaptive transforms (or dictionaries) have become increasingly popular as they can more accurately capture characteristics of the images during reconstruction. Instead of regularizing the CS inverse problem with a fixed basis, Peyr proposed a framework which used sparsity in a a tree-structured dictionary of orthogonal basis which were adapted to a given image [138]. Most of the work in dictionary-based recovery algorithms learn the dictionaries from a collection of pre-collected reference images. The trained dictionary is then employed as the sparse representation basis for the CS recovery procedure. To guide the reconstruction process, a sparsifying transform was learned from a reference image to capture the anatomical structure of unknown image in Babican's work [8]. The most well-known and widely used algorithm as a sparsifying dictionary is the K-SVD introduced by Aharon, Elad, and Bruckstein in [4].

5.4.1 Singular Value Transformation

Singular Value Transformation (SVD) is one of the data-adaptive transforms which decompose the signal through the calculation of eigenvalues and eigenvectors of the covariance matrix consisting of the signal. SVD has been used for texture characterization, image restoration and for facial recognition [126]. SVD is an effective tool for minimizing data storage and data transfer [142]. Since the approximation error for an image represented by

SVD is simply the sum of all unused singular values, removing the lowest valued high-order values will not significantly reduce the approximation accuracy. Thus using SVD as the data-adaptive sparsity basis results in a sparse representation which can be employed in the CS algorithm. The singular value decomposition of a matrix factors an $M \times N$ matrix $\mathbf{A}$ into the form

$$\mathbf{A} = \mathbf{U}\mathbf{\Sigma}\mathbf{V}^T \tag{5.5}$$

where $\mathbf{U}$ is an $M \times M$ orthonormal matrix; $\mathbf{V}$ represents an $N \times N$ orthonormal matrix, and $\mathbf{\Sigma}$ an $M \times N$ matrix containing the singular values of $\mathbf{A}$ along its main diagonal, arranged in descending order (^{T} denotes transposition). Calculating the SVD consists of finding the eigenvalues and eigenvectors of $\mathbf{A}\mathbf{A}^T$ and $\mathbf{A}^T\mathbf{A}$. The eigenvectors of $\mathbf{A}^T\mathbf{A}$ make up the columns of $\mathbf{V}$ and the eigenvectors of $\mathbf{A}\mathbf{A}^T$ make up the columns of $\mathbf{U}$. The eigenvalues of both $\mathbf{A}^T\mathbf{A}$ and $\mathbf{A}\mathbf{A}^T$ are the squares of the singular values for $\mathbf{A}$. Equation(5.5) can be expressed as:

$$\mathbf{A} = \sum_{i=1}^{p} \mathbf{u}_i \sigma_i \mathbf{v}_i^T, \quad \sigma_1 \geq \sigma_2 \geq \sigma_3 \geq \cdots, \quad \sigma_i = 0 \quad for \quad r < i \leq p \tag{5.6}$$

where r is the rank of matrix $\mathbf{A}$, p is the smaller of the dimensions M or N, and $\mathbf{u}_i$, $\mathbf{v}_i$ are the i^{th} column vectors of $\mathbf{U}$, $\mathbf{V}$ respectively, and σ_i are the singular values. The matrix $\mathbf{A}$ can be approximated by matrix $\hat{\mathbf{A}}$ with rank k by

$$\hat{\mathbf{A}} = \sum_{i=1}^{k} \mathbf{u}_i \sigma_i \mathbf{v}_i^T, \tag{5.7}$$

As the singular values are in descending order it can be seen that the error decreases towards zero in the 2-norm sense. In Fig.(5.1) the same image as shown in Fig.(5.2a) was used to assess the compression obtainable via SVD. In Fig.(5.1a) and Fig.(5.1b) reconstructions are shown from 50% and 10% of the singular values, respectively.

5.5 Data reordering impact on sparsity

Adluru and DiBella proposed a preprocessing technique to improve the reconstruction of the signals that may not fit the TV constraint well [1]. Their method used non-reordered reconstructions to obtain information about the signal to be reconstructed to determine

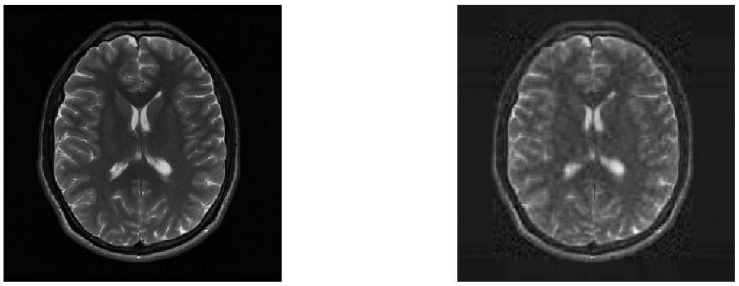

(a) **(b)**

Figure 5.1: The results of an SVD-based image compression with different compression ratios: in (a) 50% and in (b) 10% of coefficients in $\mathbf{\Sigma}$ were used to accomplish compression. The original uncompressed image is shown in Fig.(5.2a).

the orderings of the pixel intensities. They also proposed that ordering estimation can be performed from the low-resolution images when a variable density undersampling scheme is used, and from non-reordered constrained reconstructions. The TV norm corresponding to the optimal regularization parameter with an appropriate ordering, is lower than the corresponding optimal regularization parameter without reordering. Clearly, by reducing sudden variations in the rapidly varying curves, reordering gives a better match to the TV constraint. Consider a 2D signal, extracted from a brain cross-sectional slice as shown in Fig.(5.2a). In Fig.(5.2b) the pixels of the image have been reordered to yield a monotonically increasing variation starting from the lower right corner. We depict the ordering process as applying the operator R. The discrete cosine transformation (DCT) coefficients of the two images were calculated and their magnitudes are depicted in Fig.(5.2c) and Fig.(5.2d), respectively. Note that many fewer coefficients appear to have substantial magnitude in Fig.(5.2d) than in Fig.(5.2c). Subsequently the highest magnitude 5% of the coefficients were retained and the rest relaxed to zero. Finally images were reconstructed from the resulting compressed data. Fig.(5.2e) shows the result corresponding to applying conventional compression to the original image in Fig.(5.2a). Fig.(5.2f) shows the result obtained after reconstructing the compressed version of Fig.(5.2d), followed by an inverse ordering process (R^{-1}). It is clear that the results after incorporating the reordering step are superior than the others. A significant loss of high frequency information was resulted from the first decompression outcome.

To compare the reconstructed images, the normalized mean square error (NMSE) between

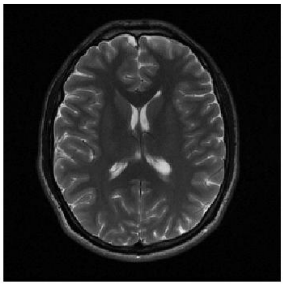

(a) Original 2D image

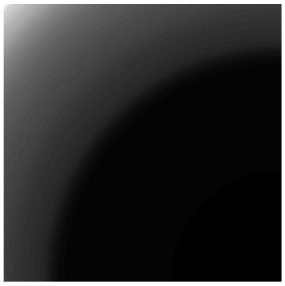

(b) Reordered image

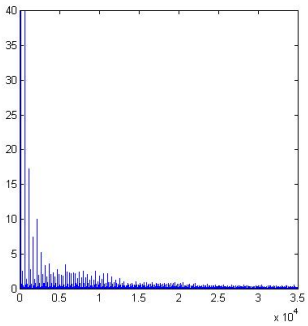

(c) DCT coefficients of the image

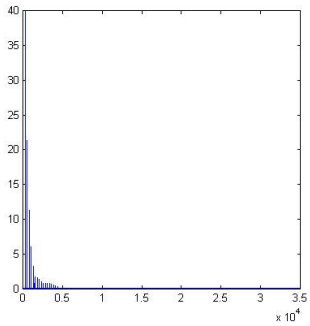

(d) DCT coefficients of the reordered image

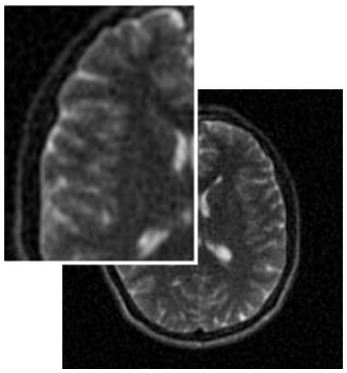

(e) Decompressed image

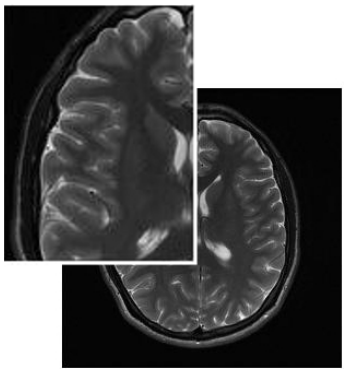

(f) Decompressed image after unsorting

Figure 5.2: (a) Illustrates the original image of an axial plane brain slice which is reconstructed from full sampled k-space and considered as the reference; (b) image (a) ordered into a a 2D monotonically decreasing variation (R); (c) DCT coefficients of (a) for which the summation of the coefficients is 5947; (d) DCT coefficients of (b) for which summation of the coefficients is 472; (e) reconstructed image using only the 5% largest DCT coefficients from (c), NMSE= 0.1823 ; (f) reconstructed image using only the 5% largest DCT coefficients from (d) and reordering (R^{-1}), NMSE= 0.0018.

the reference signal and reconstructed one was calculated by:

$$\text{NMSE} = \sqrt{\frac{\sum_{i=1}^{P}(|I_i^{reference}| - |I_i^{reconstructed}|)^2}{\sum_{i=1}^{P}|I_i^{reference}|^2}}, \tag{5.8}$$

where P denotes the number of elements within the reference signal. As reported in the captions for Fig.(5.2e) and Fig.(5.2f), the NMSE value for the reconstructed image utilizing the reordering step is significantly decreased.

The total variation of the same image as showed in Fig.(5.2a) for horizontal and vertical directions are presented in Fig.(5.3). Intensity-based sorting of the pixels have been illustrated in Fig.(5.3c) and (5.3d). The calculated l_1 norms of unsorted and sorted images prove that monotonically reordering pixels, enhance the images sparsity.

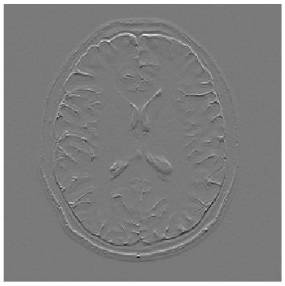

(a) Total Variation of the image in X direction

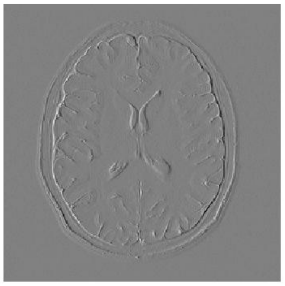

(b) Total Variation of the image in Y direction

(c) Total Variation of the reordered image in x direction

(d) Total Variation of the reordered image in Y direction

Figure 5.3: The summation of TV coefficients in (a) is 3.0870e+003, in (b) is 3.2961e+003; in (c) is 194.1450 and in (d) is 194.2693

Interestingly, reordering of data has recently found application in a very different application

of compressed sensing. To enhance CS through improving signal compressibility a method by finding a sub-optimal permutation of wireless sensor networks was proposed [110]. It was stated that their sub-optimal reordering stably maintains a more compressible view of the signal. The presented method increased signal reconstruction accuracy at the same spatial sampling rate. The signal vector was rearranged so that its sparse representation in the transform domain (the Fourier transform was used) has much of the energy of the signal concentrated on the first few frequency coefficients. Fig.(5.4) shows an example of the Sub-optimal reordering and compares the suggested reordering impact on compression accuracy with monotonic reordering.

5.6 CS applications

In recent years, the area of CS has branched out to many new fronts and has worked its way to multiple application areas. It seems that the hot topic in CS applications is MRI, which has seen much research, also one of the first paper [105] published in 2005 explained how CS highly speeds up MRI while preserving diagnostic quality. Traditional MRI scanners sequentially sample Fourier coefficients of the human body's image. We know that in conventional MRI specific grids of points in 2D or 3D k-space are acquired, and then the image may be reconstructed by the inverse transform. In another word, MRI images are sparse in the Fourier domain that has been sampled. As a result using CS recovery ideas, it is possible to sub-sample the grid and solve a linear inverse problem to recover the image without reducing the accuracy of the MRI image.

The iconic *single pixel camera* developed at Rice University is the most well-known compressed sensing hardware. The smart idea behind the camera is that the spatial resolution has been traded with the temporal resolution; for frequencies such as infrared, where each pixel is extremely expensive [197]. A micro-mirror array is placed in front of a conventional optical lens system which makes each measurement different and also encode the entire scene. The array is a grid of pixel-like mirrors named a Digital Micro-mirror Device (DMD); each micro-mirror can be oriented to either reflect the light towards a lens (on state) or away from it (off state). The mirrors are able to be turned on and off very quickly, and thus each pixel can be partially reflected as determined by the ratio between the on and off time. Then in order to convert the accumulated light intensity into a quantitative measurement, a photodiode is put in the cannon of the lens. By repeating this process M times, a number M of linear measurements can be sensed. The effect of using this micro-mirror is similar to using a binary mask. In short, particular advantage of the single pixel camera is that only one sensor (photodiode) is required while in classical digital

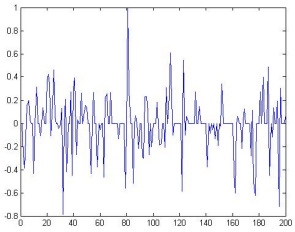

(a) signal vector

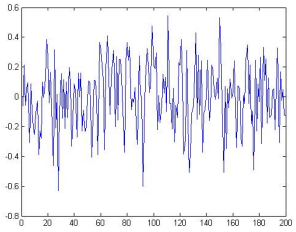

(b) DCT coefficients

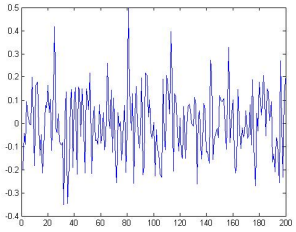

(c) recovered signal after compression

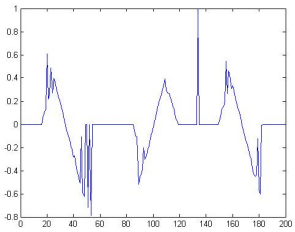

(d) Sub-Optimal reordered version of signal

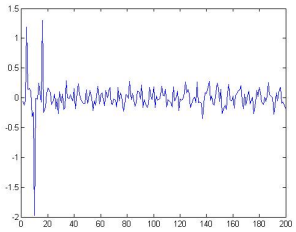

(e) DCT coefficients of the reordered signal

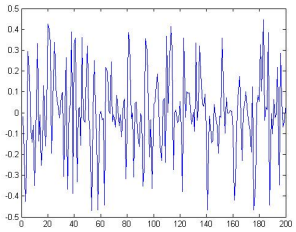

(f) recovered signal after compression

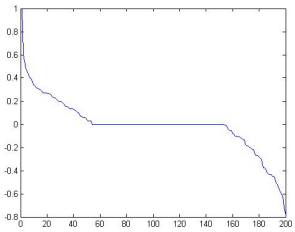

(g) monotically decreasing reorderd signal

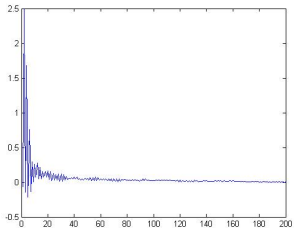

(h) DCT coefficients of the reordered signal

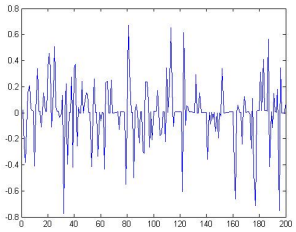

(i) recovered signal after compression

Figure 5.4: (a) depicts the original discrete signal f, (b) the DCT transform of the actual vector f, (c) reconstructed vector after retrieving 10% of largest coefficients in (b), MSE = 0.0305 (d) sub-optimally reordered f, (e) its DCT coefficients, (f) reconstructed vector after retrieving 10% of largest coefficients in (e), MSE = 0.0103 (g) monotically reordered f, (h) its DCT coefficients, (i) reconstructed vector after retrieving 10% of largest coefficients in (i), MSE = 8.3599e-004

cameras the arrays of N high-resolution sensors are too expensive or even not available, for instance in infrared imaging. This procedure is similar to the ideas used in coded aperture imaging in astronomy and microscopy.

Piecewise smoothness in the pixel basis of natural images is a fundamental assumption in digital image processing. It means that there are very few edges in the image which make the differences between the values of adjacent pixels to be zero or almost zero [79]. Also a sparsifying transform like the wavelet can be imployed to map images from the pixel domain

to the wavelet domain in which they have sparse (or approximately sparse) representations. Here, compressed sensing as a new data acquisition framework can play its role, to overcome the inefficiencies of the classical image compression approaches. Hyperspectral imaging is the practice of acquiring images across the electromagnetic spectrum (though usually not a continuum of wavelengths). It can play a useful role in applications like agriculture, mineralogy, physics, satellite imaging and surveillance. Normally hyperspectral images are more compressible than typical images, thus like in [203] CS can be play a useful role.

One of the major challenges in communication research is the problem of configuring wireless networks to enable network communication in the presence of inference [195]. Managing inference in peer to peer networks is one of the important cases where multiple sensors look to communicate with an access point. In the networked data a single transmitter needs to communicate simultaneously with multiple (N) receivers. CS can be connected to wireless communication via the key idea that at each time only a small ($k << N$) number of receivers are active. An $M \times N$ sensing matrix $\mathbf{\Phi}$ then can be maintained, such that the i^{th} columns of $\mathbf{\Phi}$ is associated with the i^{th} user.

Microarrays have been utilized commonly in biology to identify specimens, using fluorescent tags to identify where samples bind. Most samples have only a few active parts, thus using CS ideas suggests that taking many fewer measurements is possible and still accurately conclude which specimens are present [125]. Radar, quantum computing and ADC (Analog-to-Digital Converters) are some other examples of CS implications that imply much more potential for future.

5.7 CS MRI

In principle, MR images can be reconstructed from a sequence of acquisitions using various k-space trajectories which cover a whole region of k-space. Conventionally the k-space sampling pattern needs to be designed to satisfy the Shannon-Nyquist sampling criterion, which in turn depends on the resolution and field of view (FOV). Having different sparsifying transforms for MR images and the nature of MR acquisition are two key properties enabling CS to suceed in MRI. Reconstruction from Cartesian acquisitions is as simple as applying the inverse Fast Fourier Transform (FFT) to k-space dataset. In this work we consider 2D Cartesian pMRI imaging. The goal in CS MRI is to reconstruct the unknown image from limited k-space measurements. Consider a finite-length, discrete-time image $\mathbf{x}$, which can be viewed as an $N \times 1$ vector in $\Re^N$ with elements $x[n], n = 1, 2 \ldots, N$. (We treat an image by vectorizing it into a one-dimensional vector).The imaging process is commonly

modeled as

$$\mathbf{y} = \mathbf{F}_u \, \mathbf{x}, \tag{5.9}$$

where $\mathbf{F}_u \in \Re^{M \times N}$ is the undersampled Fourier encoding matrix relating the unknown image $\mathbf{x}$ to the limited k-space measurements $\mathbf{y} \in \Re^M$,. In general, one would not expect to be able to accurately recover $\mathbf{x}$ when $M < N$ but by exploiting sparsity, it is possible to accurately estimate $\mathbf{x}$ if it is *k-sparse* by itself or in some other transformation domain, with a high probability CS can reconstruct $\mathbf{x}$ exactly from only M measurements. It has been justified that measurement matrices constructed by randomly drawing entries from a certain distribution are largely incoherent with any fixed basis and ensure an exact recovery [12, 62]. For an orthonormal basis matrix, the use of a random measurement matrix leads to a sensing matrix that obeys the uniform uncertainty principle (UUP) with overwhelming probability [30]. Lustig exhibited a uniform random distribution of samples in spatial frequency does not take into account the energy distribution of MR images in the center of k-space [105]. Consequently they proposed a random variable-density sampling with denser sampling near the center of k-space which characterized the incoherence properties of pure random sampling. The designed nonuniform random undersampling leads to incoherency of the aliasing artifacts caused by k-space undersampling and has been employed in many CS MRI reconstruction methods.

Assuming for a moment that $\mathbf{x}$ exhibits sparsity in itself, one of the theoretically simplest ways to recover such a vector from its measurements is l_0-minimization. Consider the l_0 norm that counts the number of non-zero entries in $\mathbf{x}$, therefore a *k-sparse* vector has l_0 norm equal to k. The modified optimization for Eq.(5.9) is:

$$\arg\min_{x \in \Re^N} \|\mathbf{x}\|_0 \quad Subject \quad To \quad \mathbf{y} = \mathbf{F}_u \mathbf{x}, \tag{5.10}$$

In practice, the sparsity of an image $\mathbf{x}$ may only be evident after some transformations. Any image in $\Re^N$ can be represented in terms of a basis of $N \times 1$ vectors $\psi_i, i = 1, 2, \ldots, N$. For simplicity, assume that the basis is orthonormal. Thus an image $\mathbf{x}$ can be expressed as

$$\mathbf{x} = \sum_{i=1}^{N} \mathbf{s}_i \, \psi_i \quad \text{or} \quad \mathbf{x} = \mathbf{\Psi} \, \mathbf{s}, \tag{5.11}$$

where the vectors ψ_i are columns of the $N \times N$ basis matrix, $\mathbf{\Psi} = [\psi_1 | \psi_2 | \ldots | \psi_N]$ and $\mathbf{s}$ is a $N \times 1$ column vector of weighting coefficients. Since $\mathbf{\Psi}$ is assumed to be orthogonal, $\mathbf{s}_i = \psi_i^T \, \mathbf{x}$. Thus $\mathbf{s}$ is the equivalent representation of the image in the $\mathbf{\Psi}$ domain.
The image $\mathbf{x}$ is *k-sparse* if to a close approximation it is a linear combination of only K

basis vectors; that is, only K of the coefficients s_i in Eq.(5.11) are nonzero and $(N-K)$ are zero. The case of interest is when $K << N$. By substituting $\mathbf{\Psi}$ from Eq.(5.11), $\mathbf{y}$ in Eq.(5.10) can be written as synthesis-based sparse reconstruction

$$\arg\min_{s\in\Re^N}\|\mathbf{s}\|_0 \quad Subject \quad To \quad \mathbf{y}=\mathbf{F}_u\,\mathbf{\Psi}\mathbf{s}. \tag{5.12}$$

Typical formulations of the CS reconstruction problem with the analysis-based and synthesis-based regularization are in the following Lagrangian setup:

$$\hat{\mathbf{x}}=\arg\min_x\|\mathbf{y}-\mathbf{F}_u\mathbf{x}\|_2+\lambda\Gamma(\mathbf{\Omega}\mathbf{x}),\quad \hat{\mathbf{s}}=\arg\min_s\|\mathbf{y}-\mathbf{F}_u\mathbf{\Psi}\mathbf{s}\|_2+\lambda\Gamma(\mathbf{s}), \tag{5.13}$$

where $\mathbf{\Omega}$ is a linear operator (a matrix), referred as analysis dictionary (possibly redundant). Note that the analysis representation vector, $\mathbf{\Omega}\mathbf{x}$ is sparse. While the analysis approach may seem similar to the synthesis counterpart, it can be in fact very different when dealing with a redundant dictionary. The function $\Gamma(.)$ is a sparsity measure like a variant of the l_p norm with $0\leq p\leq 1$ to enforce sparsity in both cases [105]. λ is the regularization parameter which balances the trade off between the acquired data consistency and sparsity of the image representation. The key property in designing or learning the sparsifying transform is its sparsifying ability to capture the local (spatial) contextual information in an image and suppress incoherent noise, i.e., an appropriate transform should produce high-magnitude sparse coefficients such that by imposing $\Gamma(\mathbf{\Omega}\mathbf{x})$, the l_p norm significantly constrains the solution space of $\mathbf{x}$ [8]. The analytical total-variation transform imposes sparseness on the whole image domain such that finite differences in horizontal and vertical directions in the image are sparse. Typically this transform is considered as an additional constraint with the other proposed transforms to smooth the difference between the recovered values of adjacent pixels. For instance, artifacts usually exist in CS reconstructions when the wavelet transform is used alone for the sparse representation. Thus total variation (TV) terms are frequently combined with the wavelet transform to suppress these artifacts and enforce spatial homogeneity [105].

5.8 pMRI reconstruction algorithms using CS

In recent years, Parallel MRI (pMRI) has been used for accelerating the MRI scans. As discussed in chapter 2 in pMRI, multiple receiver coils are employed for the data acquisition. Due to the distinct sensitivity of each individual receiver coil to the object magnetization, the different coils receive independent measurements from the imaged object. Thus it is possible to recover the image using the undersampled data sets simultaneously acquired by

the multiple receiver coils. To achieve further acceleration, both pMRI and CS-MRI were employed in our work. In the direct application of CS recovery with pMRI to accommodate multiple receiver measurements, the distinctive coil sensitivity encoding in different receiver coils needs to be employed. The SENSE[145]-like reconstruction formulation in pMRI is presented as follows:

$$\hat{\mathbf{x}} = \arg\min_{x} \|\mathbf{y} - \mathbf{E}\mathbf{x}\|_2 \quad , \quad \mathbf{E} = \begin{bmatrix} F_u diag(\mathbf{c}_1) \\ F_u diag(\mathbf{c}_2) \\ \vdots \\ F_u diag(\mathbf{c}_M) \end{bmatrix} \quad , \quad \mathbf{y} = \begin{bmatrix} y_1 \\ y_2 \\ \vdots \\ y_M \end{bmatrix}, \tag{5.14}$$

where $\mathbf{y}$ is the vector formed from k-space data acquired in all the M channels, $\mathbf{x}$ is the unknown vector defining the desired full (FOV) image to be computed, $\mathbf{E}$ is the sensitivity encoding matrix, $\mathbf{c}_n$ denotes the coil sensitivity profile for the nth coil, and $diag(\mathbf{c}_n)$ is a diagonal matrix with the elements of vector $\mathbf{c}_n$ on the main diagonal and zero elsewhere. The direct generalization of CS in parallel imaging [208, 99] formulates the reconstruction from multi-channels, as the same convex optimization problem as CS-MRI in Eq.(5.13), except that the encoding matrix is the Fourier transform of the channel-specific sensitivity modulation $\mathbf{E}$.

$$\hat{\mathbf{x}} = \arg\min_{x} \|\mathbf{y} - \mathbf{E}\mathbf{x}\|_2 + \lambda\Gamma(\mathbf{\Omega}\mathbf{x}), \tag{5.15}$$

Worth mentioning that the incoherence between the encoding matrix $\mathbf{E}$ and the sparsifying basis $\mathbf{\Omega}$ has not been yet explored in this equation. It was discussed in [104, 102], therefore direct combination of pMRI and CS recovery (SparseSENSE) as in Eq.(5.15) has an intrinsic limitation due to the conflicting sampling requirement of pMRI and CS. Achieving incoherent aliasing artifacts in the transform domain in which the sparse signal is to be recovered is the key sampling requirement in CS. for instant using the DCT or wavelet transforms as the sparsifying transform, is equivalent to having a pseudo-random sampling pattern. On the other hand, from the pMRI point of view, having spatially far apart image elements are preferable to employ spatial sensitivity of array receivers. We know that in order to improve the effectiveness of sensitivity encoding, a regular sampling pattern is required. Therefor direct combination of pMRI and CS as in Eq.(5.15) gives rises to a challenge in terms of sampling pattern design; A sampling pattern that could sufficiently exploit sensitivity encoding in pMRI harms the conditioning of a successful CS

reconstruction.

l_1-SPIRiT Reconstruction

(iterative self-consistent parallel imaging reconstruction) SPIRiT was presented first by Lustig [106], as a generalized reconstruction framework which performs parallel imaging reconstruction. It was a coil-by-coil autocalibrating reconstruction and heavily based on the GRAPPA reconstruction but also draws its inspiration from SENSE in the sense that the reconstruction was formulated as an inverse problem. Inspired by GRAPPA, SPIRiT describes the reconstruction problem as an inverse problem governed by data consistency constraints. There are two separate consistency constraints in the approach; (a) consistency with the calibration, and (b) consistency with the data acquisition. Then these constraints will be formulated as sets of linear equations. Ultimately the desired reconstruction from k-space data will be the solution which satisfies the sets of equations best according to a suitable error measure criterion. Using iterative methods for data acquired on arbitrary k-space trajectories, the reconstruction can be solved very efficiently. In each iteration, performing a linear combination of nearby k-space values, missing k-space values are estimated.

Although, SPIRiT offers better noise performance than GRAPPA especially when the acceleration is pushed to the limit, the computational complexity of SPIRiT as an iterative reconstruction, can be more intensive than direct reconstruction. Later an extension of SPIRiT, l_1-SPIRiT, was proposed that combines SPIRiT with compressed sensing [193, 194]. l_1-SPIRiT solves a constrained non-linear optimization over the image matrix while the non-linearity of this optimization necessitates an iterative reconstruction procedure. The first requirement of CS, sparsity of representation, was reconsidered in the context of auto-calibrating parallel imaging and a modified sparsity model was presented. They showed that the wavelet transforms (sparsifying transform here) of the individual coil images are correlated. To exploit similar sparsity patterns that can be exhibited in the individual coil images, a joint sparsity model was proposed. To take the correlation into account, they jointly penalized the coefficients from different coils that are at the same spatial position. Incoherent sampling is another fundamental requirement in CS recovery which generally by random sampling of k-space is provided. However as discussed before, it is not optimized for parallel imaging. Since either large gaps or bunched samples that often occur in random sampling reduce the reconstruction conditioning and increase noise, a (gridded) Poisson-disc distribution (Random sampling with minimum distance between samples) [25] was employed for sampling. This under-sampling pattern provides high degree of incoherency and at the same time uniform distance between samples. Utilizing multiple coil, close samples in k-space are naturally correlated which enables the recovery of missing samples in

parallel imaging. In another words, bunched samples provide little additional information on the signal recovery. Whereas large gaps decrease the reconstruction conditioning of the parallel imaging. A fully sampled calibration area in the center of k-space was used to calibration in SPIRiT. Then The non-acquired k-space samples are recovered such that they are consistent with the interpolator and the acquired data.

5.8.1 Prior Estimate based compressed sensing in parallel MRI - PECS

Our group proposed Prior Estimation-based CS (PECS) in a previous paper [207]. PECS is a promising technique that exploits prior knowledge of the underlying image in pMRI reconstruction. It has been proved in various studies that the success of CS recovery is fundamentally limited by the sparsity level of the underlying image. The more compressible the signal, the sparser its Fourier, DCT, Wavelet, etc. transform is and consequently if we decrease K, then we can reconstruct the original signal from fewer samples.
With reference to section(5.8) the formulation to recover MRI images with CS method is:

$$\check{\mathbf{x}} = \arg\min_{x}(\|\mathbf{y} - \mathbf{E}\mathbf{x}\|_2 + \alpha\|\mathbf{x}\|_1 + \beta TV(\mathbf{x})), \tag{5.16}$$

$$\mathbf{y} = \mathbf{E}\mathbf{x}\ , \quad \mathbf{E} = \begin{bmatrix} diag(\mathbf{h})\mathbf{W}diag(\mathbf{c}_1) \\ \vdots \\ diag(\mathbf{h})\mathbf{W}diag(\mathbf{c}_M) \end{bmatrix}\ , \quad y = \begin{bmatrix} diag(\mathbf{h})\mathbf{y}_1 \\ \vdots \\ diag(\mathbf{h})\mathbf{y}_M \end{bmatrix}$$

where $\mathbf{x}$ and $\mathbf{y}$ represent the underlying image and the partial k-space acquisition respectively and $\mathbf{h}$ is the binary under-sampling mask with 1 and 0 corresponding to measured and skipped sample positions respectively in a specific temporal window (with a non-uniform sample density function). $\mathbf{E}$ represents the corresponding pMRI encoding matrix. The data sorting strategy proposed by Adluru (section 5.5) was used in PECS for the image recovery process. The knowledge of a prior image estimate $\acute{\mathbf{x}}$ was employed to perform sorting the the elements of the underlying image $\mathbf{x}$, resulting the sorted image $\mathbf{g}$ with a higher level of sparsity for a given transform. Hence, instead of the underlying signal $\mathbf{x}$ estimation, an attempt to recover the sorted signal $\mathbf{g}$ was made, where $\mathbf{x} \overset{R}{\rightarrow} \mathbf{g}$. PECS is therefore formulated as follows:

$$\hat{\mathbf{g}} = \arg\min_{g}(\|\mathbf{y} - \mathbf{E}_R\mathbf{g}\|_2 + \alpha\|\mathbf{\Omega}\mathbf{g}\|_1 + \beta TV(\mathbf{x})), \quad \hat{\mathbf{g}} \overset{R^{-1}}{\rightarrow} \hat{\mathbf{x}} \tag{5.17}$$

where $\hat{\mathbf{g}}$ and $\hat{\mathbf{x}}$ are the estimates of the underlying signal and the sorted signal under sorting

order R, respectively. $\mathbf{E}_R$ represents the updated encoding matrix (column changed) based on the sorting order R obtained from the reference image. The results presented showed that the data sorting allows the underlying signal to be recovered in an alternative form that possesses a higher level of sparsity, and hence leads to a better signal recovery [207]. As exact knowledge of the underlying signal (image) is not available prior to the reconstruction to gain the exact sorting order (R), we used a signal prior estimate to give an approximate sorting order R'. To perform PECS a low-resolution approximation of the image was achieved using only the central regions of k-space from multiple coil data sets. Then, the sorting order was obtained by sorting this low-resolution approximation into a 2D monotonical form, similar to Fig.(5.2). Although applying an approximate sorting order results in an imperfectly sorted signal, which is inherently less sparse than if R was used, it appeared to modify the form of reconstruction artifacts. In general, applying a data sorting modifies the form of reconstruction artifacts in PECS from those in conventional CS. There are some structured artifacts in conventional CS recovery which are dependent on the specific transform used and the signal features. In PECS on the other hand, the structured artifacts present in the sorted signal/image domain and, after imposing the inverse ordering, are likely to be become unstructured in the final reconstruction. These high-frequency noise-like variations can be suppressed in CS by assuming a smoothly varying nature of the underlying image, and using a total variation constraint.

5.8.2 PECS-based SENSE

The recovered images using SENSE method and CS recovery have distinctively different characteristics. In SENSE-like approaches, direct inversion of the measurement matrix offers a 2nd norm optimal image estimate; which leads to reconstruction noise amplification. In the CS recovery, a low noise level in the results is achievable due to the use of signal sparsity constraint as well as other constraints such as the TV constraint, but it also leads to loss of image details and contrast in the reconstruction. PECS-based SENSECS approach decouples the CS and pMRI procedure in reconstruction and applies SparseMRI and SENSE sequentially to compensate for the shortcomings of the other. SENSE reconstruction is performed to gives an image estimate that is corrupted by reconstruction noises. Then a sorting order $\acute{R}$ is obtained by sorting this reconstructed image into a 2D monotonical function. A sparsyfing transform (such as 2D DCT or wavelet) is used for the sparse representation of the monotonical function. Having the estimated sorting order, a PECS reconstruction using the same k-space measurements is performed, followed by an unsorting process to form a final reconstruction outcome. The reconstruction noise in SENSE features a non-uniform profile which the data sorting process disrupts its original structure and

hence allows it to be reduced by imposing a TV constraint. To cater the conflict in choosing a sampling pattern, a hybrid sampling pattern is proposed. A SENSE-like regular sampling pattern is first built, then a small number of additional acquisitions at the k-space center are added. These additional sample acquisitions capture the high energy components at the center of k-space and aid the PECS.

5.8.3 Singular Value decomposition (SVD)-PECS formulation

As a method of utilising the data ordering without requiring a prior estimation, we propose to reconstruct the initial image by applying singular value decomposition (SVD) to the CS algorithm. Classical approaches in CS consider non-adaptive, analytical transforms such as wavelets, total-variation, and contourlets [105, 148]. A data-adaptive transform which captures important characteristics of the images of interest, can reveal image features or anatomical structures.

Incorporating Eq.(5.5) into the optimization Equation expressed in Eq.(5.15) allows reconstruction of an image with SVD as the sparsifying transform. Direct inverse Fourier transform from the undersampled k-space is used for the initial estimate ($\mathbf{A}$) of the target $\mathbf{U}$, $\mathbf{\Sigma}$ and $\mathbf{V}$.

$$\hat{\mathbf{x}} = \arg\min_{\mathbf{x}} \|\mathbf{y} - \mathbf{E}\mathbf{x}\|_2 + \lambda_1 \Gamma(\mathbf{\Omega}\mathbf{x}) + +\lambda_2 TV(\mathbf{x})), \tag{5.18}$$

where $\mathbf{\Omega}\mathbf{x} = \mathbf{\Sigma}$ is a sparse representation of the image. Having $\mathbf{U}$ and $\mathbf{V}$, the SVD-based sparsifying transform and its inverse can be derived and be updated iteratively in the process. To reconstruct the image, the l_1 norm optimization problem is solved with the following regularization parameters $\lambda_1 = 0.03$, TV regularization parameter $\lambda_2 = 0.01$. According to our simulation, the image reconstruction quality will improve after four or five iterations in NLCG[105]. The recovered image using CS reconstruction with the SVD transformation is employed to derive the data order approximation R' and that is incorporated into the second CS recovery framework as explained in Section(5.8.1). Having R', the l_1 norm optimization problem as defined in Eq.(5.18) can reconstruct the reordered image. NLCG algorithm is repeated until the stopping criterion is met. After applying the unsorting process (R'^{-1}), to the result, a final reconstruction with high fidelity is obtained. We named this new method 'SPECS' since it represents an SVD-based modification of PECS[189]. A summary of the SPECS algorithm is presented below:

SPECS Algorithm

Initialization:

Set **y**: under-sampled k-space measurements,

E: sensitivity encoding operator,

A: initial image reconstructed by applying inverse Fourier transform directly to the under-sampled k-space data

SVD: sparsifying transform which use image **A** to generate its sparse representation $\mathbf{\Sigma}$

CS algorithm:

Solve The l_1 norm optimization problem as defined in Eq.(5.18) to reconstruct the image

SVD regularization parameter $\lambda_1 = 0.03$, TV regularization parameter $\lambda_2 = 0.01$

max number of iterations = 5

Repeat the iterations in NLCG[105] algorithm until the stopping criterion is met

Output: $\mathbf{x}_1$ reconstruction result which is used to derive sorting order R_1'.

Initialization:

Set **y**: under-sampled k-space measurements, $\mathbf{F}_u$: under-sampled Fourier transform operator

E: sensitivity encoding operator, DCT: sparsifying transform, R_1': approximate sorting order

PECS algorithm:

Solve The l_1 norm optimization problem as defined in (5.17) to reconstruct the image

DCT regularization parameter $\lambda_1 = 0.02$, TV regularization parameter $\lambda_2 = 0.02$

max number of iterations = 30

Repeat the iterations in NLCG algorithm until the stopping criterion is met

Output: reordered reconstruction

Invoke the unsorting process (R'^{-1}) to form the final reconstructed image

Final output: $\mathbf{x}_2$

5.9 Experiments on MR Images

To evaluate the performance of the proposed SPECS method an *in vivo* experimental data set was acquired on a normal volunteer. The data used was obtained using a $1.5T$ GE scanner equipped with an eight-channel head coil. A T2-weighted axial brain slice was obtained with the following parameters: FOV = $22cm$, matrix size = 256×256, TR/TE = $2270/85msec$. The phase encoding and frequency encoding directions were set to be posterior/anterior and left/right, respectively. Consent from the volunteer was obtained prior to the scan. A full k-space data set was first obtained, then various forms of sampling patterns were applied to simulate the undersampling required. The sparsifying transforms used in the two phases of the algorithm were 2D SVD and 2D DCT. Lustigs nonlinear

conjugate gradient descent toolbox [105] was modified from its initial form and used in the iterative reconstruction. A sampling pattern suitable for CS is one of the key ingredients in a successful recovery. Therefore, the k-space data were randomly undersampled along the phase-encoding direction with denser sampling near the k-space center than near the higher frequency periphery.

To investigate the reconstruction performance over different reduction factors, we compared the practicability of applying SPECS on the CS-MRI. Fig.(5.5) and Fig.(5.6) compare the reconstruction outcomes of CS, PECS, and the proposed SPECS reconstruction algorithms. In each subfigure within the figures the top left section of the image is expanded to allow closer inspection of the quality. The NMSE value (cf. Eq.(5.8)) is listed in the caption for each subfigure/reconstruction method.

In Fig.(5.5) the k-space dataset was undersampled at an acceleration factor of 2, in other words just 50% of the full set of k-space samples were retained. Fig.(5.5a) depicts the reconstructed image from the k-space data, with all missing data points replaced by zero values and after a straightforward inverse DFT. A conventional CS reconstruction is shown in Fig.(5.5b). It can be seen to generate a reconstruction with significant loss of image contrast and details, which is due to the lack of frequency components. The PECS reconstruction, incorporating a prior image approximation (a low resolution image) to derive a data ordering, is shown in Fig.(5.5c). Finally, the same direct reconstruction as shown in Fig.(5.5a) is decomposed by SVD for the first phase of the new SPECS algorithm. As seen Fig.(5.5d), the final reconstruction by the SPECS method achieved a noticeably superior outcome with a significantly lower NMSE than the other methods, yet it did not require any prior estimate.

In Fig.(5.6) the comparison was performed applying a significantly higher value of acceleration (acceleration factor = 5, or only 20% of the data acquired) on the same dataset. In general, it is seen that even after applying such a high degree of under-sampling, the proposed SPECS method achieves improved results compared with the other methods.

5.10 Discussion

Compressed sensing (CS) is a relatively new approach for the acquisition and recovery of incomplete information which exploits the inherent sparsity (explicit and implicit) of the underlying signal. The potential for incorporating image prior knowledge into CS recovery at high acceleration factors has been exploited here. In PECS, a method for incorporating prior estimation of the underlying image in the reconstruction was introduced. Instead of

recovering the transform of the image itself, the transform of a sorted image (based on the sorting required to place the pixels of a reference image in monotonic magnitude order) was recovered.

In the new method introduced here, SPECS, an alternative approach to capture the underlying information needed for optimal reordering was employed: an adaptive, data-driven sparsifying transform was employed in CS algorithm to achieve an initial, relatively poor reconstruction, $\mathbf{x}_1$. SVD was chosen as the transform, since other studies suggested that it can reveal more underlying structure of the image than the other more commonly employed transforms. Moreover, the SVD-based transform generates sparse coefficients and exhibits better sparsity than non adaptive transforms like DWT or DCT. Using $\mathbf{x}_1$ to derive an approximate data ordering, R'_1, makes the ordering process independent of prior image knowledge. The final reconstruction is performed as for PECS, exploiting the significant increase in sparsity the ordering process provides. The preliminary results presented in Fig.(5.5) and Fig.(5.6) presented that the recovered images after incorporating the obtained reordering in the second CS recovery, outperforms the PECS initial results. However SPECS requires no prior information about the image to be recovered, the only trade-off of this method is the slightly increased computational complexity compared to only using each method alone.

In contrast with the promising results achieved for compressed sensing in MRI, there is difficulty in combining the requirements for a regular sampling pattern to exploit sensitivity encoding across the array of coil signals [145] with the requirements for a random sampling pattern suited to CS [105]. Recent findings [127] have emphasized this difficulty. We argue that the data ordering step which has been incorporated into PECS and SPECS helps overcome this restriction.

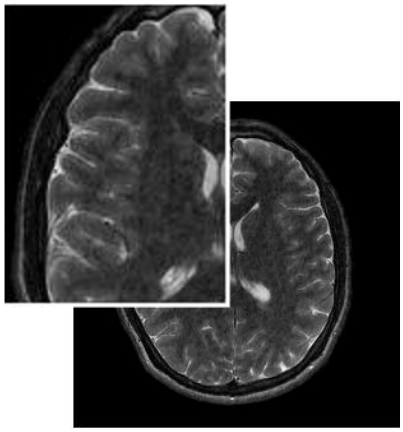

(a) Zero-filled reconstructed image

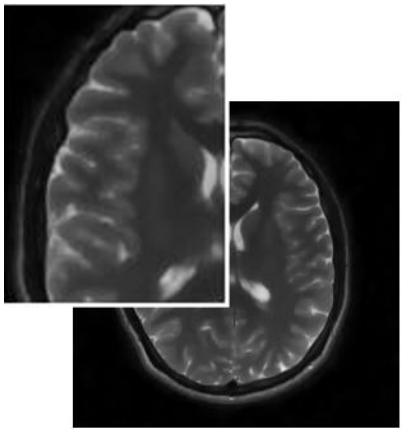

(b) CS

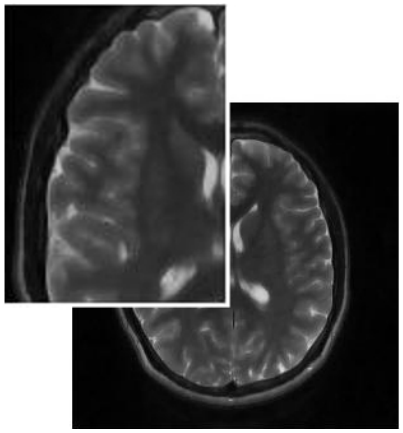

(c) PECS

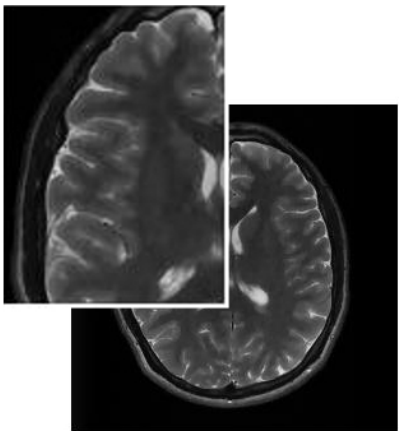

(d) SPECS

Figure 5.5: Reconstructed images from the undersampled k-space dataset for an acceleration factor AF = 2: (a) image reconstructed with zero-filled k-space; (b) reconstructed by the conventional CS method using the DCT as the sparsifying transform, NMSE = 0.1298; (c) reconstructed image by the PECS method using a low resolution image to derive the sorting order, NMSE = 0.1320; and (d) reconstructed image by the new SPECS method, NMSE = 0.0877.

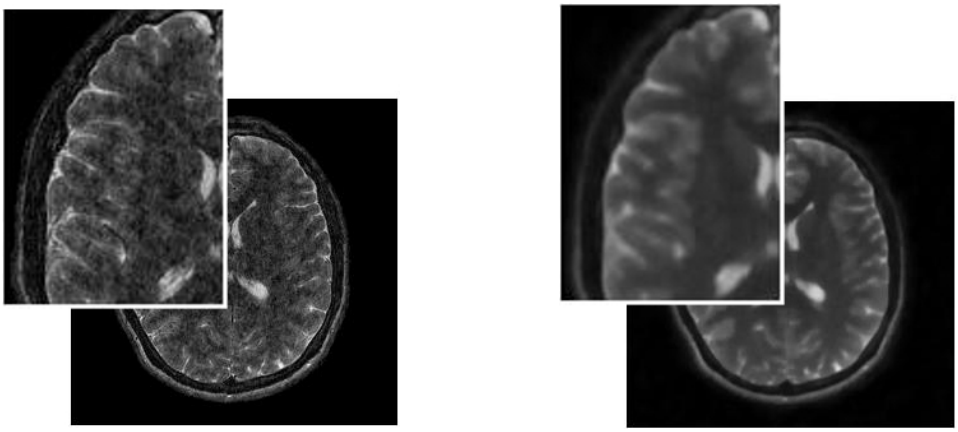

(a) Zero-filled reconstructed image **(b)** CS

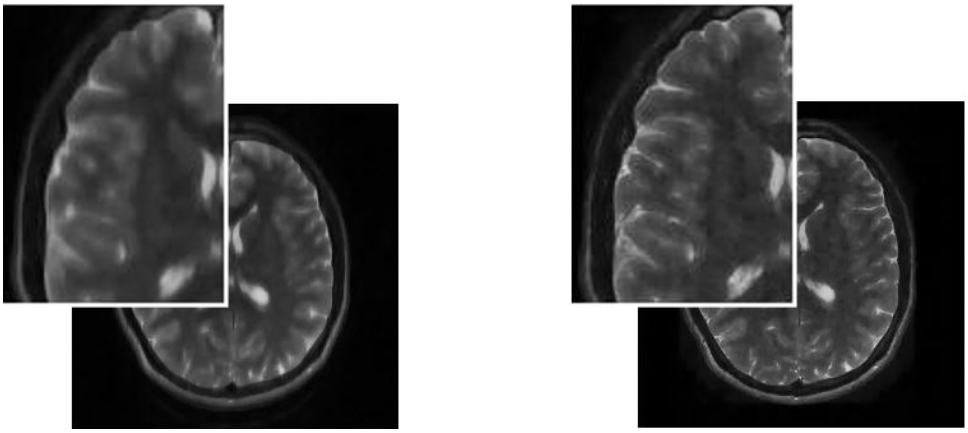

(c) PECS **(d)** SPECS

Figure 5.6: Reconstructed images from the undersampled k-space dataset for an acceleration factor AF = 5: (a) image reconstructed with zero-filled k-space; (b) reconstructed by the conventional CS method using the DCT as the sparsifying transform, NMSE = 0.1862; (c) reconstructed image by the PECS method using a low resolution image to derive the sorting order, NMSE = 0.1751; and (d) reconstructed image by the new SPECS method, NMSE = 0.1352.

Chapter 6

Compressed sensing in dynamic MRI

6.1 Motivations

Dynamic magnetic resonance imaging is an increasingly popular clinical method used to monitor spatio-temporal changes in the tissue structure. A sequence of time frames of 2/3D MR images exhibit motion or signal changes over time in an organ. The most important role of dynamic MRI is to examine motion in the heart, the lung and brain function, via perfusion imaging.

Physiological, physical and technological constraints are the main challenges in a fast data acquisition. Recent experiments proved that exploring and developing sparsity based methods leads to the improved recovered image quality in MRA. The compressed sensing technique, which aims to reconstruct high quality signals from undersampled acquisitions, can be considered a natural fit to enhance dynamic magnetic resonance imaging applications and address the trade off between spatial resolution and temporal resolution.

In this chapter, we focus on two CS techniques in CE-MRA and develop different frameworks to make accurate reconstructions from a small subset of k-space samples. The organization of this chapter is given as the following. Firstly, we describe the conventional CS methods, focusing on the two main sparsifying paths and one of the most well-known algorithms K-SVD dictionary learning. Next, we present a novel approach for training a spatio-temporal dictionary for CE-MRA using K-SVD for constructing effective dictionaries for image series. The experimental results demonstrate improved reconstructions on clinical undersampled dynamic images. To cover the second proposed approach, a brief overview of topics related to CS technique in MRA recovery and group sparse modeling is given, aiming to exploit the structure of the MR images in sparse representation. We then propose a reconstruction

method that exploits the sparse representation structure and sparsity within dynamic MR images. Our method is an extension of the PECS that allows a prior knowledge of the underlying image to be incorporated in the CS recovery. The sparse representation of prior estimate is incorporated in the reconstruction process by assigning the pixels of sparsity domain to groups. Finally, the method implementation in time-resolved CE-MRA are presented. The performance and characteristics are investigated using volunteer study.

6.2 Compressed sensing methods in CE-MRA

Dynamic Contrast Enhanced MRI (DCE-MRI) is a minimally-invasive imaging technique widely used for clinical tasks such as assessment of different vascular malformations or vascular surgery planning. To carry out such tasks with diagnostic certainty in applications like cardiac imaging or brain hemodynamics, image sequences with simultaneously high spatial and temporal resolution are demanded. Although normally the reduction of the data acquisition time in the conventional acquisition methods and reconstruction strategies sacrifices the spatial resolution. Consequently, techniques like parallel MRI [15], novel undersampling and view-ordering methodologies [124]or constrained reconstruction models [184] were introduced to accelerate dynamic MRI scanning. Low SNR and the presence of aliasing artifacts at high reduction factors are the main ill-effects in the classical parallel imaging approaches like SMASH [168], GRAPPA [70] or temporal filtering (UNFOLD) [108]. As such, it may be beneficial to consider auxiliary use of some more advanced reconstruction routines that are less subject to these limitations to avoid potential complications in improved diagnosis.

Recently, CS reconstruction approaches based on the a priori assumption that images are sparse or compressible (either intrinsically or following mathematical transformation) have been proposed to address aliasing artifacts and low spatiotemporal resolution in dynamic MRI. Strategies include Cartesian/Radial K-t FOCUSS [86, 85], joint sparsity of the multicoil images in x-y-f space [134], Motion-Adaptive Spatio-Temporal Regularization (MASTeR) [7] and k-t Group sparse [188]. With the potential to advance signal estimation, recent work has begun the important task of incorporating sparsity priors into dynamic signal estimation [164, 211]. A number of different dynamic MRI reconstruction and the emerging CS techniques apply temporal and spatial constraints such as prior information to compensate for the information loss from reduced sampling. Liang and Ying [98] showed that the temporal-frequency (y-f) support information is known a priori based on the fact that the non-periodic motion is slowly varying. As a consequence the low temporal-frequency region is included in the support of the y-f domain. The signal at the known

support is then excluded from the cost function. Then during the minimization process the signal located at the defined support will be excluded from the cost function. In their work, though for single coil case, the motion pattern of dynamic MR images was used to extract the support knowledge. The technique outcomes showed fewer artifacts, while preserving more details than the conventional CS. Later an iterative procedure for alternating between image reconstruction and support detection in x-f space was demonstrated by the same authors [98]. In each iteration, the support information was updated and parts of the signal at the known support was excluded from the cost function in the constrained minimization process. Experimental results showed learning and exploiting the support knowledge in x-f space improves the reconstruction quality. To implement the diverse temporal/spatial constraints in reconstructions of DCE-MRI data different tools have been applied to the constrained reconstruction like the l_1 norm regularization [7]or Projection onto Convex Sets (POCS) formalism with a gradient descent [37]. Another form of allowing prior knowledge of the underlying image to be intrinsically incorporated in the image recovery process was investigated in [207]. Prior estimate-based compressed sensing (PECS) was an extension of the use of data sorting as suggested by Adluru and DiBella [1]. A prior image estimate was employed to enhance the sparsity level of the image to be recovered. Spatial structure as prior information was incorporated in the CS recovery of two-dimensional cardiac cine MRI in [188]. The required information about the support region was estimated from the x-f space of the training data and used to define the group structure within. Their proposed method exploited the structure within the sparse representation of a signal by enforcing the support components to be in the form of groups. This group assignment improved signal recovery by the group sparse formulation. Another version of using spatial structure constraint was addressed in [6] to improve reconstruction of 2/3D hyperpolarized He lung MR images. In the following sections, the development and implementations of two techniques in contrast enhanced magnetic resonance angiography (CE-MRA) are presented and discussed. Dictionary learning and group sparsity as two advanced techniques in CS have been used to reduce the amount of measured data while preserving the quality of the image sequence. Firstly, a brief overview of the CS methods, followed by the discussion of reconstruction methods in MRA. Then their implementations in time-resolved CE-MRA are presented and their performances are investigated using volunteer studies.

6.2.1 Dictionary learning in CS

What we have focused on so far is that the success of sparsity-based models is critically dependent on the careful design of the sparsifying transforms. The construction of sparsifying transforms leads to the concept of a "dictionary" [117, 36, 39, 160], which is a name given

to the set of vectors, or atoms, describing the sparsifying operator. Mallat and Zhang in 1993 [117] introduced an algorithm (named matching pursuit), that decomposed a signal into a linear expansion of waveforms which were chosen from a redundant dictionary of functions. Since matching pursuit does not limit the choice of dictionaries, it provides an extremely flexible signal representation. This influential movement of transforms to dictionaries for sparse signal representation was followed up then by Chen, Donoho and Saunders [36].

Having a meaningful representation of a signal, $\mathbf{x} \in \Re^N$, involves the choice of a dictionary. A dictionary is defined as a matrix, $\mathbf{\Psi}$ consisting of a set of elementary signals or atoms in its columns, $\mathbf{\Psi} = [\mathbf{a}_1 \mathbf{a}_2 \dots \mathbf{a}_L] \in \Re^{N \times L}$ or its rows, $\mathbf{\Omega} = [\mathbf{a}_1 \mathbf{a}_2 \dots \mathbf{a}_L]^T \in \Re^{L \times N}$. When the dictionary forms a basis, it is called a complete dictionary and every signal can be represented uniquely as a linear combination of the dictionary atoms $\mathbf{x} = \mathbf{\Psi}\gamma$. In the bi-orthogonal dictionary ($L = N$) case, the linear coefficients of the representation can be achieved from $\gamma(\mathbf{x}) = \mathbf{\Omega}^{-1}\mathbf{x}, (\mathbf{\Omega} = \mathbf{\Psi}^{-1})$, the inner products of $\mathbf{x}$ and the atoms of $\mathbf{\Omega}$. To exemplify, Fourier and DCT transforms are the most well-known and simple complete transforms, suitable to sparsify uniformly smooth signals, while the wavelet transform sparsifies piecewise-smooth 1-D signals with a finite number of discontinuities. It has been shown that these dictionaries are not well equipped for representing complex and high-dimensional natural signals [160]. Due to a strict limitation on the number of atoms in the invertible dictionaries ($N = L$), their ability to represent diverse signal behavior is limited. To overcome this drawback some more general overcomplete dictionary constructions (containing L prototype signal-atoms and having more atoms than the dimension of the signal ($L \geq N$) were suggested which are more descriptive.More often than not, sparsity is expressed not in terms of an orthonormal basis but in terms of an overcomplete dictionary, since the signal of interest is not sparse in an orthonormal complete basis. Overcomplete dictionaries like curvelets [30], complex wavelets [165], contourlets [50], surfacelets [103], as well as trained dictionaries [96, 92, 160, 133] are especially advantageous for multi-dimensional signal data, where invertible dictionaries are less effective and desirable. In fact, the two equivalent views of the transform in the invertible dictionaries are associated with two distinct representation paths in the overcomplete dictionaries. Using an overcomplete dictionary, $\mathbf{\Psi} \in \Re^{(N \times L)}$ $L \geq N$, any signal can be represented via its inner products with the atoms from the dictionary (analysis method): $\gamma_a = \mathbf{\Omega}\mathbf{x}$, or as a linear combination of atoms (synthesis method): $\mathbf{x} = \mathbf{\Psi}\gamma_s$. It is worth mentioning that by allowing $L \geq N$, dualities $\mathbf{x} = \mathbf{\Psi}\gamma_s \Leftrightarrow \gamma_a = \mathbf{\Omega}\mathbf{x}$ no longer hold. In synthesis case, due to infinite number of representation solutions, when $\mathbf{\Psi}$ is a full rank matrix, a constraint needs to be set. For us the sparsest possible representation (having the fewest number of nonzero coefficients)

is favorable, thus:

$$\gamma_s = \arg\min_{\gamma} C(\gamma) \quad Subject \quad To \quad \mathbf{x} = \mathbf{\Psi}\gamma \tag{6.1}$$

where $C(\gamma)$ is a penalty function which promotes the sparsity of the representation, such as l_p cost functions with $0 \leq p \leq 1$. For example in l_0 case, $C(\gamma) = \|\gamma\|_0$, is the number of the nonzero entries in the representation. Note, in the synthesis case, the vector $\gamma_{syn} \in \Re^L$, may either be exact $\mathbf{x} = \mathbf{\Psi}\gamma_{syn}$, or approximate $\|\mathbf{x} - \mathbf{\Psi}\gamma_{syn}\|_p \leq \epsilon$ [4]. For the l_0 case, equation (6.1) presents a combinatorial form for sparse coding problems, as:

$$\gamma_s = \arg\min_{\gamma} \|\gamma\|_0 \quad Subject \quad To \quad \mathbf{x} = \mathbf{\Psi}\gamma \tag{6.2}$$

Clearly equation (6.2) promotes the sparsity of the representation, meaning that the sorted coefficients in γ needs to decay rapidly. These equations are known as NP-hard problems and over the few past years, a wide array of algorithms have been extensively investigated to find approximate solutions for it. Methods such as greedy pursuits [46, 128], convex relaxation [39, 53] and iterative shrinkage [44, 58] are some of the efficient optimization strategies for this kind of problems.

The other convenient choice for $C(\gamma)$ is the l_1 norm when $C(\gamma) = \|\gamma\|_1$. This option provides a powerful combination of robustness and convexity which is considered a stable and practical approximation of the $l_0$choice. Now the problem is given as:

$$\gamma_s = \arg\min_{\gamma} \|\gamma\|_1 \quad Subject \quad To \quad \mathbf{x} = \mathbf{\Psi}\gamma, \tag{6.3}$$

This formulation is categorized as a convex Linear Programming (LP) problem and a variety of solvers are available such as Basis Pursuit (BP) [39]. It is worth reminding that the preliminary assumption in all the methods is that the dictionary is known and fixed.

6.2.1.1 Analysis vs synthesis in inverse problem solutions

Dictionary-based signal models yield efficient regularizers for inverse problem solution. A standard inverse problem for the recovery of an unknown signal $\mathbf{x}$ from a specific subset(or family) of signals $\Delta \subset \Re^N$ which describes the acquisition process based on indirect

measurements of it, is as follows:

$$\mathbf{y} = \mathbf{T}\mathbf{x} + \mathbf{v}, \tag{6.4}$$

where indirect measurements are given in the vector $\mathbf{y} \in \Re^M$, $\mathbf{T} : \Re^N \rightarrow \Re^M$ is a (possibly nonlinear) known transform, $\mathbf{v} \in \Re^M$ is an additive system noise which is assumed to be Gaussian. In general, main task for many problems in signal processing like denoising, interpolation and image reconstruction is an inversion of the operator $\mathbf{T}$ [58], thus:

$$\mathbf{x} = \arg\min_{\acute{\mathbf{x}}} \frac{1}{2}\|\mathbf{y} - \mathbf{T}\acute{\mathbf{x}}\|_2 + \lambda R(\acute{\mathbf{x}}), \tag{6.5}$$

where $R(\mathbf{x})$ is a penalty function which assigns smaller penalties to signals more likely to belong to Δ and $\lambda > 0$ is a regularization parameter balancing the relative weight given to the fidelity-to-data and the penalty terms. $R(\mathbf{x})$ can be derived from a sparsifying transform $\mathbf{x} \rightarrow \gamma(x)$ via a sparsity measure $C(\gamma(\mathbf{x}))$:

$$R(\mathbf{x}) = C(\gamma(\mathbf{x})), \tag{6.6}$$

when $C(\mathbf{x})$ can be a norm like l_2 norm.
Concentrating on the maximum a posteriori probability (MAP) estimators, there are two popular MAP-based methods for inverse problem regularization: analysis-based and synthesis-based priors [58]. Analysis-based approach assigns probability to the signal through different forward measurements of it. So the analysis-based recovery process is:

$$\mathbf{x} = \arg\min_{\acute{x}} \frac{1}{2}\|\mathbf{y} - \mathbf{T}\left\{\acute{\mathbf{x}}\right\}\|_2 + \lambda C(\mathbf{\Omega}\acute{\mathbf{x}}), \tag{6.7}$$

Similar to the representation in equation(6.1), common choice for penalty functions $C(.)$ includes the l_p norm. The analysis approach has been applied in a variety of image processing tasks, such as denoising [56], image reconstruction [20] and compressed sensing [97]. For the synthesis-based approach, the signal is reconstructed as a combination of atom signals:

$$\mathbf{x} = \mathbf{\Psi}.\arg\min_{\gamma_s} \frac{1}{2}\|\mathbf{y} - \mathbf{T}\left\{\mathbf{\Psi}\gamma_s\right\}\|_2 + \lambda C(\gamma_s), \tag{6.8}$$

The synthesis formulation has been used in a wide range of inverse problems, including video denoising [144], tomography reconstruction [167] and image denoising [162]. Also synthesis-based methods have been employed in the modern dictionaries development for sparse image

representation, such as the ridgelet, curvelet, contourlet dictionaries [31, 50]and sparsity-based signal recovery [181]. Synthesis-based methods are receiving ever-increasing attention over the past decade and and stem in a large part from the basis pursuit method [39]. Comparing the analysis and synthesis recovery formulations in Eq.(6.7)and (6.8) reveals that they describe very similar structures. The major distinction between the two processes is in their representation way to sparsify the signal. The representation might be the forward projection of the signal on the basis elements, or the signal can be reconstructed from a linear combination of building-block atoms. The successful attempt to describe natural images as sparse combinations of atomic elements (synthesis approach) in number of studies [132] has shown the weakness in the analysis-based approach. The concept also has clear advantages in applications such as image compression, feature extraction and others. Moreover, in contrast to the analysis approach, the synthesis approach has a constructive form which provides an explicit description of the signals representation and consequently makes it more intuitive to interpret and design. At the same time, however, in the synthesis approach only a small number of atoms are used to represent each signal and this compactness rises the significance of every atom enormously. For instance in a denoising case, any wrong choice could potentially lead to additional atoms selection as compensation and deviating further from the desired description.

6.2.1.2 Sparse K-SVD dictionary learning

To have sparse and redundant representation of dataset, an ability to describe natural signals as linear combinations of a few atoms from a pre-specified dictionary is required. As such, the choice of a proper dictionary that sparsifies the signals is important to the signal recovery. Leading adaptive dictionary methods, including K-SVD, learn a set of atoms(dictionary) representing the data using sparse coding. K-SVD [161] is a powerful iterative algorithm for training sparse dictionaries to decompose the signal into dictionary atoms. K-SVD dictionary atoms are illustrated sparsely over a recognized implicit base dictionary. This dictionary has offered superior performance in image compression, 3-D computed tomography (CT) denoising and inpainting.

Two main routes to design overcomplete dictionaries for signal modeling have been developed so far: analytic and training routes. In the analytic approach signal data can be modeled by a simpler classes of mathematical functions, and then an efficient representation around simplified classes can be designed. The dictionaries of this sort are characterized by an analytic formulation, and derived from a set of mathematical assumptions made on the signal of interest family. The resulting dictionaries features fast implicit implementation but only could be as successful as their underlying models. Indeed an important disadvantage

of this approach is that the complexity of natural signals can not be modeled by these dictionaries due to their trend to be over-simplistic. The lack of adaptivity in this technique is caused by their fixed structure with quick mathematical realization. Examples of analytic dictionaries include curvelets [30], contourlets [50], Bandelets [140] or many other analytic transforms such as complex wavelet transform [165], to name just a few. The analysis approach for dictionary-based signal models has been employed in a variety of image processing tasks, including denoising [159], tomography reconstruction [20] and compressed sensing [97].

In the second approach, trained dictionaries, machine-learning techniques have been applied with a primary assumption that the structure of complex natural signal can be more accurately extracted directly from the data rather than using a mathematical description. Based on the observed signal properties, trained dictionaries replace prior assumptions on the signal behavior with a training process which constructs the dictionary. A more accurate adaptation of characteristic signal features become possible while a relatively slow implementation is the cost. Dictionary training methods address l_0 and l_1 sparsity measures, which allows the use of recently developed efficient sparse-coding techniques. The main improvement of learning (training) dictionaries is their ability to provide a higher degree of specificity to characterize the particular signal, leading to generate better results in many practical applications. Algorithms of this type include the Method of Optimal Directions [160] and the K-SVD [4].

Recently, several dictionary structures have been developed which combine the two approaches, benefiting from both the analytic and machine-learning design paradigms such as the hybrid wavelet/K-SVD dictionary [133], and the sparse dictionary [160]. As stated before, the basic model for sparse representation suggests that natural signals can be efficiently approximated as a linear combination of prespecified atom signals and the sparse linear coefficients. The process of computing the representation coefficients based on the given signal and the dictionary is so called sparse coding. The overcomplete dictionary $\mathbf{\Psi}$ that leads to sparse representations, can either be selected as a prespecified set of functions or designed by adapting its atoms to fit a given set of training signals. Aharon, Elad and Bruckstein [4] introduced and developed the l_0 analysis K-SVD algorithm for training an overcomplete dictionary. To design dictionaries based on learning, the K-SVD algorithm addressed the sparse representation task with generalizing the K-means algorithm. Very much in line with the two-step process in K-means algorithm, the algorithm is an iterative method that alternates between sparse coding of the training data based on the current dictionary (finding the coefficients) and an update stage for the dictionary atoms (assuming known and fixed coefficients) so as to better fit the training data. The algorithm's aim is

to solve the following general sparsification problem. Given a set of examples arranged as the columns of the matrix $\mathbf{X} = [\mathbf{x}_1 \mathbf{x}_2 \dots \mathbf{x}_n]$, the goal is to find a dictionary $\mathbf{\Psi} \in \Re^{N \times K}$ containing prototype signal-atoms for columns, $\{\psi_j\}_{j=1}^{K}$, to minimize the representation error,

$$\arg\min_{\Psi,\Gamma} \ \|\mathbf{X} - \mathbf{\Psi\Gamma}\|_2 \quad Subject\ To \quad \|\gamma_i\|_0 \leq T \ \ \forall i, \tag{6.9}$$

where $\mathbf{\Gamma}$ represents a sparse matrix and $\{\gamma_i\}$ are its columns. The algorithm name was taken from Singular-Value-Decomposition (SVD) process which makes the core of the atom update step, and the dictionary update stage is repeated for K times (the number of atoms). In K-SVD algorithm dictionary is updated atom by atom and simultaneously its associated sparse coefficients. Thus for a given atom K, the problem is written as:

$$\|\mathbf{x} - \sum_{j \neq k} \psi_j \gamma_j^T - \psi_k \gamma_k^T\|_2 = \|\mathbf{E}_k - \psi_k \gamma_k^T\|_2 \ , \tag{6.10}$$

where $\left\{\gamma_j^T\right\}$ are the rows of $\mathbf{\Gamma}$ and $\mathbf{E}_k$ represents the residual matrix. To obtain the updated atoms this equation needs to be minimized for ψ_k and γ_j^T.
In their work they showed that their proposed K-SVD dictionary outperforms other alternatives such as unitary DCT for both synthetic and real images in applications such as in-painting (interpolation of lost pixels) and compression. Observing the trained dictionary obtained from this algorithm clearly indicated that the resulting dictionary was structured, with noticeably regular atoms. This gives rise to the idea that the underlying structure of the dictionary atoms can be represented sparsely over a more fundamental dictionary.

A sparse dictionary, as the most recent contributions to the field of parametric dictionaries, is based on a sparsity model of the dictionary atoms over a base known dictionary, and takes the form $\mathbf{\Psi} = \mathbf{\Phi A}$ where $\mathbf{\Phi}$ is stands for a fixed analytic dictionary and A is a sparse matrix that can be adapted to the signal. A form of Sparse dictionary was compactly extended in [160] that had a fast implementation. Their proposed sparse dictionary structure was a merging form of trained and analytic dictionaries, benefiting from the advantages of the both methods. They based their algorithm on the fact that atoms in trained K-SVD dictionary $\mathbf{\Psi}$, have their sparse representation over some pre-specified base dictionary $\mathbf{\Phi}$. They attempted to balance between complexity and adaptability of the dictionary by developing a K-SVD-like learning scheme to train the sparse dictionary from a set of examples [161].

Basically sparse dictionary model suggests that any complex signal can be presented

approximately as a linear combination of pre-specified atom signals, where the linear coefficients are sparse (most of the entries are zero). The adaptability of the dictionary is provided via modification of the matrix $\mathbf{A}$, while the dictionary is efficiently trained from signal examples. Analytic dictionary computation is generally fast so the sparse dictionary has a fast implementation, whereas the matrix $\mathbf{A}$ provides signal adaptivity. This method has been shown to reduce the training set size, and as a consequence, learning a larger dictionary for large image patches, or even 3-D signal patches, is possible. The general form of a sparse approximation problem for a signal $\mathbf{x} \in \Re^N$, and a dictionary $\mathbf{\Psi} \in \Re^{N \times L}$ is as follows:

$$\widehat{\gamma} = \arg\min_{\gamma} \|\gamma\|_0 \quad Subject\ To \quad \|\mathbf{x} - \mathbf{\Psi}\gamma\|_2 \leq \epsilon, \tag{6.11}$$

where in the above expression, the atom signals are arranged as the columns of $\mathbf{\Psi}$, γ is the sparse representation of $\mathbf{x}$ and ϵ represents the acceptable error tolerance. Note that the choice of the dictionary $\mathbf{\Psi}$ is a fundamental consideration in the above model.

The idea of modeling signal and training dictionary over a wavelet transform was developed in [129]. In the Rubinstein contribution [161], an efficient and flexible sparse K-SVD dictionary structure for sparse and redundant signal representation was proposed. The same basic scheme as the original K-SVD algorithm was used to train a sparse dictionary. The algorithm goal is set to improve the dictionary iteratively by solving the optimization problem approximately:

$$\arg\min_{A,\Gamma} \|\mathbf{X} - \mathbf{\Phi A \Gamma}\|_F \qquad Subject\ \ To \qquad \begin{cases} \forall i \quad \|\gamma_i\|_0 \leq \epsilon \\ \forall j \quad \|\mathbf{a}_j\|_0 \leq p \quad , \quad \|\mathbf{\Phi a}_j\|_2 = 1 \end{cases} \tag{6.12}$$

where $\|.\|_F$ stands for the Frobenius norm, $\|A\|_F$ is defined as the square root of the matrix trace of $AA^{(H)}$ [160]. Note that p is the atom normalization constraint which is commonly added for convenience, though it does not have any practical significance to the results [161]. The notable difference between their method and the original K-SVD is a new constrained atom; $\mathbf{\Psi} = \mathbf{\Phi A}$. Therefore each modified atom needs to be updated as:

$$\{\mathbf{a}, \mathbf{g}\} = \arg\min_{a,g} \|\mathbf{E} - \mathbf{\Phi a g}^T\|_F \quad Subject\ \ To \quad \|\mathbf{a}\|_0 \leq p \quad , \quad \|\mathbf{\Phi a}\|_2 = 1 \tag{6.13}$$

$$\mathbf{E} = \mathbf{X}_I - \sum_{i \neq j} \psi_i \mathbf{\Gamma}_{i,I}$$

where $\mathbf{E}$, ψ and $\mathbf{g}^T$ are the error matrix without the j^{th} atom, updated atom and new coefficient row, respectively. The problem can be solved directly via an SVD decomposition. In practice, the exact solution needs heavy computations, as the size of $\mathbf{E}$ is directly proportional to the number of training signals. Indeed, an exact solver is not usually

required. The optimizing problem was simplified to two simpler sparse-coding problems, namely:

$$\mathbf{a} = \arg\min_{\mathbf{a},\mathbf{g}} \|\mathbf{E}\mathbf{g} - \mathbf{\Phi}\mathbf{a}\|_2 \quad Subject\ To \quad \|\mathbf{a}\|_0 \leq p \tag{6.14}$$

$$\mathbf{g} = \mathbf{E}^T\mathbf{\Phi}\mathbf{a}/\|\mathbf{\Phi}\mathbf{a}\|_2$$

where all arguments used in the above equation(6.14) are easier to compute than ones in equation(6.13).

To briefly explain the sparse K-SVD algorithm [160]; The signal set $\mathbf{x}$, base dictionary $\mathbf{\Phi}$, initial dictionary representation $\mathbf{A}_0$, target atom sparsity p, signal sparsity t and number of iterations K need to be initialized. Assume $\mathbf{A} = \mathbf{A}_0$. To determine the outputs; sparse dictionary representation $\mathbf{A}$ and sparse signal representations Γ such that $\mathbf{X} \approx \mathbf{\Phi}\mathbf{A}\mathbf{\Gamma}$ formulated in the optimization problem (6.12), the algorithm aims to iteratively improve the dictionary to achieve sparser representations of the signal $\mathbf{X}$. Signal representation (sparse-coding) formalized in the:

$$\forall i \ : \ \mathbf{\Gamma}_i = \arg\min_{\gamma} \|\mathbf{x}_i - \mathbf{\Phi}\mathbf{A}\gamma\|_2 \quad Subject\ To \quad \|\gamma\|_0 \leq \epsilon$$

needs to be updated K times. Every time signal representation updated, dictionary atoms go through updating process as well via using equation(6.14). Clearly, the optimization problem alternates between sparse-coding and dictionary update steps for a fixed number of iterations. It was shown that Sparse K-SVD is much faster than the standard and approximate K-SVD methods [161].

We have witnessed a significant advancement in the dictionary design over the past decades, beginning with simple orthogonal transforms and leading to the complex overcomplete analytic and learning dictionaries. The novel structure of sparse K-SVD sictionaries provide both adaptivity and efficiency. Its compact form makes it to be used for tasks such as compression, communication, denoising and real-time systems. Pre-specified transform matrix like overcomplete wavelets, curvelets, contourlets or short-time-Fourier transforms lead to simple and fast algorithms for the sparse representation evaluation. Also, the success of such dictionaries in applications depends on how suitable they are to sparsely describe the signals in question. In dynamic images compression, separation of texture and cartoon content in images [173, 174], inpainting [59] and denoising [4] the concept of sparsity and over-completeness have been shown to be effective.

6.2.1.3 Sparse K-SVD Dictionary Learning for MRI

The recent progress in dictionary learning promises recovering images accurately using fewer measurements than the number of unknown with high reconstruction quality. Specifically adaptive dictionaries have shown the hope of image patch-based sparsifying dictionaries in a variety of applications such as image denoising, inpainting, and demosaicing [111]. In 2010 Chen and Yen trained a patch-based dictionary using prior information in reference images [40]. The proposed variational model enforced the sparsity of the underlying image in terms of its spatial finite differences with respect to a dictionary. The experimental results showed improvement on the accuracy of reconstruction, however it was small (SNR increased by about 1.6 dB compared to wavelets transform).

In another work Ravishankar and Bresler [152] proposed employing an adaptively learning dictionary (K-SVD), and reconstructing the MRI images simultaneously from highly undersampled k-space data. In their work they assumed $\mathbf{y} \in C^m$ be the K-space measurements, the vector $\mathbf{x} \in C^P$ represents the 2D complex image which needs to be reconstructed. $\mathbf{F}_u \in C^{m \times p}$ is the undersampled Fourier encoding matrix while in the absence of noise, we have $\mathbf{F}_u \mathbf{x} = \mathbf{y}$. In image processing, the image could be decomposed into many (possibly overlapping) image patches, with each patch undergoing sparse-coding optimization. Here the image $\mathbf{x}$ was divided into $x_{i,j} \in C^n$ patches of size $\sqrt{n} \times \sqrt{n}$ pixels, indexed by (i, j) from the top left corner. In their algorithm the optimization problem was defined as follow:

$$\underset{x,\Psi,A}{\arg\min} \quad \sum_{i,j} \|\mathbf{R}_{i,j}\mathbf{x} - \mathbf{\Psi}\alpha_{i,j}\|_2 + \upsilon\|\mathbf{F}_u\mathbf{x} - \mathbf{y}\|_2 \quad s.t. \quad \|\alpha_{i,j}\|_0 \leq T_0 \ \ \forall\, i, j \tag{6.15}$$

where matrix $\mathbf{R}_{i,j} \in \{0, 1\}^{n \times p}$ extracts the patch $x_{i,j}$ from $\mathbf{x}$, $x_{i,j} = \mathbf{R}_{i,j}\mathbf{x}$. The overlapped patches were employed to create an additional averaging effect that removes noise. Clearly, the first term in the cost function ensures the quality of the sparse approximations of the image patches with respect to the dictionary $\mathbf{\Psi}$ while the second term captures the data fidelity in k-space. To make the optimization problem more robust to changes in noise level the weight υ is selected as a function of the noise level measurement σ as $\upsilon = \lambda/\sigma$ [152]. In the noiseless case the formulation could be simpler by dropping the data fidelity term from the cost and considering it as a constraint $\mathbf{F}_u\mathbf{x} = \mathbf{y}$. Also assuming l_0 or l_1 norm, the T_0 is a sparsity threshold used per patch. To avoid solving a NP-hard and non convex problem, an iterative alternating minimization procedure was proposed by involving the K-SVD dictionary learning step (explained in the former section) and a reconstruction update step. To do so, in the dictionary learning step $\mathbf{x}$ is considered as a fixed image (zero-filled Fourier reconstruction) and the dictionary and sparse representation needs to

be optimized as:

$$\underset{\Psi,A}{\arg\min} \sum_{i,j} \|\mathbf{R}_{i,j}\mathbf{x} - \mathbf{\Psi}\alpha_{i,j}\|_2 \quad S.t \quad \|\psi_k\|_2 = 1 \;\; \forall k, \quad \|\alpha_{i,j}\|_0 \leq T_0 \;\; \forall i,j \tag{6.16}$$

As explained before, the K-SVD algorithm alternates between finding the dictionary $\mathbf{\Psi}$, and the sparse representation $\mathbf{A}$. A standard Orthogonal Matching Pursuit (OMP) was employed to obtain $\mathbf{A}$ in the sparse coding step. In the dictionary update stage, each atom of the dictionary was updated jointly with the corresponding representation coefficients for the patches that currently use it. Having fixed $\mathbf{\Psi}$ and $\mathbf{A}$, the reconstruction update step could be performed as:

$$\underset{\mathbf{x}}{\arg\min} \sum_{i,j} \|\mathbf{R}_{i,j}\mathbf{x} - \mathbf{\Psi}\alpha_{i,j}\|_2 + \upsilon\|\mathbf{F}_u\mathbf{x} - \mathbf{y}\|_2 \tag{6.17}$$

The above mentioned problem is a least squares problem admitting an analytical solution. Although solving this equation directly is not favorable due to required non-trivial $P \times P$ matrix inversion. Instead a simple and accurate iterative interpolation was introduced that led to improved reconstruction error. Having optimized $\mathbf{\Psi}$ and $\mathbf{A}$, a new, updated image $\mathbf{x}$ can be reconstructed by contributing $\mathbf{x} = \mathbf{\Psi}\mathbf{A}$ which is then transformed back to the Fourier domain where it is denoted by $\mathbf{S}$. Now, the updated $\mathbf{S}$ represents a full Fourier matrix whereas $\mathbf{S}_0 = \mathbf{F}\mathbf{F}_u^H\mathbf{y}$ is the zero-filled k-space measurements. Thus:

$$\mathbf{F}_x(k_x,k_y) = \begin{cases} \mathbf{S}(k_x,k_y), & (k_x,k_y) \notin \Omega \\ \dfrac{\mathbf{S}(k_x,k_y) + \upsilon\mathbf{S}_0(k_x,k_y)}{1+\upsilon}, & (k_x,k_y) \in \Omega \end{cases} \tag{6.18}$$

where Ω represents the subset of k-space that has been sampled. The dictionary interpolated values from the equation (6.18)have been used for the non sampled Fourier frequencies while the sampled ones are filled back albeit with averaging in the presence of noise. A zero-filled Fourier reconstruction was used to the algorithm initialization. Iteratively solving equations (6.16) and (6.17) led to a better reconstruction. Using K-SVD, the algorithm provided superior reconstructions at high undersampling factors compared to CSMRI methods.

6.2.2 Proposed Dictionary Learning method in CE-MRA

Sparse representation of many fundamental signals over redundant dictionaries is a rapidly evolving field, with state of the art results in image processing [57, 112, 144]. In general,

an optimal dictionary can be chosen in two ways: (i) building a sparsifying dictionary based on a mathematical model of the data, or (ii) learning a dictionary from a training set. Adapting a dictionary for the class of the signal being reconstructed have shown a great potential in CS optimization algorithms. K-SVD as the learning algorithm have been used to train successfully Spatio-Temporal dictionaries [144, 135] in denoising of image sequences. They showed utilizing temporal dimension assisted in getting better output quality by exploring the joint coherence existed in the spatial and temporal structures. This section proposes an algorithm for learning spatiotemporal dictionaries for dynamic MR images. The details of very recent K-SVD application in 2D MRI reconstruction was explained in (6.2.1.3). Their approach iteratively alternated between adapting a dictionary using the reconstructed image from updated k-space data set and filling the undersampled k-space data set. Here we show that the image series reconstruction can be formulated as a cost function optimization problem which involves a dictionary learning step and a CS reconstruction step. In our algorithm the dictionary is adapted considering space-time coherence of the entire sequence which has been reconstructed in the previous step. The sparse and redundant representation of the image sequence was utilized for denoising and improving the recovery performance of dynamic k-space data. Experimental results validate the reconstruction efficiency of the proposed scheme in DCE MRI comparing to sliding window reconstruction.

Consider $\mathbf{y}$ as 3D K-space measurements (over a time period) and $\mathbf{x}$ as the 2D complex image which needs to be reconstructed in different time frames using sliding window technique. Sliding window reconstruction (SWR) as a technique to increase temporal resolution is illustrated in Fig. (6.1). Notice that in conventional time resolved CE MRA, the multiple acquisitions of the k-space data over the period that contrast agent is present allow a series of different time frames to be straightforwardly formed. Whereas the time intervals used in neighboring SW reconstructions overlap. This is the reason behind SWR method that offers high temporal frame rate (determined by the amount of window shift). The k-space data acquisition order proposed in SWR based on CS method is shown there. As this diagram displays a window shift of 2 data subsets offers an improvement of the temporal frame rate by a factor of 37.5 where an individual reconstruction requires 75 data subsets. However the temporal footprint, which is determined by the amount of data acquisition used for image reconstruction, is unchanged in SW reconstruction.

Let matrix $\mathbf{R}_{i,j,k}$ extracts the patch $x_{i,j,k}$ from $\mathbf{x}$, $x_{i,j,k} = \mathbf{R}_{i,j,k}\mathbf{x}$. Then $x_{i,j,k}$ is a 3D spatiotemporal patch, where the first and second dimensions are chosen in the space dimension and the third dimension is in the time frame. The spatiotemporal dictionary learning can be formulated as follow:

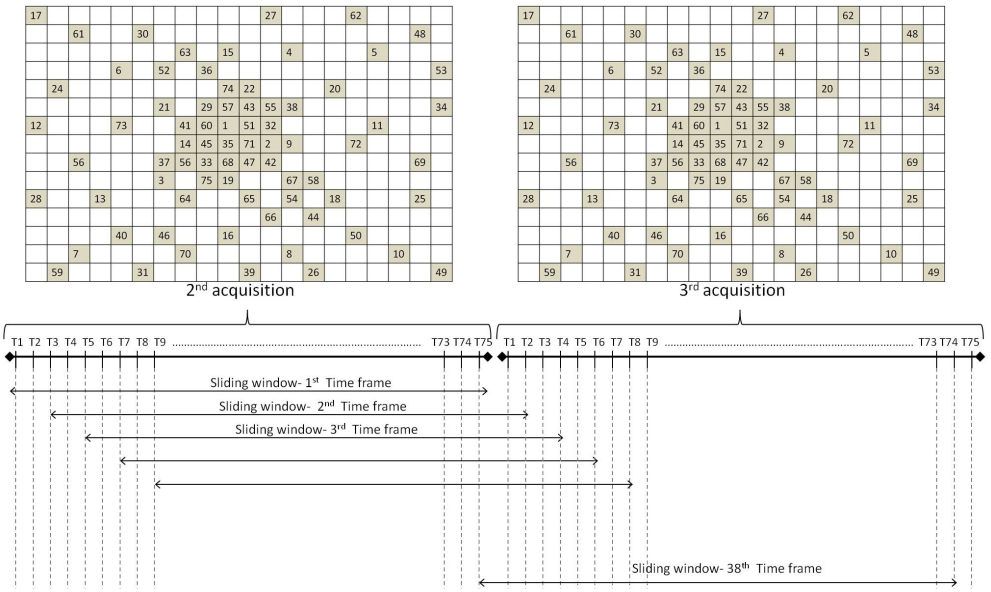

Figure 6.1: Illustration of Cartesian Sliding Window Reconstruction (SWR). The top row represents two k-space subsets that are acquired sequentially over time with an acceleration factor four (AF=4). The filled and empty pixels represent the acquired and not acquired FE lines respectively. A time-stamp (T1,T2,... T75) is specified for each FE line, which shows their priority in sampling. SWR can be performed using the consecutively acquired k-space subsets with the freedom of choosing the temporal window length and window shift. In the next row a SWR is made with a AF=4 (the same temporal window as the conventional time resolved reconstruction), the amount of window shift is 2 data subsets. As the acceleration factor goes up, the reconstructions feature a deteriorating SNR.

$$\underset{x,\Psi,A}{\arg\min} \quad \lambda\|\mathbf{\Phi x}\|_1 + \upsilon \sum_{i,j} \|\mathbf{R}_{i,j,k}\mathbf{x} - \mathbf{\Psi}\alpha_{i,j,k}\|_2 \qquad s.t. \qquad \|\mathbf{F}_u\mathbf{x} - \mathbf{y}\|_2 \leq T_1; \qquad (6.19)$$

$$\forall i,j,k \|\alpha_{i,j,k}\| \leq T_0$$

when υ *and* $\lambda \in [0,1]$. In this formulation, $\mathbf{\Phi x}$ enforces the sparsity of reconstructed image series. When υ is fixed at zero and λ at 1, the first term in the cost function enforces CS reconstruction. So, the optimization problem by dropping the dictionary learning term from the cost, can be presented as below:

$$\underset{x,\Psi,A}{\arg\min} \lambda\|\mathbf{\Phi x}\|_1 \quad s.t. \quad \|\mathbf{F}_u\mathbf{x} - \mathbf{y}\|_2 \leq T_1, \qquad (6.20)$$

Following the first image reconstruction, the K-SVD dictionary $\mathbf{\Psi}$ and its sparse represen-

tation α can be obtained then;

$$\arg\min_{\Psi,A} \sum_{i,j,k} \|\mathbf{R}_{i,j}\mathbf{x} - \mathbf{\Psi}\alpha_{i,j,k}\|_2 \quad s.t \quad \|\psi_k\|_2 = 1 \ \ \forall k, \quad \|\alpha_{i,j,k}\|_0 \leq T_0 \ \ \forall i,j,k \tag{6.21}$$

The resulted $\mathbf{\Psi}$ and α will be used to update $\mathbf{x}$. So the algorithm reconstructs the image series from the undersampled measurement $\mathbf{y}$ using a minimization procedure involving CS optimization step, a spatiotemporal dictionary learning and a reconstruction update step. Note that the sliding window reconstruction was used to produce the image series frame by frame and initialize the algorithm.

This sparsecoding algorithm along with a spatial and temporal K-SVD dictionary-learning algorithm can be summarized as follows. Firstly, a dynamic image series was obtained with a sliding window (SW) method reconstructing each frame using compressed sensing. The K-SVD dictionary treated the image sequence as a 3-D volume and is trained from undersampled frames. At this stage the algorithm perform denoising by considering 3-D (spatio-temporal) patches, a propagation of the dictionary over time, and averaging that is done on neighboring patches both in space and time. Experimental results show the images obtained from the suggested method reveal a smooth intensity change over time besides a lower level of noise which can benefit clinical diagnostic applications.

6.2.2.1 Experiments

A study was carried out in imaging the knee region of an adult volunteer. A single injection of gadolinium contrast was made to enhance the contrast in MR angiography. Cartesian sampling was employed with the phase encode (PE) samples being randomly selected according to a non-uniform sampling density peaked at the center of k-space. The following scan parameters were used in the acquisition: $TR = 4.8$ ms, $TE = 1.8$ ms and flip angle $= 45$ degree. A matrix size of $196 \times 128 \times 48$ was used to obtain a 3D volume with spatial resolution of $1 \times 1 \times 1$ mm. 20 ml of Gd-BOPTA (Multihancer) was injected as a bolus. A sampling mask was defined at acceleration factor of 4 for sample acquisitions to cover 30 sec time period. Note full sampling along frequency encoding (FE) direction allows the 3D k-space to be decomposed to its 2D multi-slice equivalent. First a data acquisition without the presence of contrast was made and that data was used to estimate the coil sensitivity profile. Also that acquisition was used to subtract from the following repetitions to eliminate the stationary background. For ease of illustration the reconstruction was performed on the individual slices to restore the entire 3D image.

Fig. (6.2) indicates Coronal plane MIP in volunteer studies reconstructed form one of

the undersampled k-space acquisitions. The dashed line in the image shows the position of the axial slice used to show the algorithm's performance in practice. Reconstructions were made with the temporal footprint of 7.5 s (acceleration factor of 4) using sliding window (SW) technique with a temporal frame rate of about 2 s. The results are presented based on a single 2D plane. Fig. (6.3) illustrates the the reconstruction results from an inverse Fourier transform and the proposed method. Fig. (6.3a) and Fig. (6.3b) display the reconstructed images at the 4th and the 14th time frames. The inverse Fourier transform with sliding window method Fig. (6.3a) and Fig. (6.3b) are very noisy while the results from the spatiotemporal dictionary model, Fig. (6.3d) and Fig. (6.3e), show improved images. The image noise level was estimated from the variance measuremens in a region of the background (see section.(6.2.1.3)). Comparing the computed variance of a selected group of pixels forming the background in the 4th slice after applying dictionary based reconstruction represents a reduction in the noise level. Fig. (6.3c) and Fig. (6.3f) show time intensity curves (TIC) of pixels in selected arterial regions which are indicated by arrows with the same colors (for the big and smaller vessel the average intensity of 6 and 4 pixels in these regions are taken respectively). The TICs were constructed from sliding window reconstructions. Notice the constructed TICs are impaired with local variations that are attributed to reconstruction artifacts. It is noticeable that using the spatiotemporal dictionary in the reconstruction, impact the pixels' intensity variation. Consistent with the underlying contrast propagation, the less noisy image series have been achieved from images recovered by inverse Fourier transform. Indeed this smoothing effect not only decreases the background noise level but also led to less contrast around the vessel's edges and inside them.

6.3 Application of Group sparsity in Dynamic Contrast Enhanced MRI

Since Compressed sensing was introduced by Donoho, signal recovery with sparsity-promoting regularization has been a topic of interest in machine learning communities. It is shown in many references that the acquisition of MR images can be speed up by applying CS in the reconstruction step. A series of images at a high frame rate from an object in motion needs to be acquired in dynamic MRI. Conceptually, it requires a short acquisition for each time frame. Despite the wide use of CS in MRI, CS reconstruction algorithms for Dynamic MRI have been limited. Before introducing our development framework, we give here an overview of some methods that have used CS for dynamic MRI reconstruction including k-t SPARSE, k-t FOCUSS and k-t Group Sparsity.

Figure 6.2: Coronal plane MIP in volunteer studies reconstructed form undersampled k-space by a factor of. The dashed line in the image shows the position of the axial used to show the algorithms performance in practice.

6.3.1 K-t SPARSE

In "k-t SPARSE" [107] Lustig for the first time applied the CS technique to MRA recovery. This method implemented a dynamic version of the standard l_1 recovery explained earlier. K_y-t space was randomly undersampled to achieve the required incoherence in the CS theory. Rather than resorting to computationally expensive combinatorial optimization algorithms, sparse solutions were obtained using computationally feasible L1 minimization algorithms. To transform the time varying cardiac images, a wavelet and the Fourier transformation were employed along the spatial and the temporal direction respectively. The coherence required for the CS was achieved by the random sampling designed in K_y-t dimension. k-t SPARSE as a spatial k-space that has been combined with temporal dimension, exploits the spatio-temporal sparsity. It can be formulated as:

$$Minimize \quad \|\mathbf{x}\|_1 \quad \text{subject to} \quad \|\mathbf{Y} - \mathbf{E}\mathbf{x}\|_2 \leq \epsilon \tag{6.22}$$

where $\mathbf{x}$ is the sparse representation of signal to be reconstructed, $\mathbf{Y}$ is the undersampled measurements and $\mathbf{E}$ represents the encoding matrix that includes Fourier transform along temporal dimension and inverse wavelet transform along spatial dimension. Lustig showed that K-t Sparse performs superior to the sliding window reconstruction. However, due to the total variational regularization used in the application of k-t SPARSE in MR angiography, cartoon-like artifacts were often observed.

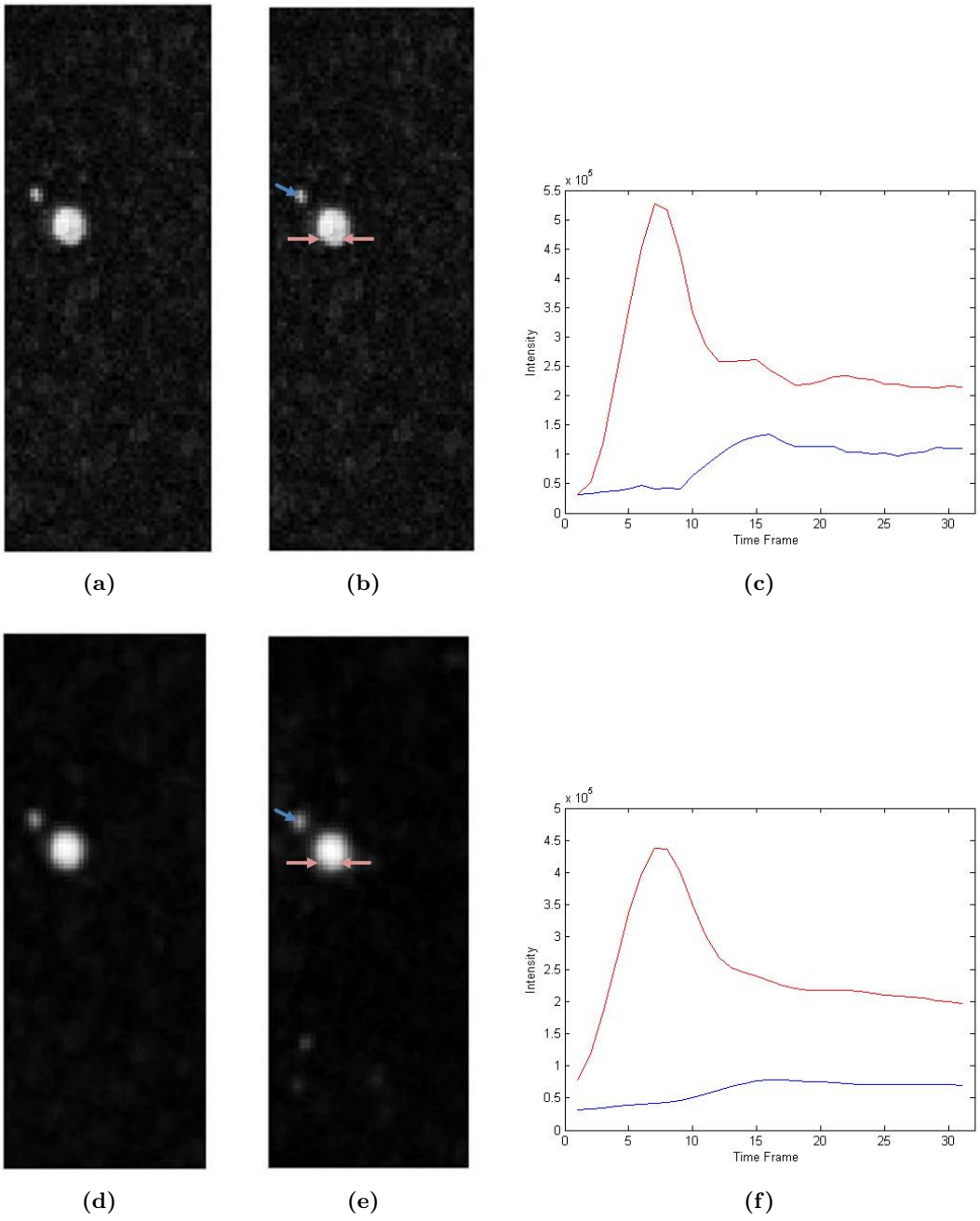

Figure 6.3: Comparing Inverse Fourier Transform and spetiotemporal dictionary method (a) SW reconstruction is made from the selected slice using Inverse Fourier. Transform. The 4-th time frame is shown; (b) the 14-th time frame ; (c) time intensity curves (TIC) of pixels in selected vessels that are pointed by arrows. Pink arrows point at the main vessel and the blue arrows point at the small vessel (the average intensity of pixels in these regions is taken); (d) the same selected slice in the 4th time frame reconstructed with the proposed method; (e) the 14-th time frame; (f) time intensity curves (TIC) of pixels in selected vessels that are respectively pointed by pink and blue arrows.

6.3.2 K-t FOCUSS

Due to existing high degree of spatiotemporal correlations in image series, there is redundancy within and among the data. Reconstruction strategies can be categorized in three main approaches, based on exploiting correlations in k-space, in time, or in both k-space and time. Partial Fourier methods, prior-information driven methods and parallel imaging are some examples of exploiting correlations in k-space. Exploiting temporal correlations, encompasses methods like view sharing methods. To exploit correlations in both k-space and time the two above mentioned approaches need to be combined. Hence, to estimate a missing data point, typically the other available data within vicinity of the point in both k-space and time should be considered. k-t BLAST and k-t SENSE [185] are two newer versions for the exploiting correlations in both k-space and time. k-t BLAST/SENSE as a model-based approach, were presented to accelerate dynamic imaging and showed its capability in overcoming the shortcomings of the aforementioned classical methods. Tsao exhibited that acquiring only a reduced amount of data and recovering the missing portion afterwards by using the correlations in k-space and in time, will lead to increased spatiotemporal resolution. The correlations in k-space and time was determined from a set of training images, which allowed the signal distribution in x-f space to be learned. k-t BLAST and k-t SENSE are nearly related, except that k-t SENSE additionally constitutes the coil sensitivities. In the above mentioned k-t approaches, spatio-temporal correlations of the signal distribution in dynamic image series are utilised to allow for undersampling in k-t space. Therefore, the k-t reconstruction approach is based on prior knowledge of the signal distribution acquired from a low-resolution training image. However, Baltes later proved that the quality of the training data influences the flow reconstruction and quantification of images [10].

k-t FOCUSS (k-t space FOCal Underdetermined System Solver (FOCUSS)) unifies k-t BLAST and k-t SPARSE while overcoming their drawbacks [86]. In the compressed sensing framework of k-t FOCUSS, prediction and residual encoding has been used, where the prediction approximately estimates the dynamic images and the residual encoding takes care of the remaining residual signals. They expected imposing the sparsity on the residual signal rather than the total signal improve the the performance of the original formulation in [86]. Have in the mind that in k-t SPARSE there was no need a priori knowledge of the spectral support. In fact, FOCUSS starts with finding a low resolution estimate of the signal in y-f space, and then this solution is pruned to a sparse signal representation by successively solving a sequence of re-weighted l_2 minimization problems. Consider k_x and k_y axis denote the readout and phase encoding direction, and $\mathbf{F}_y$ and $\mathbf{F}_t$ give the the Fourier transform along the y-direction and t-direction respectively. In the Cartesian trajectory,

the read out direction is fully sampled. Then $\mathbf{Y}$, undersampled k-t space measurements, in cardiac cine imaging, can be stacked in a vector form:

$$\mathbf{Y} = \mathbf{F}_y \mathbf{F}_t \, \mathbf{T} \tag{6.23}$$

where $\mathbf{T}(y, f)$ denotes the unknown 2-D spectral signal in the y-f domain and is decomposed into the predicted signal $\mathbf{T}_0$ and the residual signal $\Delta\mathbf{T}$; ($\mathbf{T} = \mathbf{T}_0 + \Delta\mathbf{T}$). This underdetermined linear inverse problem does not have a unique solution; hence, the following constrained minimization problem was considered:

$$Minimize \quad \|\mathbf{q}\|_2 \quad \text{subject to} \quad \|\mathbf{Y} - \mathbf{F}_y\mathbf{F}_t\mathbf{T}_0 - \mathbf{F}_y\mathbf{F}_t\mathbf{W}\mathbf{q}\|_2 \leq \epsilon \tag{6.24}$$

and

$$\mathbf{T} = \mathbf{T}_0 + \mathbf{W}\mathbf{q} \tag{6.25}$$

where $\mathbf{W}$ is a diagonal matrix that its elements can be initialized by zero padding the temporal average of the undersampled data, followed by an inverse Fourier transform or from a separate low resolution training data. Therefore imposing the sparsity on the residual signal $\Delta\mathbf{T}$ rather than the total signal is needed here. Regarding the k-t FOCUSS framework [86], the (l + 1)-th update of $\mathbf{T}$ can be optimized as follows:

$$\mathbf{T}_{l+1} = \underbrace{\mathbf{T}_0}_{prediction} + \underbrace{\boldsymbol{\Theta} - l\mathbf{F}^H(\mathbf{F}\boldsymbol{\Theta}_l\mathbf{F}^H + \lambda\mathbf{I})^{-1}(\mathbf{Y} - \mathbf{F}\mathbf{T}_0)}_{residual encoding}, \tag{6.26}$$

where $\boldsymbol{\Theta} = \mathbf{W}_l\mathbf{W}_l^H$ and λ denotes the appropriate Lagrangian parameter which is used to convert constrained optimization problem (6.25) into a un-constrained optimization problem (6.26). The novelty of FOCUSS algorithm comes from the fact that the weighting matrix $\mathbf{W}$ can be iteratively updated using the previous solution. In each iteration, the elements of the diagonal weighting matrix $\mathbf{W}$ are updated from the square root of absolute value of solution $\mathbf{T}$ in the previous iteration.

It was revealed that indeed the first iteration of k-t FOCUSS with temporal average corresponds to the k-t BLAST/SENSE algorithm [86] which then will be improved by an iterative update process [85]. In FOCUSS the sparseness is incorporated as a soft-constraint, whereas in the conventional basis pursuit or orthogonal matching pursuit the sparseness imposes the constraint as a hard-constraint. Moreover, in the dynamic MRI application the low-resolution initial estimate, essential for the convergence of FOCUSS, can be provided from interleaved low frequency k-t samples or the training data. High frequency artifacts reported in k-t SPARSE have been effectively suppressed by the hard sparseness constraint.

Another advantage over the conventional sparse optimization algorithms, such as basis pursuit or matching pursuit approaches, is that FOCUSS can be easily implemented in a computationally efficient manner [86, 85]. Since the initial estimate is used to enforce sparsity in the remaining residual y-f space, any error might have impact on recovery process. High spatio-temporal resolution imaging of simulated and in vivo experiments resulted using the proposed k-t FOCUSS from severely undersampled k-t measurements. Jung et al. also proposed other extensions of k-t FOCUSS to a more general prediction/residual encoding CS framework [87, 85]. In [87], the extended approach tried to use the motion estimation to compensate and resulting in a better prediction of the initial estimate. In the another approach [85], k-t FOCUSS algorithm was applied to radial trajectories to enhance dynamic MRI quality.

6.3.3 K-t group sparse

As argued before general form of the CS problem is given by

$$Minimize \quad \|\mathbf{x}\|_1 \quad \text{subject to} \quad \mathbf{Ax} = \mathbf{y}, \tag{6.27}$$

where $\mathbf{y} = \mathbf{Ax}$ is set, $\mathbf{A} \in \Re^{M \times N}$ can be an random Gaussian ensemble, and $\mathbf{y} \in \Re^M$ is the measurement vector. We have already noted that the l_1 norm constraint encourages sparsity in $\mathbf{x}$ for sufficiently small τ. It turns out that sparsity is usually not enough to produce state of the art results for denoising or inverse problems involving natural images [139]. Indeed, for instant wavelet coefficients of images are not only sparse, but also a local dependencies among neighboring coefficients can be recognized. These dependencies can been taken into account and improve the performances both theoretically and in practice [41, 209]. Group sparse compressed sensing (GSCS) [191], [48] as one of the recent developments in compressive sensing (CS) theory, was proposed for reconstruction of signals whose support is comprised from the union of a small number of groups (sets) from a collection of predefined groups. for example in gene expression data these groups may be gene pathways, or factor level indicators in categorical data. In group sparsity, l_1-regularization is applied to the norms of subsets of variables. Conventional CS is a special case of GSCS, when each group containing only a single element. Likewise in the sparse coding, let $\mathbf{x} \in \Re^N$ be a signal with sparsity K, while the vector $\mathbf{x}$ be partitioned into s disjoint groups denoted by $\{g_i \ : \ i = 1, \dots s\}$, g_i is an index set corresponding to the i-th group. Generally, g_i's are predefined based on prior knowledge. The mixed (q, p)-group

norm of x is defined as:

$$\|\mathbf{x}\|_{q,p} = (\sum_{i=1}^{s} \|x_{g_i}\|_p^q)^{1/q} \ , \quad for \quad p \geq 1, \tag{6.28}$$

where x_{g_i} is the sub vector of $\mathbf{x}$, and $\|.\|_p$ the conventional p norm. To generalize equation (6.27), l_1 norm can be replaced with the (1,2)-group sparsity, in a similar manner to l_1-regularisation for sparse recovery:

$$\underset{x}{Minimize} \quad \|\mathbf{x}\|_{1,2} \equiv \sum_{i=1}^{s} \|x_{g_i}\|_2 \quad \text{subject to} \quad \mathbf{Ax} = \mathbf{y}, \tag{6.29}$$

The group norm $\|\mathbf{x}\|_{1,2}$ constraint leads to sparsity in terms of groups. The $l_{1,2}$-regularization is known to facilitate group sparsity, like what l_1-regularization does for sparse recovery.

General group configurations such as overlapping groups or incomplete cover are allowed to be chosen [48]. Exploiting the underlying structure of sparse signals that have support components lying in groups led to the group sparsity structure encoding which reduce the degrees of freedom in the solution, thereby leading to better recovery performance. Based on the fact that the components within a group are likely to be either all zeros or all non-zeros simultaneously, the CS reconstruction is accomplished via a block sparse formulation. In comparison with CS, group sparsity can achieve better recovery performance with fewer measurements, thus the necessary measurement number can be reduced [77]. Different efficient CS recovery algorithms like basis pursuit denoising (BPDN) and orthogonal matching pursuit (OMP) have been well-suited to the group sparse case [61, 60, 55]. Spectral projected gradient method (SPGL1) [191] and SpaRSA [204] are two examples of the efficient first-order algorithms which have been coded and applied to a variety of problems. In [114], group sparsity was employed to exploit the wavelet coefficients of multi-contrast MR images. They showed that the correlation among the different T2-weighted images of the same anatomical slice can be incorporated to formulate group sparsity and promote optimization. Their results conclusively established the superiority of group sparsity technique over standard CS in T2-weighted MR image reconstruction. Computational and experimental results showed that on different signal recovery problems the GSCS algorithm exhibit good efficiency and strong stability and robustness compare to the conventional CS [176, 175, 113, 77, 61, 188, 54]. The significance of the results have been presented, lies in the fact that making explicit use of block-sparsity can provably provide better reconstruction qualities when non-sparse components in the sparse representation constitute large sized group. K-t group sparse reconstruction [188] exploits the group sparsity within the y-f representation of dynamic images by enforcing the support components to be in the form

of groups. In the CS reconstruction these groups perform like a constraint. Similar to the K-t BLAST/SENSE approach, a training data scan was employed to estimate the support region from the y-f space. A thresholding scheme, set above the noise level, is used to approximate the group structure. Then to group assignment, the y-f space elements are labeled based on the knowledge of the estimated support. As the groups are assigned to all elements, the signal recovery can be accomplished by the following assumptions. Set x be the y-f space to be reconstructed, y undersampled measurements in $k_y - t$ space and A as $F_y F_t$ be the encoding operator that includes Fourier transform along spatial dimension (F_y) and Fourier transform along temporal dimension (F_t). In dynamic cardiac MRI, due to the quasi periodic motion, temporal frequency domain (y-f space) produce sparse representation of the heart images. In addition to highly sparseness nature, y-f space has a group form. This feature satisfied the group sparsity condition in CS recovery theory. Experimental results on in vivo and in vitro cardiac cine imaging showed, K-t group sparse method outperforms the K-t Sparse for a given reduction factor.

6.3.4 Prior estimation Based Reconstruction in CE-MRA

The main idea supporting our previously developed PECS algorithm was exploited in MRI in the chapter 5. In this section, the implementations of PECS in contrast enhanced magnetic resonance angiography (CE-MRA) are presented. Recall that in the conventional MR imaging, an sparsifying transform is required to achieve a higher level of sparsity. As discussed before the fundamental condition for CS recovery success is the high level of sparsity in the image/signal to be reconstructed. It was demonstrated that eliminating the anatomical background, by the k-space subtraction, results in a tiny portion of the FOV. The outcome is the vascular region which is free of anatomical background and inherently sparse. Moreover it has been shown before that due to the high level of uniformity in the angiogram image series the total variation (TV) is useful in suppressing the background noise. In PECS, the elements of the underlying image are rearranged based on the knowledge of a prior image estimate, so that the sorted image reveals a higher level of sparsity for a given transform. In contrast-enhanced magnetic resonance angiography (CE-MRA), vessel-to-background contrast is achieved by a reduction in blood T1 induced by the injected contrast agent. High vascular signal is obtained after contrast agent injection and employed to visualise the blood flow and pathology of the surrounding tissues. Due to having high diagnostic accuracy, CE-MRA is widely used in clinical practice for non-invasive evaluation of peripheral arteries.

6.3.5 Prior Estimation based Compressed Sensing (PECS) formulation

With reference to the previous chapter, the formulation to recover MRI images with CS method is:

$$\check{\mathbf{x}} = \arg\min_{\mathbf{x}}(\|\mathbf{F} - \mathbf{E}\mathbf{x}\|_2 + \alpha\|\mathbf{x}\|_1 + \beta TV(\mathbf{x})), \tag{6.30}$$

$$\mathbf{F} = \mathbf{E}\mathbf{x}\ , \quad \mathbf{E} = \begin{bmatrix} diag(\mathbf{h})\mathbf{W}diag(\mathbf{c}_1) \\ \vdots \\ diag(\mathbf{h})\mathbf{W}diag(\mathbf{c}_M) \end{bmatrix}\ , \quad F = \begin{bmatrix} diag(\mathbf{h})\mathbf{F}_1 \\ \vdots \\ diag(\mathbf{h})\mathbf{F}_M \end{bmatrix}$$

where $\mathbf{x}$ and $\mathbf{F}$ represent the underlying image and the partial k-space acquisition respectively and $\mathbf{h}$ is the binary under-sampling mask with 1 and 0 corresponding to measured and skipped sample positions respectively in a specific temporal window (with a non-uniform sample density function). $\mathbf{E}$ represents the corresponding pMRI encoding matrix. It is worth noting that the data set $\mathbf{F}$ is a subtracted k-space set, so that the underlying image $\mathbf{x}$ represents an image free of anatomical background. As explained in chapter 5 in PECS, the knowledge of a prior image estimate $\acute{\mathbf{x}}$ was employed to perform sorting the the elements of the underlying image $\mathbf{x}$, resulting the sorted image $\mathbf{g}$ with a higher level of sparsity for a given transform. This can be written as:

$$\hat{\mathbf{g}} = \arg\min_{\mathbf{g}}(\|\mathbf{F} - \mathbf{E}_R\mathbf{g}\|_2 + \alpha\|\Phi\mathbf{g}\|_1 + \beta TV(\mathbf{x})), \quad \hat{\mathbf{g}} \overset{R^{-1}}{\rightarrow} \hat{\mathbf{x}} \tag{6.31}$$

where $\hat{\mathbf{g}}$ and $\hat{\mathbf{x}}$ denote the estimate of the sorted image and the final reconstructed image after unsorting respectively. $\mathbf{E}_R$ represents the updated encoding matrix (column changed) based on the sorting order R obtained from the reference image. In time resolved CE MRA, a composite image can be generated from multiple acquisitions of the k-space data over the period that contrast agent is present and then serve the reference image role in PECS reconstructing individual image time frames. The advantage of PECS in CE MRA over conventional MR imaging is that the image prior estimate contains full spatial resolution but incomplete temporal information while in conventional MR imaging, the prior estimate usually contains incomplete spatial information (low spatial resolution, noise corruption, etc). To acquire data in PECS a sampling pattern needs to be designed which meet two requirements and as a result guarantee achieving a successful CS reconstruction. As discussed in the previous chapter, a sampling pattern which feature a non uniform sample density function and achieves incoherent aliasing artifacts is favorable. For the

undersampling pattern (Mask), the data acquisition order is determined by randomly selecting the samples with an uniform weighting function (the same chance for each sample to be picked) until all the required samples are selected. By designing the sampling pattern mask corresponded to the desired characteristic for CS algorithm, a successful recovery is promised.

Overall, the PECS algorithm procedure is as follows; a sequentially acquired k-space samples are collected to generate a composite data set and generate an image corresponding to the entire data acquisition time period. This sliding composite image is then exploited to form a 2D monotonical function with a sorting order R. This sorted image has a sparse representation using a 2D DCT or wavelet transform. The obtained sorting order R will be employed in reconstructing individual time frames using k-space subsets. Accordingly, the prior estimate is an image with low temporal resolution image which includes information of the vascular regions over the entire time interval while each individual reconstructions distinguish the presence of contrast for a specific time interval. In other words the distinctness between the prior estimate and the underlying image is the outcome of the different temporal information contained in the composite data set and in the data subsets. The same dataset as Sec.(6.2.2.1) was used to exhibit PECS reconstruction results in Fig. (6.4). The Coronal plane MIPs of composite data set that was used to obtain these results is shown in Fig. (6.4a). This reference image is reconstructed using the acquired k-space dataset (undersampledc at an acceleration factor of 4). The conventional compressed sensing was used to produce Fig. (6.4b) from the same dataset but undersampled at an acceleration factor of 6. In Fig. (6.4c) another timeframe has been reconstructed employing CS. Incorporating the prior knowledge shown in Fig. (6.4a), PECS method resulted in Fig. (6.4d)and Fig. (6.4e) using the same data set as Fig. (6.4b)and Fig. (6.4c) respectively. High acceleration factors have the potential to better reveal the temporal changes, though in practice the increased level of artifacts overshadows this benefit. Comparing the PECS reconstruction outcomes with CS, It was discussed that in high acceleration factors PECS led to better image reconstructions [207]. It is seen that at acceleration factor of 6, slices at top an bottom of the 3D image have been poorly recovered and the result generally contains strip like artifacts, despite suppressing the background noise. These kind of artifacts could become diagnostic pitfalls for radiologists and lead to erroneous conclusions.

6.3.6 Prior estimation incorporation in Group Sparsity

In the previous sections, we discussed about different methods that have been applied to reconstruct dynamic MR images by employing compressed sensing algorithms. In this

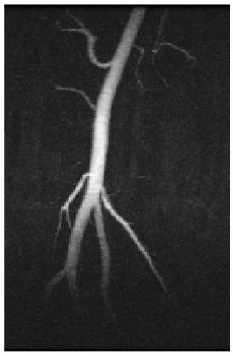

(a)

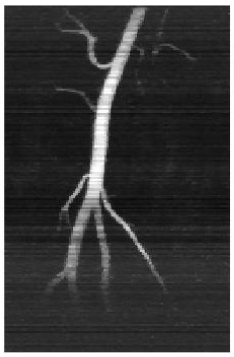

(b)

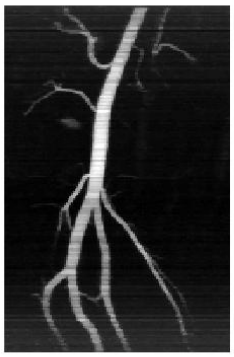

(c)

(d)

(e)

Figure 6.4: Coronal plane MIPs of the image reconstructed with different methods: (a) MIP of the Inverse Fourier transformed image, k-space data set is under-sampled at an acceleration factor of 4. This image has been used in PECS as a prior knowledge; (b-C) CS acquisition. Two reconstructions using under-sampled k-space data set (acceleration factor of 6) are made, and the resulting coronal plane MIP images are shown. Different time frames have been chosen to show the arrival of contrast agent in the arteries. (d-e) PECS acquisition. Two reconstructions using the same under-sampled k-space data set as (b) and (c) are made, and the resulting coronal plane MIP images are shown.

section we propose incorporating prior information used in PECS in the group sparsity framework to speed up CS and meanwhile enhance the sparsity in image representation.

In PECS reconstructing each time-frame, a prior estimate of the underlying image was incorporated in the CS recovery via a prior data sorting process. This procedure was explained before in chapter 5. In our proposed approach different disjoint groups(sets) are predefined based on the prior knowledge of a reference image and then will constraint the group sparse recovery algorithm. Likewise PECS, for each acquisition a reference image was obtained and transformed to the desired sparsifying transformation (Daubechies wavelets transform) to determine the group's support estimation. A k-means clustering algorithm which takes an image as input and generates a representative subset was applied to partition the data set into distinct clusters. To make the algorithm more clear, the concept of group sparsity and its implementation in the reconstruction of a single MR image have been presented in Fig. (6.5). A single frame from cardiac cine images obtained from full k-t measurements with size of $256 \times 256 \times 25$ was selected to show the impact of group sparsity on CS. The MR data were acquired from 1.5 T Philips scanner at Yonsei University Medical center in Korea. The field of view (FOV) was 345 $mm \times 270$ mm. The slice thickness was 10 mm, and the acquisition sequence was steady-state free precession (SSFP) with a flip angle of 50 degree and $TR = 3.45$ $msec$. The heart frequency was 66 bpm, and the retrospective cardiac gating was used. We thank Jong Chul Ye for making this data set available. [1] Fig. (6.5) shows the different stages of the approach for one of the frames from a cardiac cine images. We applied a 3-level wavelet transform with Daubechies to the reference image (training set) which was a low resolution reconstructed version of to-be reconstructed image. The transformed result of the reference image is shown in Fig. (6.5b). Having the sparse representation, a thresholding-based segmentation was performed to define various groups and assign each pixel to its cluster to be incorporated in Group Sparsity approach. With respect to the ground-truth, comparing the differences in Fig. (6.5c) and (6.5d) conclusively establish the superiority of group sparsity technique over the CS based technique in MR image reconstruction from partially sampled K-space data. This example is to corroborate the fact that as the anatomical structure of each slice does not change, the positions of the high valued wavelet transform coefficients are similar. It means that these sparse coefficients can be grouped according to their intensity and positions. Therefore incorporating group sparsity into the CS optimization problem can be accomplished

The overall procedure for the Group Sparsity reconstruction in CE-MRI is comparable to PECS. The FE lines within the designed sampling mask are sequentially acquired over

[1] $http://bisp.kaist.ac.kr/research_02.htm$

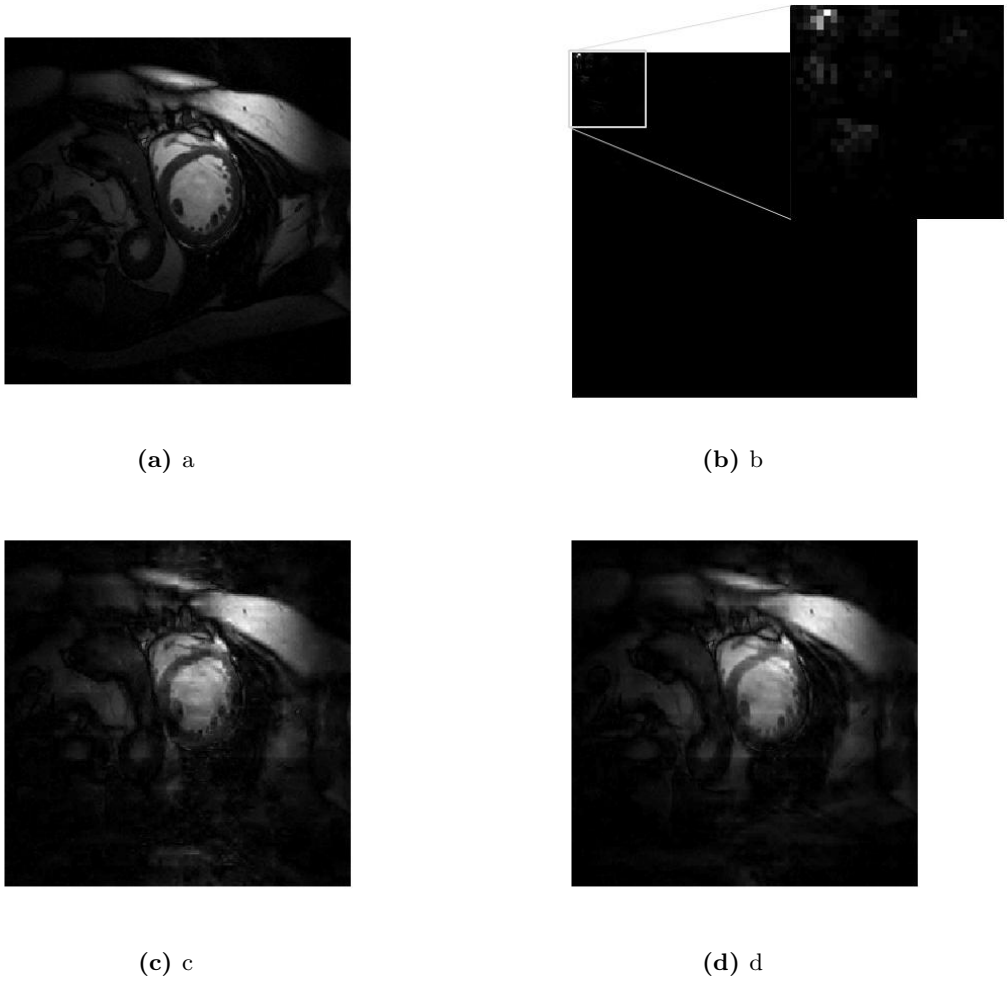

(a) a **(b)** b

(c) c **(d)** d

Figure 6.5: The results of applying group sparsity to the CS recovery of an individual MR image: in (a) A selected time-frame has been reconstructed from full sampled k-space data set. (b)The reference image has been sparsely represented by transforming it into the wavelet domain. The wavelet coefficients can be clustered in non-overlapping groups. (c)Compressed Sensing reconstructed image from four-times undersampled k-space. (d) the same k-space as (c) was used to reconstruct applying group sparsity. An apparent improvement in the image recovery is achieved with proposed Groups.

time. Combining all the samples allows a reference image to be formed either by inverse Fourier transform or a CS reconstruction (here an inverse Fourier transform is used). This composite image goes under wavelet transformation to give a sparse estimation of the image to be reconstructed. The sparse representation is used to assign groups to the elements within the wavelet domain. This groups of pixels will be introduced to the sparse solver to reconstruct images using the subsets of the k-space. Fig. (6.6) summarizes the idea of using the sliding composite image as the prior estimation in PECS and Group Sparsity method. Notice that in each acquisition, a prior image estimate can be investigated to incorporate

group sparsity in recovery. The acquisition of the individual samples defined by the mask are made in a random order until all the samples defined by the mask are acquired, the same acquisition order is repeated to cover a sufficiently long time interval. Image reconstructions can be performed using consecutively acquired samples at different acceleration factors. In contrast to GS in conventional MR imaging, in which the image prior estimate usually contain incomplete spatial domain information (lower spatial resolution, noise corruption, etc.), the prior estimate in this case contains full spatial resolution but incomplete temporal information.

To experiment with the effect of group assignment on the algorithm, different clustering strategies were implemented. Firstly 2 threshold values were chosen to cluster elements in two distinct groups, this grouping eventuated to a speedy consequence with no improvement in resolution. Then a clustering procedure was used to cluster the pixels. It was noticed that the number of groups presented to the group sparse algorithm has impact on the reconstruction outcome. It was noticed that the number of clusters need to be selected with regards to the dataset dimensions. As we employed 2D wavelet sparsifying transformer, the optimal number of groups was selected similar to one of the image dimension.

Once the groups are assigned to all elements, the image recovery can be done using group sparsity formulation:

$$\arg\min_{\mathbf{x}}(\|\mathbf{x}\|_{1,2} \quad \text{subject to} \quad \|\mathbf{F}-\mathbf{E}\boldsymbol{\Psi}\mathbf{x}\|_2 \leq \epsilon, \tag{6.32}$$

where $\mathbf{x}$ and $\mathbf{F}$ represent the sparse representation of underlying image and the partial k-space acquisition respectively, $\boldsymbol{\Psi}$ is the sparsifying transform (wavelet) in the image domain, and $\mathbf{E}$ represents the corresponding pMRI encoding matrix, see section (6.3.5). $\|\mathbf{x}\|_{1,2}$ is the (1,2)-group norm which was defined as:

$$\|\mathbf{x}\|_{1,2} = \|x_{g_1}\|_2 + \|x_{g_2}\|_2 + \|x_{g_3}\|_2 + ... + \|x_{g_s}\|_2, \tag{6.33}$$

where $\|x_{g_k}\|_2$ is the l_2 norm of the elements in $\mathbf{x}$ assigned to the k^{th} group. To investigate the uses of group assignment in image recovery, the following experiment was performed. Fig. (6.7) shows the results for Group Sparsity reconstruction using the dataset explained before in (6.2.2.1). To compare CS and GS two particular frames of the image series were selected to be shown. Fig. (6.7a) and Fig. (6.7b) have been recovered from the dataset under sampled at acceleration factor of 6. Compressed sensing was employed for image reconstruction. The same undersampled dataset were used to reconstruct images shown in

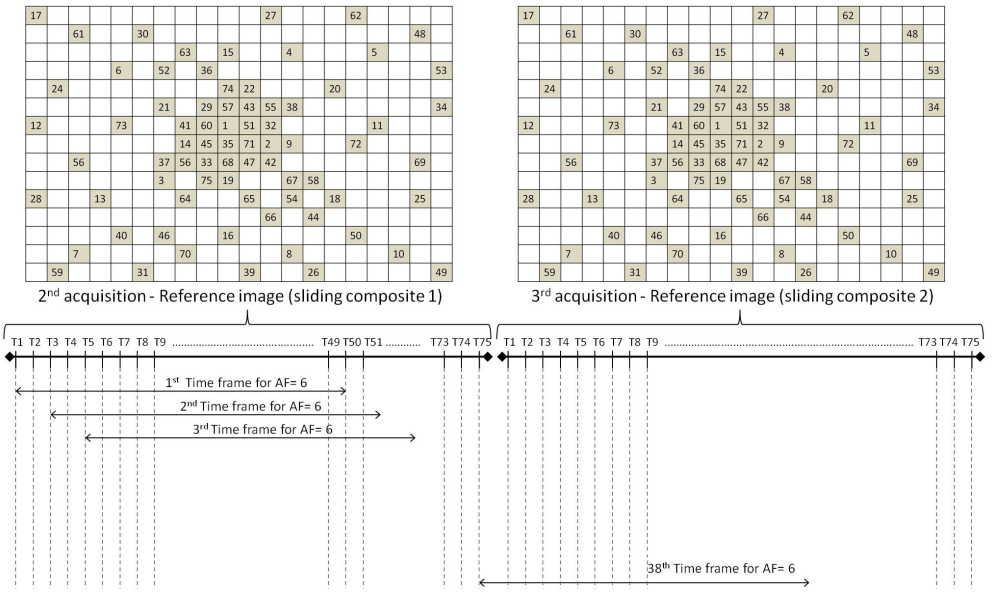

Figure 6.6: Diagram illustrating the data acquisition scheme in the proposed Group Sparsity method. A sampling mask that features incoherent aliasing artifacts (samples are randomly selected) with a non-uniform sample density function (more samples at the k-space center) is first formed (shown in the top row). Then the acquisition of the individual samples defined by the mask are made until all the samples defined by the mask are acquired, the same acquisition order is repeated to cover a sufficiently long time interval. Image reconstructions can be made using consecutively acquired samples at different acceleration factors. This diagram has exemplified sliding window reconstruction performance using under-sampled k-space dataset,AF=6, from two consecutive acquisitions.

Fig. (6.7c) and Fig. (6.7d) by applying the group sparsity. The same reference images used in PECS was incorporated in the group sparsity. The CS and group sparsity reconstructions were performed using the SPGL1 solver. [2]

6.4 Discussion

It is seen that the use of group sparsity led to better image reconstructions in the vascular regions with low contrast level that were poorly recovered in the CS. Comparing the PECS and GS, the strip artifacts that was observed in PECS have been removed. The disadvantage of this artifact is that it may lead to a misdiagnosis in clinical applications. However, spatial noise, noticeable in the background, can be observed in GS. These noises can be suppressed by applying a total variation (TV) constraint. Moreover in the PECS reconstructions Fig. (6.4d) or Fig. (6.4e), the amount of reconstruction artifacts tend to

[2]SGPL1: A solver for large-scale sparse reconstruction http://www.cs.ubc.ca/ mpf/spgl1/

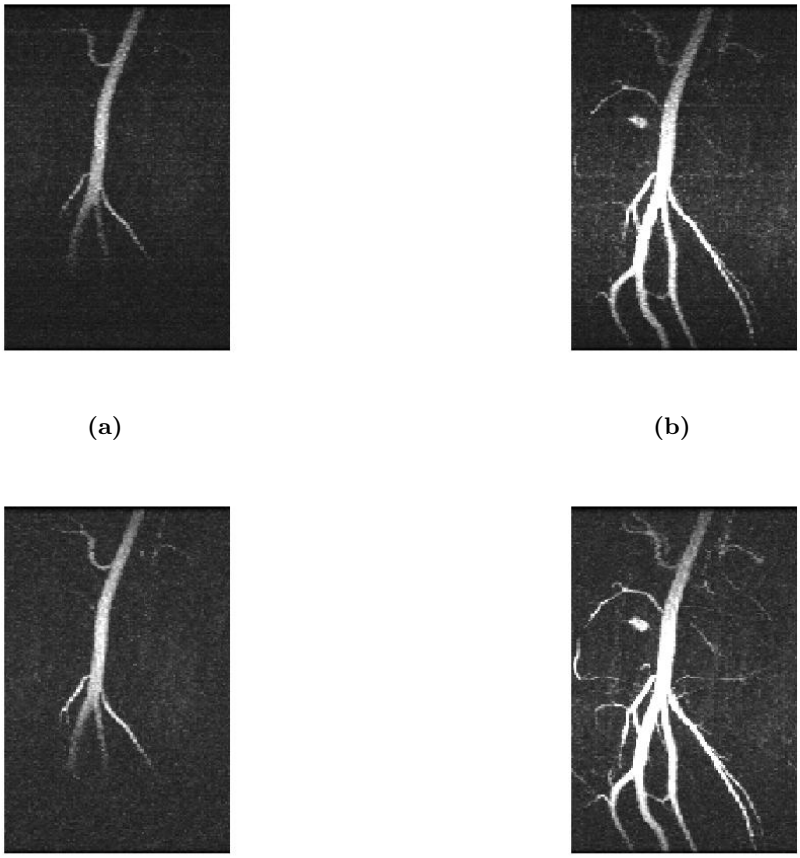

(a) **(b)**

(c) **(d)**

Figure 6.7: Coronal plane MIPs of the image reconstructed with different methods, k-space data set is under-sampled at an acceleration factor of 6 : (a-b) CS acquisition. Two reconstructions using under-sampled k-space data set are made, and the resulting coronal plane MIP images are shown. Different time frames have been chosen to show the arrival of contrast agent in the arteries. (d-e) Group Sparsity acquisition. Two reconstructions using the same under-sampled k-space data set as (b) and (c) are made, and the resulting coronal plane MIP images are shown.

vary along the longitudinal direction, slices in the middle are generally better reconstructed than the slices at both edges.

In retrospective image reconstruction both the time window length (acceleration factor) and the relative timing of each reconstruction could be selected. Time intensity curve (TIC) is used as the indicator of the arterial contrast status in in the main vessel. Fig. (6.8) shows the time intensity curves (TIC) that depict the image intensity variations over the data acquisition time period in the main arterial region. The TICs were constructed from sliding window reconstructions with a temporal frame rate of about 3.75 s and a temporal

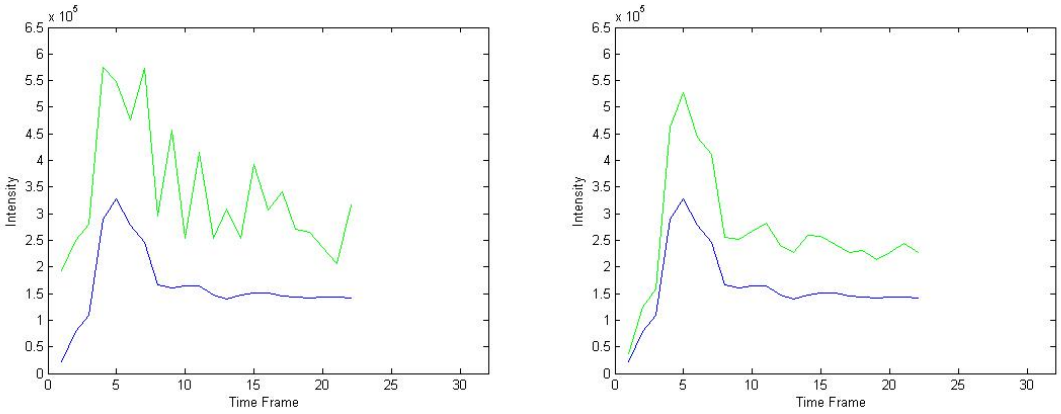

(a) **(b)**

Figure 6.8: Time intensity curve (TIC) to indicate the arterial contrast status in in the main vessel (the average intensity of 6 voxels in this region is taken). The image series were recovered from k-space dataset with the AF=6 and a sliding shift 3.75 s (a)The intensity variation in CS and IFF results has been compared. (b) comparison between TIC constructed from GS and IFF. Apparently reconstruction artifacts have been effectively reduced.

footprint of 5 s (acceleration factor of 6). The TIC corresponding to the IFF, CS and group sparse acquisition have been compared here. Fig. (6.8b) shows a smoother TIC can be achieved by Group Sparsity reconstruction, comparing to the CS result which features several spiky variations. In contrast to the standard Compressed Sensing methods, the group sparse method performs grouping on sparse elements of the signal. For a given reduction factor, the group assignment enables recovery of more non-sparse components than CS method, consequenting to a suppression of noise in the reconstruction.

The GS differs with PECS in the sense that does not need prior estimation of the image, but rather indirectly, the sparse representation incorporated in the algorithm for groups' assignment. Although imposing the prior knowledge indirectly is beneficial and safe, grouping the elements of the sparse signal and the number of groups affect the results. This suggests that a more reliable and automatic clustering method can be implemented in that makes the group sparsity recovery more stable. The same as PECS, our method carry outs the dynamic MRI reconstruction by sampling the k-space dataset in temporal dimension with a same mask. Whereas in the other methods like k-t sparse, data has been acquired. At the other hand, the wavelet coefficients that are small in value but large in the number might be noises which have been grouped and propagated in the recovery process. These large groups in size which increase the l_2 norm in the formulation (6.33) might compete with the groups that have been made from high valued coefficients. This also can be modified by an optimal grouping that can be considered for future work.

Chapter 7

Conclusions and Future Work

In this chapter, the research described in this dissertation has been summarized. Also possible interesting future works related to the contributions are highlighted.

MRI is a multi parameter imaging method, not only beneficial for illustrating the anatomical structure with high resolution, but also for reflecting the body's various kinds of functional status. Parallel (multi-channel) MRI (pMRI) technique addresses the problem of scan-time limitations in imaging scenarios. Due to rapid physiological motion in dynamic imaging applications, data undersampling has been proposed to shorten the scan time. Over the past several years, various methods and constraints have been presented to accomplish accelerated image reconstruction. We investigated the problem of image reconstruction in parallel MRI and suggested a number of improvements over existing methodologies.

In the chapter 3, a Cartesian based sliding window reconstruction method based on GUISE was discussed. Incorporating spatio-temporal constraints into the imaging process has been shown to improve the MR images quality. In GUISE, the object support constraint is incorporated in inverting the encoding matrix and eventually in the recovery procedure. Hence, the image is reconstructed by exploiting the image ROS knowledge. Since defining a tighter ROS allows a higher acceleration factor to be achieved and the SNR improvement, a new, modified segmentation approach was proposed to extract the vessel segments. In the first attempts to perform GUISE, maximum intensity projection (MIP) was used to segment the ROS which failed to adequately depict the spatial relationships of overlapping vessels. An elevated noise level in the background and low contrast between small vessels and background tissue are some examples of the disadvantages of using MIP. Significantly better CNR values are obtained with the modified MIP method according to our studies. A 3D segmentation method was introduced to form an ROS based on the modified MIP of images which resulted in a reasonably tight support region around all sizeable vessels. The work

presented were preliminary and next steps include performing more extensive studies and incorporating more accurate 3D segmentation methods into the MRA reconstruction work. In the current version of GUISE, sampling pattern is designed based on the RMS error of the reconstructed image. Using other types of error measurements in the reconstruction quality judgment could be a good area of investigation.

Since the TIC curves obtained from the CE-MRA image sequences reconstructed by GUISE showed artifacts, the novel method described in chapter 4 was developed to reduce the noise level. Imposing a set of temporal basis functions derived by KLT from a model of the contrast flow dynamics in the reconstructed images was suggested. The transient wash-in and wash-out of contrast during the recording of a sequence suggests that each time frame in a sequence is highly correlated to the next frames. The proposed method used the gamma variate curve as the prior knowledge which is a useful model for the image intensity versus time observed in locations. The presented results suggested that considerable improvement in the quality of reconstructed sequences of images in CE-MRA can be achieved by incorporating an appropriate temporal basis.

In the MRI research community, CS is rapidly attracting interest because of its demonstrated ability to speed up data acquisition. Compressed sensing seeks to reconstruct high quality MRI image from as few non-adaptive linear measurements as possible. CS image reconstruction requires the image of interest to be sparse or compressible and the encoding matrix to be incoherent with the sparsifying transform. With Fourier encoding in MRI, the achievable under-sampling is dependent of the level of sparsity and incoherence attained by the sparsifying transform. Many different sparsifying transforms have been investigated and applied in MRI reconstruction. PECS is an interesting extension of CS: based on a prior estimate of the image, the elements in the underlying image are rearranged so that the image can be recovered in an alternative form that features a much higher level of sparsity, which leads to improved image recoveries. Hence in PECS, the prior image estimate is essential and incorporated in the image reconstruction. In the method introduced in chapter 5, SPECS, a data-driven sparsifying transform was employed in the CS algorithm to achieve an estimation of the underlying image. This estimate is incorporated as image prior knowledge in the PECS to reconstruct the reordered image. In PECS, it was illustrated that data reordering enhances data sparsity and consequently improves CS recovery. Not only in contrast to PECS, SPECS requires no prior information about the recovered image, but also the SPECS results outperform PECS. As a result of performing two CS recoveries, the computational complexity has been increased slightly in SPECS. Currently in PECS, only the magnitude information of the image estimation is used in the sorting process. However, it is intuitively beneficial to take into account the

image phase information as well.

In the CS, one of the most powerful and widely successful approaches to describe natural signals, is dictionary-based signal modeling. The idea of describing the signal of interest using a dictionary of elementary atoms, controlled by sparsity forces, has had a profound impact on a wide scope of fields and tasks. Sparse dictionaries combine efficiently learned dictionaries with analytic dictionaries, leading to superior results in many applications. Learned dictionaries typically lack explicit structure and are less efficient than analytic dictionaries, however, the finer adaptation to the signal data leads to superior results in many applications. A dynamic CE-MRA application of the sparse dictionaries was developed and tested in chapter 6, where the dictionary representations were exploited to reconstruct less noisy image series. Instead of utilizing the same sampling pattern in several k-space acquisition, the optimized sampling pattern such as random or constrained random patterns can be applied in k-t space. In this manner, the x-f space (x: spatial location, f: temporal frequency) can be the sparse representation of the dynamic MR data while the sparsifying transform takes places along the temporal dimension in CS-based reconstruction method.

Imposing prior knowledge in the reconstruction algorithm has been shown that gives superior performance at higher acceleration factors. Group sparsity is the extension of the original sparsity concept in compressive sensing which is motivated by the observation that in some sparse data the nonzero coefficients are often not random but tend to be clustered. Practically, better results can be achieved in these cases by utilizing both clustering and sparsity priors. Motivated by this idea, we developed a new method in chapter 6 that constrained image recovery indirectly instead of using prior estimation of the image. Although utilizing spatial structure within the sparse representation needs less prior knowledge, grouping the elements of the sparse signal and the number of groups affect the results. Searching the optimum groups of sparse representation is one of the area required attention to be focused on. In addition, transforms other than wavelet transforms can be used for sparse representation to provide more distinct groups.

Bibliography

[1] Adluru, G. and DiBella, E. (2008). Reordering for improved constrained reconstruction from undersampled k-space data. *Int. J. Biomedical Imaging*, 2008:341684.

[2] Afacan, O., Hoge, S., Brooks, and H, D. (2009). Increasing temporal resolution in hybrid 3D EPI fMRI studies using unfold. In *Biomedical Imaging: From Nano to Macro, 2009. ISBI'09. IEEE International Symposium on*, pages 654–657. IEEE.

[3] Aggarwal, N., Bandyopadhyay, S., and Bresler, Y. (2004). Spatio-temporal modeling and adaptive acquisition for cardiac MRI. In *Proc. Int. Symp. Biomed. Imaging: Nano to Micro*, volume 1, pages 628–631. IEEE.

[4] Aharon, M., Elad, M., and Bruckstein, A. (2006). The K-SVD: an algorithm for designing of overcomplete dictionaries for sparse representation. *Signal Processing, IEEE Transactions on*, 54(11):4311–4322.

[5] Aho, A. V., Hopcroft, J. E., and Ullman, J. (1983). *Data structures and algorithms*. Addison-Wesley Longman Publishing Co., Inc., Boston, MA, USA.

[6] Ajraoui, S., Parnell, S., Parra-Robles, J., Ireland, R., and Wild, J. (2011). Improved compressed sensing reconstruction and optimised sampling patterns for very fast acquisition of hyperpolarised 3he images. *19th Annual Meeting of ISMRM, Montreal, Canada, 2011*, pages 30–32.

[7] Asif, M., Hamilton, L., Brummer, M., and Romberg, J. (2012). Motion-adaptive spatio-temporal regularization (master) for accelerated dynamic MRI. *Magnetic Resonance in Medicine*, 70(3):800–812.

[8] Babacan, S., Peng, X., Wang, X., Do, M., and Liang, Z. (2011). Reference-guided sparsifying transform design for compressive sensing MRI. In *Proc. IEEE Int. Conf. Eng. Med. Biol. Soc. EMBC*, pages 5718–5721.

[9] Baker, C., King, K., Liang, D., and Ying, L. (2011). Translational-invariant dictionaries for compressed sensing in magnetic resonance imaging. In *Proc. 8th IEEE Int. Symp. on Biomedical Imaging: From Nano to Macro*, pages 1602–1605, Chicago, USA.

[10] Baltes, C., Kozerke, S., Hansen, M., Pruessmann, K., Tsao, J., and Boesiger, P. (2005). Accelerating cine phase contrast flow measurements using k-t BLAST and k-t SENSE. *Magnetic Resonance in Medicine*, 54(6):1430–1438.

[11] Bammer, R. and Schoenberg, S. O. (2004). Current concepts and advances in clinical parallel magnetic resonance imaging. *Topics in Magnetic Resonance Imaging*, 15(3):129–158.

[12] Baraniuk, R. (2007). Compressive sensing [lecture notes]. *IEEE Signal Processing Magazine*, 24(4):118–121.

[13] Benner, T., Heiland, S., Erb, G., Forsting, M., and Sartor, K. (1997). Accuracy of gamma-variate fits to concentration-time curves from dynamic susceptibility-contrast enhanced MRI: influence of time resolution, maximal signal drop and signal-to-noise. *Magnetic Resonance Imaging*, 15(3):307–317.

[14] Blagosklonov, O., Sabbah, A., Verdenet, J., and Cardot, J. (2000). Application of karhunen-loeve transform in nuclear cardiology: spatio-temporal smoothing and quantitative image analysis. In *Proc. Int. Computers in Cardiology*, pages 299–302. IEEE.

[15] Blaimer, M., Breuer, F., Mueller, M., Heidemann, R., Griswold, M., and Jakob, P. (2004). SMASH, SENSE, PILS, GRAPPA: how to choose the optimal method. *Topics in Magnetic Resonance Imaging*, 15(4):223–236.

[16] Blakeley, N., Bones, P., Millane, R., and Renaud, P. (2003). Efficient frequency-domain sample selection for recovering limited-support images. *JOSA A*, 20(1):67–77.

[17] Blumensath, T. and Davies, M. (2009). Iterative hard thresholding for compressed sensing. *Applied and Computational Harmonic Analysis*, 27(3):265–274.

[18] Bones, P., Alwesh, N., Connolly, T., and Blakeley, N. (2001). Recovery of limited-extent images aliased because of spectral undersampling. *JOSA A*, 18(9):2079–2088.

[19] Bones, P., Vafadar, B., Watts, R., and Wu, B. (2010). Imposing spatio-temporal support in magnetic resonance angiographic imaging. In *Proc. Image Recon. from Incomplete Data VI*, volume 7800, pages 780007:1–10. SPIE.

[20] Bouman, C. and Sauer, K. (1993). A generalized gaussian image model for edge-preserving map estimation. *Image Processing, IEEE Transactions on*, 2(3):296–310.

[21] Brand, M. (2002). Incremental singular value decomposition of uncertain data with missing values. *Computer Vision-ECCV 2002*, pages 707–720.

[22] Breuer, F., Blaimer, M., Heidemann, R., Mueller, M., Griswold, M., and Jakob, P. (2005a). Controlled aliasing in parallel imaging results in higher acceleration (CAIPIRINHA) for multi-slice imaging. *Magnetic Resonance in Medicine*, 53(3):684–691.

[23] Breuer, F. A., Blaimer, M., Mueller, M. F., Seiberlich, N., Heidemann, R. M., Griswold, M. A., and Jakob, P. M. (2006). Controlled aliasing in volumetric parallel imaging (2D CAIPIRINHA). *Magnetic Resonance in Medicine*, 55(3):549–556.

[24] Breuer, F. A., Kellman, P., Griswold, M. A., and Jakob, P. M. (2005b). Dynamic autocalibrated parallel imaging using temporal GRAPPA (TGRAPPA). *Magnetic Resonance Imaging*, 53(4):981–985.

[25] Bridson, R. (2007). Fast poisson disk sampling in arbitrary dimensions. In *ACM SIGGRAPH*, volume 2007.

[26] Brown, D. G. and Riederer, S. J. (2005). Contrast-to-noise ratios in maximum intensity projection images. *Magnetic Resonance in Medicine*, 23(1):130–137.

[27] Bydder, M., Larkman, D. J., and Hajnal, J. V. (2002a). Combination of signals from array coils using image-based estimation of coil sensitivity profiles. *Magnetic Resonance in Medicine*, 47(3):539–548.

[28] Bydder, M., Larkman, D. J., and Hajnal, J. V. (2002b). Generalized SMASH imaging. *Magnetic Resonance Imaging*, 47(1):160–170.

[29] Bydder, M. and Robson, M. D. (2005). Partial Fourier partially parallel imaging. *Magnetic Resonance in Medicine*, 53(6):1393–1401.

[30] Candes, E. (2006). Compressive sampling. In *Proc. Int. Congress of Math. Madrid, Spain*, pages 1433–1452.

[31] Candes, E. and Donoho, D. (2000). Curvelets: A surprisingly effective nonadaptive representation for objects with edges. Technical report, DTIC Document.

[32] Candes, E. and Donoho, D. (2004). New tight frames of curvelets and optimal representations of objects with piecewise C2 singularities. *Communications on Pure and Applied Mathematics*, 57(2):219–266.

[33] Candes, E. and Romberg, J. (2005). Practical signal recovery from random projections. *SPIE International Symposium on Electronic Imaging: Computational Imaging III,*, San Jose, California, January.

[34] Carlson, J. and Minemura, T. (1993). Imaging time reduction through multiple receiver coil data acquisition and image reconstruction. *Magnetic Resonance Imaging*, 29(5):681–687.

[35] Chapman, B. E., Stapelton, J. O., and Parker, D. L. (2004). Intracranial vessel segmentation from time-of-flight MRA using pre-processing of the MIP Z-buffer: accuracy of the ZBS algorithm. *Medical Imaging Analysis*, 8(2):113.

[36] Chen, S., D. D. and Saunders, M. (1995). Atomic decomposition by basis pursuit. Department of Statistics.

[37] Chen, L., Schabel, M., and DiBella, E. (2010a). Reconstruction of dynamic contrast enhanced magnetic resonance imaging of the breast with temporal constraints. *Magnetic Resonance Imaging*, 28(5):637–645.

[38] Chen, S., Donoho, D., and Saunders, M. (1998). Atomic decomposition by basis pursuit. *SIAM journal on Scientific Computing*, 20(1):33–61.

[39] Chen, S., Donoho, D., and Saunders, M. (2001). Atomic decomposition by basis pursuit. *SIAM Review*, 43(1):129–159.

[40] Chen, Y., Ye, X., and Huang, F. (2010b). A novel method and fast algorithm for MR image reconstruction with significantly under-sampled data. *Inverse Problems and Imaging*, 4(2):223–240.

[41] Chesneau, C., Fadili, J., and Starck, J. (2010). Stein block thresholding for image denoising. *Applied and Computational Harmonic Analysis*, 28(1):67–88.

[42] Cheung, K. F. and Marks II, R. J. (1990). Imaging sampling below the Nyquist density without aliasing. *JOSA A*, 7(1):92–105.

[43] Chronik, B. A. and Rutt, B. K. (2001). Simple linear formulation for magnetostimulation specific to MRI gradient coils. *Magnetic Resonance in Medicine*, 45(5):916–919.

[44] Daubechies, I. (2004). *Ten lectures on wavelets*. Society for Industrial and Applied Mathematics.

[45] Davenport, R. (1983). The derivation of the gamma-variate relationship for tracer dilution curves. *Journal of Nuclear Medicine*, 24(10):945.

[46] Davis, G., Mallat, S., and Avellaneda, M. (1997). Adaptive greedy approximations. *Constructive Approximation*, 13(1):57–98.

[47] de Zwart, J. A., van Gelderen, P., Kellman, P., and Duyn, J. H. (2002). Reduction of gradient acoustic noise in MRI using SENSE-EPI. *Neuroimage*, 16(4):1151–1155.

[48] Deng, W., Yin, W., and Zhang, Y. (2011). Group sparse optimization by alternating direction method. *TR11-06, Department of Computational and Applied Mathematics, Rice University*.

[49] Ding, Y., Chung, Y., Raman, S., and Simonetti, O. (2009). Application of the Karhunen-Loeve transform temporal image filter to reduce noise in real-time cardiac cine MRI. *Physics in Medicine and Biology*, 54:3909.

[50] Do, M. and Vetterli, M. (2005). The contourlet transform: an efficient directional multiresolution image representation. *Image Processing, IEEE Transactions on*, 14(12):2091–2106.

[51] Dong, Y. and Ji, J. (2011). Compressive sensing MRI with laplacian sparsifying transform. In *Proc. IEEE Int. Conf. Biomedical Imaging: From Nano to Macro, Chicago*, pages 81–84.

[52] Donoho, D. (2006). Compressed sensing. *Information Theory, IEEE Transactions on*, 52(4):1289–1306.

[53] Donoho, D. and Elad, M. (2003). Optimally sparse representation in general (nonorthogonal) dictionaries via L1 minimization. *Proceedings of the National Academy of Sciences*, 100(5):2197–2202.

[54] Duarte, M. and Eldar, Y. (2011). Structured compressed sensing: From theory to applications. *Signal Processing, IEEE Transactions on*, 59(9):4053–4085.

[55] Eiwen, D., Taubock, G., Hlawatsch, F., and Feichtinger, H. (2010). Group sparsity methods for compressive channel estimation in doubly dispersive multicarrier systems. In *IEEE Eleventh International Workshop on Signal Processing Advances in Wireless Communications (SPAWC). IEEE*.

[56] Elad, M. (2002). On the origin of the bilateral filter and ways to improve it. *Image Processing, IEEE Transactions on*, 11(10):1141–1151.

[57] Elad, M. and Aharon, M. (2006). Image denoising via sparse and redundant representations over learned dictionaries. *Image Processing, IEEE Transactions on*, 15(12):3736–3745.

[58] Elad, M., Matalon, B., and Zibulevsky, M. (2007). Coordinate and subspace optimization methods for linear least squares with non-quadratic regularization. *Applied and Computational Harmonic Analysis*, 23(3):346–367.

[59] Elad, M., Starck, J., Querre, P., and Donoho, D. (2005). Simultaneous cartoon and texture image inpainting using morphological component analysis (MCA. *Applied and Computational Harmonic Analysis*, 19(3):340–358.

[60] Eldar, Y., Kuppinger, P., and Bolcskei, H. (2010). Block-sparse signals: Uncertainty relations and efficient recovery. *Signal Processing, IEEE Transactions on*, 58(6):3042–3054.

[61] Eldar, Y. and Mishali, M. (2009). Robust recovery of signals from a structured union of subspaces. *Information Theory, IEEE Transactions on*, 55(11):5302–5316.

[62] Fornasier, M. and Rauhut, H. (2010). Compressive sensing. In Scherzer, O., editor, *Handbook of Mathematical Methods in Imaging*, pages 187–229. Springer.

[63] Frayne, R., Grist, T. M., Korosec, F. R., Willig, D. S., Swan, J. S., Turski, P. A., and Mistretta, C. A. (1996). MR angiography with three-dimensional MR digital subtraction angiography. *Topics in Magnetic Resonance Imaging*, 8(6):366.

[64] Freeborough, P. A., Fox, N. C., and Kitney, R. I. (1997). Interactive algorithms for the segmentation and quantitation of 3-D MRI brain scans. *Computer Methods and Programs in Biomedicine*, 53(1):15–25.

[65] Gao, Y. and Reeves, S. (2000). Optimal k-space sampling in MRSI for images with a limited region of support. *IEEE Trans.*, MI-19(12):1168–1178.

[66] Gao, Y. and Reeves, S. J. (2001). Fast k-space sample selection in MRSI with a limited region of support. *Medical Imaging, IEEE Transactions on*, 20(9):868–876.

[67] Glover, G. H. and Lai, S. (1998). Self-navigated spiral fMRI: Interleaved versus single-shot. *Magnetic Resonance in Medicine*, 39(3):361–368.

[68] Golay, X., Pruessmann, K. P., Weiger, M., Crelier, G. R., Folkers, P. J., Kollias, S. S., and Boesiger, P. (2000). Presto-sense: An ultrafast whole brain fMRI technique. *Magnetic Resonance Imaging*, 43(6):779–786.

[69] Gribonval, R. and Vandergheynst, P. (2006). On the exponential convergence of matching pursuits in quasi-incoherent dictionaries. *IEEE Trans. Inf. Theory*, 52(1):255–261.

[70] Griswold, M., Jakob, P., Heidemann, R., Nittka, M., Jellus, V., Wang, J., Kiefer, B., and Haase, A. (2002). Generalized autocalibrating partially parallel acquisitions (GRAPPA). *Magnetic Resonance in Medicine*, 47(6):1202–1210.

[71] Griswold, M. A., Jakob, P. M., Chen, Q., Goldfarb, J. W., Manning, W. J., Edelman, R. R., and Sodickson, D. (1999). Resolution enhancement in single-shot imaging using simultaneous acquisition of spatial harmonics (SMASH). *Magnetic Resonance Imaging*, 41(6):1236–1245.

[72] Haacke, E. M., Brown, R. W., Thompson, M. R., and Venkatesan, R. (1999). *Magnetic Resonance Imaging: Physical Principles and Sequence Design*, volume 82. Wiley-Liss New York:.

[73] Heidemann, R. M., Griswold, M. A., Haase, A., and Jakob, P. M. (2001). Vd-auto-SMASH imaging. *Magnetic Resonance in Medicine*, 45(6):1066–1074.

[74] Hennig, J., Nauerth, A., and Friedburg, H. (1986). RARE imaging: a fast imaging method for clinical MR. *Magnetic Resonance in Medicine*, 3(6):823–833.

[75] Hu, H. H., Madhuranthakam, A. J., Kruger, D. G., Glockner, J. F., and Riederer, S. J. (2005). Combination of 2D sensitivity encoding and 2D partial fourier techniques for improved acceleration in 3D contrast-enhanced MR angiography. *Magnetic Resonance in Medicine*, 55(1):16–22.

[76] Huang, F., Akao, J., Vijayakumar, S., Duensing, G. R., and Limkeman, M. (2005). k-t GRAPPA: A k-space implementation for dynamic MRI with high reduction factor. *Magnetic Resonance Imaging*, 54(5):1172–1184.

[77] Huang, J. and Zhang, T. (2010). The benefit of group sparsity. *The Annals of Statistics*, 38(4):1978–2004.

[78] Hutchinson, M. and Raff, U. (1988). Fast MRI data acquisition using multiple detectors. *Magnetic Resonance in Medicine*, 6(1):87–91.

[79] Jain, A. (1989). *Fundamentals of Digital Image Processing*. Prentice-Hall, Inc.

[80] Jakob, P. M., Grisowld, M. A., Edelman, R. R., and Sodickson, D. K. (1998). AUTO-SMASH: a self-calibrating technique for SMASH imaging. *Magnetic Resonance Materials in Physics, Biology and Medicine*, 7(1):42–54.

[81] Jakob, P. M., Griswold, M., Hillenbrand, C., Heidemann, R., Hahn, D., and Haase, A. (2000). High speed and high resolution cardiac MRI (parallel acquisition techniques & modular imaging). *Magnetic Resonance Materials in Physics, Biology and Medicine*, 11(1):52–54.

[82] Jakob, P. M., Griswold, M. A., Edelman, R. R., Manning, W. J., and Sodickson, D. K. (1999). Accelerated cardiac imaging using the SMASH technique. *Journal of Cardiovascular Magnetic Resonance*, 1(2):153–157.

[83] Ji, J. X. and Wright, S. M. (2005). Parallel MR imaging with accelerations beyond the number of receiver channels using real image reconstruction. In *Engineering in Medicine and Biology Society, 2005. IEEE-EMBS 2005. 27th Annual International Conference of the*, pages 735–738. IEEE.

[84] Jolliffe, I. (2005). *Principal Component Analysis*. Wiley Online Library.

[85] Jung, H., Park, J., Yoo, J., and Ye, J. (2010). Radial k-t FOCUSS for high-resolution cardiac cine MRI. *Magnetic Resonance in Medicine*, 63(1):68–78.

[86] Jung, H., Sung, K., Nayak, K., Kim, E., and Ye, J. (2009). k-t FOCUSS: A general compressed sensing framework for high resolution dynamic MRI. *Magnetic Resonance in Medicine*, 61(1):103–116.

[87] Jung, H. and Ye, J. (2010). Motion estimated and compensated compressed sensing dynamic magnetic resonance imaging: What we can learn from video compression techniques. *International Journal of Imaging Systems and Technology*, 20(2):81–98.

[88] Kelton, J. R., Magin, R. L., and Wright, S. M. (1989). An algorithm for rapid image acquisition using multiple receiver coils. In *Proceedings of the SMRM 8th Annual Meeting, Amsterdam*, page 1172.

[89] Knopp, M., Weiss, E., Sinn, H., Mattern, J., Junkermann, H., Radeleff, J., Magener, A., Brix, G., Delorme, S., and Zuna, I. (1999). Pathophysiologic basis of contrast enhancement in breast tumors. *Journal of Magnetic Resonance Imaging*, 10(3):260–266.

[90] Korosec, F., Frayne, R., Grist, T., and Mistretta, C. (1996). Time-resolved contrast-enhanced 3D-MR angiography. *Magnetic Resonance in Medicine*, 36(3):345–351.

[91] Korosec, F. R., Frayne, R., Grist, T. M., and Mistretta, C. A. (2005). Time-resolved contrast-enhanced 3D MR angiography. *Magnetic Resonance in Medicine*, 36(3):345–351.

[92] Kreutz-Delgado, K., Murray, J., Rao, B., Engan, K., Lee, T., and Sejnowski, T. (2003). Dictionary learning algorithms for sparse representation. *Neural Computation*, 15(2):349–396.

[93] Kwiat, D., S. E. (1991). A decoupled coil detector array for fast image acquisition in magnetic resonance imaging. *Medical Physics*, 18(3):251.

[94] Landau, H. (1967). Necessary density conditions for sampling and interpolation of certain entire functions. *Acta Mathematica*, 117(1):37–52.

[95] Lauterbur, P. C. (1973). Image formation by induced local interactions: examples employing nuclear magnetic resonance. *Nature*, 242(5394):190–191.

[96] Lewicki, M. and Sejnowski, T. (2000). Learning overcomplete representations. *Neural Computation*, 12(2):337–365.

[97] Li, X., Wei, Z., Xiao, L., Sun, Y., and Yang, J. (2009). Compressed sensing image reconstruction based on morphological component analysis. In *IEEE*, pages 2129–2132. IEEE.

[98] Liang, D., DiBella, E., Chen, R., and Ying, L. (2011). k-t ISD: Dynamic cardiac MR imaging using compressed sensing with iterative support detection. *Magnetic Resonance in Medicine*.

[99] Liang, D., Liu, B., Wang, J., and Ying, L. (2009). Accelerating SENSE using compressed sensing. *Magn. Res. Med.*, 62(6):1574–1584.

[100] Lin, F., Wang, F. N., Ahlfors, S. P., Hmlinen, M. S., and Belliveau, J. W. (2007). Parallel MRI reconstruction using variance partitioning regularization. *Magnetic Resonance in Medicine*, 58(4):735–744.

[101] Lin, F. H., Huang, T. Y., Chen, N. K., Wang, F. N., Stufflebeam, S. M., Belliveau, J. W., Wald, L. L., and Kwong, K. K. (2005). Functional MRI using regularized parallel imaging acquisition. *Magnetic Resonance in Medicine*, 54(2):343–353.

[102] Liu, B., Zou, Y., and Ying, L. (2008). SparseSENSE: application of compressed sensing in parallel MRI. In *Information Technology and Applications in Biomedicine, 2008. ITAB 2008. International Conference on*, pages 127–130. IEEE.

[103] Lu, Y. and Do, M. (2007). Multidimensional directional filter banks and surfacelets. *Image Processing, IEEE Transactions on*, 16(4):918–931.

[104] Lustig, M., Alley, M., Vasanawala, S., Donoho, D., and Pauly, J. (2009). L1 SPIR-iT: autocalibrating parallel imaging compressed sensing. In *17th Annual Meeting of ISMRM*, page 379.

[105] Lustig, M., Donoho, D., and Pauly, J. (2007). Sparse MRI: The application of compressed sensing for rapid MR imaging. *Magn. Res. Med.*, 58(6):1182–1195.

[106] Lustig, M. and Pauly, J. (2010). SPIRiT: Iterative self-consistent parallel imaging reconstruction from arbitrary k-space. *Magnetic Resonance in Medicine*, 64(2):457–471.

[107] Lustig, M., Santos, J., Donoho, D., and Pauly, J. (2006). kt SPARSE: High frame rate dynamic MRI exploiting spatio-temporal sparsity. In *Proceedings of the 13th Annual Meeting of ISMRM, Seattle*, page 2420.

[108] Madore, B., Glover, G., and Pelc, N. (1999). Unaliasing by Fourier-encoding the overlaps using the temporal dimension (UNFOLD), applied to cardiac imaging and fMRI. *Magnetic Resonance in Medicine*, 42(5):813–828.

[109] Madsen, M. (1992). A simplified formulation of the gamma variate function. *Physics in Medicine and Biology*, 37:1597.

[110] Mahmudimanesh, M., Khelil, A., and Suri, N. (2010). Reordering for better compressibility: Efficient spatial sampling in wireless sensor networks. In *Proc. IEEE Int. Conf. on Sensor Networks, Ubiquitous, and Trustworthy Computing SUTC, Newport Beach, California*, pages 50–57.

[111] Mairal, J., Elad, M., and Sapiro, G. (2008). Sparse representation for color image restoration. *Image Processing, IEEE Transactions on*, 17(1):53–69.

[112] Mairal, J., Sapiro, G., and Elad, M. (2007). Learning multiscale sparse representations for image and video restoration (preprint). Technical report, DTIC Document.

[113] Majumdar, A. and Ward, R. (2009). Classification via group sparsity promoting regularization. In *Acoustics, Speech and Signal Processing, ICASSP . IEEE International Conference on*, pages 861–864. IEEE.

[114] Majumdar, A. and Ward, R. (2011). Accelerating multi-echo T2 weighted MR imaging: Analysis prior group-sparse optimization. *Journal of Magnetic Resonance*, 210(1):90–97.

[115] Maki, J., Prince, M., Londy, F., and Chenevert, T. (1996). The effects of time varying intravascular signal intensity and k space acquisition order on three dimensional MR angiography image quality. *Journal of Magnetic Resonance Imaging*, 6(4):642–651.

[116] Maki, J. H., Wilson, G. J., Eubank, W. B., and Hoogeveen, R. M. (2002). Utilizing SENSE to achieve lower station sub-millimeter isotropic resolution and minimal venous enhancement in peripheral MR angiography. *Journal of Magnetic Resonance Imaging*, 15(4):484–491.

[117] Mallat, S. and Zhang, Z. (1993). Matching pursuits with time-frequency dictionaries. *Signal Processing, IEEE Transactions on*, 41(12):3397–3415.

[118] Mansfield, P. (1977). Multi-planar image formation using NMR spin echoes. *Journal of Physics C: Solid State Physics*, 10(3):L55.

[119] Marks, I. and Robert, J. (1986). Multidimensional-signal sample dependency at nyquist densities. *JOSA A*, 3(2):268–273.

[120] Maronna, R. A., Martin, R. D., and Yohai, V. J. (2006). *Robust Statistics: Theory and Methods*. Wiley Chichester.

[121] McKenzie, C. A., Ohliger, M. A., Yeh, E. N., Price, M. D., and Sodickson, D. K. (2001a). Coil-by-coil image reconstruction with SMASH. *Magnetic Resonance in Medicine*, 46(3):619–623.

[122] McKenzie, C. A., Yeh, E. N., and Sodickson, D. K. (2001b). Improved spatial harmonic selection for SMASH image reconstructions. *Magnetic Resonance in Medicine*, 46(4):831–836.

[123] McRobbie, D. W. (2007). *MRI from Picture to Proton*. Cambridge University Press,.

[124] Mistretta, C., Wieben, O., Velikina, J., Block, W., Perry, J., Wu, Y., and Johnson, K. (2005). Highly constrained backprojection for time-resolved MRI. *Magnetic Resonance in Medicine*, 55(1):30–40.

[125] Mohtashemi, M., Smith, H., Walburger, D., Sutton, F., and Diggans, J. (2010). Sparse sensing DNA microarray-based biosensor: Is it feasible? In *Sensors Applications Symposium (SAS), 2010 IEEE*, pages 127–130. IEEE.

[126] Muller, N., Magaia, L., and Herbst, B. (2004). Singular value decomposition, eigenfaces, and 3D reconstructions. *SIAM review*, 46(3):518–545.

[127] Nam, S., Akcakaya, M., Hu, P., Manning, W. J., V., T., and Nezafat, R. (2010). Impact of Coil Sensitivity Estimation on MRI reconstruction methods combining compressed sensing and parallel MRI. In *Proc. of the 18th Scientific Meeting, Int. Society for Magn. Res. Med. ISMRM10, Stockholm, Sweden*, pages 518–545.

[128] Needell, D. (2009). *Topics in Compressed Sensing*. Ph.D. Dissertation, Math. , Univ. of California, Davis.

[129] Nielsen, M., Kamavuako, E., Andersen, M., Lucas, M., and Farina, D. (2006). Optimal wavelets for biomedical signal compression. *Medical and Biological Engineering and Computing*, 44(7):561–568.

[130] Niendorf, T. and Sodickson, D. (2006). Parallel imaging in cardiovascular MRI: methods and applications. *NMR in Biomedicine*, 19(3):325–341.

[131] Nishimura, D. G. (1996). *Principles of Magnetic Resonance Imaging*. Stanford University.

[132] Olshausen, B. (1996). Emergence of simple-cell receptive field properties by learning a sparse code for natural images. *Nature*, 381(6583):607–609.

[133] Ophir, B., Lustig, M., and Elad, M. (2011). Multi-scale dictionary learning using wavelets. *Selected Topics in Signal Processing, IEEE Journal of*, 5(5):1014–1024.

[134] Otazo, R., Kim, D., Axel, L., and Sodickson, D. (2010). Combination of compressed sensing and parallel imaging for highly accelerated first-pass cardiac perfusion MRI. *Magnetic Resonance in Medicine*, 64(3):767–776.

[135] Pan, Z. and Xiong, H. (2012). Sparse spatio-temporal representation with adaptive regularized dictionaries for super-resolution based video coding. In *Data Compression Conference (DCC),*, pages 139–148. IEEE.

[136] Papoulis, A. (1977). Generalized sampling expansion. *Circuits and Systems, IEEE Transactions on*, 24(11):652–654.

[137] Peters, D., Korosec, F., Grist, T., Block, W., Holden, J., Vigen, K., and Mistretta, C. (2000). Undersampled projection reconstruction applied to MR angiography. *Magnetic Resonance in Medicine*, 43(1):91–101.

[138] Peyre, G. (2007). Best basis compressed sensing. In *Proc. of Scale Space and Variational Methods in Computer Vision SSVM07*, pages 80–91.

[139] Peyre, G. and Fadili, J. (2011). Group sparsity with overlapping partition functions. *Proc. EUSIPCO 2011*, pages 303–307.

[140] Peyre, G. and Mallat, S. (2005). Surface compression with geometric bandelets. In *ACM Transactions on Graphics (TOG)*, volume 24, pages 601–608. ACM.

[141] Pipe, J. G. (1999). Motion correction with PROPELLER MRI: application to head motion and free-breathing cardiac imaging. *Magnetic Resonance in Medicine*, 42(5):963–969.

[142] Prasantha, H., Shashidhara, H., and Balasubramanya Murthy, K. (2007). Image compression using SVD. In *Int. Conf. on Computational Intelligence and Multimedia Applications ICCIMA07*, volume 3, pages 143–145.

[143] Prince, M., Chenevert, T., Foo, T., Londy, F., Ward, J., and Maki, J. (1997). Contrast-enhanced abdominal MR angiography: optimization of imaging delay time by automating the detection of contrast material arrival in the aorta. *Radiology*, 203(1):109–114.

[144] Protter, M. and Elad, M. (2009). Image sequence denoising via sparse and redundant representations. *Image Processing, IEEE Transactions on*, 18(1):27–35.

[145] Pruessmann, K., Weiger, M., Scheidegger, M., and Boesiger, P. (1999a). SENSE: Sensitivity Encoding for fast MRI. *Magn. Res. Med.*, 42(5):952–962.

[146] Pruessmann, K. P., Weiger, M., Brnert, P., and Boesiger, P. (2001). Advances in sensitivity encoding with arbitrary k-space trajectories. *Magnetic Resonance in Medicine*, 46(4):638–651.

[147] Pruessmann, K. P., Weiger, M., Scheidegger, M. B., and Boesiger, P. (1999b). Sense: sensitivity encoding for fast MRI. *Magnetic Resonance in Medicine*, 42(5):952–962.

[148] Qu, X., Cao, X., Guo, D., Hu, C., and Chen, Z. (2010). Compressed sensing MRI with combined sparsifying transforms and smoothed l_0 norm minimization. In *Proc. IEEE Int. Conf. Acous. Speech Sig. Proc. (ICASSP), Dallas*, pages 626–629.

[149] Ra, J. and Rim, C. (1993). Fast imaging using subencoding data sets from multiple detectors. *Magnetic Resonance in Medicine*, 30(1):142–145.

[150] Rabrait, C., Ciuciu, P., Ribes, A., Poupon, C., Le Roux, P., Dehaine Lambertz, G., Le Bihan, D., and Lethimonnier, F. (2008). High temporal resolution functional MRI using parallel echo volumar imaging. *Journal of Magnetic Resonance Imaging*, 27(4):744–753.

[151] Rausch, M., Scheffler, K., Rudin, M., and Radu, E. (2000). Analysis of input functions from different arterial branches with gamma variate functions and cluster analysis for quantitative blood volume measurements. *Magnetic Resonance Imaging*, 18(10):1235–1243.

[152] Ravishankar, S. and Bresler, Y. (2011). MR image reconstruction from highly undersampled k-space data by dictionary learning. *IEEE Trans. Medical Imaging*, 30(5):1028–1041.

[153] Reeves, S. J. and Heck, L. P. (1995). Selection of observations in signal reconstruction. *Signal Processing, IEEE Transactions on*, 43(3):788–791.

[154] Reeves, S. J. and Zhe, Z. (1999). Sequential algorithms for observation selection. *Signal Processing, IEEE Transactions on*, 47(1):123–132.

[155] Riabkov, D. and Bella, E. (2004). Blind identification of the kinetic parameters in three-compartment models. *Physics in Medicine and Biology*, 49:639.

[156] Riabkov, D. and Di Bella, E. (2004). Improved reconstruction of dynamic cardiac perfusion MRI with use of a reference frame. In *Biomedical Imaging: Nano to Macro, 2004. IEEE International Symposium on*, volume 2, pages 1047–1050.

[157] Roemer, P., Edelstein, W., Hayes, C., Souza, S., and Mueller, O. (1990a). The NMR phased array. *Magnetic Resonance in Medicine*, 16(2):192–225.

[158] Roemer, P., Edelstein, W., Hayes, C., Souza, S., and Mueller, O. (1990b). The NMR phased array. *Magnetic Resonance in Medicine*, 16(2):192–225.

[159] Roth, S. and Black, M. (2005). Fields of experts: A framework for learning image priors. In *In IEEE Conf. on Computer Vision and Pattern Recognition.*, volume 2, pages 860–867. IEEE.

[160] Rubinstein, R., Bruckstein, A., and Elad, M. (2010a). Dictionaries for sparse representation modeling. *Proceedings of the IEEE*, 98(6):1045–1057.

[161] Rubinstein, R., Zibulevsky, M., and Elad, M. (2008). Efficient implementation of the K-SVD algorithm using batch orthogonal matching pursuit. *CS Technion*.

[162] Rubinstein, R., Zibulevsky, M., and Elad, M. (2010b). Double sparsity: Learning sparse dictionaries for sparse signal approximation. *Signal Processing, IEEE Transactions on*, 58(3):1553–1564.

[163] Rudin, L., Osher, S., and Fatemi, E. (1992). Nonlinear total variation based noise removal algorithms. *Physica D: Nonlinear Phenomena*, 60(1):259–268.

[164] Sankaranarayanan, A., Turaga, P., Baraniuk, R., and Chellappa, R. (2010). Compressive acquisition of dynamic scenes. *Computer VisionECCV 2010*, pages 129–142.

[165] Selesnick, I., Baraniuk, R., and Kingsbury, N. (2005). The dual-tree complex wavelet transform. *Signal Processing Magazine, IEEE*, 22(6):123–151.

[166] Shannon, C. E. (1949). Communication in the presence of noise. *Proceedings of the IRE*, 37(1):10–21.

[167] Shtok, J., Elad, M., and Zibulevsky, M. (2011). Sparsity-based sinogram denoising for low-dose computed tomography. In *Acoustics, Speech and Signal Processing (ICASSP), IEEE International Conference on*, pages 569–572. IEEE.

[168] Sodickson, D. and Manning, W. (1997a). Simultaneous acquisition of spatial harmonics (SMASH): fast imaging with radiofrequency coil arrays. *Magnetic Resonance in Medicine*, 38(4):591–603.

[169] Sodickson, D. K. (1999). Simultaneous acquisition of spatial harmonics (smash): ultra-fast imaging with radiofrequency coil arrays. *Google Patents*, jun.

[170] Sodickson, D. K. (Chichester, 2000). Spatial encoding using multiple RF coils: SMASH imaging and parallel MRI. *Methods in Biomedical Magnetic Resonance Imaging and Spectroscopy*, John Wiley & Sons.:239250.

[171] Sodickson, D. K. and Manning, W. J. (1997b). Simultaneous acquisition of spatial harmonics (SMASH): fast imaging with radiofrequency coil arrays. *Magnetic Resonance in Medicine*, 38(4):591–603.

[172] Sodickson, D. K., McKenzie, C. A., Ohliger, M. A., Yeh, E. N., and Price, M. D. (2001). Recent advances in image reconstruction, coil sensitivity calibration, and coil array design for SMASH and generalized parallel MRI. *Magnetic Resonance Materials in Physics, Biology and Medicine*, 13(3):158–163.

[173] Starck, J., Elad, M., and Donoho, D. (2003). Image decomposition: Separation of texture from piecewise smooth content. In *Proc. SPIE Annual Meeting*.

[174] Starck, J., Elad, M., and Donoho, D. (2005). Image decomposition via the combination of sparse representations and a variational approach. *Image Processing, IEEE Transactions on*, 14(10):1570–1582.

[175] Stojnic, M. (2009). Strong thresholds for l2/l1-optimization in block-sparse compressed sensing. In *Acoustics, Speech and Signal Processing, 2009. ICASSP 2009. IEEE International Conference on*, pages 3025–3028. IEEE.

[176] Stojnic, M., Parvaresh, F., and Hassibi, B. (2009). On the reconstruction of block-sparse signals with an optimal number of measurements. *Signal Processing, IEEE Transactions on*, 57(8):3075–3085.

[177] Strang, G. and Nguyen, T. (1996). *Wavelets and Filter Banks*. Cambridge University Press.

[178] Sun, Y. and Parker, D. (2001). Small vessel enhancement in MRA images using local maximum mean processing. *Image Processing, IEEE Transactions on*, 10(11):1687–1699.

[179] Sun, Y. and Parker, D. L. (1999). Performance analysis of maximum intensity projection algorithm for display of MRA images. *Medical Imaging, IEEE Transactions on*, 18(12):1154–1169.

[180] Sychra, J., Bandettini, P., Bhattacharya, N., and Lin, Q. (1994). Synthetic images by subspace transforms I. principal components images and related filters. *Medical Physics*, 21:193–200.

[181] Tropp, J. (2004). Greed is good: Algorithmic results for sparse approximation. *IEEE Trans. Inf. Theory*, 50(10):2231–2242.

[182] Tropp, J. and Gilbert, A. (2005). Signal recovery from partial information via orthogonal matching pursuit. *IEEE Trans. Inform. Theory*, Preprint.

[183] Tropp, J. and Gilbert, A. (2007). Signal recovery from random measurements via orthogonal matching pursuit. *IEEE Trans. Inf. Theory*, 53(12):4655–4666.

[184] Trzasko, J., Haider, C., and Manduca, A. (2009). Practical nonconvex compressive sensing reconstruction of highly-accelerated 3D parallel MR angiograms. In *Biomedical Imaging: From Nano to Macro, ISBI'09. IEEE International Symposium on*, pages 274–277. IEEE.

[185] Tsao, J., Boesiger, P., and Pruessmann, K. (2003). klt BLAST and klt SENSE: Dynamic MRI with high frame rate exploiting spatiotemporal correlations. *Magnetic Resonance in Medicine*, 50(5):1031–1042.

[186] Turski, P. A., Korosec, F. R., Carroll, T. J., Willig, D. S., Grist, T. M., and Mistretta, C. (2001). Contrast-enhanced magnetic resonance angiography of the carotid bifurcation using the time-resolved imaging of contrast kinetics (TRICKS) technique. *Topics in Magnetic Resonance Imaging*, 12(3):175–181.

[187] Twieg, D. B. (1983). The k-trajectory formulation of the NMR imaging process with applications in analysis and synthesis of imaging methods. *Medical Physics*, 10:610.

[188] Usman, M., Prieto, C., Schaeffter, T., and Batchelor, P. (2011). k-t group sparse: A method for accelerating dynamic MRI. *Magnetic Resonance in Medicine*, 66(4):1163–1176.

[189] Vafadar, B. and Bones, P. (2012). MR images from fewer data. In *Image Reconstruction from Incomplete Data VII, Proceedings SPIE,*, pages 850003–850003. IEEE.

[190] Vafadar, B., Wu, B., and Bones, P. (2009). A statistical method for display and segmentation of 3D image data. In *Proc. Int. Conf. Image and Vision Computing New Zealand*, pages 148–152. IEEE.

[191] van den Berg, E., Schmidt, M., Friedlander, M., and Murphy, K. (2008). Group sparsity via linear-time projection. *Dept. Comput. Sci., Univ. British Columbia, Vancouver, BC, Canada*.

[192] Van Vaals, J. J., Brummer, M. E., Thomas Dixon, W., Tuithof, H. H., Engels, H., Nelson, R. C., Gerety, B. M., Chezmar, J. L., and Den Boer, J. A. (2005). Keyhole method for accelerating imaging of contrast agent uptake. *Journal of Magnetic Resonance Imaging*, 3(4):671–675.

[193] Vasanawala, S., Alley, M., Hargreaves, B., Barth, R., Pauly, J., and Lustig, M. (2010). Improved pediatric MR imaging with compressed sensing. *Radiology*, 256(2):607–616.

[194] Vasanawala, S., Murphy, M., Alley, M., Lai, P., Keutzer, K., Pauly, J., and Lustig, M. (2011). Practical parallel imaging compressed sensing MRI: Summary of two years of experience in accelerating body MRI of pediatric patients. In *Biomedical Imaging: From Nano to Macro, 2011 IEEE International Symposium on*, pages 1039–1043. IEEE.

[195] Verdu, S. (1998). *Multiuser detection*. Cambridge University Press.

[196] Vogt, F., Eggebrecht, H., Laub, G., Kroeker, R., Schmidt, M., Barkhausen, J., and Ladd, S. (2007). High spatial and temporal resolution MRA (TWIST) in acute aortic dissection. *Proc ISMRM, Berlin*, page 92.

[197] Wakin, M., Laska, J., Duarte, M., Baron, D., Sarvotham, S., Takhar, D., Kelly, K., and Baraniuk, R. (2006). An architecture for compressive imaging. In *Image Processing, IEEE International Conference on*, pages 1273–1276. IEEE.

[198] Weiger, M., Pruessmann, K., and Boesiger, P. (2002a). 2D SENSE for faster 3D MRI. *Magnetic Resonance Materials in Physics, Biology and Medicine*, 14(1):10–19.

[199] Weiger, M., Pruessmann, K. P., and Boesiger, P. (2000a). Cardiac real-time imaging using SENSE. *Magnetic Resonance in Medicine*, 43(2):177–184.

[200] Weiger, M., Pruessmann, K. P., Kassner, A., Roditi, G., Lawton, T., Reid, A., and Boesiger, P. (2000b). Contrast-enhanced 3D MRA using SENSE. *Journal of Magnetic Resonance Imaging*, 12(5):671–677.

[201] Weiger, M., Pruessmann, K. P., sterbauer, R., Brnert, P., Boesiger, P., and Jezzard, P. (2002b). Sensitivity-encoded single-shot spiral imaging for reduced susceptibility artifacts in BOLD fMRI. *Magnetic Resonance in Medicine*, 48(5):860–866.

[202] Wierzbicki, M., Guiraudon, G., Jones, D., and Peters, T. (2007). Dose reduction for cardiac CT using a registration-based approach. *Medical Physics*, 34:1884.

[203] Willett, R., Gehm, M., and Brady, D. (2007). Multiscale reconstruction for computational spectral imaging. *Computational Imaging V at SPIE Electronic Imaging*.

[204] Wright, S., Nowak, R., and Figueiredo, M. (2009). Sparse reconstruction by separable approximation. *Signal Processing, IEEE Transactions on*, 57(7):2479–2493.

[205] Wu, B., Millane, R., Watts, R., and Bones, P. (2008). Sparsified inversion for direct image recovery in MRI. In *Proc. Intl. Soc. Magnetic Resonance in Medicine*, volume 16 (CD-ROM). ISMRM.

[206] Wu, B., Millane, R., Watts, R., and Bones, P. (2009a). Improved matrix inversion in image plane parallel MRI. *Magnetic Resonance Imaging*, 27(7):942–953.

[207] Wu, B., Millane, R., Watts, R., and Bones, P. (2011). Prior estimated-based compressed sensing in parallel MRI. *Magnetic Resonance in Medicine*, 65(1):83–95.

[208] Wu, B., Watts, R., Millane, R., and Bones, P. (2009b). An improved approach in applying compressed sensing in parallel MR imaging. In *Proc. 17th Sci. Mtg., Int. Soc. Magnetic Resonance in Medicine, ISMRM09, Honolulu*, page 4595.

[209] Yu, G., Mallat, S., and Bacry, E. (2008). Audio denoising by time-frequency block thresholding. *Signal Processing, IEEE Transactions on*, 56(5):1830–1839.

[210] Zhang, H., Maki, J., and Prince, M. (2007). 3D contrast enhanced MR angiography. *Journal of Magnetic Resonance Imaging*, 25(1):13–25.

[211] Zhang, Z. and Rao, B. (2011). Sparse signal recovery with temporally correlated source vectors using sparse bayesian learning. *Selected Topics in Signal Processing, IEEE Journal of*, 5(5):912–926.